CHARACTERIZATION OF NOSX FROM *ACHROMOBACTER CYCLOCLASTES* AND CO-CRYSTALLIZATION OF N_2OR AND PAZ

by

Fumihiro Ijima

A dissertation submitted in partial fulfillment
of the requirements for the degree

of

Doctor of Philosophy

in

Biochemistry

MONTANA STATE UNIVERSITY
Bozeman, Montana

February 2013

©COPYRIGHT

by

Fumihiro Ijima

2013

All Rights Reserved

APPROVAL

of a dissertation submitted by

Fumihiro Ijima

This dissertation has been read by each member of the dissertation committee and has been found to be satisfactory regarding content, English usage, format, citation, bibliographic style, and consistency and is ready for submission to The Graduate School.

Dr. David M. Dooley

Approved for the Department of Chemistry & Biochemistry

Dr. Mary Cloninger

Approved for The Graduate School

Dr. Ronald W. Larsen

STATEMENT OF PERMISSION TO USE

In presenting this dissertation in partial fulfillment of the requirements for a doctoral degree at Montana State University, I agree that the Library shall make it available to borrowers under rules of the Library. I further agree that copying of this dissertation is allowable only for scholarly purposes, consistent with "fair use" as prescribed in the U.S. Copyright Law. Requests for extensive copying or reproduction of this dissertation should be referred to ProQuest Information and Learning, 300 North Zeeb Road, Ann Arbor, Michigan 48106, to whom I have granted "the exclusive right to reproduce and distribute my dissertation in and from microform along with the non-exclusive right to reproduce and distribute my abstract in any format in whole or in part."

Fumihiro Ijima

February 2013

ACKNOWLEDGEMENTS

I would like to acknowledge Dr. David Dooley for his insights, guidance, and helpful discussions. I would also like to acknowledge my collaborators, Dr. Martin Lawrence for help with X-ray crystallography studies, and Dr. Takamitsu Kohzuma for help with studies on pseudoazurin.

I would like to thank Dr. Nathanael Lintner, Dr. George Gauss, and Brian Eilers for their help with crystal growth and X-ray measurements, Dr. Jonathan Hilmer for measurements with mass spectrometry, Dr. Eric Shepard for measurements with EPR spectrometry, and Dr. Duane Mooney for his assistance with fluorescence spectrometry.

I would also like to thank present and previous Dooley lab members, especially Dr. Doreen Brown and Kimberly Hilmer for their patient and intensive support on my English writing, Dr. Koyu Fujita for training and helping me to handle nitrous oxide reductase as well as insightful discussions and advice, and Dr. John Bollinger for his help on the molecular biology work on NosX. I could not reach the goal without their support.

TABLE OF CONTENTS

1. INTRODUCTION 1

Nitrogen Cycle and Denitrification.....1
Metalloenzymes of Denitrification 3
Nitrate Reductase (NaR).....4
Nitrite Reductase (NiR) 6
Nitric Oxide Reductase (NOR).....10
Nitrous Oxide Reductase (N_2OR).....14
Pseudoazurin (PAz) 23
Accessory Proteins for N_2OR 26
NosR as the Regulator of the Nos Gene Expressions and the Activator of N_2OR.....29
NosD, NosF, and NosY as the Cu_Z Site Assembly System.....31
Copper Chaperon Protein NosL.....32
Flavoprotein NosX.....34
Other Nos Proteins.....36
Research Goals.....39

2. PRODUCTION AND PURIFICATION OF NOSX: GENE STRUCTURE REFINEMENT, AND OPTIMIZATION OF THE CULTURE AND PURIFICATION CONDITIONS FOR NOSX.....40

Introduction.....40
Materials and Methods.....41
Growth and Purification of NosX.....41
Promoter Refinement for NosX.....43
Subcloning of *nosX* Gene from pMLClustXst.....43
Isolation of Promoters of *Ac*NiR and *Ac*PAz.....46
Assembly of *nosX* Gene and Promoters of *Ac*NiR and *Ac*PAz on p5 plasmid.....47
Optimization of Culture Conditions for NosX.....49
Optimization of Purification Conditions for NosX.....50
Results.....51
Promoter Refinement for NosX.....51
Optimization of Culture Conditions for NosX.....53
Optimization of Purification Conditions for NosX.....58
Discussion.....59
Promoter Refinement for NosX.....60
Culture Conditions for NosX.....62
Purification Conditions for NosX.....65
Conclusions.....66

TABLE OF CONTENTS - CONTINUED

3. CHARACTERIZATION OF NOSX FROM *ACHROMOBACTER CYCLOCLASTES* 68

Introduction 68
Materials and Methods 69
Confirmation of the DNA Sequence of *nosX* Gene 69
Molecular Weight and Quaternary Structure of *Ac*NosX 69
Cofactor Identification 70
Redox Potential 71
Secondary and Tertiary Structure Predictions 72
Crystallization trials 73
Results 74
Confirmation of the DNA Sequence of *nosX* Gene 74
Molecular Weight and Quaternary Structure of *Ac*NosX 74
Cofactor Identification 75
Redox Potential 77
Secondary and Tertiary Structure Predictions 79
Crystallization Trials 84
Discussion 85
Identity Confirmation of Purified *Ac*NosX 85
Characterization of the Cofactor in *Ac*NosX 85
Structural Aspects of *Ac*NosX 87
Conclusions 90

4. INVESTIGATIONS ON THE FUNCTION OF NOSX FROM *ACHROMOBACTER CYCLOCLASTES* 91

Introduction 91
Materials and Methods 93
Expression and Purification of Pseudoazurin from *Achromobacter cycloclastes* 93
Expression and Purification of N_2OR from *Achromobacter cycloclastes* 95
Electron Transfer from *Ac*NosX to *Ac*N_2OR 98
Regeneration of the Cu_Z* State in *Ac*N_2OR with *Ac*NosX 101
Electron Transfer from Reduced *Ac*NosX to Oxidized *Ac*PAz 102
Catalytic Reaction of *Ac*N_2OR with Reduced *Ac*NosX 102
Identification of Inhibitory Factor for the N_2OR Catalytic Cycles with *Ac*PAz 103

TABLE OF CONTENTS - CONTINUED

*Ac*NosX Stabilization in Solution 104
Results 105
Electron Transfer from *Ac*NosX to *Ac*N_2OR 105
Regeneration of the Cu_Z* State in *Ac*N_2OR with *Ac*NosX 111
Electron Transfer from Reduced *Ac*NosX to Oxidized *Ac*PAz 113
Catalytic Reaction of *Ac*N_2OR with Reduced *Ac*NosX 114
Identification of Inhibitory Factor for the N_2OR Catalytic Cycles with *Ac*PAz 117
*Ac*NosX Stabilization in Solution 121
Discussion 122
Function of *Ac*NosX as an Electron Donor for *Ac*N_2OR 122
Function of *Ac*NosX for Regeneration of the Cu_Z* State in *Ac*N_2OR 126
Function of *Ac*NosX as an Electron Donor for *Ac*PAz 128
Identification of Inhibitory Factor for the N_2OR Catalytic Cycle 128
Function of *Ac*NosX in the N_2OR Catalytic Cycle 133
Stability of *Ac*NosX *in Vitro* 134
Substrate Bound N_2OR Structure from *Pseudomonas stutzeri* 136
New Hypothesis on the Electron Transfer from Cu_A to Cu_Z 136
New Definition of the Cu_Z* State 137
Conclusions 138

5. CO-CRYSTALLIZATION OF N_2OR AND PSEUDOAZURIN FROM *ACHROMOBACTER CYCLOCLASTES* 140

Introduction 140
Materials and Methods 142
Screening of Crystallization Conditions 142
Optimization of Crystallization Conditions 142
Crystal Check for Protein or Salt 143
X-ray Measurements of the Co-crystals 144
Crosslink of *Ac*N_2OR and *Ac*PAz 146
Results 148
Screening and Optimizations of Crystallization Conditions 148
Crystal Check for Protein 151
X-ray Measurements of the Co-crystals 152
Crosslink of *Ac*N_2OR and *Ac*PAz 155

TABLE OF CONTENTS - CONTINUED

Discussion.....157
Conclusions.....160

6. CONCLUDING REMARKS AND FUTURE DIRECTIONS.....161

APPENDICES 164

APPENDIX A: Supporting Information for Chapter 1.....165
APPENDIX B: Supporting Information for Chapter 2.....168
APPENDIX C: Supporting Information for Chapter 3.....171
APPENDIX D: Supporting Information for Chapter 4.....174

REFERENCES CITED.....181

LIST OF TABLES

Table Page

1.1. Structural types of N_2OR variants....38

2.1. Variables tested for effects on the yield of NosX....50

2.2. The NosX yields from the refined expression systems with the LB from RPI....52

2.3. The NosX yields from the refined expression systems with the LB from Fisher....53

2.4. The NosX yields with different LB media brands (RPI vs. Fisher)....54

2.5. The NosX yields with or without riboflavin....55

2.6. The NosX yields with different shaking speeds (100 vs. 250 rpm)....55

2.7. NosX yields following 24 or 48 hours culture post induction....56

2.8. NosX yields from the original and optimized culture conditions....58

3.1. Secondary structure predictions of *Ac*NosX by JUFO, PSIpred, and PAPIA....80

4.1. Spin quantification of EPR spectra of *Ac*N_2OR....109

4.2. Redox state assignments of each form of *Ac*N_2OR....110

4.3. *Ac*PAz oxidation during the N_2OR catalytic cycle in various buffers....119

5.1. The initial crystallization conditions for *Ac*N_2OR-*Ac*PAz co-crystal....148

5.2. Band intensities on the SDS-PAGE gel in Figure 5.9....157

LIST OF FIGURES

Figure Page

1.1. A schematic view of the nitrogen cycle 1

1.2. Crystal structures of nitrate reductase A complex from *E. coli* 5

1.3. Crystal structures of *Ac*CuNiR and cd_1NiR from *Paracoccus pantotrophus* 6

1.4. Coordination around the Cu sites in *Ac*NiR 7

1.5. The proposed catalytic mechanism for *Ac*CuNiR 9

1.6. Crystal structure of nitric oxide reductase from *Pseudomonas aeruginosa* 11

1.7. Proposed structures of hyponitrite intermediate in *trans*- and *cis*-mechanism for NOR 13

1.8. Crystal structure of a monomeric form of *Ac*N_2OR and a schematic model of the dimeric form of *Ac*N_2OR 15

1.9. Coordinations around the Cu_A and Cu_Z sites of *Ac*N_2OR 16

1.10. Calculated Cu_Z–N_2O complex and proposed catalytic mechanism for *Ac*N_2OR 20

1.11. [4Cu:2S] form of the Cu_Z site in N_2OR from *Pseudomonas stutzeri* 22

1.12. Crystal structure of *Ac*PAz and coordination environment of the Cu center 23

1.13. Calculated docking structures of *Ac*N_2OR and *Ac*PAz, and putative electron transfer pathways from the T1Cu of *Ac*PAz to the Cu_A of *Ac*N_2OR 25

1.14. The *nos* cluster from *Achromobacter cycloclastes* 26

1.15. Distribution of the Nos proteins from *Achromobacter cycloclastes* 27

1.16. Structural elements of unprocessed NosR and mutated NosR 30

LIST OF FIGURES – CONTINUED

Figure Page

1.17. NMR structure of apo-*Ac*NosL 34

1.18. The *nos* gene cluster from *Wolinella succinogenes* and distribution of the Nos proteins 37

2.1. Schematic view of the assembling process of a new NosX expression system 44

2.2. NosX yield and cell amount vs. A_{600} at induction 57

2.3. SDS-PAGE and western blot for NosX purification 59

3.1. Quaternary structure analysis of *Ac*NosX with a gel filtration column.....75

3.2. Normalized fluorescence spectra of *Ac*NosX cofactor, FAD and FMN with or without PDE.....76

3.3. Stepwise photo-reductions of *Ac*NosX and anthraquinone 2-sulfonate 78

3.4. Titration measurement of redox potential of *Ac*NosX.....79

3.5. *Ac*NosX model based on ApbE and surface electrostatic potential.....81

3.6. Hydrophobicity of the *Ac*NosX model 81

3.7. Sequence alignment of NosX proteins and ApbE.....82

3.8. Distribution of the conserved amino acids and potential FAD binding residues in the *Ac*NosX model.....83

3.9. Pictures of putative crystals from condition #1 84

4.1. Schematic view of sample preparation for the EPR measurements 99

4.2. UV/Vis spectra of reduced *Ac*NosX, oxidized *Ac*N_2OR, and *Ac*NosX reduced *Ac*N_2OR.....106

LIST OF FIGURES – CONTINUED

Figure Page

4.3. UV/Vis spectra and differential spectrum of *Ac*N_2OR samples for EPR....107

4.4. EPR spectra of *Ac*N_2OR samples at 14 K....108

4.5. Photo-reduction of *Ac*N_2OR in the absence of *Ac*NosX....112

4.6. Photo-reduction of *Ac*N_2OR in the presence of *Ac*NosX....112

4.7. UV/Vis spectra of reduced *Ac*NosX, oxidized *Ac*PAz, and *Ac*NosX reduced *Ac*PAz....114

4.8. Oxidation of *Ac*NosX during the N_2OR catalytic cycle and time course at 460 nm....115

4.9. Time course for the oxidation of free FAD during the N_2OR catalytic cycle....116

4.10. UV/Vis spectra of *Ac*PAz oxidation during the N_2OR catalytic cycle with buffer #1 and time course at A_{594} in buffer #1 - 3....117

4.11. Time course for the oxidation of *Ac*PAz during the N_2OR catalytic cycle in buffer #4 - 5....118

4.12. Time course for the oxidation of *Ac*PAz during the N_2OR catalytic cycle in buffer #6 and 7....119

4.13. The N_2OR activity in buffer #1, 2, and 6....120

4.14 UV/Vis spectra of *Ac*NosX with spermine, NaCl, and flowthrough....121

4.15. The Cu_A, Cu_Z, and chloride binding sites in the C-terminal domain of *Ac*N_2OR (iodide bound form)....132

5.1. Crystals obtained from conditions #1 - 4....149

5.2. Crystal shape transition with 150 and 250 mM lithium sulfate (condition #1)....150

LIST OF FIGURES – CONTINUED

Figure Page

5.3. Crystals obtained from modified condition #3 150

5.4. Crystals obtained from modified condition #4 151

5.5. Crystal checks with the Izit dye and SDS-PAGE for condition #1 and #4 152

5.6. Diffractions from the crystals with flash and overnight introduction of cryoprotectant.....154

5.7. SDS-PAGE and band quantification for *Ac*N_2OR-*Ac*PAz crosslink 155

5.8. *Ac*N_2OR-*Ac*PAz crosslink with activated *Ac*PAz or *Ac*N_2OR.....156

5.9. *Ac*N_2OR-*Ac*PAz crosslink in the coupling buffer with or without NaCl.....157

5.10. Expected crosslink sites of *Ac*PAz and *Ac*N_2OR.....159

LIST OF ABBREVIATIONS

A. cycloclastes or *Ac*: *Achromobacter cycloclastes*
AA: Atomic absorption
ABC: ATP binding cassette
AcN_2OR: Nitrous oxide reductase from *Achromobacter cycloclastes*
*Ac*NosX: NosX from *Achromobacter cycloclastes*
*Ac*PAz: Pseudoazurin from *Achromobacter cycloclastes*
Amp: Ampicillin
APBS: Adaptive Poisson-Boltzmann solver
AS: Anthraquinone 2-sulfonate
ATP: Adenosine triphosphate
BCA: Bicinchoninic acid
*Bj*NosX: NosX from *Bradyrhizobium japonicum*
BLAST: Basic local alignment search tool
BSA: Bovine serum albumin
Buffer P: 100 mM phosphate, 150 mM NaCl, 10 % glycerol, pH 7.0
Buffer PE: 100 mM phosphate, 150 mM NaCl, 10 % glycerol, and 10 mM EDTA, pH 7.0
Buffer W: 100 mM Tris, 150 mM NaCl, 10 % glycerol, and 1 mM EDTA, pH 8.0
BV: Benzyl viologen
CASH: Carbohydrate binding proteins and sugar hydrolases
CBB: Coomassie Brilliant Blue
CD: Circular dichroism
cd_1NiR: Heme cd_1 containing nitrite reductase
CuNiR: Cu containing nitrite reductase
CV: Column volume
DFT: Density functional theory
DT: Dithionite
E. coli: *Escherichia coli*
EDC: 1-Ethyl-3-[3-dimethylaminopropyl] carbodiimide hydrochloride
EDTA: Ethylenediaminetetraacetic acid
EPR: Electron paramagnetic resonance
ESI: Electrospray ionization
FAD: Flavin adenine dinucleotide
FMN: Flavin mononucleotide
Gm: Gentamicin
GST: Glutathione S-transferase
IPTG: Isopropyl β-D-1-thiogalactopyranoside
LMCT: Ligand-metal charge transfer
M. hydrocarbonoclasticus: *Marinobacter hydrocarbonoclasticus*
MBP: Maltose binding protein
MPD: 2-methyl 2,4-pentanediol
MV: Methyl viologen

LIST OF ABBREVIATIONS – CONTINUED

MW: Molecular weight
N_2OR: Nitrous oxide reductase
Nap: periplasmic nitrate reductase
NaR: Nitrate reductase
Nas: Assimilatory nitrate reductase
NHS: N-hydroxysuccinimide
NiR: Nitrite reductase
NOR: Nitric oxide reductase
p5: pBBR1MCS-5
PAz: Pseudoazurin
PCR: Polymerase chain reaction
PDB: Protein databank
PDE: phosphodiesterase I
*Pd*NosX: NosX from *Paracoccus denitrificans PD1222*
PEG: Polyethylene glycol
PEG mme: PEG monomethylether
SDS-PAGE: Sodium dodecyl sulfate polyacrylamide gel electrophoresis
*Sm*NosX: NosX from *Sinorhizobium meliloti*
SSRL: Stanford Synchrotron Radiation Lightsource
T1Cu: Type I copper
T2Cu: Type II copper
W. succinogenes or *Ws*: *Wolinella succinogenes*
WT: wild type

ABSTRACT

Nitrous oxide (N_2O) is known as a greenhouse gas and an ozone-depleting substance. Denitrifying bacteria such as *Achromobacter cycloclastes* emit N_2O into the atmosphere during the denitrification process. Up to seventy percent of the total N_2O emission on the earth is derived from this process. N_2O is a very stable substance and its lifetime in the atmosphere is 114 years. Investigation of N_2O reductase (N_2OR) and its accessory proteins may ultimately be useful in the design of catalytic systems, either biological or chemical, for the control of N_2O level.

The first aim of this research is to characterize NosX, which is one of the accessory proteins for N_2OR. Although NosX was shown to be involved in the activation of N_2OR, the structure and function of NosX and the mechanism of NosX on N_2OR activation are still unknown. Furthermore, NosX has never been isolated and probed. In this study, culture conditions for NosX expression in *A. cycloclastes* (*Ac*NosX) were optimized to obtain adequate amounts of *Ac*NosX (chapter 2), and *Ac*NosX was characterized with UV/Vis, fluorescence, EPR, and MS spectrometry (chapter 3). The structure of *Ac*NosX was investigated by computational and modeling methods (chapter 3). Crystallization trials were also undertaken. The mechanism of N_2OR activation by *Ac*NosX was studied with UV/Vis and EPR spectrometry (chapter 4). We demonstrated that *Ac*NosX was redox active and donated electrons to the Cu sites of *Ac*N_2OR. The information revealed from this research will help to fully understand the activation mechanism of N_2OR with NosX.

The second aim of the research is to investigate the interaction between *Ac*N_2OR and its potential physiological electron donor, pseudoazurin (PAz) (chapter 5). X-ray crystallographic techniques were utilized to determine the structure of the *Ac*N_2OR-*Ac*PAz complex and conditions were identified that grew crystals that included both *Ac*N_2OR and *Ac*PAz. Although the crystals showed diffraction patterns, further optimization is required to identify the complex structure. The information from this research will be important to elucidate the docking mechanism for electron transfer between N_2OR and PAz.

CHAPTER 1

INTRODUCTION

Nitrogen Cycle and Denitrification

Nitrogen circulates within the air, soil, water, and organic matter. This process is called the nitrogen cycle and is composed of nitrogen fixation, nitrification, and denitrification as represented in Figure 1.1 (1; 2).

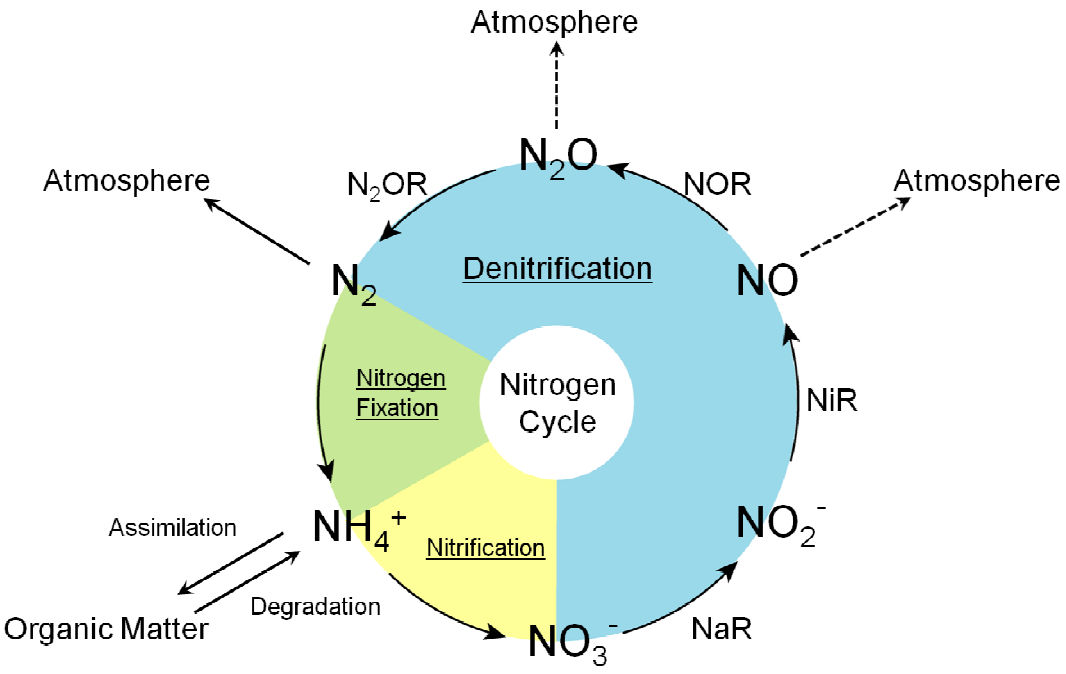


Figure 1.1. A schematic view of the nitrogen cycle.

Denitrification is a process that reduces nitrate (NO_3^-) to dinitrogen (N_2) in four steps ($NO_3^- \rightarrow NO_2^- \rightarrow NO \rightarrow N_2O \rightarrow N_2$) (3) and is a respiratory system that uses nitrogen oxides as electron sinks under anaerobic/micro-aerobic conditions.

Denitrification is performed by bacteria and archaea in soils, rivers, oceans, and under extreme environments (e.g. high pressure, pH, and/or temperature) (4). The denitrification process is important because it releases fixed nitrogen to the atmosphere, ultimately balancing nitrogen distribution among air, soil, and water (5). Each step in the denitrification process is catalyzed by distinct metalloenzymes (see next section).

Denitrification directly influences the environment (6). Denitrifying bacteria such as *Achromobacter cycloclastes* (*Ac*) reduce surplus nitrogen oxides in contaminated soil and water. It is reported that nitrate and nitrite from fertilizer are the major water pollutants, which are leached mainly from farmlands (6; 7). From this perspective, it is significant to study the bacterial denitrification pathway that can effectively decrease excess nitrogen oxides in the environment.

Denitrifying bacteria may also emit nitrous oxide (N_2O) into the atmosphere during this process (Figure 1.1). It is estimated that ~ 70 % of the total N_2O emission on the earth is derived from the denitrification process (8). To date, N_2O is the third most abundant (9 %) greenhouse gas in the atmosphere following carbon dioxide (72 %) and methane (18 %) (6; 9). Although the abundance ratio of N_2O in the atmosphere is less significant than CO_2, N_2O still has a large impact on the environment since the global-warming potential of N_2O is ~ 300 times higher than that of CO_2 (10; 11). N_2O is also known as an ozone-depleting substance (6). N_2O is reported to be the most alarming ozone-depleting substance since N_2O emission is expected to be the most abundant among ozone-depleting compounds throughout the 21st century (10). In addition, N_2O is very stable and its lifetime in the atmosphere is 114 years (10). Thus, it is important to

study the mechanism of N_2O reduction by N_2OR and its accessory proteins for possible biological or chemical catalytic systems to remove N_2O from the atmosphere.

Metalloenzymes of Denitrification

The equation below (Eq.1) represents the denitrification process (7):

$$2NO_3^- + 10e^- + 12H^+ \rightarrow N_2 + 6H_2O \qquad \text{(Eq. 1)}$$

This equation is a summation of the four successive reactions below (Eq. 2 - 5):

$$NO_3^- + 2e^- + 2H^+ \rightarrow NO_2^- + H_2O \qquad \text{(Eq. 2)}$$

$$NO_2^- + e^- + 2H^+ \rightarrow NO + H_2O \qquad \text{(Eq. 3)}$$

$$2NO + 2e^- + 2H^+ \rightarrow N_2O + H_2O \qquad \text{(Eq. 4)}$$

$$N_2O + 2e^- + 2H^+ \rightarrow N_2 + H_2O \qquad \text{(Eq. 5)}$$

These reactions are catalyzed by nitrate reductase (NaR) (Eq. 2), nitrite reductase (NiR) (Eq. 3), nitric oxide reductase (NOR) (Eq. 4), and nitrous oxide reductase (N_2OR) (Eq. 5), respectively (Figure 1.1). The conversion of N_2O to N_2 is exergonic ($\Delta G^{\circ\prime} = -339.5$ kJ/mol) and energetically favorable (12).

Nitric oxide (NO) is a toxic metabolite in denitrification which is produced by NiR and detoxified by NOR (Eq. 3 & 4). The expressions and activity levels of NiR and NOR are known to be tightly regulated to keep the NO concentration low in the cell (13). In contrast, nitrous oxide (N_2O), which is another metabolite in denitrification (Eq. 4 & 5), does not show any obvious toxicity to the cell (3). Thus, there is not a strict requirement for the cell to regulate N_2OR expression and activity (14). Some denitrifying bacteria do not always express N_2OR even though they contain an intact *nos* gene cluster,

which codes for proteins to express active N_2OR (15). Also, other denitrifying bacteria can survive without the *nos* gene cluster (15). In addition, when the environment becomes anaerobic and denitrification respiration starts, the N_2OR expression from the *nos* gene cluster is induced far later than the expressions for the other denitrifying related reductases (NaR, NiR, and NOR) (14). Thus, N_2O is transiently accumulated in cultures. N_2OR activity in whole cells becomes obvious 20 ~ 40 hours after the conditions become anaerobic (14; 16). These observations imply that the reduction of N_2O does not seem to be an absolute requirement for the denitrifying organisms (14). This seems to be a factor of N_2O emission from the denitrifying organisms in the presence of excess nitrogen oxides, which potentially cause the environmental problems such as global warming and ozone layer destruction. An overview of each metalloenzyme will be described below.

Nitrate Reductase (NaR)

Nitrate reductases are molybdenum containing enzymes that catalyze the reduction of nitrate to nitrite (Eq. 2). The physiological significance of nitrate reductases for organisms has been reported as respiration (to generate energy) and assimilatory ammonification (to incorporate nitrogen into a biomolecule) (7; 17). According to the function and its location, nitrate reductases are categorized in several types such as respiratory nitrate reductase (NaR), assimilatory nitrate reductases (Nas), and periplasmic nitrate reductases (Nap). NaR is a cytoplasmic membrane bound protein and responsible for denitrification (7; 17; 18). Nas is responsible for nitrate assimilation whereas the function of Nap, which is a soluble protein located in the periplasm, is still unclear (18).

Although the molecular structure of NaR from *A. cycloclastes* (*Ac*NaR) has not been identified, several crystal structures of NaR are available in the protein databank (PDB). Nitrate reductase A from *E. coli* (PDB code: 1Q16) is a cytoplasmic membrane-bound quinol-nitrate oxidoreductase (Figure 1.2) (19). According to the BLAST (Basic Local Alignment Search Tool) search, the structure of *Ac*NaR is expected to be homologous to the structure in Figure 1.2.

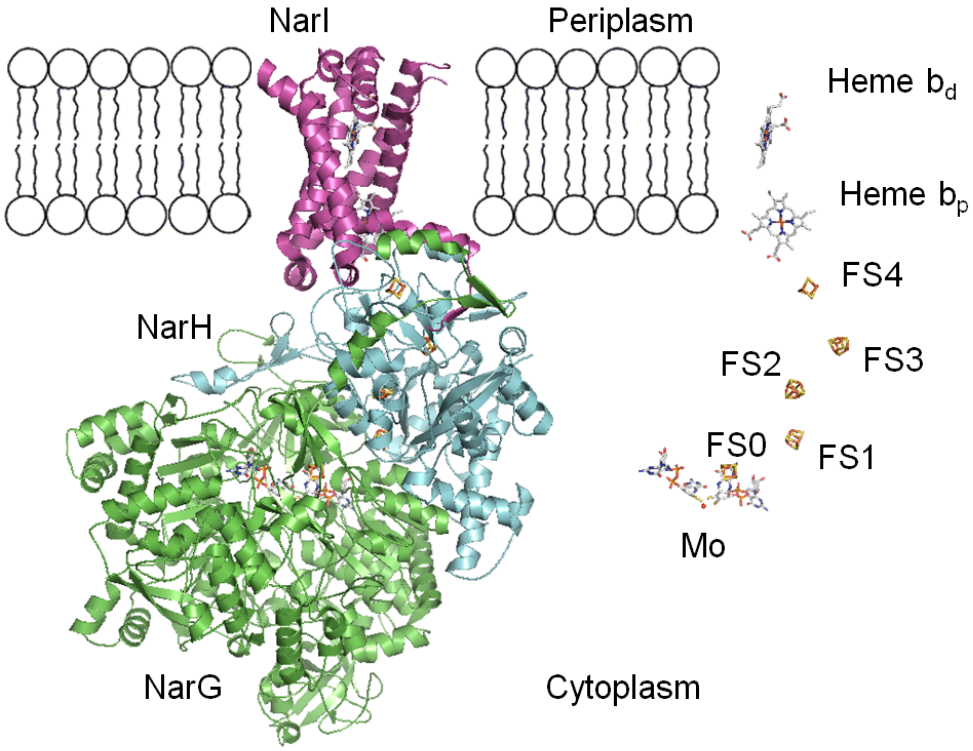


Figure 1.2. Crystal structures of nitrate reductase A complex (NarGHI) from *Escherichia coli*.

NaR is composed of three subunits (NarG, NarH, and NarI) (Figure 1.2). NarG has one Mo binding site, which is the active center, and one [4Fe-4S] cluster (FS0). NarH includes one [3Fe-4S] cluster (FS4) and three [4Fe-4S] clusters (FS1, FS2, and FS3), and

NarI includes two *b*-type hemes (b_p and b_d). Electrons that are required to reduce nitrate on the active site are expected to be provided from the quinol pool in the cell membrane via these redox active metal sites (quinol → b_d → b_p → FS4 → FS3→ FS2 → FS1 → FS0 → Mo → nitrate) (7). The mechanism of nitrate reduction at the active site of NaR is still under investigation.

Nitrite Reductase (NiR)

There are two distinct types of nitrite reductases that contain either copper (CuNiR) or heme (cd_1NiR) as cofactors. Both NiRs catalyze the same reaction, namely the reduction of nitrite (NO_2^-) to nitric oxide (NO) (Eq. 3). NiR is an important enzyme in agriculture since it releases nutrient elements (nitrogen oxides) present in farm land to the atmosphere (7).

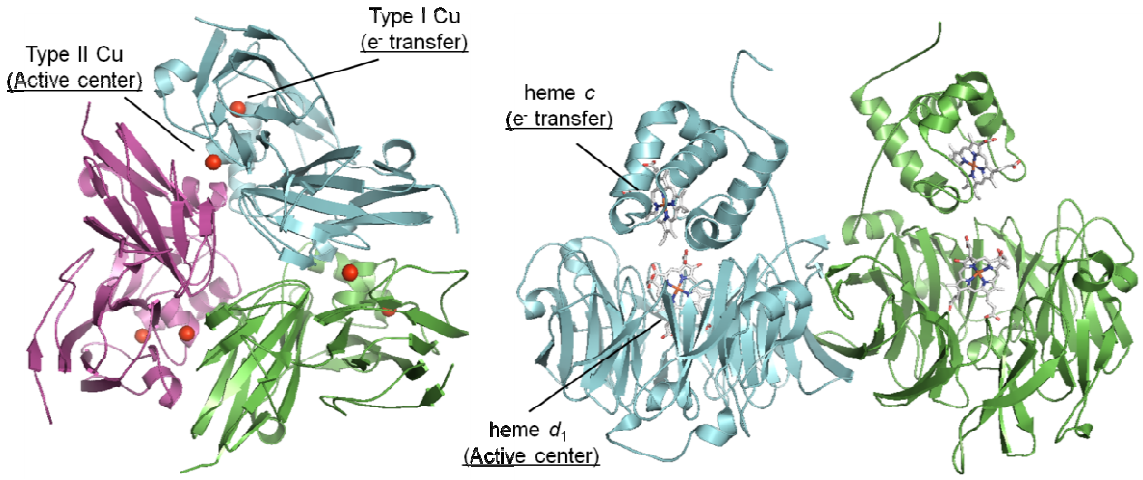


Figure 1.3. Crystal structures of *Ac*CuNiR (left) and cd_1NiR from *Paracoccus pantotrophus* (right).

CuNiR from *A. cycloclastes* (*Ac*CuNiR) is a homotrimer (~ 40 kDa per monomer) and includes two copper ions (type I and II coppers) per monomer (20), whereas cd_1NiR from *Paracoccus pantotrophus* is a homodimer (~ 60 kDa per monomer) and has one heme *c* and one heme d_1 per monomer (21) (Figure 1.3). Both proteins are located at the periplasmic space. It is reported that typical denitrifying organisms have either CuNiR or cd_1NiR exclusively (7). For instance, *A. cycloclastes* contains CuNiR but not cd_1NiR. However, both types of NiR are observed in *Pseudomonas* and *Alcaligenes* (7). The structure and proposed mechanism of *Ac*CuNiR will be further described.

*Ac*CuNiR has two coppers per monomer. One copper site is classified as type I (T1Cu) and the other is type II (T2Cu) (Figure 1.3, 1.4).

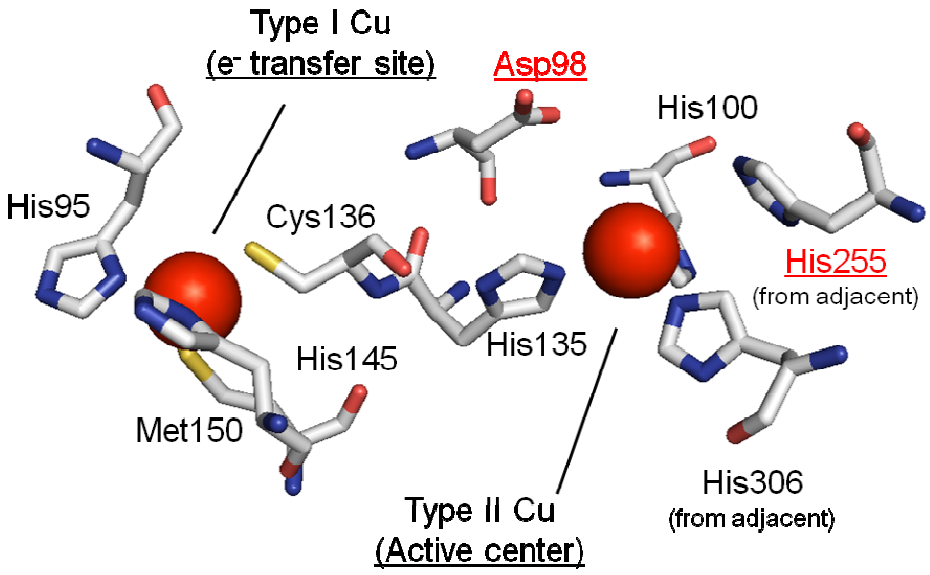


Figure 1.4. Coordination around the Cu sites in *Ac*CuNiR.

The type I Cu (T1Cu) site in *Ac*CuNiR is coordinated with two histidines (His95 and His145), one cysteine (Cys136), and one methionine (Met150) (Figure 1.4). The

geometry of T1Cu is an axially flattened tetrahedron (7) and is stable in both Cu(I) and Cu(II) states. Therefore, this Cu site is suitable for electron relay, and it transfers electrons to the active center (7; 22). The type II Cu (T2Cu) site in *Ac*CuNiR works as the active center, and is located at the boundary surface of two monomers. This site is coordinated with three histidines (His100 and His135 from one monomer, and His306 from a neighboring monomer) and one water molecule (Figure 1.4) (7). Asp98 and His255, which are located above the copper center, are expected to be involved in the catalytic reaction (see below for detail).

The T1Cu and T2Cu centers are categorized by spectroscopic (UV/Vis and EPR) properties that are derived from ligands and its geometries around the coppers (22). In the UV/Vis spectrum, the oxidized T1Cu center (e.g. pseudoazurin from *A. cycloclastes*) shows a strong absorption peak around 600 nm due to ligand-metal charge transfer (LMCT) transitions from the thiolate group of cysteine to Cu(II) (22; 23). According to the absorption spectrum, the T1Cu protein shows a blue color and it is called a “blue copper protein” (24). Once the Cu is reduced, however, the LMCT band is abolished since the d orbitals of Cu(I) are fully occupied with electrons thereby preventing LMCT (25). In contrast, both oxidized and reduced T2Cu centers do not show the LMCT absorption peak because there is no thiolate ligand on the T2Cu site (26). In the EPR spectra, both oxidized T1Cu and T2Cu centers (e.g. NiR from *Alcaligenes xylosoxidans* and laccase from *Rhus vernicifera*) show small hyperfine splittings whereas reduced forms of the centers become EPR silent since Cu(I) is S = 0 (26; 27).

The mechanism of the catalytic reaction by CuNiR has been proposed based on the crystal structure (Figure 1.5) (28). Structural analysis of *Ac*CuNiR reveals a channel that leads the substrate to the T2Cu active site located ~ 12 Å from the protein surface (28). Since the entry site of the channel is negatively charged, nitrite is expected to enter the active site as a protonated form (HNO_2) to avoid electrostatic repulsion (28).

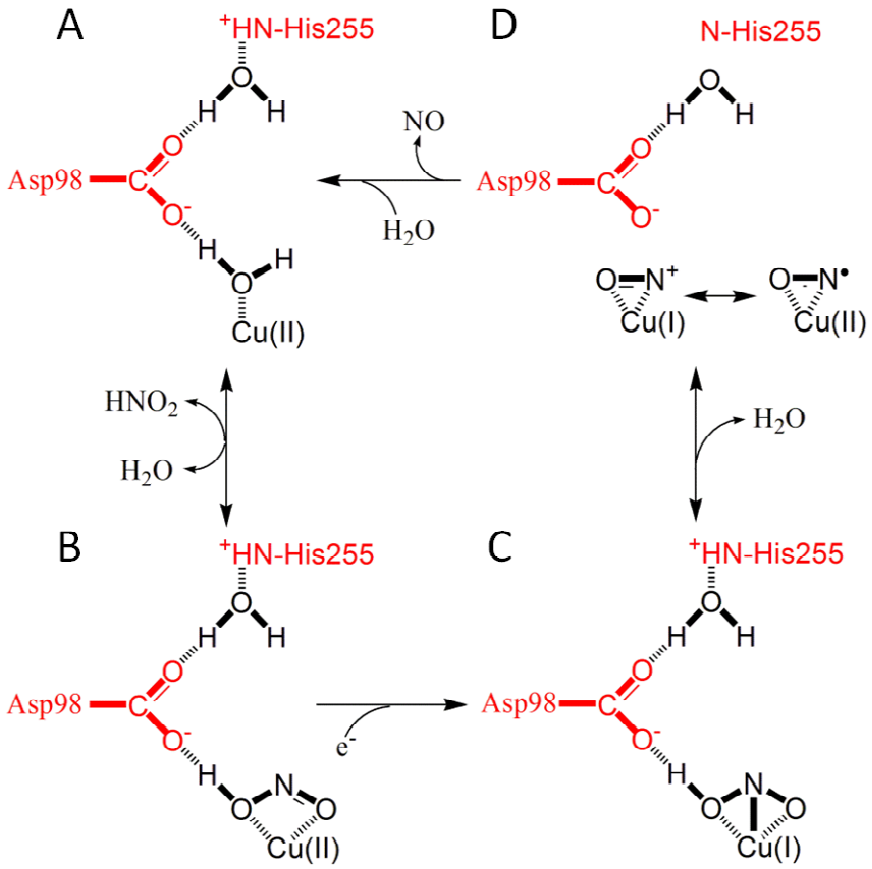


Figure 1.5. The proposed catalytic mechanism for *Ac*CuNiR (28).

In the resting state, the substrate binding site on the T2Cu is occupied with a water molecule (Figure 1.5A). Deprotonated Asp98, protonated His255, and the T2Cu are connected with water molecules via hydrogen bonds (Figure 1.5A). When the substrate

(HNO_2) comes into the active center, the water molecule on the T2Cu is replaced by the substrate, and HNO_2 binds to the T2Cu via *O*-coordination (Figure 1.5B). After the substrate binds to the T2Cu site, the Cu is reduced by an electron from the T1Cu, and the coordination of the substrate is changed (Figure 1.5C). The proton on His255 is transferred to the activated substrate to form NO and H_2O (Figure 1.5D) (28). The product (NO) leaves from the active center and a water molecule binds to the oxidized T2Cu ion (Figure 1.5A).

In CuNiR from *Pseudomonas chlororaphis*, redox potentials of the T1Cu and T2Cu have been determined to be 298 mV and 172 mV at pH 7.6, respectively (29). According to the relative redox potentials, the electron transfer from T1Cu to T2Cu is energetically unfavorable (29). However, the redox potential of T2Cu is increased in the presence of the substrate, which facilitates the electron transfer (29). This observation indicates that there is a redox regulation mechanism by substrate binding in this NiR. In contrast, such a mechanism will not be required in *Ac*CuNiR since the redox potentials of T1Cu and T2Cu without the substrate are already favorable for electron transfer (T1Cu = 240 mV, T2Cu = 250 mV at pH 7.0) (30).

Nitric Oxide Reductase (NOR)

Nitric oxide reductase is a membrane bound protein. It catalyzes the reduction of nitric oxide (NO) to nitrous oxide (N_2O) (Eq. 4) (8). NORs have been categorized in three classes (cNOR, qNOR, and qCuNOR) according to the kinds of electron donor sources (electron transfer proteins or quinols) and acceptor sites (heme or Cu_A sites) bound to the proteins (31). The structures of the active sites among the different classes

are expected to be homologous (7). To date, only one structure of NOR (cNOR from *Pseudomonas aeruginosa*) has been determined with X-ray crystallography (PDB code: 3O0R) (Figure 1.6) (32).

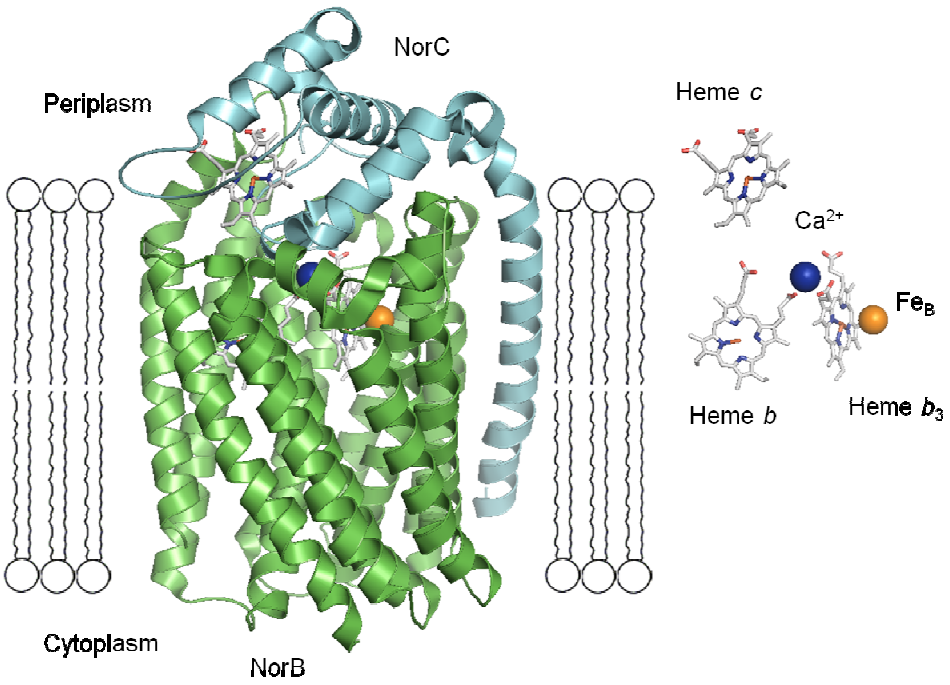


Figure 1.6. Crystal structure of nitric oxide reductase from *Pseudomonas aeruginosa*.

cNOR has been found in denitrifying bacteria such as *Pseudomonas stutzeri* (33), *Paracoccus denitrificans* (34), *Pseudomonas aeruginosa* (35), and *Marinobacter hydrocarbonoclasticus* (transferred from *Pseudomonas nautica*) (17). NOR from *A. cycloclastes* (*Ac*NOR) was also expected to be categorized as a cNOR since almost all the denitrifying bacteria (except *Ralstonia eutropha* (36)) have been found to have this type of NOR to date (7). Although characterization of *Ac*NOR has not been reported, protein sequence alignment analysis of *Ac*NOR by Clustal W showed close similarity to those of cNORs (Appendix A: Figure S1.1 and S1.2).

cNOR is composed of two subunits, NorB and NorC (Figure 1.6). cNOR receives electrons from electron transfer proteins such as cytochrome *c* and/or cupredoxin (T1Cu containing electron transfer protein such as pseudoazurin) in the periplasm. NorB includes three iron sites, heme *b*, heme b_3, and Fe_B while NorC has one heme *c*. The heme *c* in NorC works as an electron acceptor from the electron donor proteins in the periplasm. The heme *b* in NorB receives the electron from the heme *c* and transfers it to the binuclear active site (electron donor → Heme *c* → Heme *b* → heme b_3 and Fe_B).

qNOR has been isolated from pathogens (37). These pathogens do not have the other denitrifying related enzymes such as NaR and NiR (7). Macrophages produce NO as a part of the immunological response to kill pathogens (38). These facts imply that qNOR acts in the detoxification of NO rather than respiration to nitrogen oxides (8; 39). Since the amino acid sequence of qNOR is homologous to NorC in the N-terminal region and NorB in the C-terminus region, qNOR is hypothesized to arise through the gene fusion of NorC and NorB (7). qNOR has also been proposed to be the ancestor of all three types of NOR since the electron transfer system with quinones is thought to be older than the system with cytochromes (31). This class of NOR functions as a monomer and uses quinol for the electron source (40). This enzyme does not have a heme *c* site to receive electrons. Instead, the heme *b* directly receives an electron from the quinol pool in the membrane and transfers it to the active center.

NOR from *Bacillus azotoformans*, which is a gram-positive soil bacterium, was classified as qCuNOR (41). To date, this is the only NOR that is categorized in this class. *Bacillus azotoformans* is a denitrifier and has membrane-bound types of NaR, NiR, NOR,

and N_2OR (42). qCuNOR is composed of two subunits as well as cNOR. Although the catalytic subunit is homologous to NorB in cNOR, the smaller subunit that is similar to NorC has a dinuclear copper center; a Cu_A site serves as the electron transfer site instead of heme *c*. qCuNOR can utilize both menaquinol and membrane bound cytochrome c_{551} as electron sources (43). The NOR activity with menaquinol is 4 times higher than the activity using cytochrome c_{551} as an electron source (43).

Several catalytic mechanisms have been proposed for NOR and these are still controversial because some of the key experimental data conflicts with one another (7). The proposed mechanisms are referred to as *trans*- and *cis*-mechanisms (Figure 1.7). In the *trans*-mechanism, one NO molecule binds to the heme b_3 site and the other NO molecule binds to the Fe_B site (Figure 1.7, left). Alternatively, two NO molecules bind to the Fe_B site in the *cis*-mechanism (Figure 1.7, right).

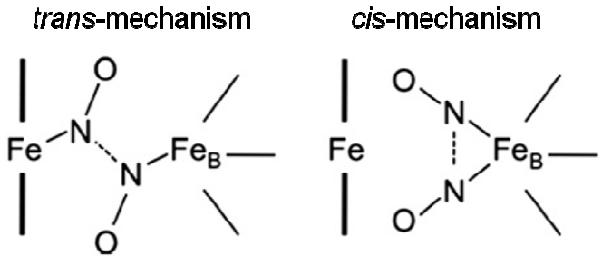


Figure 1.7. Proposed structures of hyponitrite intermediate in *trans*- and *cis*-mechanism for NOR (8).

Several studies on cNOR from *Pseudomonas aeruginosa* with EPR and ultra-rapid freeze quench techniques have shown data that are consistent with the trans-mechanism (8; 35; 44). The signals for the Fe_B (II)–NO and the penta-coordinated heme b_3 Fe (II)–NO complexes were observed in the EPR spectra (35). The *cis*-mechanism is supported by a

study on cytochrome *bo* (heme–Cu_B protein) from *E. coli*, which data indicated two NO molecules were bound to the Cu_B site (45).

Nitrous Oxide Reductase (N_2OR)

Conversion of N_2O to N_2 is catalyzed by N_2OR, which is the last step in the denitrification pathway (Eq.5). In the absence of oxygen, N_2O is used as the terminal electron acceptor in the anaerobic respiratory chain (4; 46). N_2O respiration has been observed in a number of species in a wide variety of environments, such as soil bacteria, phototrophic and chemoautotrophic bacteria, pathogens, marine organisms, piezophiles (high pressure-like deep sea bacteria and archaea), sulfur- and halorespirers, thermo- and psychrophilic (cold-like) bacteria, and extremophilic (extreme condition-like) archaea (4; 12; 47; 48; 49). Subsequently, the *nos* gene cluster that is required for the active N_2OR expression has been found in many bacteria and archaea (50; 51; 52; 53; 54). The initial research on *Pseudomonas stutzeri* suggested that N_2OR was a Cu containing enzyme since Cu specifically induced N_2OR expression under anaerobic conditions (4).

N_2OR has a conserved twin-arginine sequence in the N-terminal signal peptide region, which is recognized by the Tat (twin arginine translocation) pathway that transports folded proteins across the cytoplasmic membrane (50; 55). The mutation of the twin-arginine motif in N_2OR from *Pseudomonas stutzeri* resulted in accumulation of unprocessed N_2OR in the cytoplasm, which did not contain any copper (56). The result indicated that the Cu_A and Cu_Z sites were assembled in the periplasm. In contrast, N_2OR from *Wolinella succinogenes* has a sec-type signal peptide for the Sec (secretory) pathway that transports unfolded proteins through the cytoplasmic membrane (4; 51).

Most N_2ORs including from *A. cycloclastes* are soluble head-to-tail homodimers (Figure 1.8) located in the periplasmic space, although there have been several membrane-associated N_2ORs reported (57; 58). N_2OR is O_2 sensitive and exposure of N_2OR from *A. cycloclastes* (*Ac*N_2OR) to air results in both loss of Cu content and irreversible enzymatic activity (11). However, N_2OR from *Marinobacter hydrocarbonoclasticus* (formerly *Pseudomonas nautica*) maintains a relatively high activity even under aerobic conditions, and what activity is lost can be reversibly restored with a standard activation process with reduced methyl viologen (MV) (55).

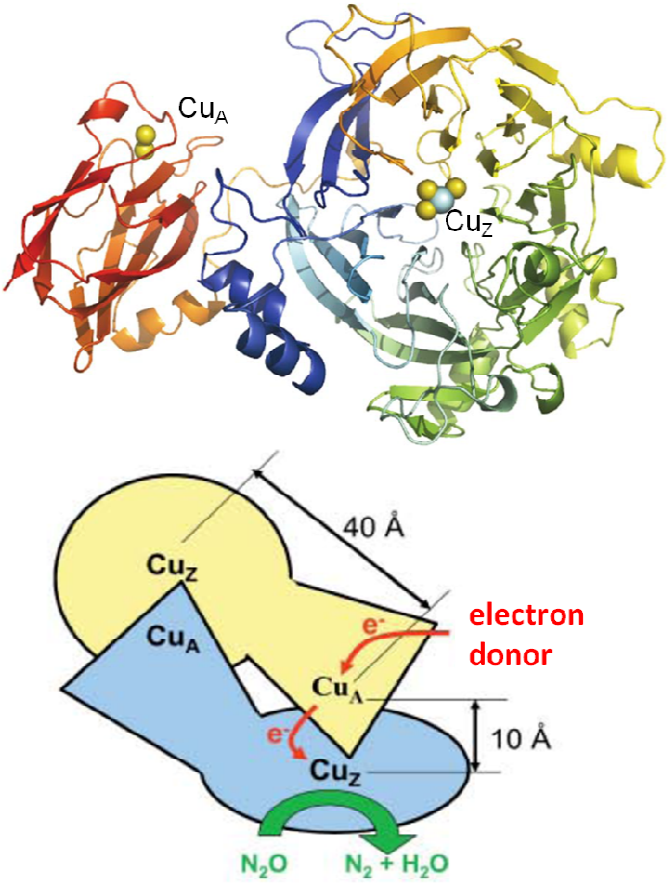


Figure 1.8. Crystal structure of a monomeric form of *Ac*N_2OR (59) and a schematic model of the dimeric form of *Ac*N_2OR (60).

To date, N_2OR structures from *Marinobacter hydrocarbonoclasticus* (61), *Paracoccus denitrificans* (62), *Achromobacter cycloclastes* (59) and *Pseudomonas stutzeri* (63) have been solved. These structures are highly homologous (12). N_2OR is typically composed of two domains, the C-terminal domain that includes the Cu_A site and the N-terminal domain that holds the Cu_Z site (see below for details).

The C-terminal domain of N_2OR contains a cupredoxin motif that contains one Cu_A center (Figure 1.9, left) (64). This domain is homologous to the Cu_A center of bovine cytochrome *c* oxidase (65). In the Cu_A center in *Ac*N_2OR, two copper ions are bridged by two conserved cysteines (Cys578 and Cys582), and the oxidized Cu_A site exists in a mixed-valence state [Cu(1.5) – Cu(1.5)] which is energetically more favorable than the [Cu(I) – Cu(II)] state (4; 55).

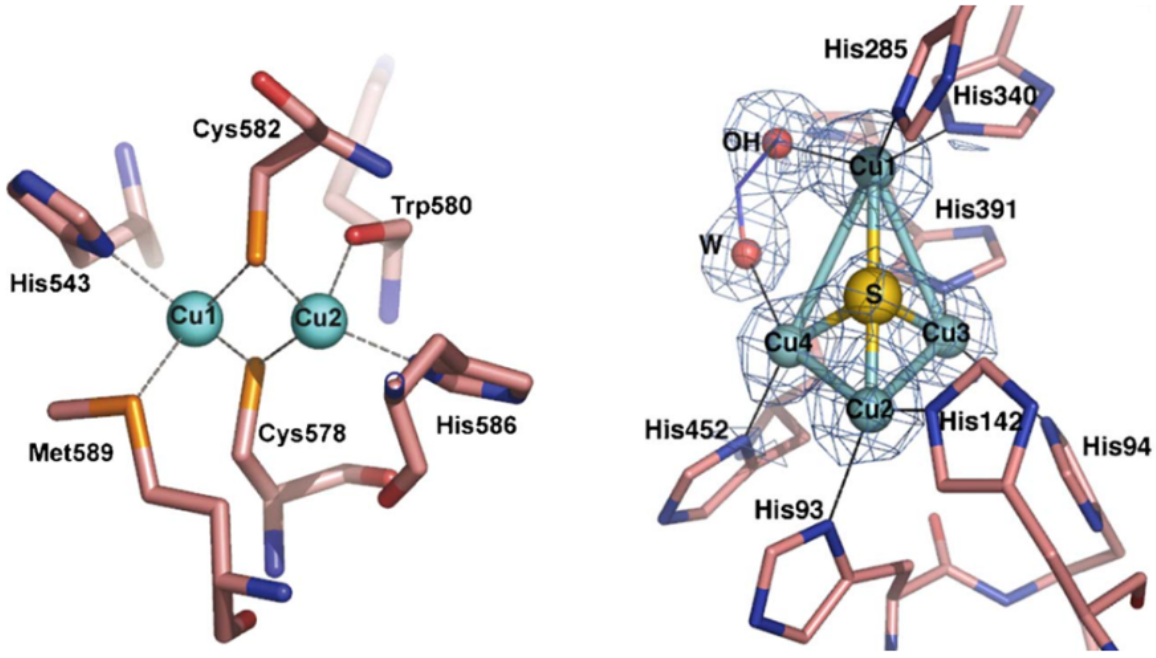


Figure 1.9. Coordinations around the Cu_A (left) and Cu_Z sites (right) of *Ac*N_2OR (59).

The Cu_A site can exist either in an oxidized form [Cu(1.5) – Cu(1.5)] or reduced form [Cu(I) – Cu(I)] following electron transfer, whereas the [Cu(II) – Cu(II)] form has never been observed for any Cu_A center to date (4). The Cu_A site is expected to relay an electron from electron donors (such as pseudoazurin and cytochrome *c*) to the Cu_Z site (7; 55). The reorganization energy of the Cu_A site during the redox reaction is estimated to be lower than the one of typical T1Cu site (4). Therefore, the binuclear Cu_A sites in cytochrome *c* oxidase and N_2OR are thought to be more suitable for electron transfer than the mononuclear T1Cu site (4). In addition, the Cu_A domain is important for the structural stability of N_2OR from *Pseudomonas stutzeri* according to results from a domain study (4). No N_2OR expression was observed when this domain was deleted, although the corresponding *nosZ* transcript was detected in Northern blot analysis (66). Since the redox potentials of Cu_A in cytochrome *c* oxidase from murine and N_2OR from *Paracoccus pantotrophus* have been determined as 250 mV (67) and 260 mV (68), respectively, the redox potential of the Cu_A site in *Ac*N_2OR is also expected to be in this range.

The large N-terminal domain of N_2OR consists of a seven-bladed β-propeller fold which contains the Cu_Z center (Figure 1.9, right) (61). To date, the Cu_Z center has been found only in N_2OR, and it is known as the first biologically active Cu-S cluster (61; 69). The four coppers in the cluster are labeled as Cu_I (upper side of the sulfide), Cu_{II} (lower), Cu_{III} (right), and Cu_{IV} (left) (Figure 1.9, right). The substrate (N_2O) is expected to bind on Cu_I and Cu_{IV} and will be described later (70; 71). The presence of sulfide in the Cu_Z center was determined with ^{34}S isotope labeling of N_2OR from *Pseudomonas stutzeri* and

resonance Raman spectroscopy (72; 73). The N_2OR structure from *Paracoccus denitrificans* solved to 1.6 Å resolution confirmed that the Cu_Z site is a unique μ4-sulfide bridged tetranuclear copper center (74). Additionally, a chloride ion is bound close (6.2 Å) to Cu_I in the Cu_Z site in all four N_2OR crystal structures (61; 62; 59; 63). This chloride shares one of the ligands of the Cu_I in N_2OR from *Paracoccus denitrificans* (74). It is suggested that this chloride probably influences the redox potential of Cu_I so that this copper is stabilized in the Cu(II) state, which is preferable for N_2O binding (74). The N-terminal domain of N_2OR is responsible for dimerization and the residues at the dimer interface are well conserved (4). The dimerization of N_2OR is facilitated by ionic and hydrophobic interactions between the monomers, and chelating interactions of two calcium ions which are located at the dimer interface (61; 74). The dimerization is thought to be essential for the catalytic reaction. The distance between the Cu_A and Cu_Z sites within a monomer unit is 40 Å, which is too far for rapid electron transfer. However, the distance between the Cu_A and Cu_Z sites across the dimer interface is 10 Å, implying that electron transfer reactions between subunits are favorable (Figure 1.8) (75; 76). The redox potential of Cu_Z from *Paracoccus pantotrophus* was determined to be 60 mV, which is not suitable for the electron transfer from the Cu_A site (~ 250 mV) (68). The mechanism of electron transfer from the Cu_A site to the Cu_Z center is still unknown.

Three redox states of N_2OR have been observed; the dithionite-reduced form, the fully reduced form, and the oxidized form (70; 77; 78). When *Ac*N_2OR is isolated from the cell extract, dithionite is added to the sample during the purification to avoid oxidation by O_2 contamination (11). Thus, the *Ac*N_2OR is purified as the dithionite-

reduced form and is referred to as the “as-purified” form or the resting form. In the dithionite-reduced N_2OR the Cu_Z site is partially reduced ([1Cu(II)•3Cu(I)], S = 1/2), while the Cu_A site is fully reduced (Cu(I) – Cu(I), S = 0) (79). The Cu_Z site can be further reduced by prolonged incubation (~ 3 hours) with reduced MV *in vitro* (70; 77). This state is catalytically active and is referred to as the fully reduced form or the active form ([4Cu(I)], S = 0) (70). In the oxidized form of N_2OR, the Cu_Z site is assigned to [2Cu(II) •2Cu(I)], and is EPR silent (S = 0) because of antiferromagnetic coupling between the coppers (80). This form can be observed after the fully reduced form is reacted with N_2O or oxidized with potassium ferricyanide (77; 11). The Cu_A site is also oxidized (Cu(1.5) – Cu(1.5), S = 1/2) with potassium ferricyanide.

The catalytic mechanism of N_2O reduction at the Cu_Z site has been proposed based on the crystal structures and density functional theory (DFT) calculations (70; 71). In the resting state of Cu_Z ([1Cu(II)•3Cu(I)]), N_2O binds to Cu_I and Cu_{IV}. The substrate is expected to bind to the Cu_Z site as the “μ-1,3-N_2O bridging mode” (N atom binds to Cu_I and O atom binds to Cu_{IV}, Figure 1.10) (79). When the Cu_Z–N_2O complex is reduced to the fully reduced form ([4Cu(I)]), the geometry of N_2O on the Cu_Z site is altered. The N–N bond and N–O bond distances are stretched 0.03 and 0.07 Å, respectively, and the N–N–O bond angle bends from 180 ° to 139 ° (Figure 1.10, step 1) (70). This N_2O geometry shift facilitates the two-electron transfer from Cu_I and Cu_{IV} to the substrate (70). After the N–O bond is cleaved and product (N_2) is released (Figure 1.10, step 2), the remaining oxygen atom from the substrate will be subsequently protonated (Figure 1.10, step 3) and released as H_2O (Figure 1.10, step 5). The conserved Lys397 in N_2OR from

Marinobacter hydrocarbonoclasticus (Lys412 in *Ac*N_2OR), which is 4 Å away from the Cu_{IV} atom, is proposed to facilitate the catalytic reaction by acting as a proton source (81).

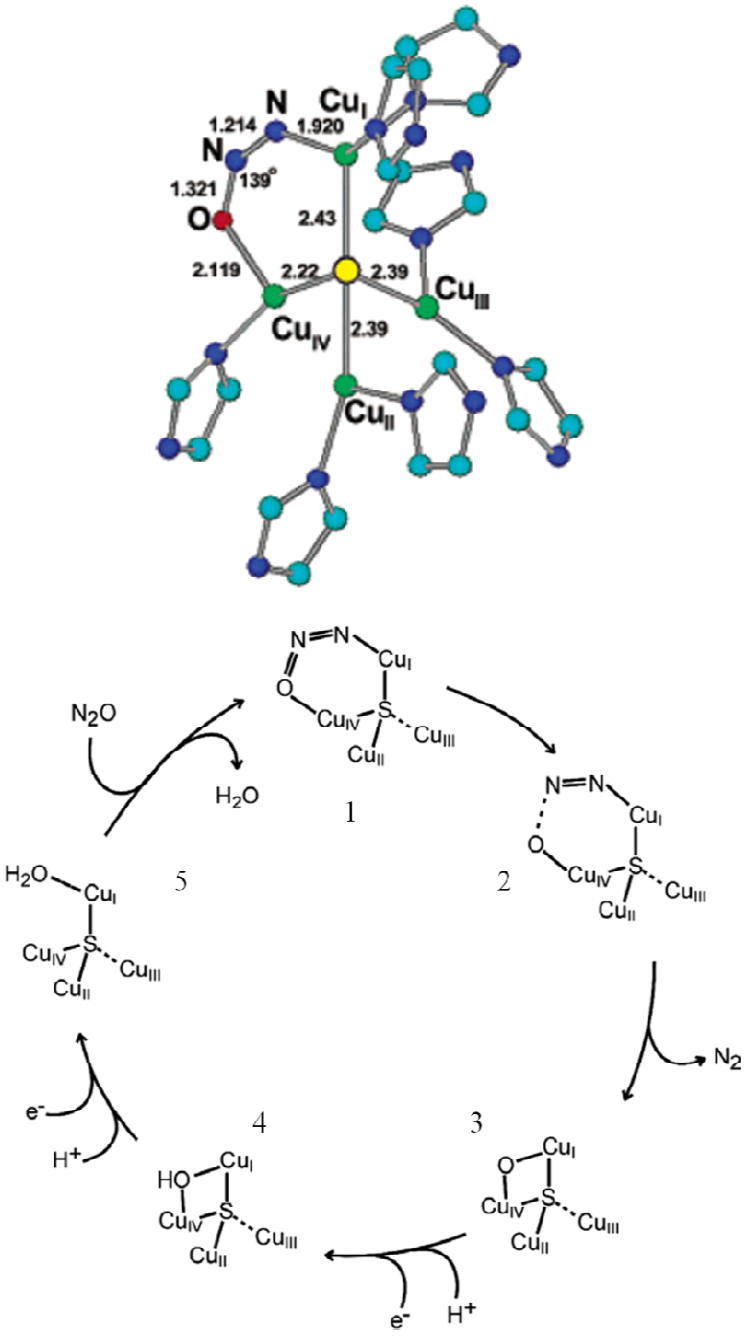


Figure 1.10. Calculated Cu_Z–N_2O complex and proposed catalytic mechanism for N_2OR (7; 71).

Two states (Cu_Z and Cu_Z*) of the Cu_Z center have been characterized (68). The Cu_Z state is considered to be enzymatically active, whereas the Cu_Z* state is inactive and redox inert (68; 69). The Cu_Z* state is generated by O_2 exposure of the enzyme (68) and gene inactivation of *nosR* and/or *nosX*, as will be described later (82; 83). In *Ac*N_2OR, both Cu_Z and Cu_Z* states seem to have almost identical absorption peaks at 640 nm in UV/Vis spectra (11; 77). In N_2OR from *Pseudomonas stutzeri*, the Cu_Z and Cu_Z* states show peaks at 382 and 384 cm^{-1} in resonance Raman spectra, which are excited at 647 nm (73). These spectroscopic features of the Cu_Z and Cu_Z* states indicate that the structures of these states are highly similar, although the redox behavior of the states is significantly different. In N_2OR from *Marinobacter hydrocarbonoclasticus*, the Cu_Z* state is associated with an absorption peak at 640 nm in the UV/Vis spectrum as the protein is purified in the presence of oxygen (84). Although the Cu_Z* state in *Ac*N_2OR cannot be reduced with MV, the Cu_Z* state in N_2OR from *M. hydrocarbonoclasticus* can be fully reduced with MV and shows almost identical activity to that of the Cu_Z state (84). The mechanisms of O_2 resistance and reversibility from the Cu_Z* to the Cu_Z state of N_2OR from *M. hydrocarbonoclasticus* are still unclear.

Recently, a structural relationship between the Cu_Z and Cu_Z* states was proposed in N_2OR from a crystal structure of substrate bound N_2OR from *Pseudomonas stutzeri* (63). This structure revealed the presence of an extra sulfide ion bound at the Cu_Z site ([4Cu:2S] form) (Figure 1.11, left) (63). The authors suggested that the Cu_Z and Cu_Z* states corresponded to the [4Cu:2S] and [4Cu:1S] forms, respectively (63). The 2nd sulfide in the Cu_Z site was located at the place where the substrate and inhibitor (iodide

anion) were thought to be bound (59).

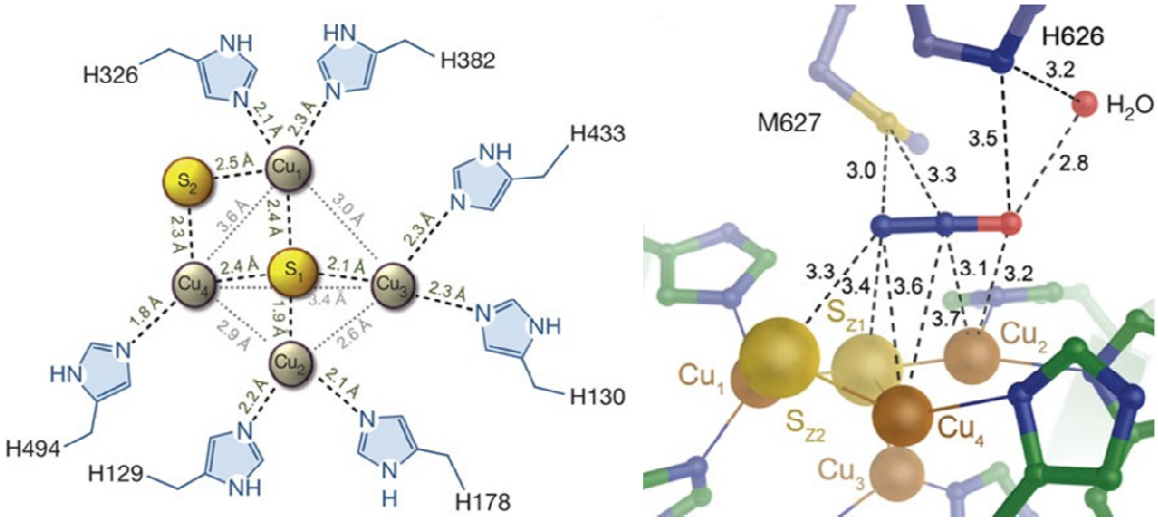


Figure 1.11. [4Cu:2S] form of the Cu_Z site in N_2OR from *Pseudomonas stutzeri* (PDB: 3SBR) (63). Newly found 2nd sulfide between Cu_1 and Cu_4 (left) and location of the substrate between the Cu_A and Cu_Z sites (right).

They found that the 2nd sulfide was highly oxygen sensitive and was lost when the enzyme was exposed to air. This observation was consistent with the fact that the Cu_Z* state was generated following O_2 exposure. The N_2OR structures that had been determined previously were all crystallized under aerobic conditions, whereas N_2OR from *Pseudomonas stutzeri* was purified and crystallized under strictly anaerobic conditions. Therefore, it is resumed that the other N_2ORs (from *Marinobacter hydrocarbonoclasticus*, *Paracoccus denitrificans*, and *A. cycloclastes*) also have the 2nd sulfide in the Cu_Z site under strictly anaerobic conditions. The substrate bound form of the crystal structure revealed that N_2O was located between the Cu_A and Cu_Z sites (Figure 1.11, right) (59; 63). The distance between the O atom of N_2O and the Cu_{II} of the Cu_Z site was 3.2 Å, whereas the distance between this O atom and His626, which is the ligand of

the Cu_A site, is 3.5 Å. The authors propose that the substrate receives electron(s) directly from the Cu_A site, instead of receiving the electrons from the Cu_Z site as described in Figure 1.10 (7; 71).

Pseudoazurin (PAz)

Pseudoazurin is a T1Cu containing protein located in the periplasm (Figure 1.12, PDB code: 1BQR) (85). PAz works as a common electron transfer protein for the denitrifying enzymes such as CuNiR (86), cd_1NiR (87; 88), NOR (89), and N_2OR (90; 91). PAz has a mononuclear copper center, and exists in two redox states, Cu(I) (reduced state) and Cu(II) (oxidized state). Expression levels of PAz in *Paracoccus denitrificans* are regulated by the transcriptional activator FnrP, which is responsible for protein expression under anaerobic conditions and will be further described in the next section (88).

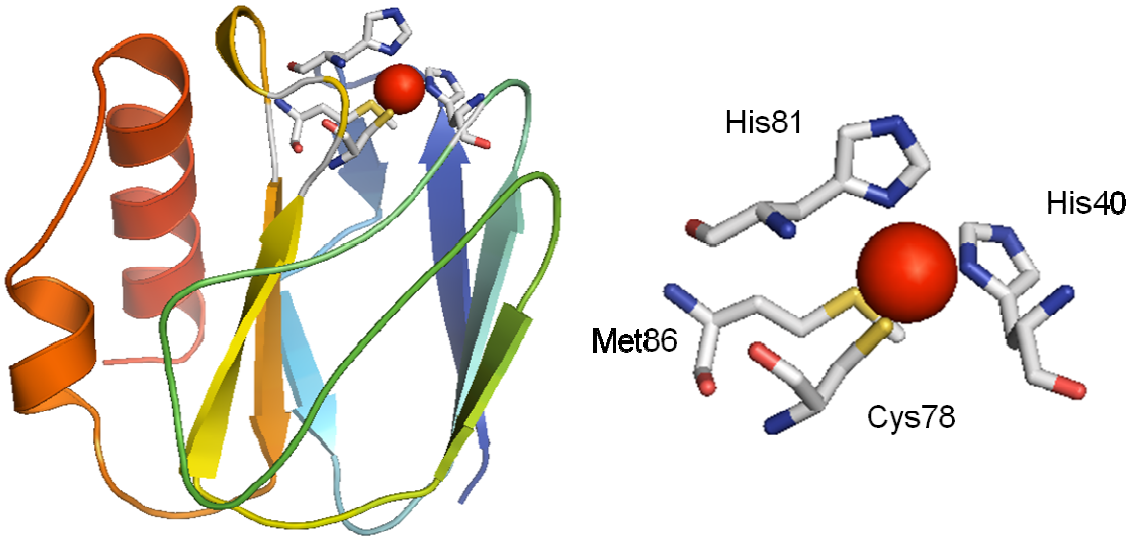


Figure 1.12. Crystal structure of *Ac*PAz (1BQR) and coordination environment of the Cu center.

Since PAz is required to interact with several structurally different proteins for electron transfer, the donor-acceptor interactions are achieved in a “pseudo-specific” manner (87). The pseudo-specific interaction is based on a combination of a hydrophobic patch and surrounding positively or negatively charged patches on the surface of two proteins, which is less specific than a structure-based interaction (87). In the case of the N_2OR-PAz complex, electron transfer is facilitated by the hydrophobic patches on N_2OR and PAz, and several positive residues (Lys) on PAz and negative residues (Glu/Asp) on N_2OR that are located adjacent to the hydrophobic patches (see chapter 5) (87).

Recently, putative docking structures of *Ac*N_2OR and *Ac*PAz were calculated in our lab (91). The top three candidates of the *Ac*N_2OR-*Ac*PAz docking structures are shown in Figure 1.13A. The three *Ac*PAz structures in orange, green and blue in Figure 1.13 indicate the binding orientations of *Ac*PAz on *Ac*N_2OR. Additionally, the electron transfer pathways from the T1Cu of *Ac*PAz to the Cu_A site of *Ac*N_2OR were also calculated based on the three docking structures (Figure 1.13B). The calculations indicated that *Ac*PAz interacted with *Ac*N_2OR through the hydrophobic patch as mentioned above. The calculated electron transfer pathways from *Ac*PAz to *Ac*N_2OR were consistent with the previous studies on N_2OR and PAz from *Paracoccus pantotrophus* (92) and on N_2OR and cytochrome c_{552} from *M. hydrocarbonoclasticus* (93).

Pseudoazurin from *Paracoccus pantotrophus* (formerly *Thiosphaera pantotropha*) donates electrons to N_2OR *in vitro* (90). Additionally, several possible docking sites for electron transfer between N_2OR and PAz from *Paracoccus pantotrophus* were calculated

and the plausible electron transfer pathways from PAz to Cu_A in N_2OR are identified (92). In additional investigations in *Paracoccus pantotrophus*, oxidized PAz is shown to dramatically enhance the nitrite reduction by cd_1NiR and facilitate the release of product NO (94). This result shows that PAz works not only as an electron donor but also as a "facilitator" of its binding partner's function, as possibly mediated by electron exchange between Cu in PAz and heme in cd_1NiR.

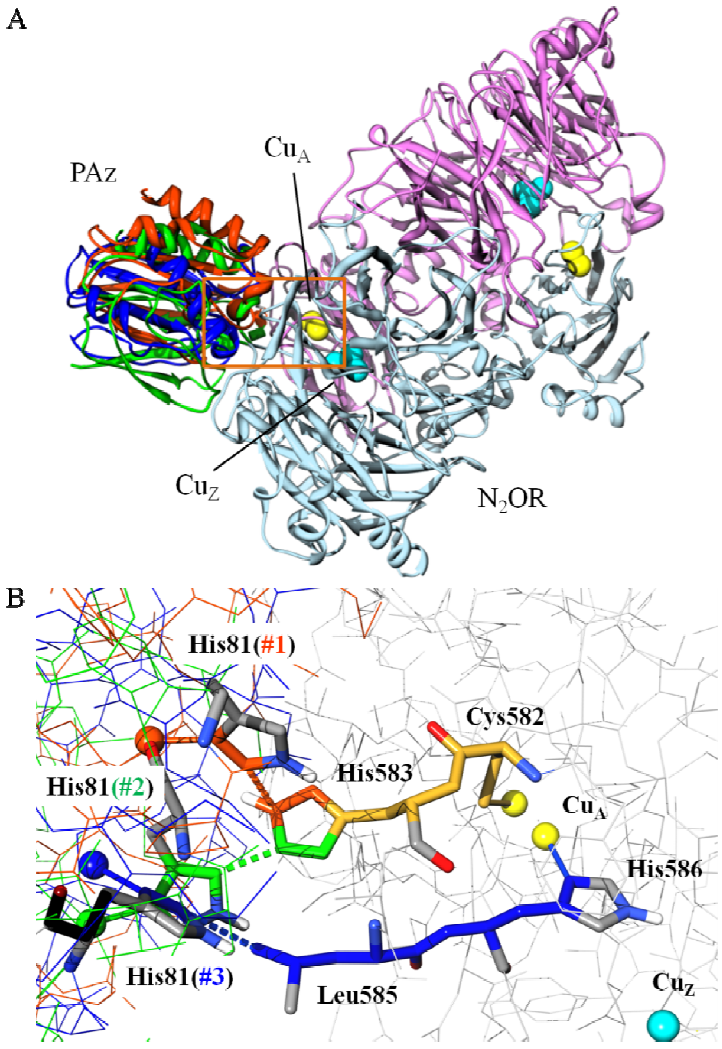


Figure 1.13. (A) Calculated docking structures of *Ac*N_2OR (2IWF) and *Ac*PAz (1BQR), and (B) putative electron transfer pathways from the T1Cu of *Ac*PAz to the Cu_A of *Ac*N_2OR (91).

Accessory Proteins for N_2OR

Nitrous oxide reductase (N_2OR) requires accessory proteins to be expressed and activated (12; 55). Although Nos proteins have been characterized in several denitrifying bacteria, the functions of the accessory proteins on N_2OR are still somewhat unclear. For example, NosX from *Paracoccus denitrificans* was shown to be involved in the activation of N_2OR *in vivo* (83). However, the mechanism by which NosX activates N_2OR is still unknown. Investigations on the roles of each accessory protein are important in order to understand the assembly of the cofactors (Cu_A and Cu_Z) in N_2OR and the activation process of N_2OR for reduction of N_2O. This study is mainly focused on the expression and characterization for function and structure of NosX from *A. cycloclastes* (*Ac*NosX) *in vitro*. An overview of the accessory proteins for N_2OR will be described.

The nitrous oxide reductase gene cluster (*nos* cluster) in *A. cycloclastes* was identified in 1998 (53). Seven protein coding regions including *nosR*, *nosZ* (structural N_2OR gene), *nosD*, *nosF*, *nosY*, *nosL*, and *nosX* were identified and arranged in four transcriptional units consisting of *nosR*, *nosZ*, *nosDFYL*, and *nosX* (Figure 1.14) (52).

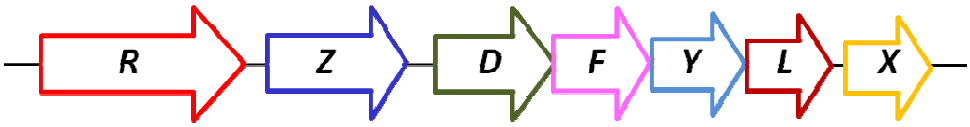


Figure 1.14. The *nos* cluster from *Achromobacter cycloclastes*.

The Nos proteins from these genes are thought to be expressed across the periplasmic and cytoplasmic regions (Figure 1.15). The proteins that structures have already been solved

are shown with the structures whereas the proteins without the structural information are represented by circles (soluble proteins) and squares (membrane bound proteins).

The *nos* clusters have also been isolated from denitrifying bacteria such as *Pseudomonas stutzeri* (*nosRZDFYL*) (95; 50), *Paracoccus denitrificans* (*nosRZDFYLX*) (96), *Sinorhizobium meliloti* (*nosRZDFYLX*) (97; 52), *Pseudomonas aeruginosa* (*nosRZDFYL*) (98), *and Bradyrhizobium japonicum* (*nosRZDFYLX*) (99). The *nosRZDFYL* gene set is the most frequently observed sequence (55). In several species, the *nosX* gene has not been identified. To date (as of January 2012), 351 of *nosZ* (N_2OR) genes have been registered in the NCBI database, whereas only 92 of *nosX* genes have been identified in the *nos* clusters.

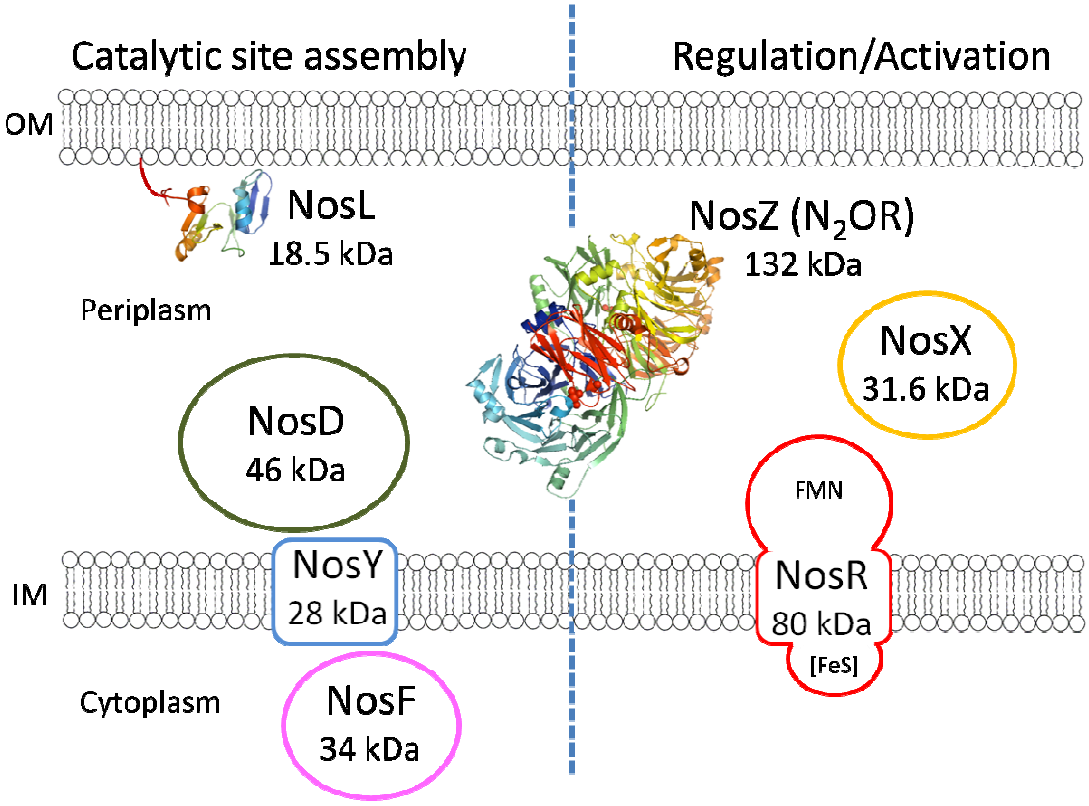


Figure 1.15. Distribution of the Nos proteins from *Achromobacter cycloclastes*.

In the non-denitrifying organism *Pseudomonas putida*, it is shown that the expressions of *nosRZDFY* genes, but not *nosL* and *X*, are sufficient to construct a holo-N_2OR (100). It is believed that NosD, NosF, and NosY are responsible for biosynthesis of the Cu_Z site (50). The functions of the Nos proteins will be described in this section.

Under denitrifying conditions, *nos* gene expression is activated by transcriptional factors that are the FNR-CRP family proteins. It has been shown that three transcriptional factors are involved in the *nos* gene expression; Fnr, Dnr, and Nnr. Fnr is responsible for the protein expression in response to anaerobic conditions, whereas Dnr and Nnr upregulate the protein expression in the presence of NO (101). Dnr in *Pseudomonas aeruginosa* and DnrD in *Pseudomonas stutzeri* regulate the *nos* gene expression (55; 102; 103), whereas both FnrP and NNR equally contribute to the whole cell N_2OR activity in *Paracoccus denitrificans* (101). In *A. cycloclastes*, it is still unclear which transcriptional factor regulates the *nos* cluster expression.

According to the mechanisms for the *nos* gene expression, *nosR* promoter activity is increased with NO, but not N_2O, in *Pseudomonas aeruginosa* (98). Additionally, NO shows strong upregulation for the expressions of the *nosR*, *nosZ*, and *nosDFYL* in *Pseudomonas stutzeri* (103). The NO signal transduction pathway in *Pseudomonas stutzeri* is summarized as follows; NO produced by NiR activates DnrD, which facilitates the expression of *nosR*, and NosR further stimulates expression of *nosZ* and the *nosDFYL* operon: NO → DnrD → *nosR*/NosR → *nosZ* and *nosDFYL* (55; 50). It is still unclear whether the expression of *nosX* is also upregulated by the transcriptional factors because the effects of transcriptional factors on *nos* cluster expression have only been investigated

on the bacteria that do not have the *nosX* gene. Even though anaerobic conditions are required for the *nos* gene expression and N_2OR activity, a low level of O_2 is also required for maximum *nos* gene expression and/or cell growth in *Pseudomonas stutzeri* and *Sinorhizobium meliloti* (104; 105). Micro-aerobic conditions were also required to culture *A. cycloclastes* in our lab (Bollinger, J. *et al.* unpublished results).

NosR as the Regulator of the Nos Gene Expressions and the Activator of N_2OR

NosR from *A. cycloclastes* (GenBank code: AAD09156.1) is expected to be an 80 kDa membrane bound protein (53). The *nosR* gene is shown to be essential for expression of N_2OR in *Pseudomonas stutzeri* (82), in *Pseudomonas aeruginosa* (98), and in *Bradyrhizobium japonicum* (99). The *nosR* expression is regulated with the transcription factor DnrD in response to NO in *Pseudomonas stutzeri*, as mentioned earlier (103). NosR is a transmembrane protein containing a flavin mononucleotide (FMN) binding domain on the periplasmic side and two [4Fe-4S] binding motifs on the cytoplasmic side (82; 106) (Figure 1.15). The Fe content of recombinant NosR from *Pseudomonas stutzeri* is determined as 7.9 atoms per molecule, and acid-labile sulfur is detected in the protein (82). These results confirm the presence of two [4Fe-4S] clusters in NosR. NosR and DnrD are essential to activate transcriptions of *nosZ* and *nosDFYL* in *Pseudomonas stutzeri* (50; 106). However, the precise mechanism of NosR is still unclear since NosR does not have any features of transcription factors (82). To date, it is presumed that NosR might interact with DnrD for *nosZ* expression (82).

NosR is also shown to be essential in maintaining N_2OR activity *in vivo* (82).

Whole cell N_2OR activity is observed only in the presence of both the periplasmic FMN domain and the cytoplasmic [4Fe-4S] domain of NosR. Either the FMN or [4Fe-4S] domain truncated NosR expressions in *Pseudomonas stutzeri* resulted in loss of N_2OR activity in the cell (Figure 1.16, b and c).

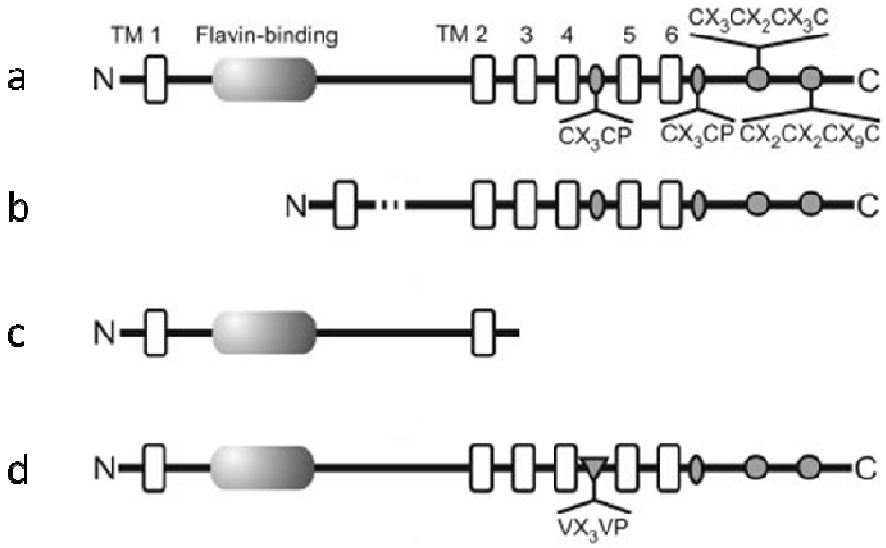


Figure 1.16. Structural elements of unprocessed NosR (a) and mutated NosR (b-d) (82).

Further, Cys → Val mutations of one of the [4Fe-4S] sites, which is located between the fourth and fifth transmembrane helices and exposed to the cytoplasmic side, show that this site is indispensable for N_2OR activity (Figure 1.16, d) (82). Since a low initial N_2OR activity is observed, it is suggested that the N_2OR inactivation is due to the absence of electron supply after the first catalytic turnover, which further indicates that NosR might serve as an electron source for N_2OR. This observation also indicates that NosR is not involved in the biosynthesis of the active center of N_2OR (Figure 1.15). Indeed, Cu contents of N_2ORs from the strains which express intact or truncated NosRs were almost the same (82). It is suggested that NosR donates electrons to N_2OR through

electron transfer proteins such as pseudoazurin, *c*-type cytochromes, and/or NosX, as will be discussed in chapter 4 (82; 83). Additionally, the Cu_Z* proportion in N_2OR is increased in the presence of truncated *nosR* mutants (82). This suggests that NosR helps maintain the Cu_Z site in a catalytically active state and/or regenerates the Cu_Z* state to the Cu_Z state.

NosD, NosF, and NosY as the Cu_Z Site Assembly System

NosD, NosF, and NosY are essential for biosynthesis of the Cu_Z site (100). Deletion of either *nosD*, *nosF*, or *nosY* resulted in loss of the Cu content in N_2OR from *Pseudomonas stutzeri* (95; 107). Sequence analyses of NosD, NosF, and NosY reveal that these proteins are homologous to the bacterial ATP binding cassette (ABC) transporter proteins (108). The typical ABC transporter system is composed of three units; a cytoplasmic ATP/GTP binding protein (analogous to NosF), a transmembrane protein (NosY), and a periplasmic protein (NosD) (109). This system transports small molecules and/or proteins across the cell membrane using the energy generated by ATP/GTP hydrolysis. Since Cu_Z site assembly requires four coppers and a sulfur atom, the NosDFY complex is expected to transport sulfide and/or Cu from the cytoplasm to N_2OR in the periplasm (Figure 1.15) (100; 109).

NosD from *A. cycloclastes* (*Ac*NosD, GenBank code: AAD09158.1) is predicted to be a 46 kDa periplasmic protein (53; 110). Amino acid sequence analysis of *Ac*NosD identified two CASH (carbohydrate binding proteins and sugar hydrolases) domains, although the function of these domains was unclear (111). Recombinant *Ac*NosD has

been overexpressed in *E. coli* and purified for characterization in our lab (53). However, recombinant NosD was expressed in inclusion bodies. Purification of NosD from the overexpressed strain *Ac*/pMLnos, in which whole Nos proteins were expected to be overexpressed, has also been tried several times, but was not successful (Bollinger, J. *et al.* unpublished results).

NosF from *A. cycloclastes* (GenBank code: AAD09159.1) is a 34 kDa cytoplasmic protein (Figure 1.15) (53). An ATP/GTP binding site was identified by sequence analysis (53). Tagging of a maltose binding protein (MBP) to NosF from *Pseudomonas stutzeri* enabled expression of stable NosF in an *E. coli* over-expression system (50). The ATP/GTPase activity assay of the MBP-NosF fusion protein show that NosF can hydrolyze both ATP and GTP, although with varying efficiency, whereas no CTPase or ADPase activity is detected (50). This result indicates that Cu_Z assembly is coupled with ATP/GTP hydrolysis.

According to sequence analysis, NosY from *A. cycloclastes* (*Ac*NosY, GenBank code: AAD09160.1) is expected to be a six-transmembrane protein with a size of 28 kDa (Figure 1.15) (53). *Ac*NosY is composed of 273 amino acids (aa) and is highly hydrophobic. The alanine and leucine contents of *Ac*NosY are 59 aa (21.6 %) and 53 aa (19.4 %), respectively. Since few studies on NosY have been reported, there is little additional information on this protein.

Copper Chaperon Protein NosL

NosL from *A. cycloclastes* (*Ac*NosL, GenBank code: AAD09161.1) is a periplasmic protein (18.5 kDa) whose N-terminal end is expected to be anchored to the

outer membrane (Figure 1.15) (53; 108). The N-terminal domain of this protein includes Leu-(Ala/Ser)-(Gly/Ala)-Cys motif which is a Type-II signal peptidase recognition sequence and leads the protein to the outer membrane (53; 112). Recombinant *Ac*NosL was overexpressed in *E. coli* for characterization (108). *Ac*NosL is a monomeric copper binding protein, which has selective affinity to Cu(I) but not to Cu(II) (108). The copper on *Ac*NosL will be released as the Cu(I) is oxidized to Cu(II). This observation indicates that NosL delivers copper ions to the Cu_A and/or Cu_Z sites of N_2OR, although it is still unclear whether NosL works independently or in concert with the NosDFY complex.

Although NosL is assumed to be a metallochaperone for the biosynthesis of the Cu sites in N_2OR, NosL is not required to produce catalytically active holo-N_2OR in the non-denitrifying organism *Pseudomonas putida* (100). Inactivation of NosL in *Pseudomonas stutzeri* also shows no apparent effect on N_2OR synthesis (113). These observations indicate that there is an alternative system to transport coppers to N_2OR in the host (112). It is likely that NosL has some functional role during N_2OR biosynthesis because many denitrifiers have the conserved *nosDFYL* gene set in common (55).

The apo form of *Ac*NosL structure has been determined with NMR (112). *Ac*NosL is composed of two sequential ββαβ motifs whose structure is homologous to the mercury binding protein MerB, although amino-acid homology of the two proteins is very low. The structural analysis of apo-*Ac*NosL revealed that there are disordered regions in both the N-terminal (Met1 - Pro34) and C-terminal (Asp161 - Gly175) ends (112). One of the ligands for Cu(I) in *Ac*NosL is expected to be Met109 (Met127 in the PDB data), which is well conserved among NosL sequences from various species (Figure

1.17) (112). Cys24 and Met26 are also assumed to be the Cu ligands, but the structure is not identified since these are in the N-terminal disordered region (112).

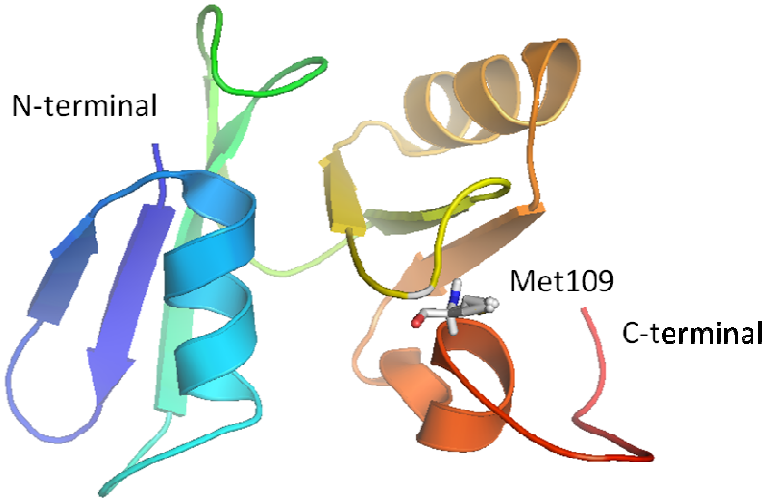


Figure 1.17. NMR structure of apo-*Ac*NosL (PDB code: 2HQ3).

Flavoprotein NosX

The *nosX* gene was originally found in *Sinorhizobium meliloti* in 1997 (52). Gene inactivation experiments imply that NosX interacts with NosR (52). Although the *nosX* gene has been identified in many denitrifying bacteria (55), NosX has never been isolated and characterized *in vitro* prior to our work. The *nosX* gene is shown to be essential for N_2O reduction activity in *Sinorhizobium meliloti* (52) and *Paracoccus denitrificans* (114). Inactivation of the *nosX* gene in *Paracoccus denitrificans* results in loss of N_2O reduction *in vivo*, even though N_2OR from the cells can be activated *in vitro*, as described below (83). This result suggests that NosX is required for N_2OR activation. In contrast, the *nosX* gene has not been found in *Pseudomonas stutzeri* (115), *Pseudomonas aeruginosa* (116), and *Pseudomonas fluorescens* (117). This observation suggests that

these strains may have other cellular components that can substitute for the NosX function.

The function of NosX has been discussed in several papers. In 2000, Saunders *et al*. proposed that NosX was involved in Cu_A biosynthesis in *Paracoccus denitrificans* (114). NirX, which was a product of *nirX* in the *nir* (nitrite reductase) gene cluster, was homologous to NosX (37 % identity and 49 % similarity) and was only found in *Paracoccus denitrificans*. NosX and NirX were thought to be functional homologues and each protein could be substituted with the other protein. Thus, single mutation of either *nosX* or *nirX* did not change any apparent phenotype. However, once both *nosX* and *nirX* genes were knocked out, the N_2OR activity in whole cells was diminished. The authors measured EPR and UV/Vis spectra of crude cell extracts that were obtained from either WT or the double mutant strain. The signals from the Cu_A site of N_2OR were observed in the sample from WT, but not from the mutant strain. They concluded that the functions of NosX and NirX were involved in the biosynthesis of the Cu_A site. In yeast, the Cu_A site in cytochrome *c* oxidase is constructed with a copper chaperone protein termed Sco1 (118). The authors' hypothesis indicated that NosX corresponds to Sco1 for the Cu_A biosynthesis in denitrifying bacteria. However, no metal binding site has been identified among NosX sequences (53; 99; 52).

Another hypothesis regarding NosX function was proposed in 2005 by Wunsch *et al* (83). They also investigated the *nosX nirX* double knock out mutant in *Paracoccus denitrificans* and found that purified N_2OR from the mutant strain possessed the Cu_A site. Although the N_2OR activity *in vivo* was deficient as Saunders *et al* observed, the isolated

N_2OR was catalytically active *in vitro*. The result indicated that NosX was not a Cu chaperone for Cu_A biosynthesis, but instead maintained N_2OR activity. Additionally, the Cu_Z* state proportion in purified N_2OR was apparently increased in the absence of NosX expression. This phenotype was similar to the *nosR* mutants as described before, and it implied the existence of an electron transfer pathway from NosR to N_2OR via NosX to sustain N_2OR activity (83; 82).

Structural characterization of NosX has not been reported to date. The BLAST search of the NosX sequence from *A. cycloclastes* (*Ac*NosX, GenBank code: AAD09162.2) revealed that the *Ac*NosX sequence resembles the ApbE superfamily proteins, for which structural information is available in the PDB. Although the function of the ApbE protein is still ambiguous, it has been proposed to be involved in thiamine (vitamin B) biosynthesis (119) and Fe-S cluster metabolism (120). Recently, the crystal structure of the ApbE protein from *Salmonella enterica* was solved (PDB code: 3PND) and revealed that it bound FAD as a cofactor (121). This structure has an unique FAD-binding motif which can be applied to NosX and will be described in chapter 3.

Overexpression trials of *Ac*NosX in *E. coli* have been attempted in our lab. The purified recombinant *Ac*NosX from *E. coli* did not include any bound cofactor. Reconstitution of FAD, which was identified as the cofactor for NosX in chapter 3, into NosX by dialysis was unsuccessful (Bollinger, J. *et al.* unpublished results).

Other Nos Proteins

Several different types of N_2OR and its *nos* accessory proteins have been reported (4). *Wolinella succinogenes* (*Ws*) is a close relative of *Helicobacter pylori*, although this

strain is not pathogenic. The genome sequence of *Ws* revealed that it had an unusual N_2OR and accessory Nos proteins (51). The *nos* cluster in *Ws* included *nosZDFYL* and four new *nos* genes, *nosG*, *nosC1*, *nosC2*, and *nosH* (Figure 1.18A). *nosR* and *nosX* genes were not observed in this cluster. There were also several potential open reading frames in the cluster labeled as *Ws0918*, *Ws0925*, and *Ws0928* in Figure 1.18. In addition to the typical domains for the Cu_A and Cu_Z sites, *Ws*N_2OR included a cytochrome *c* domain in the C-terminal region (Figure 1.18B), which had never been observed in any other denitrifying bacteria.

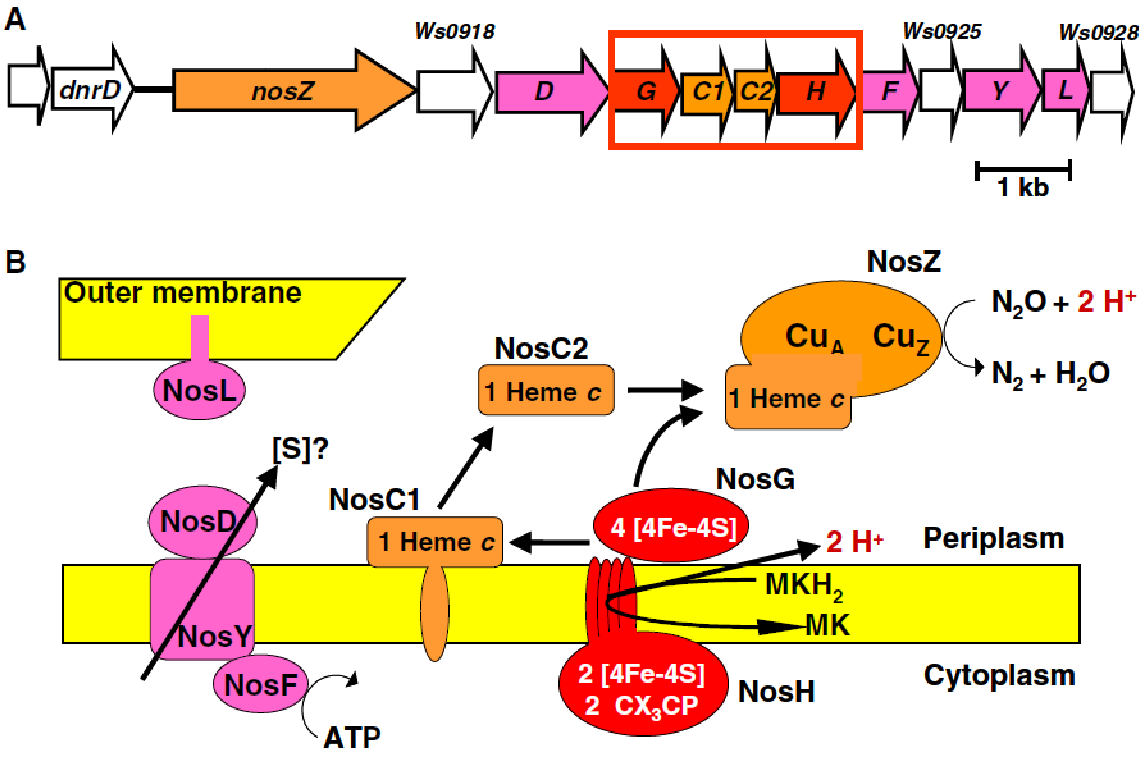


Figure 1.18. The *nos* gene cluster from *Wolinella succinogenes* (A) and distribution of the Nos proteins (B) (51).

The sequence analysis reveals that NosG and NosH are homologous to NapG and NapH, which are accessory proteins for periplasmic nitrate reductase (Nap). NosH is a membrane bound protein (Figure 1.18) and shows similarity to the C-terminal domain of NosR (Fe-S cluster motifs on the cytoplasmic side), which implies that NosH substitutes for the function of NosR. NosG also has conserved Fe-S cluster binding motifs, and is expected to form a complex with NosH which transports electrons from menaquinol to N_2OR (Figure 1.18) (51). According to the unprecedented heme domain of *Ws*N_2OR and these unique accessory proteins, the *Ws*N_2OR is categorized in a variant group as "H-type", whereas the typical N_2ORs have been categorized as "Z-type" (Table 1.1) (4).

Designation	Organisms	Catalytic site	Domain order	Accessory proteins
Z	*Paracoccus denitrificans* *Achromobacter cycloclastes* etc.	Cu-S	Tat signal, beta-propeller, cupredoxin	NosR(X) NosDFYL
H	*Wolinella succinogenes* *Magnetospirillum magnetotacticum*	Cu-S	Sec signal, beta-propeller, cupredoxin, C-domain	NosGHC NosDFYL
A (hypothetical)	*Haloferax volcanii* *Pyrobaculum aerophilum*	Cu-S?	Unknown	NosDFYL

Table 1.1. Structural types of N_2OR variants (4).

In addition to the Z- and H-types, hypothetical N_2ORs that are categorized as "A-type" have been reported in two archaea (Table 1.1) (4). *Haloferax volcanii* and *Pyrobaculum aerophilum* are identified as denitrifiers since genome analyses reveal that these archaea have NiR and NOR, and *nosDFYL* genes. There is also evidence that

Pyrobaculum aerophilum produces NO, N_2O, and N_2 from nitrate (122). However, no *nosZ* gene is identified in the genomes of these archaea. These results suggest that there is a different type of N_2OR in these archaea. Since these archaea have *nosDFYL* genes which are responsible for Cu_Z site biosynthesis, the unknown N_2OR is expected to have a similar Cu-S cluster (Table 1.1).

Research Goals

The focus of this research was to establish expression conditions and purification methodologies for NosX and to characterize the structure and function of NosX from the soil bacterium *Achromobacter cycloclastes*. Although several mutational experiments on the *nosX* gene *in vivo* have been reported (83; 114), no investigation prior to these studies had been carried out on the properties of isolated NosX. This is the first study that identifies the conditions to obtain sufficient amounts of NosX for biochemical characterization. The information revealed from this research will help to elucidate the activation mechanism of N_2OR with NosX and control of N_2O metabolism. It also will be a basis for future applications that could be relevant to such broad environmental issues as water pollution, ozone depletion, and global warming (123).

The interaction between N_2OR and its potential physiological electron donor pseudoazurin was also investigated with co-crystallization techniques to determine the docking structure of *Ac*N_2OR and *Ac*PAz, and to understand the mechanism of the electron transfer reaction. The information from this project is important in clarifying the docking and electron transfer mechanisms between N_2OR and PAz.

CHAPTER 2

PRODUCTION AND PURIFICATION OF NOSX: GENE STRUCTURE REFINEMENT, AND OPTIMIZATION OF THE CULTURE AND PURIFICATION CONDITIONS FOR NOSX

Introduction

The overexpression of the gene products from the *nos* cluster of *A. cycloclastes* was facilitated by subcloning of the entire gene cluster into the multi-copy, broad host range vector pML10 (124; 125). The plasmid was transferred into *A. cycloclastes* for homologous expression. The plasmid strain is referred to as *Ac*/pMLnos. The yield of *Ac*N_2OR from *Ac*/pMLnos was 10 ~ 100-fold higher than the yield from *Ac* without the plasmid (126). For NosX purification, a factor Xa protease site (-Ile-Glu-Gly-Arg-), an Ala-Ser linker, and a strep-tag II sequence (-Trp-Ser-His-Pro-Gln-Phe-Glu-Lys) were inserted on the 3' end of the *nosX* gene in the pMLnos plasmid (125). The strain including this plasmid is referred to as *Ac*/pMLClustXst.

Initial expression levels of NosX in *Ac*/pMLClustXst were significantly lower compared to that of *Ac*N_2OR. A typical yield of each protein from 10 g of cells was about 10 ~ 20 mg for *Ac*N_2OR and less than 0.1 mg for NosX. It was critical to improve the NosX yield for characterization and experiments. While it was reported that *nosR* gene and NosR protein regulate the expression levels of *nosZ* and *nosDFYL* (106; 50), the regulation mechanism for *nosX* gene expression was still unclear. A weak promoter sequence for *nosX* transcription had been identified in the upstream flanking region of the

nosX gene from *A. cycloclastes* (Bollinger, J. *et al.* unpublished results). It was also observed that the expression levels of NiR and PAz in *Ac* was high under denitrification conditions, which was indicative of strong promoter sequences for these protein expressions. Therefore, to improve NosX production, we replaced the weak promoter for NosX with either the *Ac*NiR or *Ac*PAz promoters. Factors and conditions that were thought to influence NosX expression and yield were also investigated. In addition, the purification protocol for NosX was modified to remove biotinylated proteins from *Ac* cell extract.

Materials and Methods

Growth and Purification of NosX

Ac/pMLClustXst was streaked on a LB plate with 50 µg/mL gentamicin (Gm50) and incubated at 30 °C for 3 days. A single colony from the plate was used to inoculate 10 mL LB media (Gm50) which was left overnight at 30 °C and shaking at 250 rpm. The culture was inoculated to 200 mL LB (Gm50) culture for 8 hours and further scaled-up to 2 L × 4 flasks until an A_{600} = 1.0 ~ 1.4 was reached. Expression of Nos proteins was induced by the addition of 20 mL of 1 M KNO_3 (final conc. 10 mM) and 4 mL of 50 mM $CuSO_4$ (final conc. 100 µM) per flask. The shaking speed was reduced to 100 ~ 125 rpm for micro-aerobic conditions. After 24 hours, the cultures were harvested by centrifugation for 10 minutes at 4 °C at 10800 × g (Sorvall GS3 rotor). The cell pellet (~30 g) obtained was frozen at -80 °C immediately or kept at 4 °C overnight for further

purification. Conditions of each culture and yields of cell and NosX are listed in APPENDIX B (Table S2.1) with culture number (#1 - 85).

The following steps for NosX purification were performed on ice or at 4 °C, under aerobic conditions unless otherwise noted. Twenty to thirty grams of cell pellet was re-suspended in 20-30 mL of 100 mM Tris, 150 mM NaCl, 1 mM EDTA, and 10 % (w/v) glycerol at pH 8.0 (Buffer W). A small amount of DNaseI was added to the suspension. To lyse the cells, the suspension was passed through a French pressure cell twice, at a pressure between 60 and 70 MPa. The cell lysate was centrifuged for 60 min at 39000 ×g (Sorvall SS-34 rotor). As a modified purification protocol (see discussion), 40 % ammonium sulfate precipitation was applied to the supernatant, prior to avidin treatment. Ammonium sulfate was added to the supernatant (40 % saturation) and incubated for 1 hour while stirring (~ 400 rpm). After centrifuging and re-suspension of the precipitate with ~ 20 mL of Buffer W, avidin (12.5 U for every 10 g of cells) was added to the re-suspended solution and incubated for at least 30 min while stirring (~ 200 rpm). The solution was centrifuged for 30 min at 39000 ×g. The supernatant was decanted and loaded onto a strep-tactin sepharose column (2 mL, 10 × 25 mm; IBA-GmbH) equilibrated with Buffer W. The column was washed with five column volumes of Buffer W. Proteins bound to the column were eluted with Buffer W plus 2.5 mM desthiobiotin (IBA-GmbH) and collected in 1 mL fractions. NosX was identified by its yellow color and UV/Vis spectra. The eluted NosX was concentrated using an Amicon Ultrafree-4 10K centrifugal filter (Millipore). A typical yield of NosX was 1~2 mg from 30 g cells from optimized culture conditions (see “Optimization of Culture Conditions for NosX”

section). Stocks of NosX were stored at -20 °C. After several purifications, all NosX stocks were thawed, concentrated to 1~2 mL (~ 6 mg/mL) and loaded onto a Superdex 200 gel filtration column (16 × 600 mm; GE Healthcare). The column was equilibrated with 100 mM phosphate, 150 mM NaCl, 10 % (w/v) glycerol, with or without 10 mM EDTA, pH 7.0 (Buffer P (without EDTA) or Buffer PE (with EDTA)) depending on the experiment. The NosX containing fraction eluted between 80 and 100 min with a flow rate at 1 ml/min. The eluted sample was concentrated with an Amicon Ultra Centrifugal Filter 10 K (Millipore) and stored at -20 °C if not used immediately. To determine the purity of NosX, 12.5 % gels were used to run SDS-PAGE analysis (Bio-Rad) and stained with Coomassie Brilliant Blue (CBB).

Promoter Refinement for NosX

Subcloning of *nosX* Gene from pMLClustXst. The constructions of the new NosX expression system with *Ac*NiR or *Ac*PAz promoters are summarized in Figure 2.1. The plasmid pMLClustXst was purified from *Ac*/pMLClustXst with a QIAprep Spin Miniprep Kit (Qiagen). Since the yield of plasmid from *Ac* was very low, the purified plasmid was transferred into the *E. coli* strain, Top10F' (Invitrogen) by electroporation for plasmid propagation. Colony screening was carried out with an LB plate with 10 µg/mL gentamicin (Gm10). A colony was picked up and cultured for further plasmid purification. The purified plasmid was used for the following experiments. The strep-tagged *nosX* gene from the *nos* cluster in the plasmid was amplified with PCR using two primers (Figure 2.1A). The primer sequences were as follows;

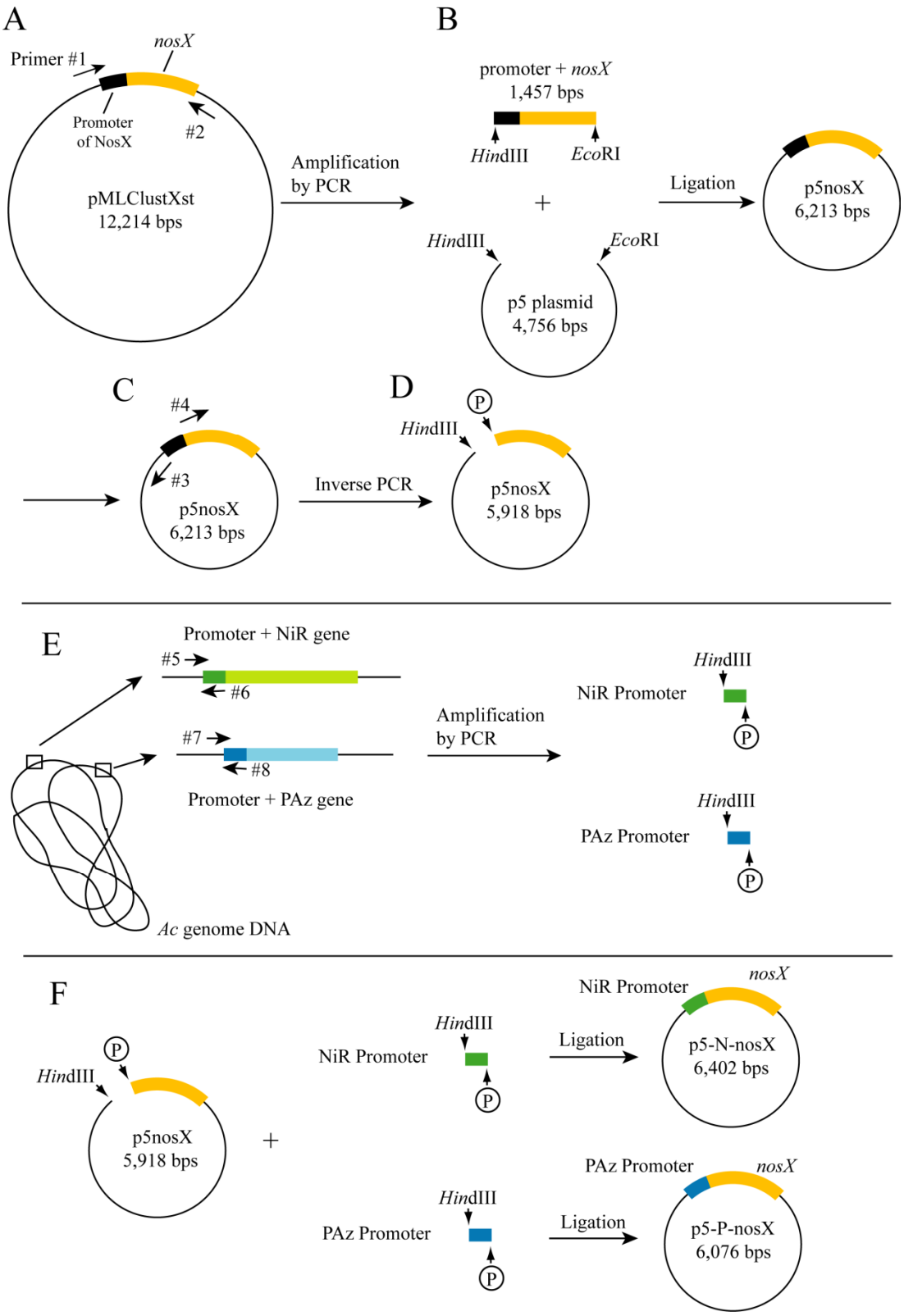


Figure 2.1. Schematic view of the assembling process of a new NosX expression system

Primer #1: 5’- ATATCGAAGCTTGCAACGTGGGACCAGCCCGG -3’
*Hin*dIII recognition site

Primer #2: 5’- ATATCGGAATTCCTTCTCGATGGGCGCGGAACAG -3’
*Eco*RI recognition site

The settings for PCR were programmed as follows; Step 1, 98 °C for 1 min (initial denaturation), Step 2, 98 °C for 30 sec (denaturation), Step 3, 70 °C for 30 sec (annealing), Step 4, 72 °C for 30 sec (extension), 30 cycles for Step 2 - Step 4, Step 5, 72 °C for 5 min (final extension). The product (1457 bps) including *Hin*dIII and *Eco*RI recognition sites in 5’ and 3’ ends were inserted into the cloning vector pBBR1MCS-5 (referred to as p5 plasmid) (Figure 2.1B) and transferred to Top10F’ by electroporation. The colonies were incubated on an LB plate (Gm10) at 37 °C for overnight. Colony PCR screening was carried out to find the colony that included the *nosX* inserted p5 vector (p5-*nosX*, 6213 bps). The plasmids were extracted from several colonies and amplified with PCR using a Taq polymerase (Bio-Rad), primers #1 and #2. The settings for colony PCR follow; Step 1, 94 °C for 2 min 30 sec (initial denaturation), Step 2, 94 °C for 1 min (denaturation), Step 3, 62 °C for 1 min (annealing), Step 4, 72 °C for 1 min 30 sec (extension), 40 cycles for Step 2 - Step 4, Step 5, 72 °C for 5 min (final extension). The colony that showed the right size of PCR product (1457 bps) on a gel was selected and used for further experiments. The p5-*nosX* plasmid was purified from the colony, and the promoter region was removed by inverse PCR using a high fidelity Phusion DNA polymerase (Bio Labs) and two primers (Figure 2.1C). The primer sequences follow;

Primer #3: 5’- CGTTGCAAGCTTATCGATACCGTCG -3’
*Hin*dIII recognition site

Primer #4: 5’- P-ATGCTGCTGACCCGACGCCG -3’
Phosphorylated primer on 5’ side

The settings for inverse PCR follow; Step 1, 100 °C for 2 min (initial denaturation), Step 2, 100 °C for 30 sec (denaturation), Step 3, 64 °C for 30 sec (annealing), Step 4, 72 °C for 3 min (extension), 30 cycles for Step 2 - Step 4, Step 5, 72 °C for 5 min (final extension). The PCR product (5918 bps) was further processed with *Hin*dIII for ligation with the promoter of *Ac*NiR or *Ac*PAz (Figure 2.1D).

Isolation of Promoters of *Ac*NiR and *Ac*PAz. The DNA sequences prior to *Ac*NiR and *Ac*PAz genes were expected to be efficient promoters under denitrifying conditions because the expression levels of these proteins were high under the conditions. To replace the original promoter for NosX with these promoters, the DNA regions were isolated from *Ac* genomic DNA.

The promoter of *Ac*NiR was amplified by PCR and two primers. Gene sequences of *Ac*NiR and *Ac*PAz were obtained from NCBI nucleotide database: *Ac*NiR gene code is Z48635, and *Ac*PAz gene code is Z48669. The primer sequences were designed as follows;

Primer #5: 5’- GTCCAAGCTTGAAGCCATAGGAGAAGAGCACC -3’
*Hin*dIII recognition site

Primer #6: 5’- P-CTTGCTCTCCTTCGGCGC -3’
Phosphorylated primer on 5’ side

The settings for PCR were programmed as follows; Step 1, 98 °C for 1 min (initial denaturation), Step 2, 98 °C for 30 sec (denaturation), Step 3, 70 °C for 30 sec (annealing), Step 4, 72 °C for 30 sec (extension), 40 cycles for Step 2 - Step 4, Step 5,

72 °C for 5 min (final extension). The product (484 bps) was processed with *Hin*dIII for ligation with p5-*nosX* without its promoter (Figure 2.1E).

The promoter of *Ac*PAz was amplified from *Ac* genome DNA as the *Ac*NiR promoter was amplified. The primer sequences are as follows;

Primer #7: 5'- ATGCAAGCTTGCTCATGCGGTCATTAATATAGG -3'
*Hin*dIII recognition site

Primer #8: 5'- P-CGTCTTCTCCATTTGAGCGACC -3'
Phosphorylated primer on 5' side

The settings for PCR are as follows; Step 1, 98 °C for 1 min (initial denaturation), Step 2, 98 °C for 5 sec (denaturation), Step 3, 67 °C for 30 sec (annealing), Step 4, 72 °C for 15 sec (extension), 40 cycles for Step 2 - Step 4, Step 5, 72 °C for 5 min (final extension). The product (165 bps) was processed with *Hin*dIII for ligation with the p5-*nosX* (Figure 2.1E).

Assembly of *nosX* Gene and Promoters of *Ac*NiR and *Ac*PAz on p5 plasmid. The *Hin*dIII processed *Ac*NiR or *Ac*PAz promoters (Figure 2.1E) were assembled to p5-*nosX* plasmid with ligation. The *Ac*NiR or *Ac*PAz promoter was mixed with p5-*nosX* (without its own promoter) and incubated with T4 DNA ligase at 16 °C overnight (Figure 2.1F). The assembled plasmids were referred to as p5-Np-*nosX* (with *Ac*NiR promoter, 6402 bps) and p5-Pp-*nosX* (with *Ac*PAz promoter, 6076 bps). These plasmids were transferred into the *E. coli* strain DH10β by the heat shock method. The colonies were cultured on a LB plate (Gm15) at 37 °C overnight. Several colonies for both plasmids were selected and checked with the colony PCR screening method using the Taq polymerase and primer #5 (for *Ac*NiR promoter) or

#7 (for *Ac*PAz promoter) and #2 (for *nosX* gene). The colony PCR was carried out to confirm whether the selected colonies included the plasmid with the expected DNA sequence. The settings for the colony PCR were programmed as follows; Step 1, 94 °C for 2 min 30 sec (initial denaturation), Step 2, 94 °C for 1 min (denaturation), Step 3, 56 °C for 1 min (annealing), Step 4, 72 °C for 1 min 30 sec (extension), 40 cycles for Step 2 - Step 4, Step 5, 72 °C for 5 min (final extension). The colonies that showed the right size of PCR products (1638 bps for *Ac*NiR promoter + *nosX*, and 1312 bps for *Ac*PAz promoter + *nosX*) on a gel were selected and the plasmids were purified for DNA sequencing. Three primers were used to confirm the sequence. The sequences follow:

Primer #9: 5'- CCATGATTACGCCAAGCGCGCAATTAACCC -3'

Primer #10: 5'- CGCTTCGATCCGACGGTACAGCCGCTC - 3'

Primer #11: 5'- CCCCTCTCGGCACGACCTTCGATCAAGC - 3'

Primers #9 - #11 were designed to sequence different regions of the *nosX* gene on p5 plasmid. Primer #9 was for the upstream range of p5-*nosX* gene. Primer #10 was for the middle range of *nosX*, and primer #11 was for the downstream range. Sequence-confirmed plasmids were transferred into *A. cycloclastes* using electroporation. *Ac*/p5-Np-*nosX* and *Ac*/p5-Pp-*nosX* were cultured individually to check the NosX expression levels (n = 1). After induction, the shaking speed was reduced to 125 rpm and the media was cultured for 24 hours. Cells were harvested and purified with a strep-tactin sepharose column. Additionally, *Ac*/p5-Np-*nosX* and *Ac*/p5-Pp-*nosX* were cultured using LB media from Fisher brand and the NosX yields were compared (n = 1) because of the observation in the next section.

Optimization of Culture Conditions for NosX

The growth conditions of *Ac*/pMLClustXst were modified to identify potential factors that may have affected the NosX yield. Harvested cell amounts and NosX yields from each modified condition were compared to the amounts and yields from the original culture conditions to determine the effectiveness of the modification. The following conditions were considered:

1. LB media (purchased from RPI (n = 7) or Fisher (n = 7))
2. Riboflavin (with (n = 6) or without 50 mg/flask (n = 8))
3. Aerobic/micro-aerobic condition (250 (n = 5) or 100 rpm after induction (n = 7))
4. Incubation time after induction (24 (n = 5) or 48 hours (n = 7))
5. A_{600} at induction (A_{600} = 0.8 ~ 3.8 (n = 16))

"n =" stands for the number of trials performed. For example, "RPI (n = 7)" indicates that *Ac*/pMLClustXst was cultured with LB media purchased from RPI for seven trials and the harvested cell amount and the NosX yield were measured.

Ac/pMLClustXst was cultured with modified conditions as described above. Only a single modification was made to the original culture condition to permit systematic comparisons. Unless otherwise noted, once a factor was revealed to be effective in increasing the NosX yield, the factor was used for following optimization steps. The culture conditions that were used in each optimization step are summarized in Table 2.1.

#		LB	Riboflavin	Shaking speed	Time	A_{600}	Average yield
1	A	RPI	-	100 rpm	24 h	N/A	0.25 ± 0.13 mg
	B	Fisher	-	100 rpm	24 h		1.32 ± 0.74 mg
2	A	Fisher	0 mg	100 rpm	24 h	1.2-1.6	0.63 ± 0.28 mg
	B	Fisher	50 mg	100 rpm	24 h		0.48 ± 0.40 mg
3	A	Fisher	-	100 rpm	24 h	1.1-1.9	0.70 ± 0.22 mg
	B	Fisher	-	250 rpm	24 h		1.57 ± 0.87 mg
4	A	Fisher	-	250 rpm	24 h	1.1-3.8	1.57 ± 0.87 mg
	B	Fisher	-	250 rpm	48 h		3.23 ± 1.20 mg
5		Fisher	-	250 rpm	48 h	1.0	3.21 - 5.98 mg
		Fisher	-	250 rpm	48 h	3.8	2.54 mg

Table 2.1. Variables tested for effects on the yield of NosX

Optimization of Purification Conditions for NosX

The purification process of NosX was monitored by western blot using strep-tactin-AP (alkali phosphatase) that would detect the strep-tagged protein (NosX) and biotinylated proteins. To remove biotinylated proteins in the *Ac* cell extract, a 40 % ammonium sulfate precipitation method was applied before the sample was loaded onto the strep-tactin column. The effectiveness of this additional purification step was determined by western blot. Samples were selected from the following purification steps: the supernatant after cell lysis and centrifugation, supernatant and precipitate from 40 % ammonium sulfate precipitation, and the elution fraction from the strep-tactin sepharose column. Each sample was denatured at 100 °C for 5 min in the presence of sodium dodecyl sulfate (SDS) and 2-mercaptoethanol, and two identical SDS-PAGE gels (12.5 %) were prepared (200 V, 30 min). One of the gels was stained with CBB for comparison with the result from the western blot. The other gel was electro-blotted to a PVDF membrane (Millipore) (90 V, 60 min) at 4 °C. The membrane was washed with 20

mL of TBS buffer (Tris 1.5 g, NaCl 4.0 g, KCl 0.1 g in 500 mL H_2O). The membrane was further treated with 10 mL of blocking solution (TBS + 2 % BSA) for 1 hour, and 10 mL of TTBS (TBS + 0.05 % Tween 20) for 10 min. The membrane was then soaked into 20 mL of antibody solution (TTBS + 2 % BSA + 2 µL strep-tactin-AP) for 1.5 hours. The residual strep-tactin-AP on the membrane was washed with 10 mL × 3 of TBS and the membrane was developed with BCIP/NBT solution (Sigma) for 10 min.

Results

Promoter Refinement for NosX

The *nosX* gene from pMLClustXst and the promoter genes of NiR and PAz from *Ac* genome DNA were amplified with PCR. Since the GC content in the *nosX* gene was relatively high, several modifications of the PCR settings and the GC reaction buffer (BioLabs, for high GC content DNA) were required for successful amplification. Those DNA fragments (*Ac*NiR promoter + *nosX* gene (Np-*nosX*) and *Ac*PAz promoter + *nosX* gene (Pp-*nosX*)) were successfully assembled on p5 plasmid and the sequences were confirmed. The putative Dnr/DnrD binding sites (TTGAT-CT-ATCAA for *Ac*NiR promoter and TTGAC-GCGC-ATCAA for *Ac*PAz promoter) were observed at 292 bps upstream of *nosX* gene in p5-Np-*nosX* and at 90 bps upstream of *nosX* gene in p5-Pp-*nosX*, respectively. The typical DNR binding motif is TTGA(T/C)-N_4-(A/G)TCAA (127).

Ac/p5-Np-*nosX* and *Ac*/p5-Pp-*nosX* were cultured with 2 L ×4 flasks of LB media (purchased from RPI, Gm50) and purified to see if expression level of NosX was enhanced (n = 1). The cell yields of the new expression systems were relatively higher

(36.8 g for *Ac*/p5-Np-*nosX* and 31.0 g for *Ac*/p5-Pp-*nosX*) than the cell yield of *Ac*/pMLClustXst (average of culture #1 - 19 was 23.9 ± 5.8 g) (Table 2.2). The NosX expression levels (per 10 g of cell) in *Ac*/p5-Np-*nosX* and *Ac*/p5-Pp-*nosX* were 0.10 and 0.13 mg/10 g cell respectively, which were almost the same degree of *Ac*/pMLClustXst (0.10 ± 0.08 mg/10 g cell) (Table 2.2). Since the cell yields were higher with the refined plasmids, the total NosX yields were slightly higher in both *Ac*/p5-Np-*nosX* (0.37 mg) and *Ac*/p5-Pp-*nosX* (0.40 mg) than *Ac*/pMLClustXst (0.28 ± 0.26 mg) (Table 2.2). In total, the NosX yields from *Ac*/p5-Np-*nosX* and *Ac*/p5-Pp-*nosX* were increased 1.32-fold and 1.43-fold from the yield from *Ac*/pMLClustXst under the original culture conditions. No significant difference between *Ac*/p5-Np-*nosX* and *Ac*/p5-Pp-*nosX* was observed in terms of cell amounts and NosX yields.

Culture #	Strain/plasmid	Cell yield (g)	NosX	
			Total yield (mg)	mg/10g cell
1 - 19	*Ac*/pMLClustXst	23.9 ± 5.8	0.28 ± 0.26	0.10 ± 0.08
20	*Ac*/p5-Np-*nosX*	36.8	0.37	0.10
21	*Ac*/p5-Pp-*nosX*	31.0	0.40	0.13

Table 2.2. The NosX yields from the refined expression systems with the LB from RPI

In additional experiments, the expression levels of NosX in *Ac*/p5-Np-*nosX* and *Ac*/p5-Pp-*nosX*, which were cultured with LB media from Fisher, were also examined and compared (n = 1). As will become apparent in the next section, the LB media from Fisher significantly (~ 5-fold) enhanced the NosX yield from *Ac*/pMLClustXst (0.25 ± 0.13 (RPI) vs. 1.32 ± 0.74 (Fisher), Table 2.4). Thus, the same conditions were applied to culture with the new NosX expression systems. With the LB media from Fisher, the

NosX yields from the new expression systems were 0.43 mg and 0.34 mg respectively (Table 2.3), which were almost the same level of the yields with the LB media from RPI (0.37 mg and 0.40 mg) (Table 2.2). No significant increase of the NosX yields was observed in either *Ac*/p5-Np-*nosX* or *Ac*/p5-Np-*nosX* with the LB media purchased from Fisher (Table 2.3). Since the effectiveness to obtain NosX using *Ac*/pMLClustXst and the LB media from Fisher was more significant (~ 5-fold) than using the new expression systems (1.32-fold and 1.43-fold), following optimization of culture conditions for NosX expression was carried out using *Ac*/pMLClustXst and the LB media from Fisher.

Culture #	Strain/plasmid	Cell yield (g)	NosX	
			Total yield (mg)	mg/10g cell
22 - 34	*Ac*/pMLClustXst	23.0 ± 6.0	1.20 ± 0.66	0.54 ± 0.27
29	*Ac*/p5-Np-nosX	26.3	0.43	0.16
28	*Ac*/p5-Pp-nosX	21.0	0.34	0.16

Table 2.3. The NosX yields from the refined expression systems with the LB from Fisher

Optimization of Culture Conditions for NosX

Culture conditions were optimized for NosX expression based on five factors: LB media (purchased from RPI or Fisher), riboflavin addition, aerobic or micro-aerobic condition (100 or 250 rpm after induction), incubation time after induction (24 or 48 hours), and A_{600} at induction (0.8 - 3.8).

The LB media purchased from Fisher brand showed the most significant effect on the NosX expression based on the five factors investigated. *Ac*/pMLClustXst was cultured with 2 L × 4 flasks of the LB media from RPI (culture #1-5, 8, 14, n = 7) or

Fisher (culture #22, 24, 25, 30-33, n = 7), and harvested cell amounts and purified NosX yields were compared (Table 2.4). Although cell yield with the LB from Fisher was lower (21.6 ± 4.8 g) than one with the LB from RPI (28.7 ± 4.0 g), NosX expression level per cell with the Fisher brand was ~ 6 times higher than that with media purchased from RPI (Table 2.4, 0.62 ± 0.28 mg/10g cell for Fisher vs. 0.09 ± 0.05 mg/10g cell for RPI). The factor(s) in the LB media from Fisher, which enhanced the NosX yield, has not been identified. Due to the significant enhancement on the NosX yield with the LB media from Fisher brand, this LB media was decided to use in the following optimization steps as mentioned in the method section (Table 2.1).

LB media	Cell yield (g)	NosX	
		Total yield (mg)	mg/10g cell
RPI	28.7 ± 4.0	0.25 ± 0.13	0.09 ± 0.05
Fisher	21.6 ± 4.8	1.32 ± 0.74	0.62 ± 0.28

Table 2.4. The NosX yields with different LB media brands (RPI vs. Fisher). Condition that showed higher NosX yield was highlighted.

It was expected that the cofactor biosynthesis for NosX in *A. cycloclastes* might be a limiting factor for the NosX expression. The cofactor of NosX has been confirmed to be FAD as will be described in chapter 3. Riboflavin composes a part of FAD and thus it was added in culture media for supporting FAD biosynthesis. *Ac*/pMLClustXst was cultured in comparable conditions with (culture #44, 47, 49, 50-52, n = 6) or without 50 ~ 100 mg/flask of riboflavin (culture #37, 39-43, 46, 53, n = 8). 12 L (2 L × 6 flasks, instead of 4 flasks) of LB media was used for following cultures for efficient purification. Although varying amount (50 ~ 100 mg) of riboflavin was added to each flask, 2 L of the

media was saturated with 50 mg of riboflavin and the rest of it was precipitated because of low solubility. No apparent difference was observed in terms of the amount of riboflavin per flask. Cell yield from the culture with riboflavin was relatively lower (26.5 ± 6.4 g) than without riboflavin (34.4 ± 9.3 g) (Table 2.5). No significant positive effect of riboflavin on the NosX yield was observed.

Riboflavin	Cell yield (g)	NosX	
		Total yield (mg)	mg/10g cell
+	26.5 ± 6.4	0.48 ± 0.40	0.16 ± 0.10
–	34.4 ± 9.3	0.63 ± 0.28	0.18 ± 0.07

Table 2.5. The NosX yields with (+) or without riboflavin (–). Condition that showed higher NosX yield was highlighted.

The shaking speed after induction was either reduced to 100 rpm (micro-aerobic conditions, culture #37, 39-43, 46, n = 7) or kept at 250 rpm (aerobic conditions, culture #54-56, 61-62, n = 5) after induction to elucidate the effect of oxygen on NosX yield. Unexpectedly, the NosX expression level was constant under both aerobic and micro-aerobic conditions (Table 2.6, 0.20 ± 0.06 for 100 rpm vs. 0.23 ± 0.14 for 250 rpm). With shaking speed set at 250 rpm, the total NosX yield became twice the cell yield of that obtained at 100 rpm (Table 2.6).

Speed (rpm)	Cell yield (g)	NosX	
		Total yield (mg)	mg/10g cell
100	35.8 ± 9.1	0.70 ± 0.22	0.20 ± 0.06
250	75.3 ± 7.7	1.57 ± 0.87	0.23 ± 0.14

Table 2.6. The NosX yields with different shaking speeds (100 vs. 250 rpm). Condition that showed higher NosX yield was highlighted.

Incubation time (24 hours (n = 5) or 48 hours (n = 7)) after induction was examined to investigate whether the NosX yield was enhanced with prolonged culture (Table 2.7). The results showed that the cell amount and the NosX yield per cell were increased ~ 35 % and ~ 40 % respectively in the 48-hour culture compared to the 24-hour culture. In total, the NosX yield increased about two-fold in the 48-hour culture (Table 2.7).

Culture	Cell yield (g)	NosX	
		Total yield (mg)	mg/10g cell
24 h	75.3 ± 7.7	1.57 ± 0.87	0.23 ± 0.14
48 h	102.4 ± 4.5	3.23 ± 1.20	0.32 ± 0.12

Table 2.7. NosX yields following 24 or 48 hours culture post induction. Condition that showed higher NosX yield was highlighted.

Typically, proteins are expressed at a rapid rate in “log phase” during cell growth and at a slow rate during “stationary phase”. Thus, a mid-log phase (A_{600} = 0.6 - 1.0 in the case of *E. coli*) is known to be the best timing for induction. In *A. cycloclastes*, the correlation of absorption at 600 nm and the growth phase is still not clear, thus induction was carried out at several different A_{600} values to determine the best time to induce to maximize NosX yield. The expression of denitrification proteins, including NosX, were induced through addition of nitrate and copper when A_{600} was between 0.8 and 3.8 (culture #63-67, 72-80, 82-83, n = 16. Correlation between the NosX yield and the A_{600} at induction time was investigated by comparing the cell yield and NosX yield from each culture. No clear correlations among A_{600} at induction, the harvested cell amount, and the

NosX yield were observed (Figure 2.2). However, the highest NosX yield was obtained when A_{600} was 1.0.

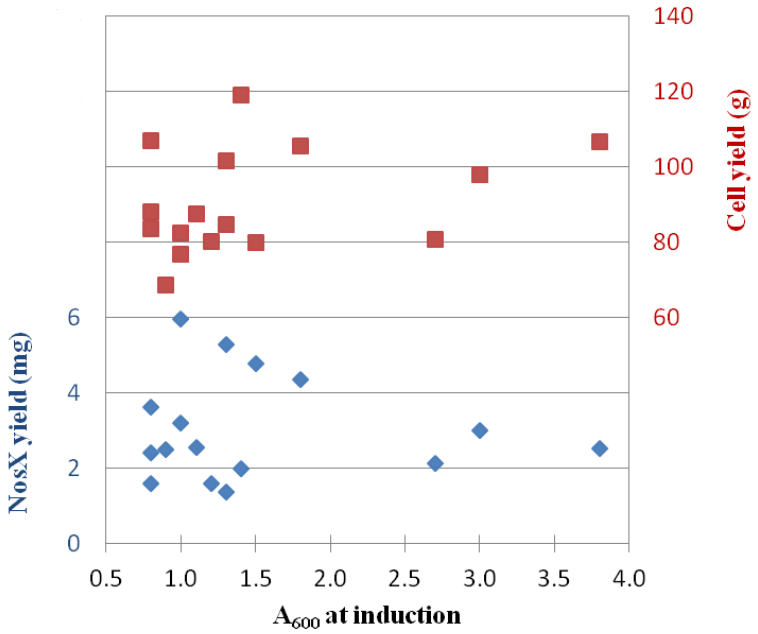


Figure 2.2. NosX yield and cell amount vs. A_{600} at induction

The optimized culture conditions were determined as follows;

1. LB media purchased from Fisher brand enhanced NosX yield six-fold.
2. Riboflavin did not have any positive effect on NosX yield.
3. Incubation with 250 rpm increased NosX yield two-fold.
4. 48-hour incubation increased NosX yield two-fold.
5. Induction at A_{600} = 1.0 seemed to be the best for NosX yield.

The NosX yield under the original growth conditions was 0.28 ± 0.26 mg (culture #1 - 19, n = 19). After optimization, yield was improved to 5.22 ± 0.54 mg in the best case (culture #79-80, 84, n = 3) (Table 2.8). On average, the optimized culture conditions

produced ~ 19-fold higher amount of NosX when compared to the original growth conditions.

Condition	Cell yield (g)	NosX	
		Total yield (mg)	mg/10g cell
Original	23.9 ± 5.8	0.28 ± 0.26	0.10 ± 0.08
Optimized	76.8 ± 6.6	5.22 ± 0.54	0.68 ± 0.06

Table 2.8. NosX yields from the original and optimized culture conditions

Optimization of Purification Conditions for NosX

During the NosX purifications, binding capacity of the strep-tactin column was irreversibly decreased by biotin (vitamin B_7) in the *Ac* cell extract. It has been known that *A. cycloclastes* has several biotinylated proteins which potentially interfere with the purification using the strep-tag affinity system (Bollinger, J. *et al.* unpublished results). Therefore, it was desirable to remove biotinylated proteins from the cell extract before loading it on the strep-tactin column. An ammonium sulfate fractionation method was applied. The results of the SDS-PAGE and western blot of NosX purification are shown in Figure 2.3. The labels (#1 - 4) in Figure 2.3 indicate the supernatant after cell breakage and centrifugation (#1), supernatant and precipitate from 40 % ammonium sulfate precipitation (#2 and #3), and the elution fraction from the strep-tactin sepharose column (#4). Marker proteins (M) were pre-stained in red (72 kDa) and blue (130, 95, 55, 43, 34, 26, 17, and 11 kDa). Thus, these marker bands are also visible on the western blot membrane (Figure 2.3, right). In preliminary experiments, it was found that NosX was precipitated at 40 % saturation of ammonium sulfate, which was also apparent in Figure

2.3 (#2) since no NosX band was observed in the supernatant of 40 % ammonium sulfate precipitation. Three biotinylated proteins (130, 70, and 20 kDa) and NosX (31 kDa) were detected by the western blot. These four proteins were observed in the cell extract from *Ac*/pMLClustXst (#1), although minimally. The 130 kDa biotinylated protein was successfully removed by the 40 % ammonium sulfate precipitation (#2, #3).

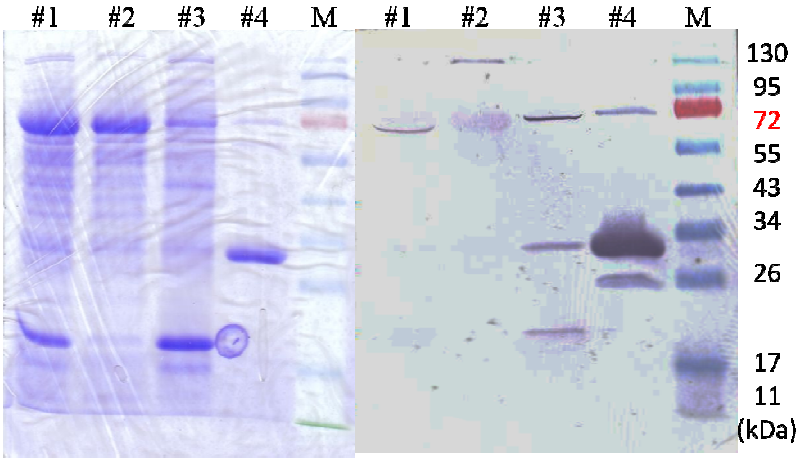


Figure 2.3. SDS-PAGE (left) and western blot (right) for NosX purification. #1, cell extract; #2 and #3, supernatant and precipitate from 40 % ammonium sulfate precipitation; #4, elution fraction; M, marker

In this purification process, however, the 70 and 20 kDa biotinylated proteins could not be removed from the NosX containing fraction before loading the sample onto the strep-tactin affinity column (#3). The 70 kDa protein was observed in both #3 and #4, whereas the 20 kDa protein was not observed in the elution fraction (#4).

Discussion

The expression level of NosX in *Ac*/pMLClustXst was very low using the original culture conditions and it became necessary to improve yields in order to carry out

biochemical characterization of this protein. Overexpression of NosX in *E. coli* and cofactor reconstitution trials for the heterologously expressed NosX had failed in our lab (Bollinger, J. *et al.* unpublished results). Thus, we attempted to enhance the NosX yield from the *Ac* homologous expression system (pMLClustXst) by modifying the plasmid and optimizing the culture conditions for further characterization of NosX (chapter 3 and 4). Additionally, the NosX purification procedure with the strep-tag was also modified for sustainable purification.

Promoter Refinement for NosX

The expression level of NosX was low, suggesting that the native NosX promoter in the *nos* cluster was not potent. In *A. cycloclastes*, the expression level of PAz (*Ac*PAz) was revealed to be high (91). It was also observed that the expression level of NiR in *A. cycloclastes* (*Ac*NiR) was significant (Ijima, F. *et al.* unpublished observation). These observations indicated that the promoters of *Ac*PAz and *Ac*NiR were expected to be potent. As the expression levels of *Ac*NiR and *Ac*PAz were known to become high under denitrifying conditions, these promoters included putative Dnr/DnrD binding motifs which were not observed in the native NosX promoter. Thus, the NosX promoter was replaced with the promoters of *Ac*NiR and *Ac*PAz to enhance the NosX expression level. Unexpectedly, the expression levels of NosX between p5-(Np/Pp)-*nosX* and pMLClustXst expression systems were almost the same (Table 2.2, *Ac*/p5-Np-*nosX* (0.10 mg/10 g cell), *Ac*/p5-Pp-*nosX* (0.13 mg/10 g cell), and *Ac*/pMLClustXst (0.10 ± 0.08 mg/10 g cell)). It is still unknown why the expression level of NosX was not enhanced by these potent promoters. There are several possibilities to explain this observation. First, it

might be possible that mRNAs of *nosX* in the cell are unstable and NosX expression does not reach expected levels. Second, it is possible that NosX in the cell is unstable and degrades quickly before isolation. As will be discussed in chapters 3 and 4, NosX is unstable *in vitro*. This observation might imply that there are additional protein components that stabilize NosX *in vivo*. If the amounts of these additional components are insufficient in the NosX overexpressed cell, it might result in degradation of NosX. Third, the promoters of *Ac*NiR and *Ac*PAz might not be effective for NosX overexpression from the plasmids. To evaluate these hypotheses, additional investigations will be required.

The combination of *Ac*/pMLClustXst and the LB media purchased from Fisher resulted in much higher NosX efficiency (~ 5-fold) relative to *Ac*/p5-(Np/Pp)-*nosX* (1.3 - 1.4-fold) (Table 2.4). Interestingly, the LB media from Fisher did not show a positive effect for the NosX yield on p5-(Np/Pp)-*nosX* expression systems (Table 2.3). One of differences between *Ac*/pMLClustXst and *Ac*/p5-(Np/Pp)-*nosX* was that the whole set of Nos proteins were expected to be overexpressed in *Ac*/pMLClustXst whereas only NosX was overexpressed in *Ac*/p5-(Np/Pp)-*nosX*. Therefore, the overexpressed Nos proteins might be involved in the enhancement effect on NosX expression levels with the unknown factor in the LB from Fisher. As mentioned in chapter 1, it has been reported that NosR acts as a positive regulatory element for the expressions of the other Nos proteins (106; 50). Hence, in this hypothesis, overexpressed NosR in *Ac*/pMLClustXst would be the most plausible candidate that would enhance NosX expression. Although the expression level of NosR in *Ac*/pMLClustXst was not monitored directly, it was

plausible that NosR was also overexpressed because active N_2OR (NosZ) in *Ac*/pMLClustXst was 10 - 100-fold overexpressed compared to *Ac* without the plasmid (125). Further, this enhancement mechanism with the unknown factor in LB media from Fisher was expected to be independent (or could be remotely related) from transcriptional factor Dnr/DnrD for the following reason. *Ac*/p5-(Np/Pp)-*nosX*, which had Dnr/DnrD binding sites in the promoter, did not show the enhancement of the NosX expression, whereas the *nosX* gene in *Ac*/pMLClustXst, which did not have Dnr/DnrD binding site in the promoter, showed the enhancement.

Culture Conditions for NosX

Culture conditions were optimized to increase the NosX yield from *Ac*/pMLClustXst. Three conditions (LB media, aeration speed, and prolonged incubation time) were identified as positive factors on the NosX yield. Since there were still fluctuations on the yield after the optimizations, existence of another unknown factor on the NosX expression is implied.

In the presence of oxygen, aerobic respiration is expected to occur preferentially rather than denitrification (3). Although dissolved oxygen in the LB media was not monitored during the cultures, the media agitated at 250 rpm was assumed to be aerobic because significant increase of the cell yield was observed (Table 2.6, 35.8 ± 9.1 g for 100 rpm vs. 75.3 ± 7.7 g for 250 rpm). It was reasonable that the cell yield was increased under the aerobic conditions (250 rpm) because the aerobic respiration system is more efficient with regard to energy generation for cell proliferation than nitrate respiration (denitrification). However, the NosX expression level was consistent under both aerobic

and micro-aerobic conditions (Table 2.6, 0.23 ± 0.14 mg/10 g cell for 250 rpm and 0.20 ± 0.06 mg/10 g cell for 100 rpm). Initially, it was expected that expression of NosX would be decreased under the aerobic conditions since the expression of Nos proteins were controlled by the transcriptional factor Dnr/DnrD and NosR. It was reported that transcription of *dnrD* was activated in O_2-limited cells in *Pseudomonas stutzeri* (128) and *nos* gene expression was activated under anaerobic conditions (55). It was also known that NosR had Fe-S clusters in the cytoplasmic region that were expected to regulate expression of the other Nos proteins (82; 106). Since the Fe-S cluster is oxygen sensitive, the regulation ability of NosR is expected to be perturbed in aerobic conditions. In contrast, it was also reported that denitrification could occur even under aerobic conditions, which was referred to as aerobic denitrification (129). Although no advantage on nitrate respiration under aerobic conditions was known, this phenomenon has been observed in denitrifying bacteria such as *Paracoccus denitrificans* (130) and *Pseudomonas stutzeri* (105). The observation on the NosX expression under aerobic conditions might suggest that aerobic denitrification by *Achromobacter cycloclastes* is occurring. It was also reported that a small amount of N_2OR was expressed constitutively in *Pseudomonas stutzeri* even under aerobic conditions (105; 50). The consistent expression of NosX could be also explained as NosX was expressed constitutively at a low level in *Ac*.

Currently, there are two hypotheses to explain the result that the expression level of NosX was constant under the aerobic and micro-aerobic conditions. The first hypothesis is that the DnrD/NosR regulation systems for the Nos protein expression in *Ac*

might be relatively insensitive to oxygen. This hypothesis is supported by the facts that denitrification can occur under aerobic conditions and N_2OR was constitutively expressed under aerobic conditions. If the DnrD/NosR could function under aerobic conditions as well, it explained why the expression level of NosX was consistent under both aerobic and micro-aerobic conditions. The second hypothesis is based on the traditional concepts for denitrification, that is, denitrification does not function in the presence of abundant oxygen. This hypothesis is supported by the fact that many proteins related to denitrification are sensitive to oxygen. In this hypothesis, the expression of NosX should be independent, at least in part, from the oxygen sensitive DnrD/NosR regulation systems. Instead, there might be another expression mechanism for NosX that is oxygen resistant, although there has been no report supporting this hypothetical expression mechanism to date.

The protein expression levels vary with time, and therefore the incubation time needs to be optimized to maximize the particular protein yield. It was reported that there was a lag between the expressions of NiR and NOR and the expression of the *nos* genes (14). This can be explained as follows: after potassium nitrate was added to the LB media, denitrifying bacteria start using nitrate for respiration. As described in chapter 1, nitrate will be converted to nitrite and NO by NaR and NiR in the denitrification process (Figure 1.1). Once NO starts to be generated, it strongly enhances the expression of the *nos* genes via Dnr/DnrD (102; 55; 99), subsequently resulting in the expression of N_2OR and its accessory proteins are started to be expressed. Therefore, a considerable time lag is expected for expression of the Nos proteins. Indeed, the results showed that the NosX

expression level per cell was increased in the elongated (48-hour) cultures (Table 2.7), consistent with this expectation.

Purification Conditions for NosX

Protein purification with an affinity tag is a commonly known technique to isolate target proteins with one step. The strep-tag, which is a widely used affinity purification system, was attached to the C-terminal part of NosX (125). As will be revealed in chapters 3 and 4, NosX requires a high salt concentration (150 mM NaCl) for its stabilization. Thus, affinity techniques are essential for the purification of NosX because standard ion exchange techniques that require low salt conditions cannot be used.

Biotin is a critical contaminant that interrupts the purification process using the strep-tactin column. In *E. coli*, the total amount of biotin in cell lysate is negligible (~ 1 nmol in 1 g cell) and only 20 µg (per 1 g cell) of avidin, which binds to biotin and inhibits the irreversible binding between biotin and the strep-tactin resin, was required for column maintenance (131). Thus, the strep-tag is an excellent option for protein purifications from *E. coli*. However, this affinity purification system was found to be not suitable for the protein purification from *Achromobacter cycloclastes* because there are a considerable amount of biotinylated proteins (20, 70, and 130 kDa proteins, Figure 2.3) in the cell extract. Indeed, even with the 4-fold amount of avidin treatment (12.5 U for 10g cell (~ 86 µg/g cell)) compared to the prep from *E. coli*, the binding capacity of the strep-tactin column was gradually and irreversibly reduced.

Although the 130 kDa protein was successfully removed from the NosX containing fraction by the ammonium sulfate precipitation, the 20 and 70 kDa proteins

could not be removed with the present purification protocol. According to the western blot (Figure 2.3), the 70 kDa protein was observed in both #3 and #4, indicating that this protein still had affinity to the column, but the interaction between this protein and the column resin was reversible and thus could be eluted. In contrast, the 20 kDa protein was not observed in the elution fraction (#4) and it indicated that this protein irreversibly bound to the column. Therefore, the 20 kDa protein was likely contributing to the reduction of the column capacity. The reason that avidin could not neutralize biotin in the 20 kDa protein was probably that bulky avidin (MW = 66 kDa) could not access biotin in the 20 kDa protein because of steric hindrance. For further investigations, the protocol needs to be improved to remove the 20 kDa protein prior to loading the sample to the strep-tactin column. Ion exchange and hydroxylapatite columns could not separate the biotinylated proteins from the NosX containing fraction under high salt conditions (data not shown). Alternatively, GST (Glutathione S-Transferase) or MBP (Maltose-Binding Protein) tag systems might be better choices for both purification and protein stabilization of NosX, since these tags, which are very stable and soluble proteins, may significantly improve the stability of the fused protein in solution. As mentioned in chapter 1, NosF was successfully purified and characterized as a MBP tagged protein (50).

Conclusions

Two new expression systems for NosX (*Ac*/p5-(Np/Pp)-*nosX*) were successfully constructed with strong promoters for *Ac*NiR (Np) and *Ac*PAz (Pp). The expression levels of NosX in *Ac* with the new expression systems were examined and compared. The

new systems showed 1.3 ~ 1.4-fold higher yields of NosX than *Ac*/pMLClustXst. In addition, we determined the NosX yield was significantly enhanced (5 - 6-fold) when *Ac*/pMLClustXst was cultured with the LB media purchased from Fisher bland. Five factors during culture were optimized for NosX expression using *Ac*/pMLClustXst. After the optimizations, the NosX yield was ~ 19-fold increased compared to the original conditions.

CHAPTER 3

CHARACTERIZATION OF NOSX FROM *ACHROMOBACTER CYCLOCLASTES*

Introduction

Several papers have explored the function of NosX by deleting the *nosX* gene *in vivo* (114; 52; 83). In *Paracoccus denitrificans*, the function of NosX has been connected to activation of N_2OR *in vivo* (83). However, NosX has not previously been isolated and fully investigated. Gaining functional and structural information of NosX is essential to understanding the putative mechanism of N_2OR activation by this protein.

Further, it is known that several proteins interact with more than one protein in the denitrification process. For example, NirX in *Paracoccus denitrificans* was shown to interact with N_2OR although this protein was expected to work on NiR because it was coded in the *nir* gene cluster (83). NosX in *Paracoccus denitrificans* was implied to interact with both N_2OR and NiR (132). Pseudoazurin and cytochrome c_{550} are also known to donate electrons to several enzymes such as NiR, NOR, and N_2OR (88; 91; 86; 89). These observations indicate that NosX from *A. cycloclastes* (*Ac*NosX) may indeed interact with several proteins other than N_2OR. Characterization of the biochemical properties of *Ac*NosX will provide critical insight into potential interactions between NosX and other proteins of the denitrification system.

In the previous chapter, the culture conditions were successfully optimized to enhance *Ac*NosX yields, which enabled us to carry out the studies in the remainder to this

thesis. In this chapter, the properties of *Ac*NosX were investigated *in vitro*. The structure of *Ac*NosX was also investigated by crystallization and homology modeling methods.

Materials and Methods

Confirmation of the DNA Sequence of *nosX* Gene

The *nosX* gene in pMLClustXst and pTrcClust were sequenced to confirm the sequence that was registered in the GenBank. The pTrcClust plasmid included whole *nos* cluster from the *Ac* genome DNA and was the original template for the other derivative such as pMLClustXst. The primer sequences were as follows;

NosX sequence primer #1: GACGCCGGTGGAGACCGGCTCGG

NosX sequence primer #2: CGCTTCGATCCGACGGTACAGCCGCTC

NosX sequence primer #3: CCCCTCTCGGCACGACCTTCGATCAAGC

The three primers were designed to read anterior region, middle region, and posterior region of *nosX* sequence. 1 µg of DNA and 10 pmol of primer were mixed and sent to the University of Iowa for sequence.

Molecular Weight and Quaternary Structure of *Ac*NosX

The molecular weight of *Ac*NosX was measured with micrOTOF-MS (Bruker Daltonics) with an electrospray ionization (ESI) source. 4 µL of *Ac*NosX (150 µM in Buffer W) was mixed with 4.5 µL of 0.1 % formic acid and injected to a Luna C8 cartridge column (Phenomenex Inc.) that was connected to the micrOTOF-MS at a flow rate 200 µL/min. *Ac*NosX in the column was eluted with buffer A (0.1 % formic acid, 99.9 % H_2O) and buffer B (0.1 % formic acid, 99.9 % acetonitrile). Subsequently, the

mass spectra of *Ac*NosX were measured in the 300-3000 m/z range in the positive mode. The data was analyzed with the Bruker Daltonics DataAnalysis version 3.3.

The quaternary structure of *Ac*NosX in solution was determined using a gel filtration column as previously described (121). The column was equilibrated with Buffer W. The calibration was conducted using a gel filtration standard (Bio-Rad) containing thyroglobulin (bovine, 670 kDa), gamma globulin (bovine, 158 kDa), ovalbumin (chicken, 44 kDa), myoglobin (horse, 17 kDa), and vitamin B_{12} (1.35 kDa). The void volume (Vo) was determined with thyroglobulin. The molecular weight of *Ac*NosX was calculated with a plot of log molecular weight of the standard versus the elution volumes over the void volume (Ve/Vo). The quaternary structure of *Ac*NosX was deduced from the molecular weight.

Cofactor Identification

The identity of the cofactor bound to *Ac*NosX was determined using a fluorescence spectroscopy method, as previously described (133). The *Ac*NosX concentration was determined with absorption at 450 nm and the molecular extinction coefficient of ε_{450} = 11570 M^{-1} cm^{-1} (134). 1000 µL of 10 µM *Ac*NosX in 20 mM Tris (pH 8.0) was denatured by incubation at 100 °C for 10 min. The denatured protein was removed by centrifugation at 14000 rpm for 10 min. 15 µL of phosphodiesterase I (PDE) solution (362 mU) was added to the supernatant that included the *Ac*NosX cofactor. Fluorescence and UV/Vis spectra of *Ac*NosX, the extracted *Ac*NosX cofactor, and the cofactor with PDE were measured and compared. The samples were excited at 455 nm, and the emission spectra were measured between 470 and 670 nm. Positive and negative

controls were measured where the same amount of PDE solution was added to 1000 µL of either 10 µM FAD or FMN in 20 mM Tris (pH 8.0). Fluorescence and UV/Vis spectra were measured before and after addition of PDE to the samples.

Redox Potential

The redox potential of *Ac*NosX was determined using the method described by Massey (135) with slight modifications. As preliminary experiments, *Ac*NosX and anthraquinone 2-sulfonate (AS, redox dye, E = -225 mV) were individually photo-reduced and monitored by UV/Vis spectroscopy to determine the molecular extinction coefficients of oxidized and reduced forms under the experimental conditions. Also, the appropriate incubation time following photo-reduction, which was necessary for equilibration among the electron transfer reactions involving *Ac*NosX, AS, and benzyl viologen (BV), was determined by monitoring UV/Vis spectra.

*Ac*NosX, a mixture of AS and BV in 100 mM phosphate, 150 mM NaCl, 10 % glycerol, 10 mM EDTA, pH 7.0 (Buffer PE), and an anaerobic cuvette were individually purged with Ar gas for at least 1 hour on ice. The oxygen purge for the *Ac*NosX solution was carried out by gently blowing Ar gas on the surface of the protein solution. The sample was tapped once every 10 to 15 min. The buffer with reagents was intensively purged with Ar gas to remove dissolved oxygen in the solution. After anaerobic conditions were established, *Ac*NosX and reagents were injected in the cuvette. Final concentrations of *Ac*NosX and AS were 10 µM, and BV was 1 µM. AS, BV, and EDTA were used as an internal standard, a mediator in electron transfer, and electron source in the photochemical reaction, respectively. The cuvette was illuminated in the ice/water

bath for 15 sec using a Xe arc lamp (175 W, Lambda-LS/17, Sutter Instrument Company) and an IR cut-off filter. The cuvette was incubated for 10 ~ 15 min in the dark while stirring at 10 °C to let the both redox pairs of $NosX_{ox}/NosX_{red}$ and AS_{ox}/AS_{red} reach equilibrium. After incubation, the UV/Vis spectrum was recorded. The light exposure and UV/Vis measurements were repeated until no more changes were observed in the spectra. At each equilibrium state, the concentrations of oxidized and reduced *Ac*NosX ($[NosX_{ox}]$, $[NosX_{red}]$) were calculated with the equation $[NosX_{red}] = [NosX_{total}] - [NosX_{ox}]$ and using the Lambert-Beer equation ($A= \varepsilon_{red}[NosX_{red}] + \varepsilon_{ox}[NosX_{ox}]$). The concentrations of oxidized and reduced AS ($[AS_{ox}]$, $[AS_{red}]$) were also calculated similarly. The data were analyzed with the Nernst equation as previously described (136). Measurements were completed in triplicate.

Secondary and Tertiary Structure Predictions

The secondary structure of *Ac*NosX was predicted from the sequence using three different methods: JUFO (137), PSIpred (v3.0) (138), and PAPIA (139). The secondary structures of *Ac*PAz (PDB code: 1BQR) and *Ac*N_2OR (PDB code: 2IWF) were also predicted by those sequences to check the accuracy of the methods. Structural ratios of helix, sheet, and random coil content in *Ac*NosX were calculated by the three methods and compared with a homology model (described below).

A three-dimensional *Ac*NosX structure was generated by homology modeling with the ApbE protein from *Salmonella enterica* (121) (PDB code: 3PND). Sequences of both *Ac*NosX and ApbE were aligned by T-Coffee (140) and a homology model was

generated with the aligned sequence and Swiss-Model (alignment mode) (141). The coordinates of FAD from ApbE were superimposed onto the model structure.

The electrostatic potential and hydrophobicity of the *Ac*NosX model surface were calculated by PyMOL using the Adaptive Poisson-Boltzmann Solver (APBS) (142) and rTools (143) plugins. Additionally, the sequences of *Ac*NosX (Genbank accession code: AAD09162), *Paracoccus denitrificans PD1222* (*Pd*NosX, CAB53356), *Sinorhizobium meliloti* (*Sm*NosX, AAB69119), and *Bradyrhizobium japonicum* (*Bj*NosX, CAA05524) were aligned by Clustal W 2.1 (144) and compared with the sequence and structure of ApbE protein to identify possible correlations between conserved regions and the FAD binding motif. The results were displayed with BoxShade 3.21 (145). The conserved amino acids among NosX proteins and potential FAD binding residues were mapped on the homology model of *Ac*NosX to identify candidates for functionally important regions in *Ac*NosX.

Crystallization Trials

Crystallization of *Ac*NosX was attempted for structural studies. The *Ac*NosX concentration was adjusted to 5 mg/mL in 5 mM Tris, 150 mM NaCl, and 10 % glycerol (pH 8.0). Screening reagents (96 × 7 plates = 672 conditions) were purchased from Hampton research and Emerald BioSystems Inc. Screening plates were set up with a Honeybee protein crystallization system (Genomic Solutions). The samples were crystallized with the sitting drop method under 4 °C. The conditions that showed crystal-like structures were used for further optimizations using a 24-hole plate and the hanging drop method. Optimization of the conditions was carried out by changing concentrations

of salt, buffer, and precipitant. The amount of crystallization solution in the reservoir was 1 mL, and 2 µL each of the solution and *Ac*NosX were mixed on a cover glass and incubated at 4 °C.

Results

Confirmation of the DNA Sequence of *nosX* Gene.

The *nosX* gene in pMLClustXst and pTrcClust were sequenced to determine if there was an error in the sequence of *Ac*NosX. The results showed that both pMLClustXst and pTrcClust had A159 (GCT) whereas V159 (GTC) was registered in the Genbank. The data in the Genbank was obtained from the sequence of pTrcClust and was obviously misread. The corrected sequence fitted closely to the measured molecular weight.

Molecular Weight and Quaternary Structure of *Ac*NosX

The molecular weight of *Ac*NosX was determined to be 30806.58 Da by the micrOTOF-MS, which was different from the theoretical molecular weight of 30835 Da. This result indicated that there was an error in the sequence from either the pMLClustXst plasmid or the sequence data in the Genbank database (code: AAD09162.2). To confirm, the *nosX* gene in pMLClustXst and pTrcClust were sequenced (see next section for details). The result indicated that V159 (GTC) (V183 with the signal peptide) in the Genbank should be A159 (GCT). This correction shifted the theoretical molecular weight to 30807 Da, which was very close to the measured value of 30806.58 Da.

The quaternary structure of *Ac*NosX was measured using a gel filtration column and standard markers. *Ac*NosX and the standard markers were individually applied to the column and the elution times were monitored. The molecular weights of the standards and *Ac*NosX were plotted versus the elution volume over void volume (Ve/Vo) (Figure 3.1). The elution position of the purified *Ac*NosX (Ve/Vo = 1.76) is indicated by an empty square that is labeled as NosX in Figure 3.1. The calculated molecular weight of *Ac*NosX in Buffer W from the plot was 31583 Da which was close to the molecular weight of one holo-*Ac*NosX with one FAD molecule bound (31592.6 Da). This result indicated that *Ac*NosX was monomeric under the experimental conditions.

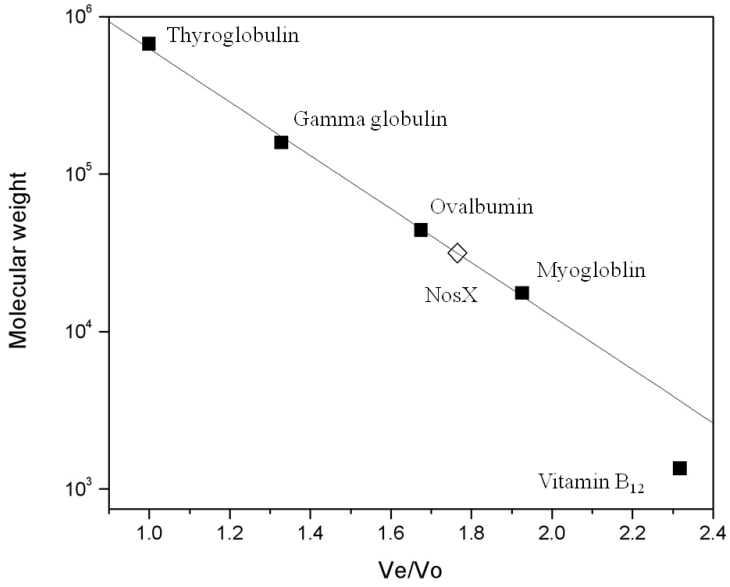


Figure 3.1. Quaternary structure analysis of *Ac*NosX with a gel filtration column

Cofactor Identification

PDE converts flavin adenine dinucleotide (FAD) to flavin mononucleotide (FMN) by breaking a phosphodiester bond. The fluorescence intensity of FMN is ~ 10-fold

stronger than FAD (133). In the control experiments, FAD showed a significant increase of fluorescence intensity with PDE (Figure 3.2B) whereas the intensity of FMN did not change, as expected (Figure 3.2C). The fluorescence spectrum of the extracted cofactor from *Ac*NosX showed a significant increase of intensity in the presence of PDE (Figure 3.2A, blue). The result was almost identical to the control experiment for FAD, and clearly showed that the cofactor bound to *Ac*NosX was FAD.

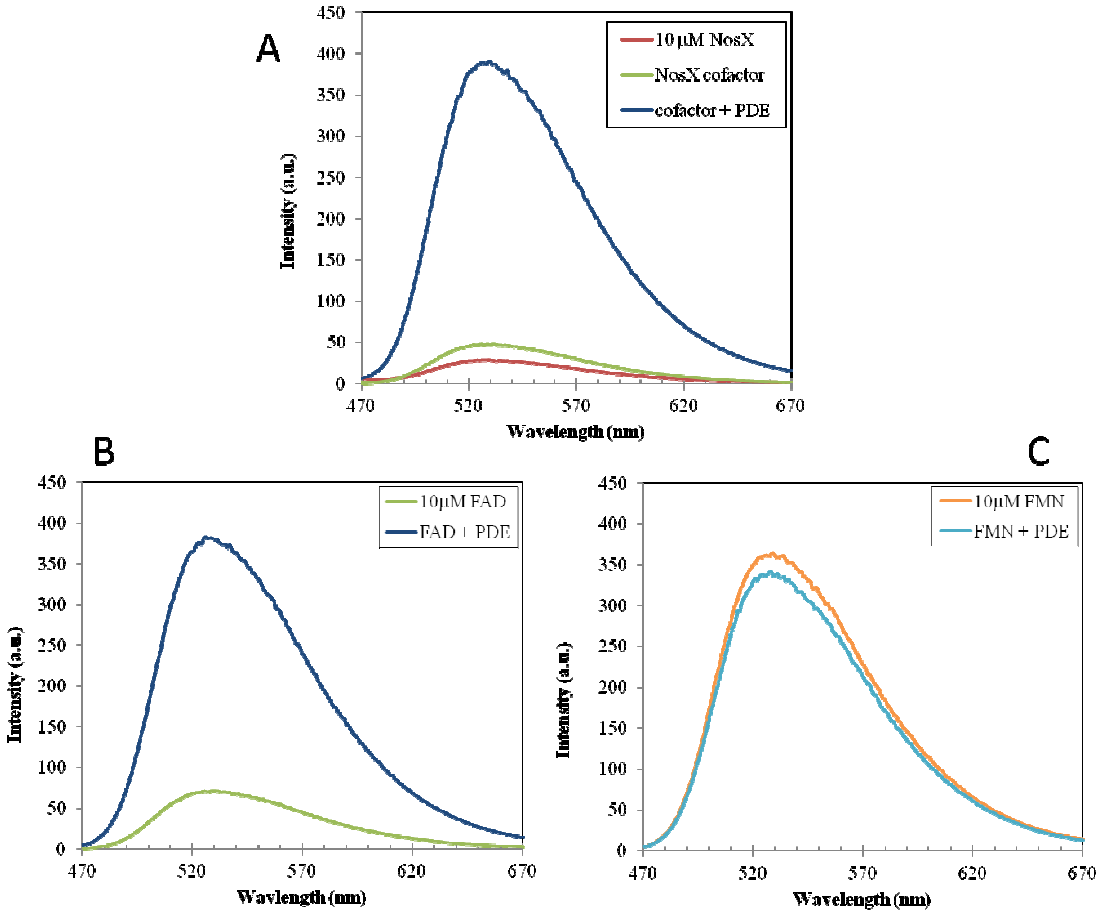


Figure 3.2. Normalized fluorescence spectra (10 µM) of (A) *Ac*NosX cofactor, (B) FAD and (C) FMN with or without PDE

Redox Potential

*Ac*NosX and anthraquinone 2-sulfonate (AS) were individually photo-reduced and monitored by UV/Vis spectroscopy. The absorption peaks at 374 and 460 nm of oxidized *Ac*NosX were diminished as the protein was reduced (Figure 3.3A). Oxidized AS showed a peak at 330 nm, which decreased upon reduction, whereas peaks at 381 and 400 nm concomitantly increased (Figure 3.3B). Isosbestic points were observed at 338 nm for *Ac*NosX (Figure 3.3A) and 355 nm for AS (Figure 3.3B). The concentrations of *Ac*NosX and AS during the photo-reduction were determined using the absorptions at 355 nm for *Ac*NosX and 338 nm for AS. The molecular extinction coefficients of *Ac*NosX at 355 nm were calculated as $\varepsilon_{355,\,ox} = 9626\ M^{-1}\ cm^{-1}$ (fully oxidized form) and $\varepsilon_{355,\,red} = 5184\ M^{-1}\ cm^{-1}$ (fully reduced form). The molecular extinction coefficients of AS at 338 nm were also calculated as $\varepsilon_{338,\,ox} = 4673\ M^{-1}\ cm^{-1}$ and $\varepsilon_{338,\,red} = 1458\ M^{-1}\ cm^{-1}$. It should be noted that any increasing peak around 540 - 700 nm, which is indicative of the semiquinone form of FAD (146), was not observed during the stepwise photo-reduction of *Ac*NosX (Figure 3.3A). It was also confirmed that 10 min of incubation was sufficient to reach a state of equilibrium for the electron transfer reaction among *Ac*NosX, AS, and BV since no spectral change was observed in the UV/Vis spectra after 10 min (data not shown).

The redox potential of *Ac*NosX was determined by photo-reduction in the presence of AS as an internal standard. Typical UV/Vis spectra of the sample at various equilibrium states are shown in Figure 3.4. The plotting of $\log([NosX_{ox}]/[NosX_{red}])$ versus $\log([AS_{ox}]/[AS_{red}])$ according to Minnaert (146) gave a linear line with a slope of

0.95 and intercept of 0.201 (Figure 3.4, inset). The redox potential of *Ac*NosX under the experimental conditions was calculated to be -231 ± 0.6 mV.

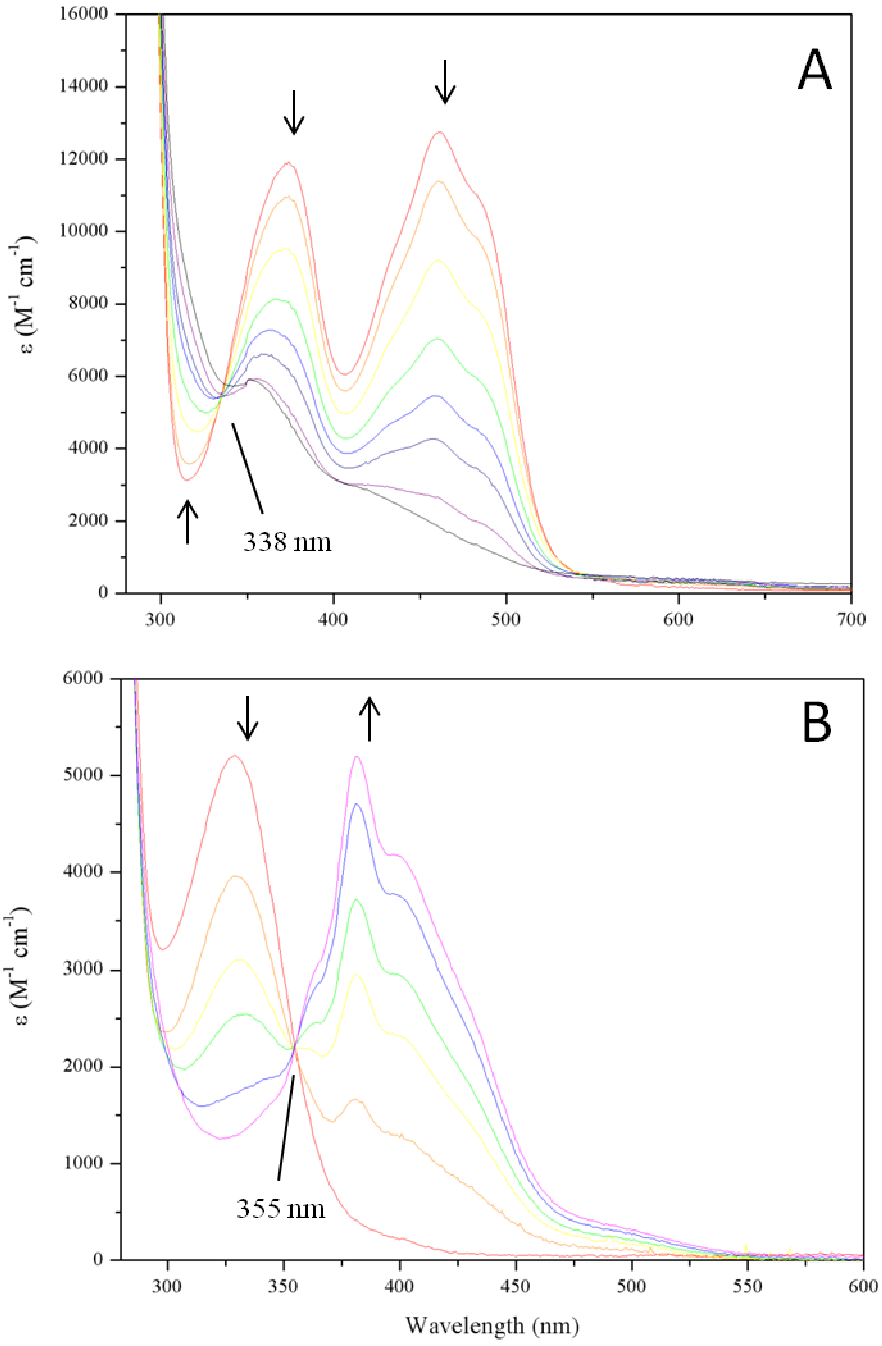


Figure 3.3. Stepwise photo-reductions of *Ac*NosX (A) and anthraquinone 2-sulfonate (B)

This method to determine the redox potential using a redox dye was based on the premise that there was no significant binding between the protein (*Ac*NosX) and the dye (AS) (136). After redox measurements, the samples were injected onto a gel filtration column and *Ac*NosX and AS were clearly separated based on information from the elution profile and UV/Vis spectra (data not shown). This result showed that *Ac*NosX did not bind AS significantly under our experimental conditions.

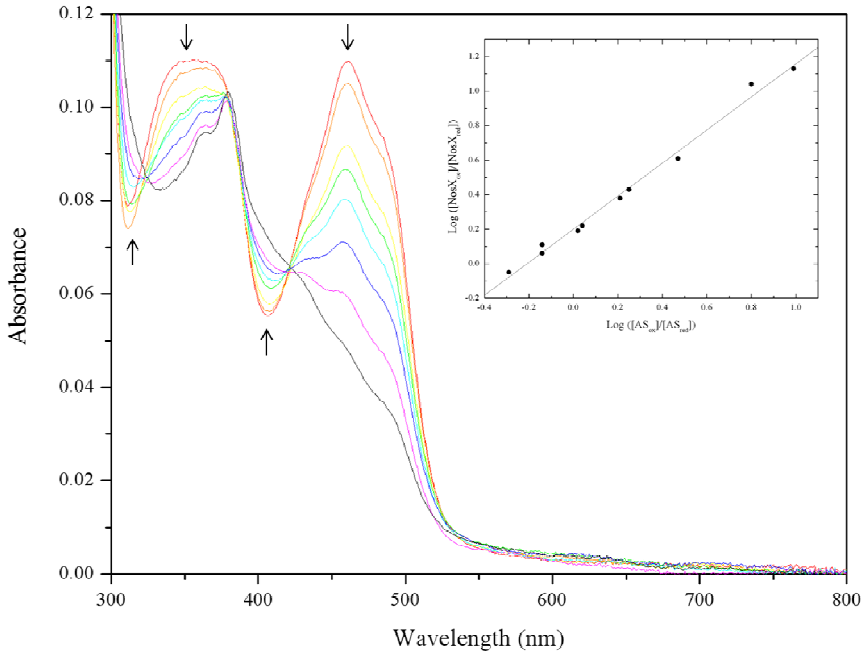


Figure 3.4. Titration measurement of redox potential of *Ac*NosX

Secondary and Tertiary Structure Predictions

Comparison of the secondary structure predictions of *Ac*NosX by JUFO, PSIpred, and PAPIA are shown in Table 3.1. The accuracies of each program were evaluated using the sequences and structures of *Ac*PAz and *Ac*N_2OR. Among the three programs, PSIpred

showed the highest accuracy on secondary structure prediction (93.3 % for *Ac*PAz and 85.4 % for *Ac*N_2OR). The predicted values for *Ac*NosX structure with PSIpred (helix: 32 %, sheet: 24 %, and coil: 44 %) were very close to the ratio of each component (helix: 36 %, sheet: 22 %, and coil: 42 %) in the generated *Ac*NosX model, suggesting the model structure was reasonable.

		JUFO	PSIpred	PAPIA	*Ac*NosX model
*Ac*PAz		75.8%	93.3%	68.5%	-
AcN_2OR		72.4%	85.4%	65.4%	-
*Ac*NosX	Helix	36%	32%	36%	36%
	Sheet	25%	24%	12%	22%
	Coil	39%	44%	52%	42%

		Calculation by PSIpred	PAz (1BQR)
PAz	Helix	14.5%	15.3%
	Sheet	33.1%	33.9%
	Coil	52.4%	50.8%
	Accuracy	93.3%	

		Calculation by PSIpred	N_2OR (2IWF)
N_2OR	Helix	9.8%	8.5%
	Sheet	30.5%	35.3%
	Coil	59.7%	56.2%
	Accuracy	85.4%	

Table 3.1. Secondary structure predictions of *Ac*NosX by JUFO, PSIpred, and PAPIA (upper) and calculated values of PAz and N_2OR by PSIpred (lower)

The homology model of *Ac*NosX generated with ApbE and its surface electrostatic potential are shown in Figure 3.5. The electrostatic potential map on the surface of *Ac*NosX model showed a putative FAD binding pocket that was negatively charged. This negatively charged pocket was also observed in the FAD binding site of ApbE protein (Appendix C, Figure S3.1). The Tyr46 (Tyr70 with the signal peptide) residue which was well conserved in NosX from various species was located close to the

isoalloxazine ring of FAD for a pi stacking interaction in the model (Figure 3.5). This observation indicated that Tyr46 might be important to hold the FAD cofactor in *Ac*NosX.

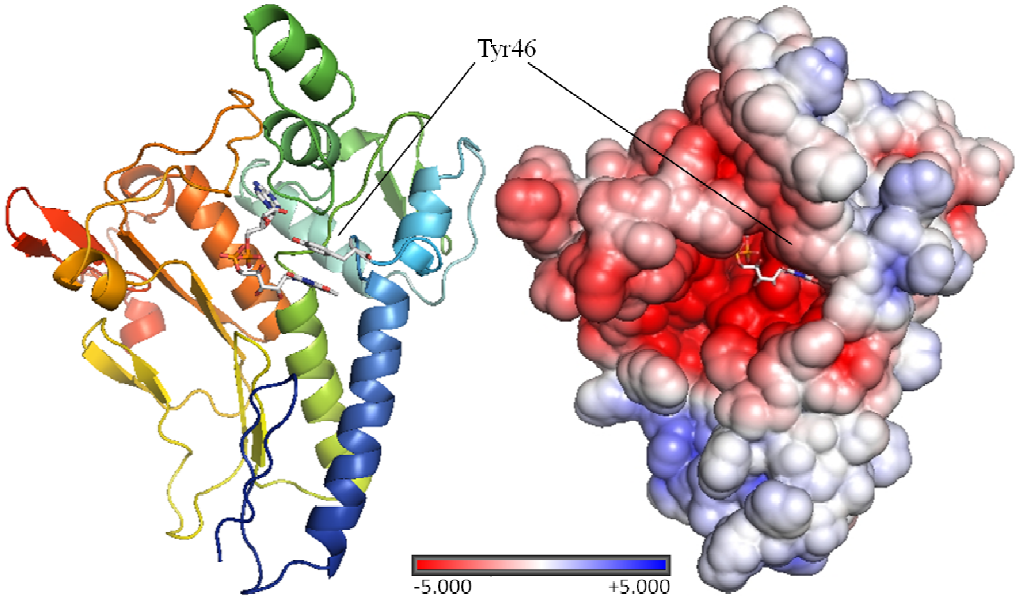


Figure 3.5. *Ac*NosX model based on ApbE and surface electrostatic potential

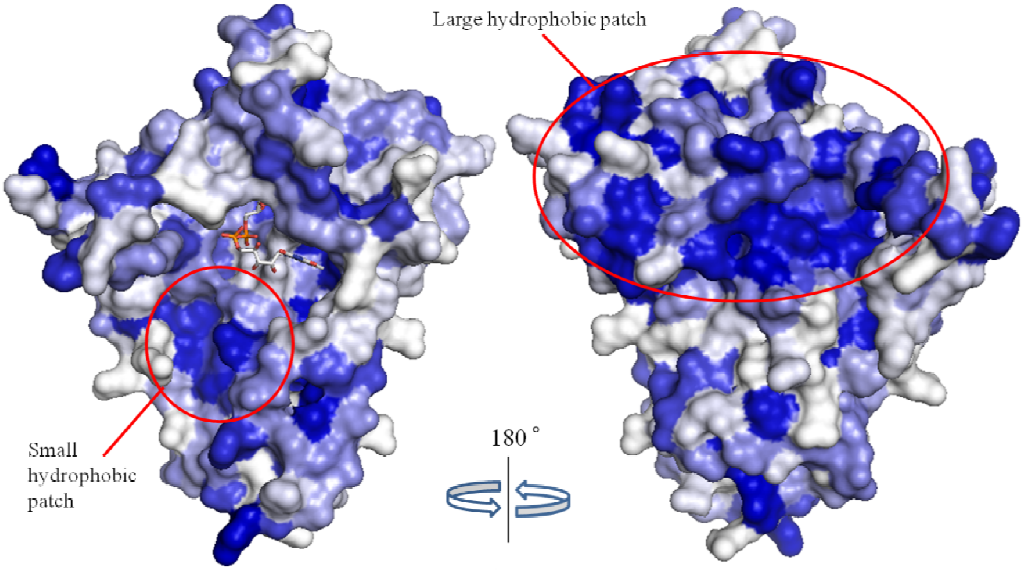


Figure 3.6. Hydrophobicity of the *Ac*NosX model

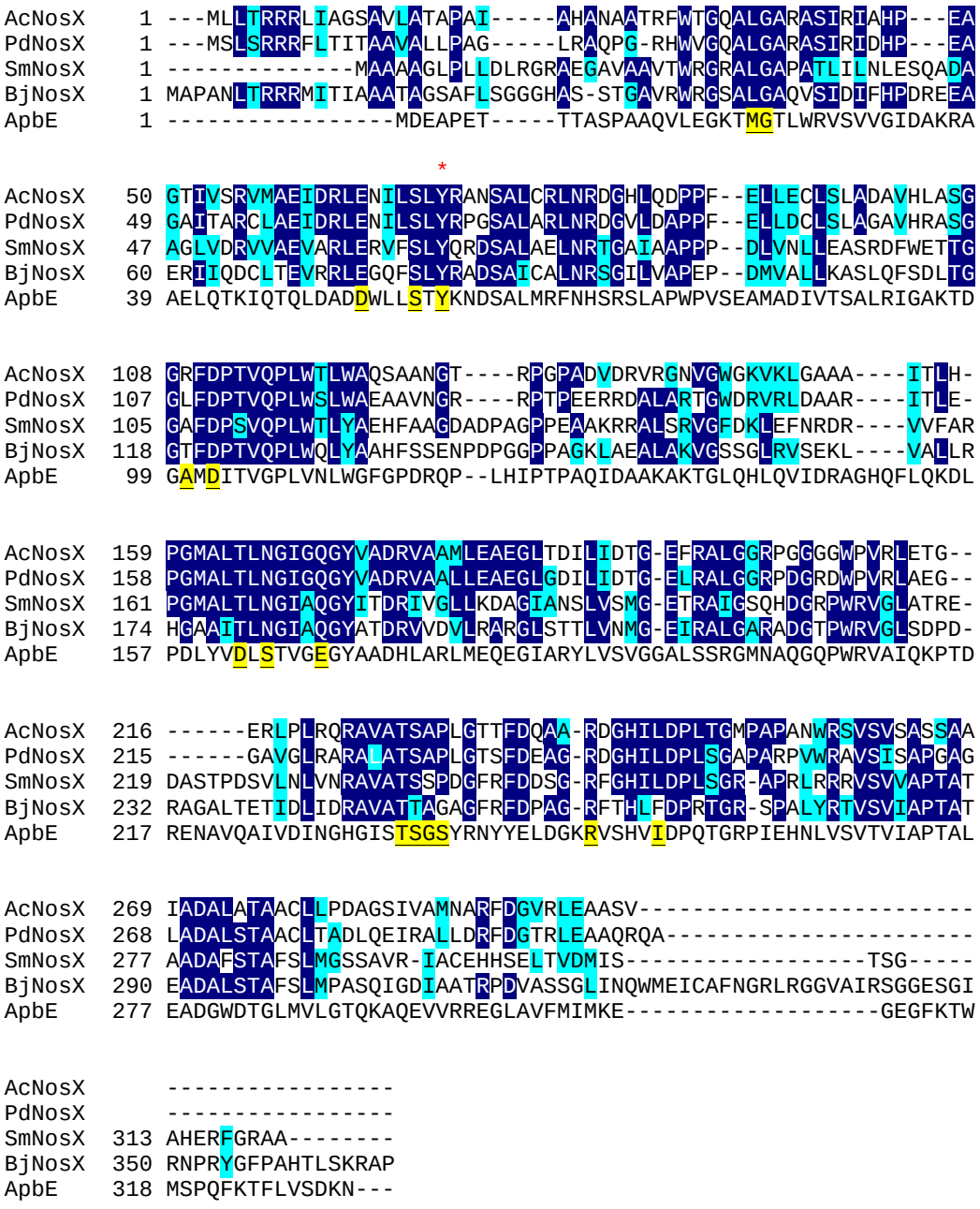


Figure 3.7. Sequence alignment of NosX proteins and ApbE

NosX from *Achromobacter cycloclastes* (*Ac*NosX), *Paracoccus denitrificans* (*Pd*NosX), *Sinorhizobium meliloti* (*Sm*NosX), *Bradyrhizobium japonicum* (*Bj*NosX) and ApbE from *Salmonella enterica* were aligned with Clustal W (Figure 3.7). Conserved

amino acids among the NosX proteins are highlighted in blue and light blue, and the amino acids involved in FAD binding in ApbE protein are highlighted in yellow and underlined. Well conserved Tyr70 was emphasized with "*" (will be described in discussion).

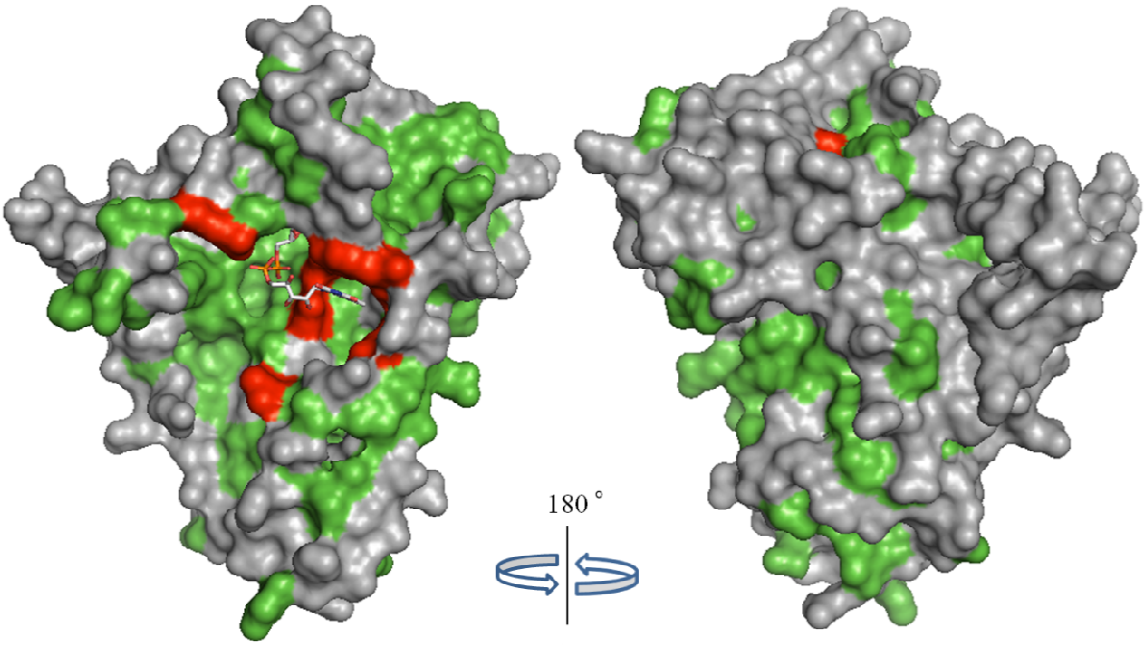


Figure 3.8. Distribution of the conserved amino acids (green) and potential FAD binding residues (red) in the *Ac*NosX model

The conserved amino acids of *Ac*NosX are also highlighted in green in the *Ac*NosX model (Figure 3.8). The residues that interact with FAD in ApbE protein (Met41, Gly42, ASP72, Ser76, Ala119, Glu121, Asp181, Ser183, Glu187, Arg267 and Ile272) correspond to the conserved residues in the *Ac*NosX sequences (Leu12 (L36 with the signal peptide in Figure 3.7), Gly13 (G37), Glu40 (E64), Ser44 (S68), Tyr46 (in Figure 3.5, Y70), Asp87 (D111), Thr140 (T164), Asn142 (N166), Gln146 (Q170), Arg216 (R240) and Leu221 (L245)). The potential FAD binding residues are highlighted in red

(Figure 3.8). This mapping on the model reveals that many of the conserved amino acids are located in the plausible FAD binding pocket, and the small hydrophobic patch (Figure 3.6) was composed of well conserved amino acids.

Crystallization Trials

Crystallization conditions for *Ac*NosX were screened with reagent kits and a screening robot. Since *Ac*NosX starts precipitating from ~ 6 mg/mL (~ 200 µM) and at room temperature within an hour, protein concentration for the screening was adjusted to 5 mg/mL (158.2 µM) and the plate was incubated at 4 °C. At days 1, 7, and 14 after the plate preparation, similar wedge-like structures were observed in three conditions at E-11 in plate #1, 2, and 4.

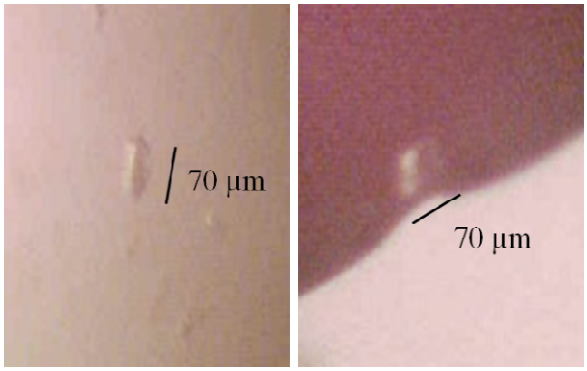


Figure 3.9. Pictures of putative crystals from condition #1

The first condition was 100 mM HEPES, 20 mM $MgCl_2$, 22 % (w/v) Poly(acrylic acid sodium salt) 5100, pH 7.5 and the second condition was 100 mM Bis-Tris propane, 500 mM succinic acid, pH 7.0. The third condition was 4% (v/v) Tacsimate (pH 5.0) and 12 % (w/v) PEG3350. Since the crystals were observed in the same spot (E-11) in different plates, it is possible that the crystals were due to the contamination of the buffer

injection needle for E-11. However, further crystallization trials under the first conditions produced additional crystals (~ 10 × ~ 10 × ~ 70 µm, Figure 3.9) on a large scale plate. These crystals were dissolved after several weeks. To date, the crystal formation process has been poorly reproducible.

Discussion

Identity Confirmation of Purified *Ac*NosX

Identity of the purified yellow protein was confirmed to be *Ac*NosX with several aspects. DNA sequencing of the *nosX* gene from *Ac* indicated that the molecular weight of apo-*Ac*NosX was 30807 Da, which was almost identical to the measured value of the purified protein (30806.58 Da). Further, the strep-tag that was attached on the C-terminal end of *Ac*NosX was detected from the purified protein in chapter 2 by Western blot (Figure 2.2). Additionally, N-terminal amino acid sequence of the purified protein has shown that the first 12 amino acids were identical to the expected sequence from *nosX* gene sequence (134). These results, together with the previous data, confirmed that *Ac*NosX was expressed and purified as intended.

Characterization of the Cofactor in *Ac*NosX

The cofactor of *Ac*NosX was determined to be FAD (Figure 3.2). One *Ac*NosX molecule was expected to have one FAD molecule according to the following observations: (1) The molecular weight of holo-*Ac*NosX was estimated at 31583 Da by the gel filtration column (Figure 3.1), which was close to the sum (31592.5 Da) of apo-*Ac*NosX (30807 Da) and one FAD (785.5 Da). (2) The fluorescence intensity of PDE

treated *Ac*NosX cofactor (10 µM) was comparable intensities of PDE treated FAD and FMN (10 µM) (Figure 3.2), which indicated that 10 µM of *Ac*NosX included 10 µM of FAD.

FAD was expected to be bound to *Ac*NosX non-covalently. The micrOTOF-MS detected the apo form of *Ac*NosX (30807 Da). The ESI process of the micrOTOF-MS is sufficiently mild to keep covalent bonds intact. Thus, if *Ac*NosX and FAD were bound covalently, the holo form should be detected. Additionally, FAD in *Ac*NosX was extracted to the supernatant after boiling of the protein sample (Figure 3.2A). Further, addition of spermine to *Ac*NosX resulted in ejection of FAD to solution (Figure 4.11, in chapter 4). These results consistently indicated that FAD was non-covalently bound to *Ac*NosX.

There are three redox states for FAD in electron transfer reactions; oxidized, semiquinone, and reduced forms. Thus, the total amount of *Ac*NosX during the redox reaction could be expressed with the following equation: $[NosX_{total}] = [NosX_{ox}] + [NosX_{semi}] + [NosX_{red}]$. The UV/Vis spectra during the experiments for the redox determination were measured at the equilibrium state. It was possible that the semiquinone form was transiently generated during the electron transfer reaction. However, the semiquinone form was not detected in the equilibrium state (Figure 3.3A). This observation indicated that the semiquinone form of *Ac*NosX was unstable and it immediately became either oxidized or reduced form. Thus, the $[NosX_{semi}]$ term was negligible at least in the equilibrium state. This observation supported that it was

adequate to use the equation $[NosX_{total}] = [NosX_{ox}] + [NosX_{red}]$ for the calculations to determine the *Ac*NosX concentrations.

The redox potential of *Ac*NosX was determined as -230 mV at pH 7.0. *Ac*PAz reduced only the Cu_A site (~ 250 mV (67)) in *Ac*N_2OR *in vitro* (see chapter 4, Figure 4.2). This was probably because the redox potential of *Ac*PAz was 260 mV (147) and it was not potent enough to reduce the Cu_Z site (~ 60 mV (68)). Since the redox potential of *Ac*NosX was revealed to be lower than those values, *Ac*NosX might be able to donate electrons to the Cu_Z site as well as the Cu_A site in *Ac*N_2OR. The electron transfer between *Ac*NosX and *Ac*N_2OR *in vitro* will be further investigated and discussed in chapter 4.

Structural Aspects of *Ac*NosX

Four FAD-binding protein families have been reported (148). Recently, ApbE was shown to have a new FAD-binding motif (121). According to the sequence identity (23.5 %) and similarity (38.7 %) between *Ac*NosX and ApbE (Figure 3.7), NosX is also expected to have this new FAD-binding motif.

*Ac*NosX structure was investigated with computational and crystallization methods. Homology modeling of *Ac*NosX, sequence-based secondary structure predictions for *Ac*NosX, and comparative analysis of NosX proteins and ApbE sequences provided structural insights for *Ac*NosX. The crystallization trials for *Ac*NosX required further optimization of the conditions for structure determination. The rationale for selecting NosX sequences from *Ac*, *Sm*, and *Bj* for the comparative analysis was that these bacteria were relatively well studied with respect to denitrification and located on different branches in a phylogenetic tree, which was generated based on the NosX

sequences (Appendix C, Figure S3.2). Well conserved amino acids among such distantly related NosX proteins are expected to be important for the function and/or structure of NosX. Indeed, the sequence alignment showed good agreement between the well conserved residues in NosX proteins and the residues that formed the FAD binding pocket in ApbE (Figure 3.7). These conserved amino acids were located close to or within the FAD binding pocket in the *Ac*NosX model (Figure 3.8), indicating that the corresponding conserved amino acids were likely to be involved in cofactor recognition.

Tyr46 (Tyr70 with the signal peptide), which was one of the well conserved amino acids among the species, which is indicated with "*" in Figure 3.7, was located close to the isoalloxazine ring of the FAD in the model (Figure 3.5). The ring stacking between FAD and aromatic amino acids has been well observed in many FAD binding proteins (149). In ApbE protein, the same type of ring stacking was observed between FAD and Tyr78 (121). This Tyr78 residue was also well conserved and found to be essential to FAD binding (121). These observations indicate that Tyr46 in *Ac*NosX is likely to play a similar role in cofactor binding. Further, Gly13 (Gly37 with the signal peptide) in *Ac*NosX is also well conserved, which corresponds to well conserved Gly42 in ApbE protein (Figure 3.7). This residue was shown to function in FAD binding as well (121).

NosX from *Paracoccus denitrificans* was involved in the N_2OR activation *in vivo* (83). Also, we found that *Ac*NosX had a redox active cofactor, FAD (Figure 3.2, 3.4). These results lead us to propose a hypothesis that *Ac*NosX donates electrons to *Ac*N_2OR (see chapter 4 for detail). It has been revealed that the pseudo-specific interaction

between *Ac*PAz and *Ac*N_2OR is important for electron transfer (see detail for chapter 1) (87; 93). According to the pseudo-specific electron transfer mechanism (87), it was expected that *Ac*NosX should have a hydrophobic patch and surrounding positively charged patches to interact with *Ac*N_2OR for electron transfer, if *Ac*NosX binds to the similar place where *Ac*PAz binds for electron transfer. The electrostatic potential and hydrophobicity on the surface of the *Ac*NosX model showed that there was a small hydrophobic patch composed of well conserved residues, and it was located close to the putative FAD binding site (Figure 3.6, 3.8). Further, positively charged residues were observed next to the hydrophobic patch (Figure 3.5). These results suggested that *Ac*NosX may bind and donate electrons to *Ac*N_2OR similarly to *Ac*PAz.

NosX has been suggested to interact with the membrane bound protein, NosR (52; 83). The electron transfer pathway from NosR to N_2OR through NosX in *Paracoccus denitrificans* has been implied (83). There is a large hydrophobic patch on the back side of the FAD binding site in the *Ac*NosX model (Figure 3.6). Since there are almost no conserved amino acids in the hydrophobic patch (Figure 3.6, 3.8), this patch was less likely to be responsible for protein interaction with partner proteins. Instead, this hydrophobic patch might interact with the membrane surface during the electron transfer between *Ac*NosX and *Ac*NosR since *Ac*NosX would get closer to the membrane to interact with *Ac*NosR. NosR from *Pseudomonas stutzeri* was reported to have an FMN binding domain in the periplasm (82). *Ac*NosX was expected to interact with this domain to receive electrons. Since the redox potential of *Ac*NosX was -230 mV, the redox

potential of FMN in *Ac*NosR would be a similar or lower value than -230 mV for energetically favored electron flow.

Conclusions

The data revealed from this project supported and complemented the hypothesis by Wunsch *et al* (83), which stated that NosX is involved in N_2OR activation. To the best of our knowledge, this is the first time that NosX was purified and characterized. It was determined that *Ac*NosX was a soluble, FAD containing protein and was redox active. Computational analysis of *Ac*NosX structure suggested that well conserved amino acids were involved in the cofactor binding and the protein-protein interaction with *Ac*N_2OR. The large hydrophobic patch might be important to facilitate the protein-protein interaction with *Ac*NosR by interacting with the membrane. Together with previous data, these observations suggest that *Ac*NosX is a physiological electron donor for *Ac*N_2OR in sustaining N_2OR activity and potentially mediates electron transfer from *Ac*NosR to *Ac*N_2OR.

CHAPTER 4

INVESTIGATIONS ON THE FUNCTION OF NOSX FROM *ACHROMOBACTER CYCLOCLASTES*

Introduction

In denitrifying bacteria, pseudoazurin (PAz) and cytochrome *c* have been reported to be common electron donors for the denitrifying enzymes NiR, NOR, and N_2OR (88; 86; 89; 87). The electron transfers from PAz and cytochrome *c* to N_2OR were reported in several bacteria such as *Paracoccus pantotrophus* (PAz and cytochrome c_{551}) (90), *Marinobacter hydrocarbonoclasticus* (formerly *Pseudomonas nautica*) (cytochrome c_{552}) (150), *Paracoccus denitrificans* (PAz and cytochrome c_{550}) (89). We also reported that PAz from *A. cycloclastes* (*Ac*PAz) could donate electrons to *A. cycloclastes* N_2OR (*Ac*N_2OR) (91). Furthermore, PAz and cytochrome *c* were shown to sustain the catalytic reaction of N_2OR (150; 91).

Two states of the Cu_Z site in N_2OR have been characterized; the Cu_Z state (enzymatically active) and the Cu_Z* state (inactive) (68; 69). The Cu_Z* state may be generated with O_2 exposure of N_2OR and/or mutations of several Nos proteins (see below for detail) (82; 68; 83). Therefore, the Nos proteins (NosX and NosR) are expected to display reactivity towards the Cu_Z* state. Both the Cu_Z and Cu_Z* states in *Ac*N_2OR show the absorption peak at 640 nm in the UV/Vis spectrum (11; 77). The structural difference between two states has been unclear. Recently, the structure of N_2OR from *Pseudomonas stutzeri* was solved (63). The Cu_Z site in this structure included an extra sulfide (Figure

1.10). It was hypothesized that the difference between the Cu_Z state and the Cu_Z* state was derived from the presence or absence of the extra sulfide. That is, the Cu_Z state is the [4Cu:2S] form and the Cu_Z* state is the [4Cu:1S] form.

The function of NosX was shown to be involved in the activation of the Cu_Z site in *Paracoccus denitrificans* (83). Deletion of the *nosX* and *nirX* genes resulted in a loss of N_2OR activity and an increase of the Cu_Z* state *in vivo* (83). Although it was not mentioned in the paper, PAz and cytochrome c_{550} were expressed as WT and could donate electrons to N_2OR in the double mutant strain. Thus, the results suggested that NosX has a function that is distinct from the functions of PAz and cytochrome c_{550}, since the N_2OR activity was inhibited even in the presence of PAz and cytochrome c_{550}. Isolated N_2OR from the double mutant strain could be activated with reductants *in vitro* (83). The results suggested that NosX was involved in the activation of the catalytic center (the Cu_Z site) of N_2OR.

As presented in chapter 3, NosX from *A. cycloclastes* (*Ac*NosX) is a redox active FAD protein (E = -230 mV). This observation together with the previous data lead us to the hypothesis that *Ac*NosX donates electrons to *Ac*N_2OR to activate the catalytic center and/or to regenerate the inactive Cu_Z* state to the catalytically active Cu_Z state. In this chapter, the function of *Ac*NosX was investigated to probe the possible activation mechanism for *Ac*N_2OR. It is important to investigate the N_2OR activation process to fully understand the mechanism of N_2O reduction by N_2OR. As mentioned in chapter 1, this information may be a basis for future applications that could help reduce broad environmental issues that are caused by uncontrolled N_2O emission (123). Additionally,

the electron transfer reaction between *Ac*NosX and *Ac*PAz was also examined. The electron transfer between *Ac*NosX and *Ac*N_2OR was measured by UV/Vis spectroscopy and confirmed by electron paramagnetic resonance (EPR) *in vitro*. The regeneration of the Cu_Z* state was also attempted with photo-reduction in the presence of *Ac*NosX *in vitro*. Further, the N_2OR catalytic reaction was monitored in the presence of an excess amount of *Ac*NosX to see if *Ac*NosX was able to sustain catalytic turnover.

Materials and Methods

Expression and Purification of Pseudoazurin from *Achromobacter cycloclastes*

PAz from *A. cycloclastes* (*Ac*PAz) was overexpressed and purified from *E. coli* (JM109/pTrc99A-paz). The plasmid pTrc99A-paz was provided from Prof. T. Kohzuma (Ibaraki University, Japan) (151). The plasmid was inserted to *E. coli* JM109 strain with electroporation. JM109/pTrc99A-paz was streaked on LB plate with 100 μg/mL of ampicillin (Amp100) and incubated at 37 °C for overnight. A single colony from the plate was suspended to 200 mL LB media (Amp100) and cultured for overnight at 37 °C while shaking at 250 rpm. The culture (30 mL) was inoculated to 900 mL of LB media (Amp100) in a 3 L baffled flask. 6 flasks of the inoculated LB media were incubated at 37 °C for ~ 2 hours until A_{600} became 0.6. 1.5 mL of 300 mM IPTG (final conc. 500 μM) and 1.8 mL of 50 mM $CuSO_4$ (final conc. 100 μM) per a flask were added to the media to induce the PAz expression. After 8 hours, the cultures were centrifuged with 10800 × g (Sorvall GS3 rotor) for 10 minutes at 4 °C to collect the cell. The cell pellet (~ 25 g) was kept at 4 °C overnight for purification or -80 °C for storage.

Overexpressed *Ac*PAz in *E. coli* was isolated from the harvested cell. The cell pellet (~ 25 g) was suspended to an equal amount (~ 30 mL) of 50 mM Phosphate buffer (pH 6.0). The overexpressed *Ac*PAz was extracted from the cell with a French pressure cell at ~ 70 MPa. The cell debris was removed with centrifugation at 39000 ×g (Sorvall SS-34 rotor) for 60 min. The *Ac*PAz containing fraction was separated from the crude supernatant with the ammonium sulfate precipitation method (40 % saturation). The sample with ammonium sulfate was incubated for 1 hour while stirring (~ 400 rpm) at 4 °C. After centrifuging the sample for 30 min at 39000 ×g, the supernatant (~ 50 mL) was dialyzed with 5 L of 5 mM Phosphate (pH 6.0) for 3 ~ 5 hours and with 5 L of 20 mM Phosphate (pH 6.0) with a dash of potassium ferricyanide for overnight. *Ac*PAz was fully oxidized with the oxidant to facilitate the following purification process by making *Ac*PAz visible. The sample was centrifuged for 30 min at 39000 ×g to remove proteins that precipitated during dialysis. The supernatant was loaded onto a SP-sepharose column (20 mL, 10 × 260 mm) which was equilibrated with 50 mM Phosphate (pH 6.0). After washing the column with five column volumes of 50 mM Phosphate (pH 6.0), proteins on the column were eluted with 500 mM Phosphate (pH 6.0). Fractions that included *Ac*PAz were detected with A_{600} and collected. The *Ac*PAz containing fraction (~ 30 mL) was dialyzed with 5 L of 20 mM Phosphate (pH 6.0) for overnight. After centrifuging the sample for 30 min at 39000 ×g, the supernatant was loaded onto the SP-sepharose column which was equilibrated with 50 mM Phosphate (pH 6.0). *Ac*PAz was eluted with a linear gradient (50 – 500 mM Phosphate, pH 6.0) method, and concentrated with an Amicon Ultra Centrifugal Filter 3K (Millipore). The purity of *Ac*PAz was checked with

SDS-PAGE analysis using 12.5 % gels and Coomassie Brilliant Blue (CBB) staining. On average, ~ 100 mg of *Ac*PAz could be obtained from 25 g of cells. The concentration of *Ac*PAz and Cu content were calculated using a BCA protein assay kit (Pierce) and an atomic absorption spectrometer (AA, SpectrAA220, Varian), respectively. When the Cu content of *Ac*PAz was lower than 80 %, the sample was dialyzed with Cu containing buffer to reconstitute the Cu site of apo-*Ac*PAz. The sample was dialyzed with 1 L of 20 mM Tris (pH 8.0) with 1 mM $CuSO_4$ for 4 ~ 5 days. The sample was further dialyzed with 5 L of 20 mM Tris (pH 8.0) without $CuSO_4$ for 2 ~ 3 days to remove excess free Cu in the sample. Typically, the Cu content of *Ac*PAz after dialysis became over 90 %. Concentration of Cu loaded *Ac*PAz was estimated with A_{594} and ε_{594} = 3700 M^{-1} cm^{-1} (147). The ratio of absorptions at 280 nm over 594 nm (A_{280}/A_{594}) of pure and fully Cu loaded *Ac*PAz was about 1.4.

Reduced *Ac*PAz was obtained by incubation of purified *Ac*PAz with 100-fold excess of dithionite. To prevent protein precipitation, oxidized *Ac*PAz (~ 5 mL) was gradually put into 30 mL of 100 mM Phosphate (pH 7.0) with dithionite. The residual reductant was removed with an Amicon ultrafiltration membrane (YM-5, Millipore) under anaerobic conditions using Ar bubbled (~ 1 hour) Buffer P (100 mM Phosphate, 150 mM NaCl, 10 % (v/w) glycerol, pH 7.0).

Expression and Purification of N_2OR
from *Achromobacter cycloclastes*

N_2OR from *A. cycloclastes* (*Ac*N_2OR) was homologously overexpressed in *Ac*/pML*nos*. *Ac*/pML*nos* was cultured as previously described (see chapter 2). The

culture was carried out with 2 L of LB media × 4 flasks for 24 hours under micro aerobic conditions. A typical cell yield was ~ 30 g. The harvested cell pellet was immediately frozen at -80 °C or kept at 4 °C overnight for purification.

AcN_2OR was purified as previously described (11). During the purification process, the sample was kept under anaerobic conditions to minimize O_2 exposure which results in low Cu content and low activity. Typically, ~ 10 g of cell was suspended with ~ 20 mL of 20 mM Tris (pH 8.0) with a dash of dithionite. The suspended cells were lysed with the French pressure cell twice at ~ 70 MPa. The cell lysate was ultracentrifuged for 60 min at 45000 rpm (Sorvall Ti50 rotor) at 4 °C, and supernatant was anaerobically transferred to a DEAE fast-flow column (120 mL, 25 × 240 mm), which was equilibrated with 20 mM Tris (pH 8.0). All buffers in this purification were purged with Ar gas at least 30 min right before use and included 250 µM sodium dithionite to remove residual oxygen in buffers. Proteins bound on the column were eluted with a linear gradient method with 20 mM Tris, 500 mM NaCl, pH 8.0. *Ac*N_2OR containing fractions (~ 60 mL) were collected and diluted with 250 mL of 20 mM Tris (pH 8.0) to reduce salt concentration. The sample was loaded onto a DEAE column (34 mL, 25 × 70 mm). *Ac*N_2OR on the column was eluted with 20 mM Tris, 500 mM NaCl, pH 8.0. *Ac*N_2OR containing fractions (~ 15 mL) were collected and diluted with 50 mL of 20 mM Tris (pH 8.0) to reduce salt concentration. The sample was then applied to a Mono Q column (8 mL, 10 × 100 mm) that was equilibrated with 20 mM Tris (pH 8.0). The buffer in the column was exchanged to 20 mM Bis-Tris (pH 6.5) and bound proteins on the column were eluted with a linear gradient method. *Ac*N_2OR was eluted from the column around

30 – 70 min. The sample buffer was exchanged with an Amicon (YM-30 filter) several times to reduce the salt concentration. At the final step, *Ac*N_2OR was applied to a cytochrome *c* agarose affinity column (8 mL, 10 × 100 mm) and eluted by a linear gradient. The *Ac*N_2OR containing fractions were eluted around 43 – 70 min. The sample buffer was exchanged with an Amicon with 20 mM Tris (pH 8.0, without dithionite) and concentrated to 1 ~ 2 mL. This *Ac*N_2OR sample was called the as dithionite reduced form or the "as purified" form. The protein concentration was estimated with A_{280} and ε_{280} = 105,000 M^{-1} cm^{-1}. Typical *Ac*N_2OR yield from 10 g cell pellet was 10 ~ 15 mg. Cu content was measured with atomic absorption spectrometer (AA). Typically, the N_2OR samples that were used for the following measurements contained 4.0 ~ 5.0 Cu/monomer.

The N_2OR activity assay was also carried out under anaerobic conditions. 10.5 µM *Ac*N_2OR in 50 mM Phosphate (pH 7.0) was activated in the presence of 2 mM methyl viologen (MV) and 1 mM dithionite (DT) at 25 °C for 3 hours. 2 µL of activated *Ac*N_2OR was injected to the mixture of 2700 µL of 50 mM phosphate, 300 µL of 5 mM BV and 2 µL of 100 mM DT in an anaerobic cuvette with a total volume of 3004 µL. The time course of absorption change at 600 nm was monitored for 2 min to see the background of the auto-oxidation rate of BV. After 2 min, 80 µL of N_2O saturated 50 mM phosphate (bubbled with N_2O gas at least 1 hour at room temperature) was injected to the anaerobic cuvette and to begin the catalytic reaction. Absorption changes, which indicated the oxidation of BV (= electron transfer to *Ac*N_2OR), were measured for 3 min. The activity (U/mg) was calculated by the absorption change between 0.12 and 0.18 min after N_2O was injected as described previously (11). The typical activity of sample was ~

80 U/mg at 25 °C. To investigate the inhibition effect of chloride on the N_2OR activity (see below), the activity assay was carried out with various buffers: 50 mM phosphate (pH 7.0), 50 mM phosphate + 150 mM NaCl (pH 7.0), and 50 mM phosphate + 50 mM Na_2SO_4 (pH 7.0). The procedure was the same as described above. Prior to N_2O injection, N_2OR was incubated in each buffer for 5 min. The BV oxidation was monitored for 5 min in the presence of N_2O.

Fully oxidized *Ac*N_2OR was prepared by the incubation of the "as purified" form of *Ac*N_2OR with a 100-fold excess amount of potassium ferricyanide. The oxidant was removed with gel filtration. PAz reduced *Ac*N_2OR was obtained with the incubation of an excess amount of reduced *Ac*PAz and fully oxidized *Ac*N_2OR in the molar ratio of 30 to 1 (monomer base). *Ac*PAz was removed with a gel filtration column. All samples were exchanged to Buffer P (100 mM phosphate, 150 mM NaCl, 10 % glycerol, pH 7.0) under anaerobic conditions.

Electron Transfer from *Ac*NosX to *Ac*N_2OR

The redox state of fully oxidized *Ac*N_2OR or PAz reduced *Ac*N_2OR in the presence and absence of reduced NosX were monitored with UV/Vis spectroscopy and electron paramagnetic resonance (EPR). The following experiments were carried out under anaerobic conditions. *Ac*NosX in Buffer PE (100 mM Phosphate, 150 mM NaCl, 10 % glycerol, 10 mM EDTA, pH 7.0) was photo-reduced by illuminating in the ice/water bath for 3-5 min intervals using a Xe arc lamp (175 W) and an IR cut-off filter. Typically, fully reduced *Ac*NosX was obtained within 15 - 30 min.

The electron transfer from *Ac*NosX to *Ac*N_2OR was measured by UV/Vis spectroscopy. An equimolar (17.8 µM) amount of reduced *Ac*NosX and fully oxidized *Ac*N_2OR were mixed in an anaerobic cuvette and the UV/Vis spectra were measured at 4 °C to stabilize NosX. As a negative control, Buffer PE was photo-reduced for 15 min in the anaerobic cuvette under the same conditions and mixed with oxidized *Ac*N_2OR. The UV/Vis spectrum was measured to check if the illuminated Buffer PE could reduce *Ac*N_2OR.

EPR spectra were measured to investigate the redox state of the Cu sites in *Ac*N_2OR which was reduced with *Ac*PAz and/or *Ac*NosX. The sample preparation process for the EPR measurements is summarized in Figure 4.1. Fully oxidized *Ac*N_2OR (#2) and PAz reduced *Ac*N_2OR (#3) were prepared as described in the method section. Dithionite reduced *Ac*N_2OR (#1, as purified) was oxidized with an excess amount (100-fold) of potassium ferricyanide to obtain fully oxidized *Ac*N_2OR (#2, oxidized). Excess amount of ferricyanide was removed.

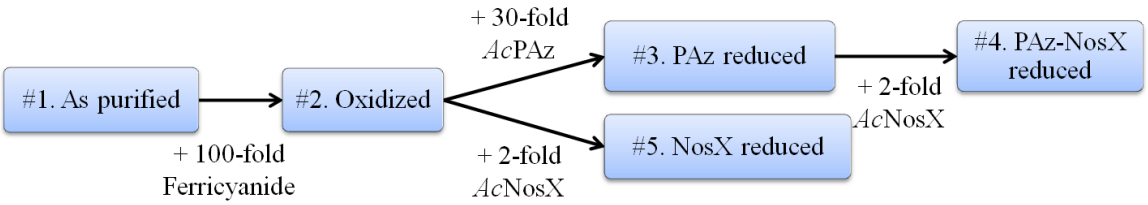


Figure 4.1. Schematic view of sample preparations for the EPR measurements

The fully oxidized *Ac*N_2OR (#2) was further reduced with an excess amount (30-fold) of *Ac*PAz (#3, PAz reduced). PAz and NosX reduced *Ac*N_2OR (#4, PAz-NosX reduced), and NosX reduced *Ac*N_2OR (#5, NosX reduced) were prepared by mixing either PAz

reduced *Ac*N_2OR (#3) or fully oxidized *Ac*N_2OR (#2) with 2× molar excess of reduced *Ac*NosX in a glove box (O_2 < 1 ppm, Coy laboratory products Inc.). These samples were prepared sequentially from one sample (#1). The excess amount of *Ac*NosX was not removed from the samples because of the following reasons: (1) Oxidized and reduced forms of *Ac*NosX are diamagnetic. Thus, it would not contribute to the EPR spectra and was negligible for the measurements. (2) If any signal from *Ac*NosX was observed in the EPR spectra, it would indicate the presence of a semi-quinone form of *Ac*NosX. It was desirable to confirm the presence or absence of the semi-quinone form under conditions similar to those used to determine the redox potential. In chapter 3, the equation ($[NosX_{red}] = [NosX_{total}] - [NosX_{ox}]$), which assured the absence of the semi-quinone form under the equilibrated states, was used to determine the redox potential of *Ac*NosX. Recall that the original equation was $[NosX_{red}] = [NosX_{total}] - [NosX_{ox}] – [NosX_{semi}]$, but $[NosX_{semi}]$ term that corresponds to the concentration of the semi-quinone form of *Ac*NosX was assumed to be negligible. The final concentrations of each N_2OR sample were 146.8 µM (as purified, 300 µL), 79.2 µM (oxidized, 300 µL), 50.4 µM (PAz reduced, 300 µL), 36.2 µM (PAz-NosX reduced, [N_2OR]:[NosX]=1:2.2, 300 µL), and 67.6 µM (NosX reduced, [N_2OR]:[NosX]=1:2.5, 260 µL). Samples were placed in EPR quartz tubes and rapidly frozen with liquid nitrogen. For spin quantification, Cu(triethanolamine) standard solutions (0, 25, 50, 100 µM, 300 µL) were prepared. EPR spectra of the samples and the standards were collected at 14, 20 and 30 K respectively using an EMX X-band spectrometer (Bruker) equipped with a liquid helium cryostat and temperature controller (Oxford instruments). Typical EPR parameters were: microwave

frequency, 9.38 GHz; microwave power, 1.16 mW; time constant, 163.84 msec; sweep time 83.89 sec. After EPR measurements, UV/Vis spectra of the samples were measured at room temperature. Each sample was collected from the EPR quartz tube in the glove box (O_2 < 1 ppm). If necessary, the samples were diluted with Buffer P (100 mM Phosphate, 150 mM NaCl, 10 % glycerol, pH 7.0) to increase the volumes to measure the spectra. After the UV/Vis and EPR measurements, the Cu contents of the samples were measured by AA.

Regeneration of the Cu_Z* State
in *Ac*N_2OR with *Ac*NosX

As a preliminary experiment, *Ac*N_2OR was incubated in Buffer PE (100 mM Phosphate, 150 mM NaCl, 10 % glycerol, and 10 mM EDTA, pH 7.0) for 4 hours to investigate the effect of EDTA on the Cu sites of N_2OR. 1000 µL of ~ 30 µM *Ac*N_2OR in Buffer PE was incubated in an anaerobic cuvette at room temperature. The UV/Vis spectra of the sample were monitored for 4 hours.

Photo-reduction of oxidized *Ac*N_2OR was monitored in the absence and presence of *Ac*NosX to see if *Ac*NosX was able to reduce the Cu_Z* state in *Ac*N_2OR. The sample preparation was carried out in the glove box (O_2 < 1 ppm). 23 µM of *Ac*N_2OR in Buffer PE was photo-reduced on ice/water for 5 min in an anaerobic cuvette, and UV/Vis spectrum was measured. The sample was further exposed to the light for 5 min until no change was observed spectrally. After *Ac*N_2OR was reduced up to the limit of photo-reduction system, oxidized *Ac*NosX was added to the sample. The ratio between *Ac*N_2OR

and *Ac*NosX was 1 to 1 (20 µM). The cuvette was further exposed to the light for 10 min and UV/Vis spectra were measured until no further change was observed.

Electron Transfer from Reduced *Ac*NosX to Oxidized *Ac*PAz

The electron transfer pathway from *Ac*NosX to *Ac*PAz was investigated *in vitro*. The following procedures were carried out under anaerobic conditions since reduced *Ac*NosX was sensitive to oxygen. ~ 500 µL of 105 µM NosX in Buffer PE (pH 7.0) was photo-reduced in an anaerobic cuvette with ice and water. The progress of *Ac*NosX reduction was monitored by UV/Vis where a spectrum was taken every 10 min. After the *Ac*NosX was fully reduced, 171 µL of reduced *Ac*NosX was injected to 429 µL of oxidized *Ac*PAz in Buffer P (pH 7.0) and the electron transfer was monitored by UV/Vis at 4 °C. Final concentrations of *Ac*NosX and *Ac*PAz were 30 µM at a 1:1 ratio.

Catalytic Reaction of *Ac*N_2OR with Reduced *Ac*NosX

The N_2OR catalytic reaction in the presence of an excess amount of reduced *Ac*NosX was monitored. All procedures were carried out under anaerobic conditions. The conditions for the measurements were the same as the N_2OR activity assay with two modifications: *Ac*NosX was used for electron source instead of BV, and Buffer P (pH 7.0) was used to stabilize *Ac*NosX during the measurements instead of 50 mM phosphate (pH 7.1). 10.5 µM *Ac*N_2OR in Buffer P was activated in the presence of 2 mM MV and 1 mM DT at 25 °C for 3 hours. 1330 µL of 100 µM *Ac*NosX in Buffer PE (pH 7.0) was photo-reduced. 2 µL of activated *Ac*N_2OR, 1330 µL of photo-reduced *Ac*NosX, 1668 µL

of Buffer P was mixed in an anaerobic cuvette. The total volume of the sample was 3 mL. Final concentrations of each component were, 6.8 nM *Ac*N_2OR, 44 µM *Ac*NosX, 4.3 mM EDTA, 1.3 µM MV, and 0.7 µM DT. UV/Vis spectra were monitored for 10 min at 10 °C to determine the background auto-oxidation rate of *Ac*NosX. After 10 min, 80 µL of N_2O saturated Buffer P (bubbled with N_2O gas at least 1 hour at room temperature) was injected to the anaerobic cuvette and UV/Vis spectra were further collected for 20 min.

For control experiments, the catalytic reactions of *Ac*N_2OR in the presence of an excess amount of reduced *Ac*PAz or free FAD were also monitored using Buffer P (pH 7.0) or 50 mM phosphate (pH 7.0). *Ac*PAz and FAD were fully reduced with equimolar amounts of dithionite. Final concentrations of each experiment were 75.6 µM *Ac*PAz vs. 6.8 nM *Ac*N_2OR and 72.0 µM FAD vs. 6.8 nM *Ac*N_2OR.

Identification of Inhibitory Factor for the N_2OR Catalytic Cycle with *Ac*PAz

It was determined that Buffer P inhibited the N_2OR catalytic reaction when reduced *Ac*PAz was used as an electron donor instead of reduced BV. To identify which component of the buffer inhibited the reaction, the following buffers were prepared and the N_2OR activity was checked with these buffers; (#1) 50 mM potassium phosphate (pH 7.0), (#2) 50 mM potassium phosphate + 150 mM NaCl (pH 7.0), (#3) 50 mM potassium phosphate + 10 % glycerol (pH 7.0), (#4) 50 mM potassium phosphate + 150 mM KCl (pH 7.0), (#5) 50 mM sodium phosphate (pH 7.0). As negative controls, (#6) 50 mM potassium phosphate + 50 mM Na_2SO_4 (pH 7.0, I = 0.242, the same ionic strength as buffer #2), and (#7) 129 mM potassium phosphate (pH 7.0, I = 0.241) were also applied

to prove if high ionic strength inhibited the electron transfer reaction. *Ac*N_2OR was activated as previously described with 50 mM potassium phosphate (pH 7.0). 2 µL of the activated *Ac*N_2OR, 250 µL of reduced *Ac*PAz (932 µM) in 50 mM potassium phosphate (pH 7.0), and 2752 µL of one of those buffer (#1 - 5) were mixed. For the negative control experiments, 200 µL of reduced *Ac*PAz (932 µM) and 2802 µL of buffer (#6 - 7) were used. The total sample volume was 3004 µL. The final concentrations of *Ac*N_2OR and *Ac*PAz were 7 nM and 77.6 µM. UV/Vis spectra of the samples were monitored for 5 min to monitor the background auto-oxidation of *Ac*PAz. After 5 min, 80 µL of N_2O saturated 50 mM potassium phosphate (pH 7.0) was anaerobically injected to the sample to start the catalytic reaction and the UV/Vis spectra were monitored for 20 - 25 min.

*Ac*NosX Stabilization in Solution

It was essential to remove NaCl from the *Ac*NosX sample to investigate whether *Ac*NosX could sustain the N_2OR catalytic cycle. To find conditions that stabilized *Ac*NosX in the absence of NaCl, six reagents (arginine, ammonium sulfate, spermine, spermidine, Triton X-100, and Tween 20) that were known as protein stabilizers (152; 153; 154; 155) were individually added to *Ac*NosX samples. To remove NaCl, *Ac*NosX in Buffer W (100 mM Tris, 150 mM NaCl, 1 mM EDTA, and 10 % (w/v) glycerol, pH 8.0) was applied to a gel filtration column that was equilibrated with 100 mM phosphate, 10 % glycerol, pH 7.0. The eluted *Ac*NosX fraction was gently mixed and aliquoted to 1 mL × 8 tubes. 50 µL of stock solutions of candidate reagents (arginine (4.2 M), ammonium sulfate (2.1 M), spermine (4.1 M), spermidine (4.1 M), Triton X-100 (2.1 %), Tween 20 (2.1 %), and NaCl (3.15 M)) were added to the *Ac*NosX samples immediately.

Final concentrations of each reagent were arginine (200 mM), ammonium sulfate (100 mM), spermine (200 mM), spermidine (200 mM), Triton X-100 (0.1 %), Tween 20 (0.1 %), and NaCl (150 mM). The sample with NaCl was a positive control and the sample without any reagent was a negative control. The eight samples were incubated at 4 °C overnight. Precipitations in the samples were checked visually at 2, 4, and 8 hours. After the incubation, samples were centrifuged for 10 min at 14000 rpm and measured by UV/Vis spectra.

Results

Electron Transfer from *Ac*NosX to *Ac*N_2OR

The electron transfer from reduced *Ac*NosX to oxidized *Ac*N_2OR was monitored by UV/Vis spectroscopy. When an equimolar amount of reduced *Ac*NosX (Figure 4.2, black) and oxidized *Ac*N_2OR (Figure 4.2, red) were mixed, an increase in absorption at 374 and 460 nm from *Ac*NosX and the decrease in absorption between 550 and 800 nm from *Ac*N_2OR were observed (Figure 4.2, blue). The absorption changes in the spectrum indicate the oxidation of *Ac*NosX and the reduction of *Ac*N_2OR. In a negative control, Buffer PE was photo-reduced and mixed with oxidized *Ac*N_2OR. The illuminated Buffer PE did not reduce *Ac*N_2OR (data not shown). The control experiment confirmed that *Ac*NosX but not any other components in Buffer PE reduced *Ac*N_2OR. These results demonstrated that *Ac*NosX donated electrons to *Ac*N_2OR under the experimental conditions.

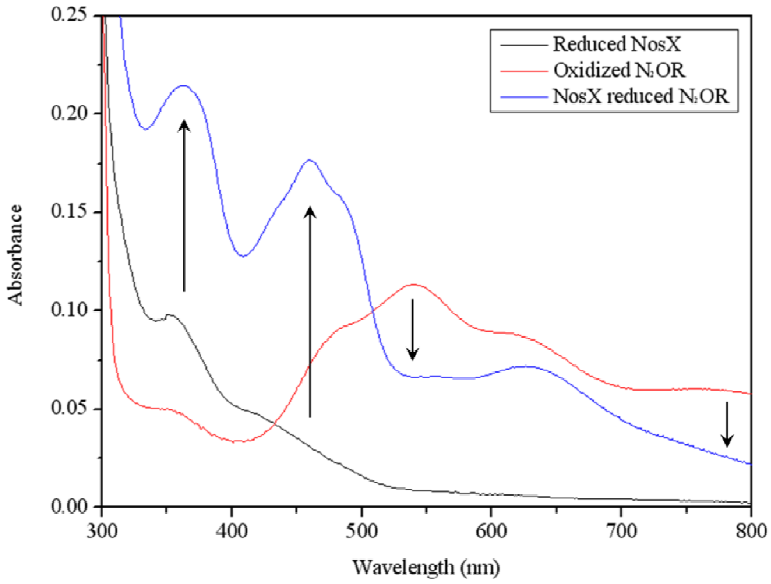


Figure 4.2. UV/Vis spectra of reduced *Ac*NosX, oxidized *Ac*N_2OR, and *Ac*NosX reduced *Ac*N_2OR

The various forms of *Ac*N_2OR including "as purified" (#1), fully oxidized (#2), PAz reduced (#3), PAz and NosX reduced (#4), and NosX reduced (#5) were measured by UV/Vis and EPR spectroscopy (Figure 4.3, 4.4). The UV/Vis spectra of the EPR samples are shown in Figure 4.3. The spectra were normalized based on Cu concentrations. The spectra were normalized with the N_2OR concentration (23.5 µM) for comparison. The spectrum of PAz reduced N_2OR (#3) showed that absorption peaks of *Ac*N_2OR were decreased compared to the spectrum of fully oxidized N_2OR (#2), indicating that *Ac*PAz donated electrons to *Ac*N_2OR (Figure 4.3, green). The differential spectrum (Figure 4.3, blue) of fully oxidized (#2) and PAz reduced (#3) N_2OR showed peaks at ~ 480, ~ 530, and ~ 810 nm. For clarity, *Ac*NosX containing samples (PAz-NosX reduced N_2OR (#4) and NosX reduced N_2OR (#5)) were not shown in Figure 4.3

because absorption from *Ac*NosX was so strong that peaks from *Ac*N_2OR were buried in it. The spectra of #4 and #5 were essentially similar to the blue spectrum in Figure 4.2.

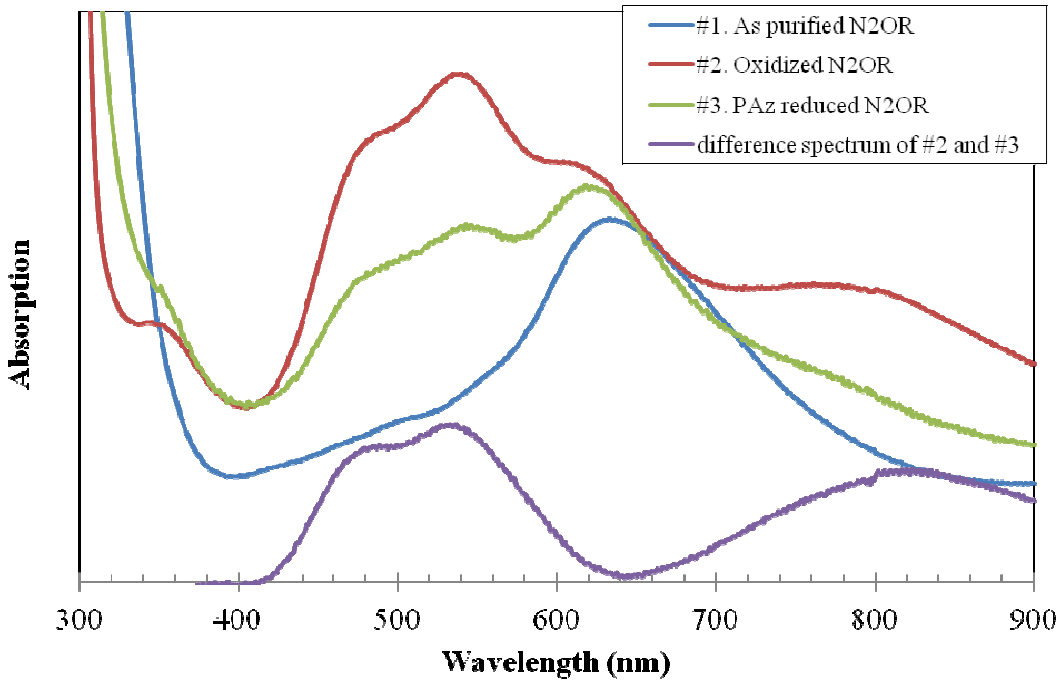


Figure 4.3. UV/Vis spectra and differential spectrum of *Ac*N_2OR samples for EPR

The EPR spectra of the samples showed the degrees of reduction for the Cu sites in *Ac*N_2OR which were reduced with *Ac*PAz and/or *Ac*NosX (Figure 4.4). The EPR spectra were normalized with the N_2OR concentrations (36 μM) for comparison. The integrated intensities of each spectrum, which are indicative of the amount of oxidized Cu, are summarized in Table 4.1. Amounts of oxidized Cu (per monomer) in the *Ac*N_2OR samples at 14, 20, and 30 K were estimated with spin quantification using Cu standard curves that were measured at each temperature (see Appendix D: Figure S4.1 for EPR spectra and standard curves of the Cu standard). The integrated EPR intensities ($\times 10^5$) of

AcN_2OR samples at 14 K (Figure 4.4) were calculated as follows; 2065 (#2, fully oxidized) > 1379 (#3, PAz reduced) ≈ 1271 (#5, NosX reduced) > 692 (#1, as purified) > 396 (#4, PAz-NosX reduced). The oxidized Cu in each sample was calculated as 0.32 (#1, as purified), 1.02 (#2, oxidized), 0.66 (#3, PAz reduced), 0.22 (#4, PAz-NosX reduced), and 0.59 (#5, NosX reduced) (Table 4.1). The intensity of the EPR spectrum for NosX reduced N_2OR (sample #5, Int = 1271 × 10^5 at 14 K) was obviously lower than the intensity of fully oxidized N_2OR (sample #2, Int = 2065 × 10^5 at 14 K), confirming that *Ac*NosX reduced *Ac*N_2OR.

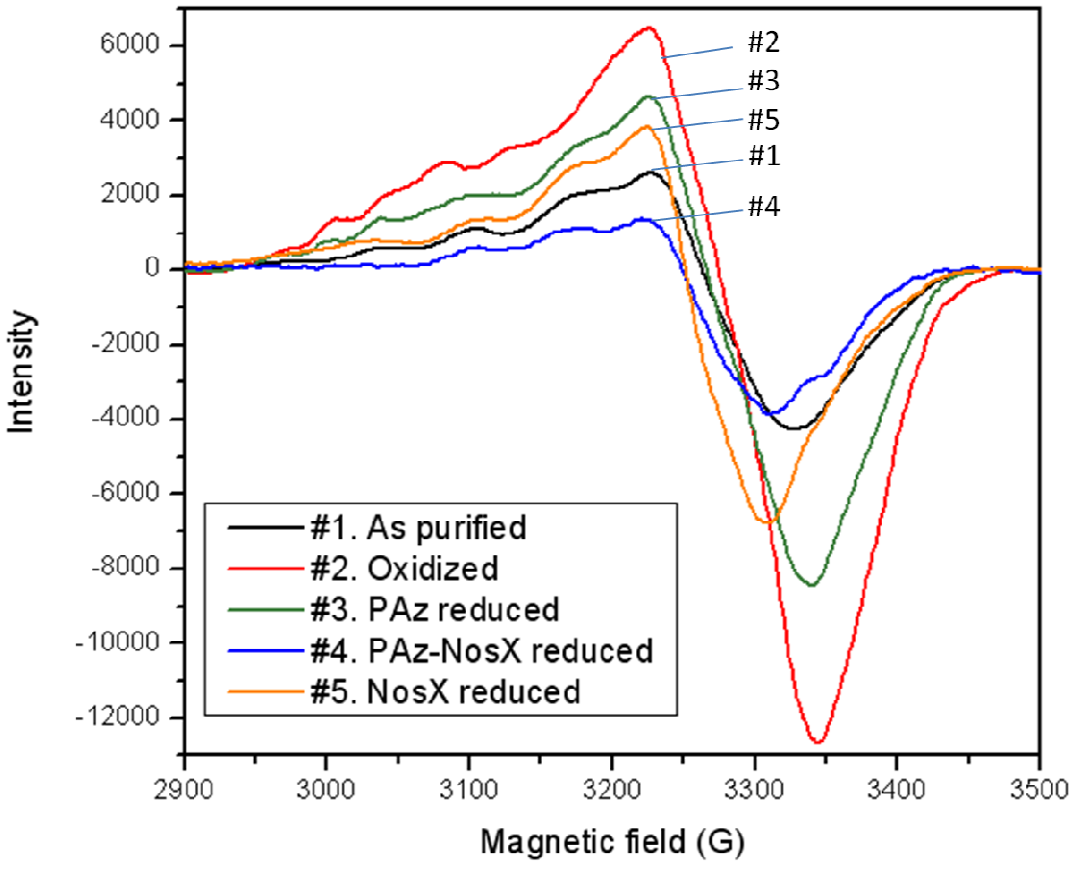


Figure 4.4. EPR spectra of *Ac*N_2OR samples at 14 K (normalized by protein concentration at 36 μM)

The Cu contents of the samples were determined by AA after the EPR and UV/Vis measurements. The total Cu amounts per N_2OR monomer of each sample were estimated as follows; #1 (as purified) = 4.0, #2 (fully oxidized) = 2.9, #3 (PAz reduced) = 3.2, #4 (PAz-NosX reduced) = 3.5, #5 (NosX reduced) = 2.9. The Cu amounts of #2 (2.9) and #5 (2.9), #3 (3.2) and #4 (3.5) should be comparable since the differences between them were only with or without *Ac*NosX (Figure 4.1). The Cu amount of fully oxidized N_2OR (#2, Cu = 2.9/monomer) was significantly lower than "as purified" form (#1, Cu = 4.0/monomer).

No.	N_2OR sample (normalized to 36 μM)	Temp	Integrated Intensity ($\times 10^5$)	Cu^{2+}/monomer	Ave. Cu^{2+}/monomer
1	As purified	14 K	692	0.33	0.32
		20 K	566	0.31	
		30 K	395	0.31	
2	Oxidized	14 K	2065	1.05	1.02
		20 K	1570	1.02	
		30 K	1077	1.00	
3	PAz reduced	14 K	1379	0.69	0.66
		20 K	1061	0.66	
		30 K	709	0.63	
4	PAz-NosX reduced	14 K	396	0.18	0.22
		20 K	496	0.26	
		30 K	295	0.21	
5	NosX reduced	14 K	1271	0.64	0.59
		20 K	909	0.55	
		30 K	653	0.57	

Table 4.1. Spin quantification of EPR spectra of *Ac*N_2OR

It was revealed that incubation of "as purified" form of *Ac*N_2OR with 100-fold excess amount of ferricyanide resulted in decrease of Cu content in N_2OR (Appendix D: Table

S4.1, Figure S4.2). The activities of *Ac*N_2OR in Table S4.1 (Exp #3) were determined to be 122.3 ± 5.1 U/mg for as purified form and 94.9 ± 4.1 U/mg for oxidized form after incubation with reduced MV.

According to the oxidized Cu amounts derived from the spin quantification with the EPR spectra and total Cu amounts obtained from the AA results, oxidized Cu ratios (oxidized Cu/total Cu) in each *Ac*N_2OR sample were calculated as follows; #1 = 8.0 % (oxidized Cu/total Cu = 0.32/4.0 = 8.0 %), #2 = 35.2 % (1.02/2.9 = 35.2 %), #3 = 20.6 % (0.66/3.2 = 20.6 %), #4 = 6.3 % (0.22/3.5 = 6.3 %), #5 = 20.3 % (0.59/2.9 = 20.3 %). According to the calculated ratio, the redox state of each sample was assigned as in Table 4.2. Theoretical oxidized Cu ratios were calculated as oxidized Cu over fully Cu loaded N_2OR (6 Cu/monomer) (e.g. sample #1, oxidized Cu/total Cu = 1/6 = 16.7 %). In sample #2 in Table 4.2, three out of six coppers in *Ac*N_2OR were expected to be oxidized. Thus, oxidized Cu ratio was calculated as 50 %. However, two oxidized Cu in the Cu_Z site could not be detected with EPR because two spins in the Cu_Z site were supposed to be canceled out with anti-ferromagnetic coupling (80). Thus, apparent oxidized Cu ratio would be calculated as 16.7 % (oxidized Cu/total Cu = 1/6 = 16.7 %).

			Oxidized Cu (%)	
	Cu_A	Cu_Z	Maximum*	Measured
#1. As purified	Cu(I) • Cu(I)	1Cu(II) • 3Cu(I)	16.7	8.0
#2. Fully oxidized	Cu(1.5) • Cu(1.5)	2Cu(II) • 2Cu(I)	16.7	35.2
#3. PAz reduced	Cu(I) • Cu(I)	2Cu(II) • 2Cu(I)	33.3	20.6
#4. PAz-NosX reduced	Cu(I) • Cu(I)	1Cu(II) • 3Cu(I)	16.7	6.3
#5. NosX reduced	Cu(I) • Cu(I)	2Cu(II) • 2Cu(I)	33.3	20.3

* Maximum values were calculated with the assigned structures and oxidation states of the Cu sites

Table 4.2. Redox state assignments of each form of *Ac*N_2OR

No radical signal from a semiquinone form of *Ac*NosX was observed in the EPR spectra of sample #4 and #5 (Figure 4.4). The result supported the idea that *Ac*NosX exists in either its fully reduced or oxidized form in the equilibrium state. This observation was consistent with the data from the UV/Vis spectra of the stepwise photo-reduction for *Ac*NosX (Figure 3.3, left). Thus, the equation, [Total NosX] = [oxidized NosX] + [reduced NosX] + [semiquinone NosX], can be approximated to [Total NosX] = [oxidized NosX] + [reduced NosX], which was used to determine the redox potential of *Ac*NosX. The result showed that the approximation was reasonable.

Regeneration of the Cu_Z* State
in *Ac*N_2OR with *Ac*NosX

For a control experiment, *Ac*N_2OR was incubated in Buffer PE for 4 hours under anaerobic conditions to check the effect of EDTA on *Ac*N_2OR. Although a minor decrease in absorption intensity on the UV/Vis spectra was observed, the spectral change was slight and negligible within the time scale of the following measurements (Appendix D: Figure S4.3).

Purified N_2OR always includes a certain percentage of the Cu_Z* state (69). To investigate if *Ac*NosX was able to regenerate the Cu_Z* state, oxidized *Ac*N_2OR was photo-reduced in the absence and presence of *Ac*NosX. 23 µM of oxidized *Ac*N_2OR was photo-reduced in Buffer PE under anaerobic conditions (Figure 4.5). The arrows indicate decrease of the absorption that was caused by the reduction of Cu centers in *Ac*N_2OR. The sample was gradually reduced and did not show significant absorbance changes after 30 min of light exposure.

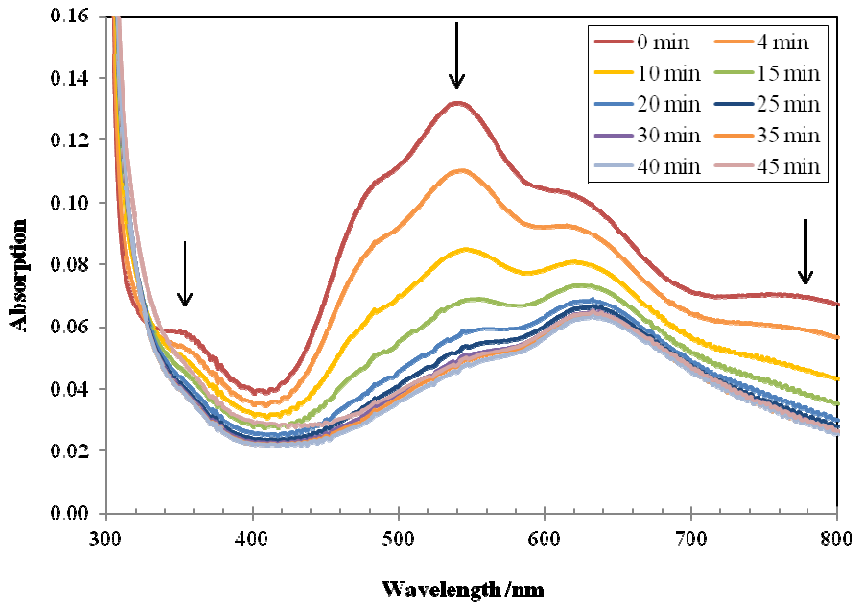


Figure 4.5. Photo-reduction of *Ac*N_2OR in the absence of *Ac*NosX
Arrows indicate decrease of absorption peaks

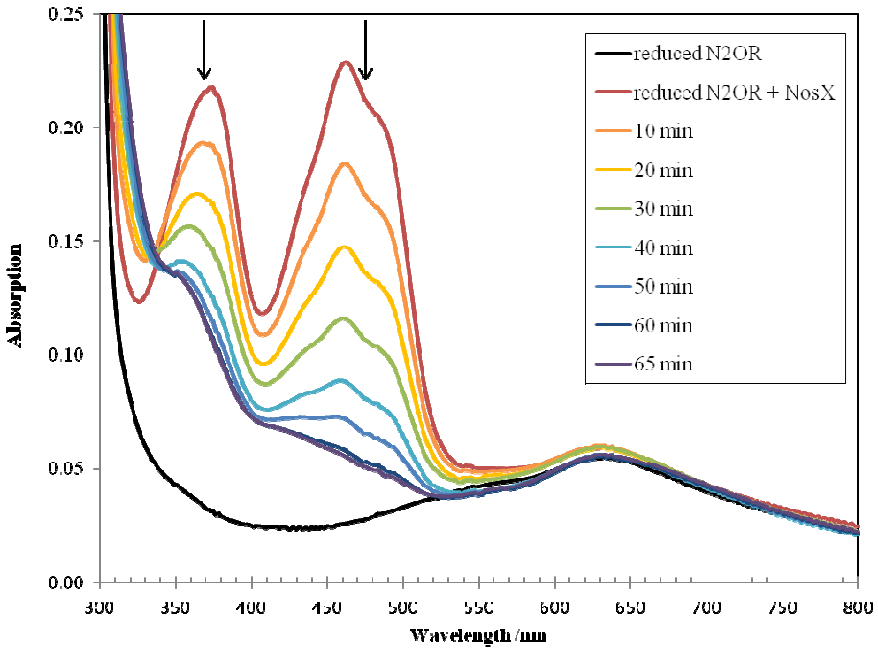


Figure 4.6. Photo-reduction of *Ac*N_2OR in the presence of *Ac*NosX
Arrows indicate decrease of absorption peaks

The spectrum after photo-reduction still had a shoulder around 540 nm which was assigned to the 2Cu(II) • 2Cu(I) form in the Cu_Z site. The peak at 640 nm was assigned to the partially oxidized Cu_Z (1Cu(II) • 3Cu(I)) form and Cu_Z* form, both of which have the absorption peak at the same wavelength (11; 77). The result shows that photo-reduction can reduce the Cu_A completely and the Cu_Z site partially (Figure 4.5, black).

After reduction of *Ac*N_2OR was reached to the limit of photo-reduction system, oxidized *Ac*NosX was anaerobically added to the cuvette. The cuvette was further photo-reduced in the presence of oxidized *Ac*NosX (Figure 4.6). If *Ac*NosX was able to reduce those partially oxidized Cu_Z (1Cu(II) • 3Cu(I)) and/or Cu_Z* centers, the peak at 640 nm should decrease. The arrows point to decreases in absorption which indicate a reduction of *Ac*NosX. After 65 min, no more changes were observed by UV/VIS. *Ac*NosX was fully reduced by the light and the absorption peak at 640 nm from the Cu_Z site of *Ac*N_2OR did not show any intensity change in the presence of reduced *Ac*NosX.

Electron Transfer from Reduced *Ac*NosX to Oxidized *Ac*PAz

The reduction of *Ac*PAz with *Ac*NosX was investigated with UV/Vis spectroscopy. The UV/Vis spectra of oxidized *Ac*PAz (30 µM), reduced *Ac*NosX (30 µM), and mixture of both proteins (30 µM each) are shown in Figure 4.7. When oxidized *Ac*PAz and reduced *Ac*NosX were mixed under anaerobic conditions, the increase of peaks at 374 and 460 nm and decrease of peaks at 594 and 780 nm were observed (Figure 4.7, blue). These spectral changes clearly indicated the oxidation of FAD in *Ac*NosX and reduction of Cu in *Ac*PAz. The result indicated that *Ac*NosX donated electrons to *Ac*PAz.

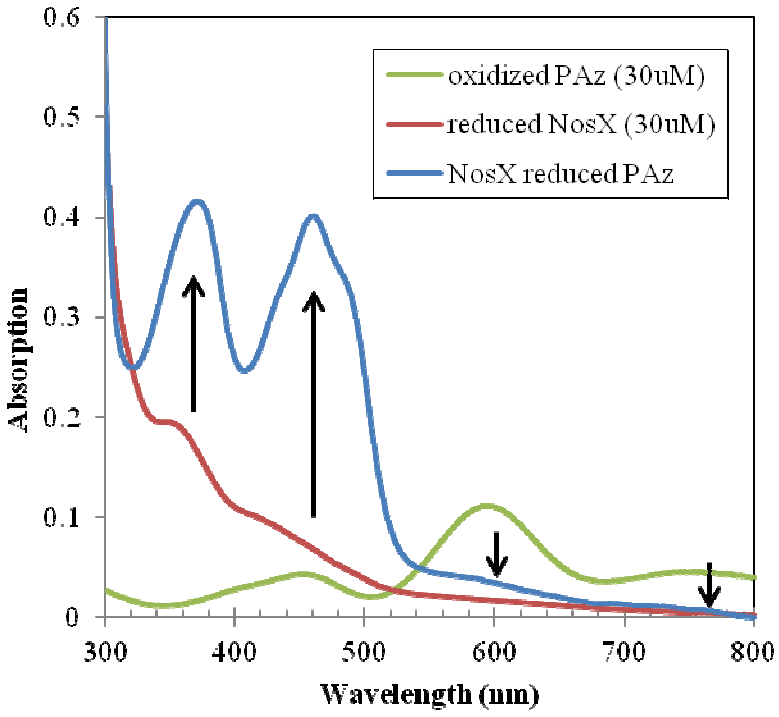


Figure 4.7. UV/Vis spectra of reduced *Ac*NosX, oxidized *Ac*PAz, and *Ac*NosX reduced *Ac*PAz

Catalytic Reaction of *Ac*N_2OR with Reduced *Ac*NosX

Previously, it was shown that an excess amount of reduced *Ac*PAz could sustain the N_2OR catalytic cycle by donating electrons to *Ac*N_2OR *in vitro* (91). Since *Ac*NosX was also shown to donate electrons to *Ac*N_2OR, the questions of whether *Ac*NosX able to sustain the N_2OR catalytic reaction was investigated. The UV/Vis spectra of reduced *Ac*NosX (44 µM) and a catalytic amount of *Ac*N_2OR (6.8 nM) in the presence or absence of N_2O are shown in Figure 4.8. The time course of the absorption change at 460 nm was monitored for 30 min (Figure 4.8, right). After monitoring the background auto-oxidation rate of *Ac*NosX for 10 min, N_2O saturated buffer (80 µL) was injected at 11 min. If *Ac*NosX donated electrons to *Ac*N_2OR during the catalytic reaction, the *Ac*NosX

oxidation rate should be significantly increased after N_2O was injected as observed in Figure 4.9 and 4.10. The oxidation rates of *Ac*NosX before and after N_2O injection were calculated as slopes of trend lines (linear regression) for the absorption change at 460 nm. The equations are shown in Figure 4.8 (right). The result showed that no significant increase in the oxidation rates of *Ac*NosX was observed between before (0.0012 min^{-1}) and after (0.0013 min^{-1}) the N_2O injection (Figure 4.8, right). The result indicated that *Ac*NosX did not support the N_2OR catalytic cycle under the experimental conditions.

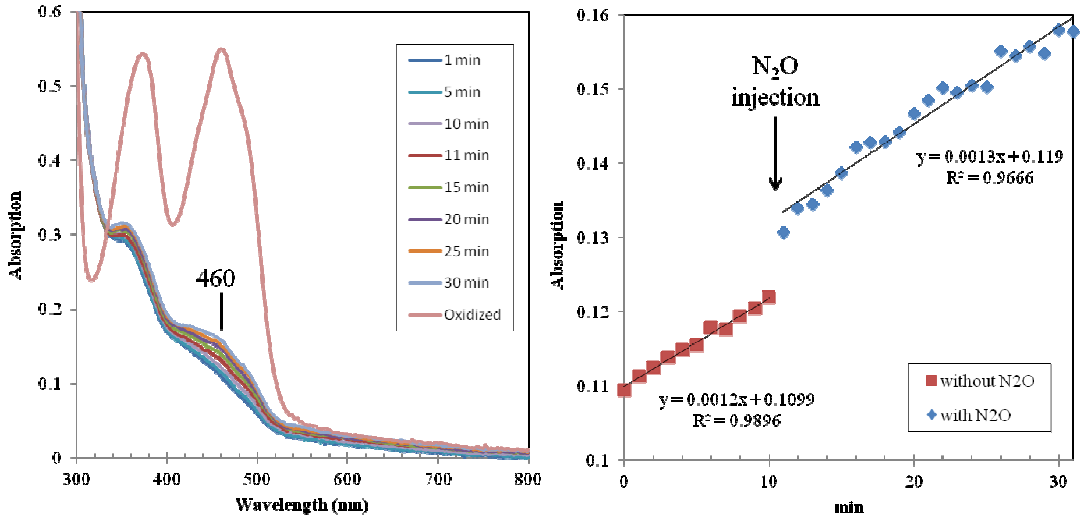


Figure 4.8. Oxidation of *Ac*NosX during the N_2OR catalytic cycle (left) and time course at 460 nm (right)

However, according to the control experiment with reduced *Ac*PAz, the electron transfer from *Ac*PAz to *Ac*N_2OR was not observed under the same conditions using Buffer P (data not shown). This observation indicated that electron transfer from reduced *Ac*NosX to *Ac*N_2OR during the catalytic cycle may be inhibited by a component in Buffer P.

Therefore a series of investigations to determine if Buffer P and its components inhibited the catalytic reaction were carried out in the next section.

The N_2OR catalytic cycle in the presence of excess free FAD (72.0 µM FAD vs. 6.8 nM N_2OR) in 50 mM Potassium Phosphate (pH 7.0) was monitored with UV/Vis spectra (Figure 4.9) as a further control.

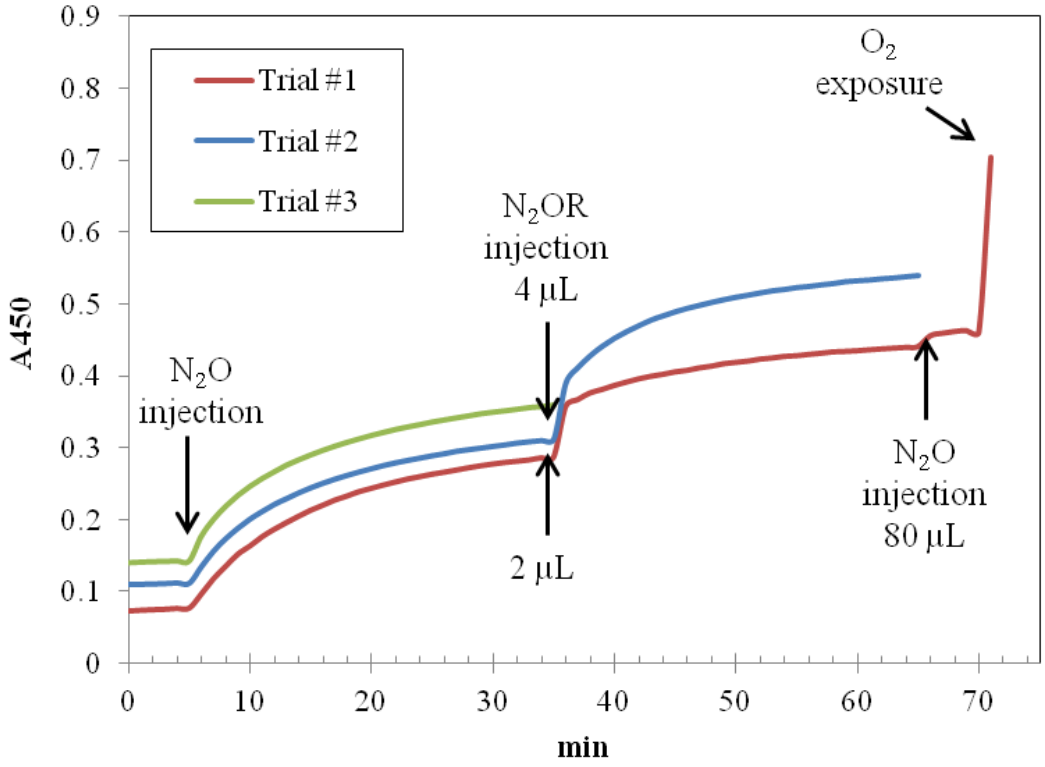


Figure 4.9. Time course for the oxidation of free FAD during the N_2OR catalytic cycle

The result showed that the electron transfer from reduced free FAD to *Ac*N_2OR during the catalytic cycle was observed, but it stopped within 30 min. Another injection of activated *Ac*N_2OR (6.8 nM (trial #1) or 13.6 nM (#2)) at 35 min induced further FAD oxidation, but the FAD oxidation stopped within 30 min again. At 66 min, N_2O saturated

buffer was injected (Figure 4.9, trial #1), but no further FAD oxidation was observed. At 71 min, the anaerobic cuvette was opened and sample could be further oxidized by air, indicating that there was still enough amount of free FAD in the sample at 66 min.

Identification of Inhibitory Factor for the N_2OR Catalytic Cycle with *Ac*PAz

Buffer P was composed of 100 mM Phosphate, 150 mM NaCl, and 10 % glycerol. Since the N_2OR catalytic cycle with reduced *Ac*PAz was originally observed in 50 mM Phosphate, the concentration of phosphate was reduced to 50 mM in following experiments. The oxidations of *Ac*PAz during the N_2OR catalytic cycle were monitored to determine if NaCl or glycerol was the component that inhibited the catalytic cycle. 50 mM Potassium Phosphate (pH 7.0) (buffer #1), 50 mM Potassium Phosphate with 150 mM NaCl (pH 7.0) (buffer #2), or 10 % glycerol (buffer #3) were used for the measurements (Figure 4.10).

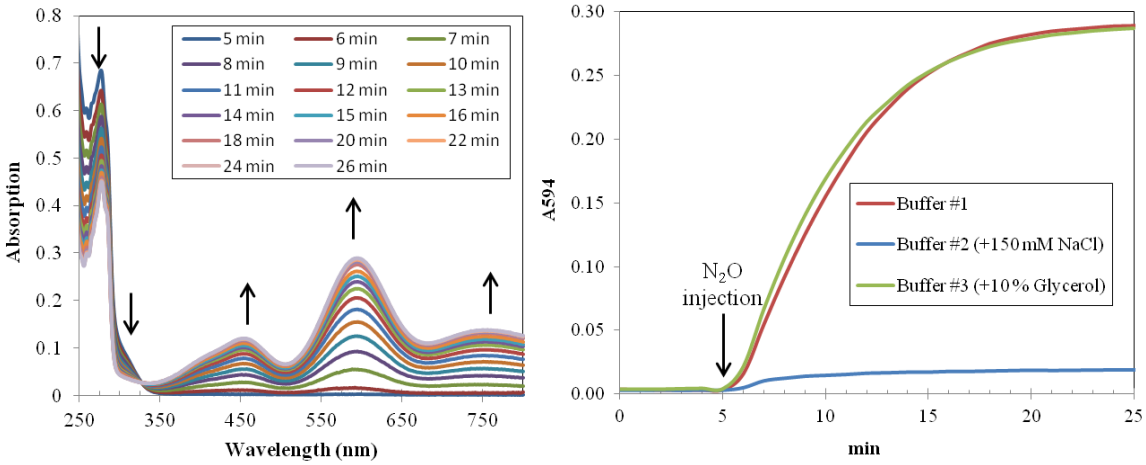


Figure 4.10. UV/Vis spectra of *Ac*PAz oxidation during the N_2OR catalytic cycle with buffer #1 (left) and time course at A_{594} in buffer #1 - 3 (right)

The result showed that buffer #2 (with 150 mM NaCl) inhibited *Ac*PAz oxidation during the N_2OR catalytic cycle, whereas *Ac*PAz was fully oxidized as *Ac*N_2OR received electrons from *Ac*PAz in buffer #1 and #3 (Figure 4.10, right, Table 4.3).

To determine if Na^+ or Cl^- inhibited the catalytic reaction, the *Ac*PAz oxidation during the N_2OR catalytic reaction were also measured with 50 mM Potassium Phosphate + 150 mM KCl (pH 7.0) (buffer #4), 50 mM Sodium Phosphate (pH 7.0) (buffer #5) (Figure 4.11, Table 4.3). The results showed that the chloride ion inhibited *Ac*PAz oxidation during the N_2OR catalytic cycle.

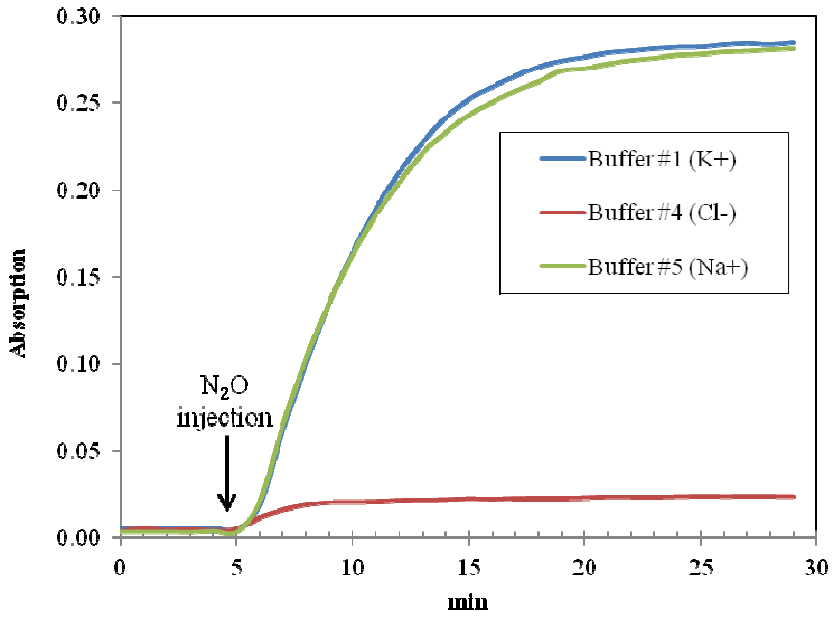


Figure 4.11. Time course for the oxidation of *Ac*PAz during the N_2OR catalytic cycle in buffer #4 - 5

As control experiments, if ionic strength of buffer affected to the electron transfer from *Ac*PAz to *Ac*N_2OR during the catalytic cycle was investigated using 50 mM

Potassium Phosphate + 50 mM Na_2SO_4 (pH 7.0, I = 0.242) (buffer #6), and 129 mM Potassium Phosphate (pH 7.0, I = 0.241) (buffer #7) (Figure 4.12). The oxidation of *Ac*PAz was slightly perturbed in both buffer #6 and 7. The behavior of *Ac*PAz oxidations in buffer #6 and 7 were almost identical, suggesting that the slight perturbation of *Ac*PAz oxidation was due to high ionic strength.

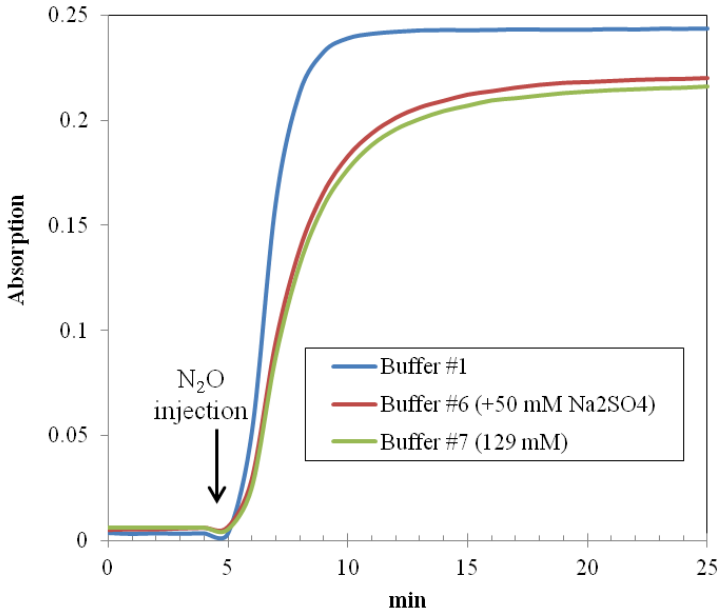


Figure 4.12. Time course for the oxidation of *Ac*PAz during the N_2OR catalytic cycle in buffer #6 and 7

#	Phosphate*	K^+*	Na^+*	Cl^-*	SO_4^-*	glycerol	Ionic strength	PAz oxidation
1	50	50					0.092	Yes
2	50	50	150	150			0.242	No
3	50	50				10%	0.092	Yes
4	50	200		150			0.242	No
5	50		50				0.092	Yes
6	50	50	100		50		0.242	Yes
7	129	129					0.241	Yes

(* unit = mM)

Table 4.3. *Ac*PAz oxidation during the N_2OR catalytic cycle in various buffers

The N_2OR activities in buffer #1 (50 mM Phosphate), buffer #2 (50 mM Phosphate + 150 mM NaCl), and buffer #6 (50 mM Phosphate + 50 mM Na_2SO_4) were measured to investigate if chloride and ionic strength affected the N_2OR activity. Typical results are shown in Figure 4.13.

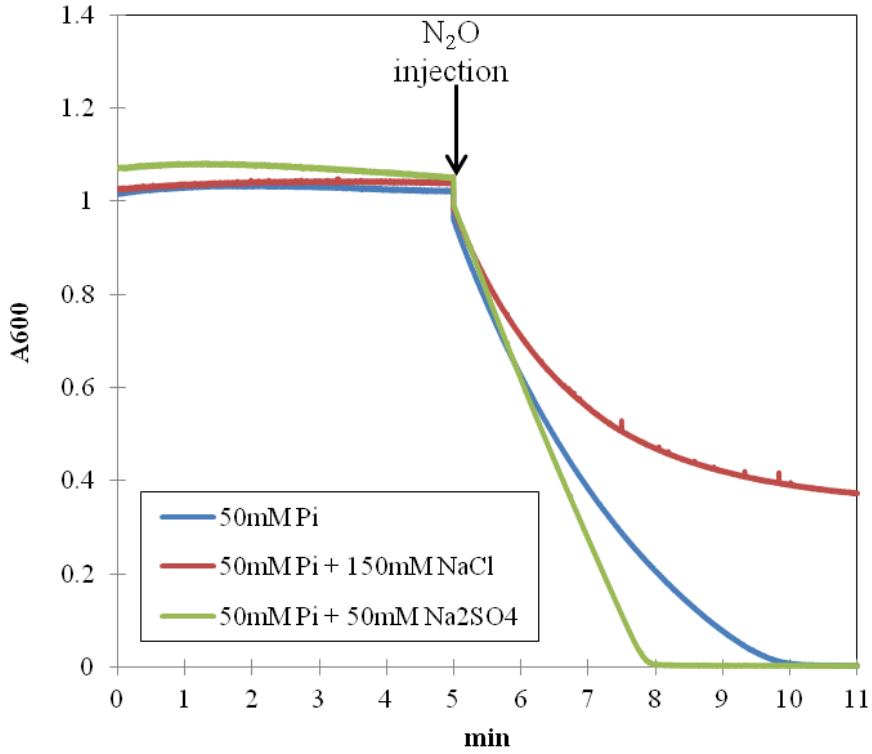


Figure 4.13. The N_2OR activity assay in buffer #1, 2, and 6

N_2O saturated buffer #1 was injected to the cuvette at 5 min and the activity was calculated with the slope between 5.12 and 5.18 min. The N_2OR activities were 147.4 ± 8.70 U/mg in buffer #1, 134.9 ± 6.68 U/mg in buffer #2, and 156.5 ± 4.33 U/mg in buffer #6. The activities in the buffers were almost comparable at the beginning of N_2O catalytic cycle, but the activity in buffer #2 was significantly decreased within 5 min. An increase

in ionic strength did not reduce the activity since the activity in buffer #6, which ionic strength was the same as buffer #2, was not decreased (Figure 4.13).

*Ac*NosX Stabilization in Solution

Stabilizing abilities of arginine (200 mM), ammonium sulfate (100 mM), spermine (200 mM), spermidine (200 mM), Triton X-100 (0.1 %), Tween 20 (0.1 %), and NaCl (150 mM) on *Ac*NosX *in vitro* were checked by monitoring protein precipitations after 2, 4 and 8 hours at 4 °C. After two hours, samples with arginine, ammonium sulfate, spermidine, Triton X-100, Tween 20, and sample without reagent showed significant precipitation, whereas samples with spermine and NaCl did not show such turbidity in the solution. After eight hours, samples were centrifuged and UV/Vis spectra were measured (Figure 4.14).

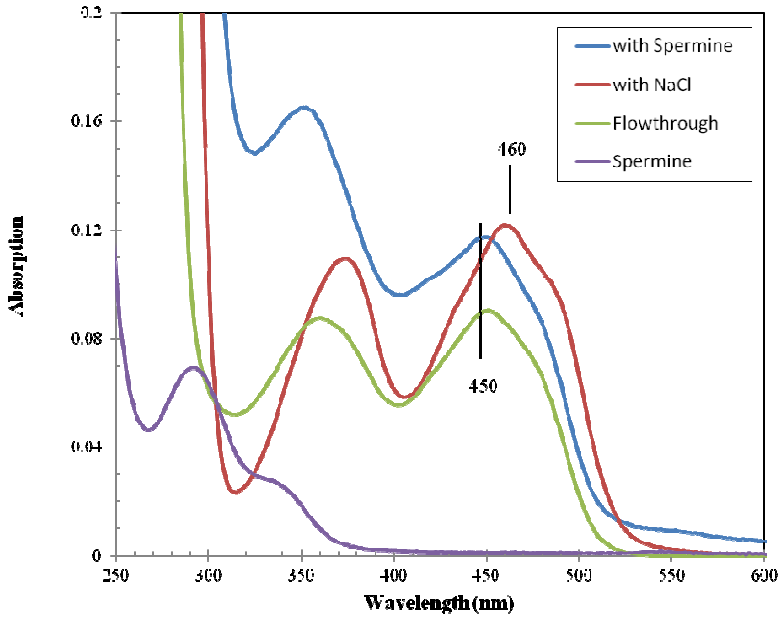


Figure 4.14. UV/Vis spectra of *Ac*NosX with spermine, NaCl, and flowthrough

Although the samples with spermine and NaCl also showed minor precipitation, the amount was significantly suppressed compared to other samples. The results indicated that spermine seemed to be an encouraging candidate for an *Ac*NosX stabilizer. However, it turned out that spermine pulled FAD out from *Ac*NosX based on the following observations: (1) the UV/Vis spectrum of *Ac*NosX with spermine showed an absorption peak shift from 460 nm to 450 nm which was identical to free FAD (Figure 4.14, blue). (2) Concentration of *Ac*NosX with spermine by an Amicon ultrafiltration (YM-10) resulted in FAD in the flowthrough (Figure 4.14, green). As a result, only NaCl kept *Ac*NosX intact in solution under the experimental conditions.

Discussion

Function of *Ac*NosX as an Electron Donor for *Ac*N_2OR

To determine the function of *Ac*NosX, electron transfers from *Ac*NosX to *Ac*N_2OR (oxidized and PAz reduced form) were investigated. Both *Ac*NosX and *Ac*PAz were shown to reduce the Cu_A site of *Ac*N_2OR (Figure 4.2, 4.3). In the UV/Vis spectrum that showed *Ac*NosX reduced *Ac*N_2OR (Figure 4.2, blue), the peak at 800 nm that was derived from the Cu_A site (63) was decreased. This observation indicated that *Ac*NosX reduced the Cu_A site in *Ac*N_2OR. It was not clear in the spectrum whether *Ac*NosX could donate electrons to the Cu_Z site due to the absorption peak from *Ac*NosX. The differential spectrum of fully oxidized (#2) and PAz reduced (#3) N_2OR (Figure 4.3, blue) was almost identical to the Vis spectra of the Cu_A site in N_2OR from *Pseudomonas stutzeri* (peaks at 485, 525, and 795 nm) (63) and Cu_A reconstituted *Ac*N_2OR expressed in *E. coli*

that did not have the Cu_Z site (peaks at 484, 531, and 796 nm, Fujita *et al*. unpublished results). If *Ac*PAz could reduce the Cu_Z site, there should be additional peak(s) around 550 and 640 nm, which were derived from the Cu_Z site, in the differential spectrum (63). However, no such peak or shoulder was observed in the spectrum (Figure 4.3, blue). Thus, it was indicated that *Ac*PAz reduced only the Cu_A site, but not the Cu_Z site. Also, it further indicated that electron transfer from Cu_A to Cu_Z did not occur under the experimental conditions. *Ac*N_2OR was reduced with 30-fold excess amount of reduced *Ac*PAz. The ratio between *Ac*PAz and *Ac*N_2OR was physiologically realistic since the abundance ratio of PAz vs. N_2OR in WT of *A. cycloclastes* was shown to be ~ 40:1 (91).

*Ac*NosX appeared to be capable of reducing the Cu_Z site of *Ac*N_2OR. The redox state of the Cu_Z site in the dithionite reduced N_2OR was assigned to 1Cu(II) • 3Cu(I) form with DFT calculations based on experimental data (156; 79). The redox state of the Cu_Z site in the fully oxidized N_2OR was also assigned to 2Cu(II) • 2Cu(I) form (84). Further, the fully reduced form of the Cu_Z site was determined to be 4Cu(I) form (70; 77). According to the EPR and AA data together with the previous information, the redox states of the Cu_Z sites in PAz reduced N_2OR (sample #3) and PAz-NosX reduced N_2OR (sample #4) were assigned to 2Cu(II) • 2Cu(I) form and 1Cu(II) • 3Cu(I) form, respectively (Table 4.2). This result indicated that *Ac*NosX could reduce the Cu_Z site at least from [2Cu(II) • 2Cu(I)] to [1Cu(II) • 3Cu(I)]. There are two possibilities on the Cu_Z reduction mechanism by *Ac*NosX. First, *Ac*NosX directly reduces the Cu_Z site and second, *Ac*NosX facilitates the electron transfer from Cu_A to Cu_Z, which *Ac*PAz could not. To

clarify this hypothesis, *Ac*N_2OR without the Cu_A site by mutation would be required for further study.

The observations on the electron transfer reactions among *Ac*N_2OR, *Ac*PAz, and *Ac*NosX were consistent with the redox potentials of these proteins. Although the redox potentials of the Cu centers in *Ac*N_2OR have not been determined yet, it was expected that the redox potentials of the Cu_A and Cu_Z site were ~ 250 mV and ~ 60 mV, respectively (see chapter 1) (68). The redox potentials of *Ac*PAz and *Ac*NosX were determined as 260 mV (147) and -230 mV (see chapter 3). The redox potential of *Ac*PAz (260 mV) was comparable with the one of the Cu_A site (~ 250 mV), which enabled *Ac*PAz to donate electrons to the site. However, the redox potential of the Cu_Z site was too low for *Ac*PAz to donate electrons to that site. Therefore, *Ac*PAz was expected to donate electrons only to the Cu_A site, but not Cu_Z site. Indeed, the results were as expected (Figure 4.3). In contrast, *Ac*NosX was expected to reduce both the Cu sites because the redox potential of *Ac*NosX (-230 mV) was lower than the redox potentials of the Cu_A (250 mV) and Cu_Z (60 mV) sites. The EPR data confirmed this expectation (Table 4.1, 4.2).

The percentage of oxidized Cu in the fully oxidized N_2OR was determined as 35.2 % (Table 4.2). This observation was different from the theoretical value (16.7 %). This result was explained as follows. In the fully oxidized N_2OR, the two spins on the Cu_Z site (2Cu(II) • 2Cu(I)) should be cancelled out with anti-ferromagnetic coupling (80), and only one spin on the Cu_A site (Cu(1.5) • Cu(1.5)) should be detectable with the EPR. However, the data from AA indicated that the total Cu amount in the sample #2 was ~ 3

per monomer on average, which was caused by ferricyanide incubation (Table S4.1, Figure S4.2). Thus, it was highly likely that many of the Cu_Z sites in *Ac*N_2OR molecules included less than four coppers, which resulted in the disappearance of the anti-ferromagnetic interaction. In this case, the spin(s) on the Cu_Z site would be detectable in the EPR and the percentage of oxidized Cu would increase. Also, it might be possible that the Cu loss by ferricyanide results in higher Cu(II) content.

Although *Ac*NosX was shown to be a more potent reductant than *Ac*PAz, the percentages of oxidized Cu in the sample #3 (PAz reduced N_2OR) and #5 (NosX reduced N_2OR) were calculated as almost the same level (20.6 and 20.3 %, respectively, Table 4.2). This result appeared to disagree with the conclusion. This observation is explained as follows. In the sample #3, fully oxidized *Ac*N_2OR was reduced with 30-fold excess mount of *Ac*PAz, whereas fully oxidized *Ac*N_2OR was reduced with only 2-fold amount of *Ac*NosX in the sample #5. Since *Ac*NosX could not be concentrated more than 200 μM, addition of 2-fold *Ac*NosX to the sample was the maximum limit in the experiment. If enough amount of *Ac*NosX could be added to the sample, it was likely that the Cu sites in fully oxidized N_2OR (Cu_A = Cu(1.5) • Cu(1.5), Cu_Z = 2Cu(II) • 2Cu(I)) would be reduced to Cu_A = Cu(I) • Cu(I), Cu_Z = 1Cu(II) • 3Cu(I), which was identical to the sample #1 (as purified) and #4 (PAz-NosX reduced) (Table 4.2).

We determined that incubation of *Ac*N_2OR with an excess amount of ferricyanide resulted in decrease of Cu content in *Ac*N_2OR (Appendix D: Table S4.1, Figure S4.2). It was not clear how ferricyanide removed Cu from *Ac*N_2OR. It is possible that an excess amount of ferricyanide oxidized the Cu clusters in *Ac*N_2OR and “super-oxidized” forms

such as [Cu(II)-Cu(II)] and [4Cu(II)] might be generated. Such species might be unstable since the species have never been observed (4). Consequently, the "super-oxidized" clusters might decompose and the Cu content of oxidized N_2OR decreased. The oxidized *Ac*N_2OR still showed activity (94.9 ± 4.1 U/mg) after incubation with reduced MV, and the UV/Vis spectrum clearly showed absorption peaks from the Cu_A and Cu_Z sites (Figure 4.3). These results indicated that the Cu loss by oxidation with ferricyanide was expected to occur randomly in both Cu_A and Cu_Z sites, rather than either Cu_A or Cu_Z cluster was specifically decomposed.

To date, reduction of the partially oxidized Cu_Z (1Cu(II) • 3Cu(I)) form to the active form (4Cu(I)) requires a long incubation time (~ 3 hours) with reduced MV, which is not physiologically relevant (70; 77). There should be a more efficient reduction mechanism to reduce 1Cu(II) • 3Cu(I) form *in vivo*. *Ac*NosX was one of the candidates. However, the EPR and UV/Vis data suggested that *Ac*NosX could not reduce the 1Cu(II) • 3Cu(I) form under the experimental conditions (Table 4.2, Figure 4.6). The mechanism that reduces the 1Cu(II) • 3Cu(I) form *in vivo* is still unclear.

Function of *Ac*NosX for Regeneration of the Cu_Z* State in *Ac*N_2OR

The N_2OR activity in *Paracoccus denitrificans* was diminished in the NosX and NirX double mutant strain although PAz and cytochrome *c* should still be able to donate electrons to N_2OR (83). Since direct correlation between the Cu_Z* proportion and NosX deletion was observed, NosX was expected to be involved in the regeneration of the Cu_Z* state *in vivo*. However, *Ac*NosX could not regenerate the Cu_Z* state under the

experimental conditions (Figure 4.6). If reduced *Ac*NosX was able to regenerate the Cu_Z* state, the peak at 640 nm should decrease. The peak did not change in the presence of reduced *Ac*NosX. It might be possible that *Ac*NosX requires other factor(s) to reduce the Cu_Z* state *in vivo*. For instance, it was shown that the deletion or modification of NosR resulted in the same phenotype as the NosX knockout strain in *Pseudomonas stutzeri* (82). This observation imply that the regeneration of the Cu_Z* state requires both NosX and NosR to form a complex that enables to regenerate the Cu_Z* state.

Another possibility is that NosX does not regenerate the Cu_Z* state, but it inhibits the generation of the Cu_Z* state. This hypothesis can also explain the observations that the proportion of Cu_Z* state was increased in the absence of NosX (83). In any case, the structure and properties of the Cu_Z* state are still uncertain, and the current data do not support a direct role for *Ac*NosX in converting Cu_Z* to Cu_Z. As will be discussed later, a new definition of the Cu_Z* state was proposed based on the new structure of N_2OR from *Pseudomonas stutzeri* (63). The authors proposed that the Cu_Z* state is the [4Cu:1S] form and the Cu_Z state is the [4Cu:2S] form. This hypothesis can be interpreted that the regeneration of the Cu_Z* state requires re-construction of the Cu_Z site by adding a sulfide ion to the [4Cu:1S] form. If this can be applied to *Ac*N_2OR, it is expected that *Ac*NosX cannot regenerate the Cu_Z* state because it was shown that NosX was not involved in the Cu_Z site construction (100). In such case, it is plausible that *Ac*NosX works as a “cofactor” to keep the Cu_Z site active and inhibit the generation of the Cu_Z* state.

Function of *Ac*NosX as an Electron Donor for *Ac*PAz

*Ac*NosX donated electrons to oxidized *Ac*PAz (Figure 4.7). The redox potential of *Ac*PAz (260 mV) is very close to the redox potential of the Cu_A site (~ 250 mV) (157; 68; 147). As shown in previously (Figure 4.2), *Ac*NosX could donate electrons to the Cu_A site. Therefore, it was expected that *Ac*NosX could also reduce *Ac*PAz. The result suggested that there was an electron transfer network among NosX, PAz, and N_2OR in the periplasm of *A. cycloclastes*. However, the physiological relevance of the electron transfer pathway from *Ac*NosX to *Ac*PAz is still unknown. It was shown that the abundance ratio of PAz and N_2OR in WT of *A. cycloclastes* was ~ 40:1 (91). Although the ratio of *Ac*NosX and *Ac*N_2OR in WT has never been monitored, the ratio of *Ac*NosX and *Ac*N_2OR in the overexpression strain for Nos proteins (*Ac*/pMLClustXst) was 1: 25 ~ 50, which was calculated from the yields of the proteins. Assuming the abundance ratio of *Ac*NosX and *Ac*N_2OR in WT was the same as the overexpression strain, the ratio among *Ac*PAz, *Ac*N_2OR, and *Ac*NosX in the periplasm would be 40:1:0.03. Thus, the total abundance of *Ac*NosX *in vivo* is expected to be considerably smaller than that of *Ac*PAz. Therefore, the contribution of *Ac*NosX in reducing *Ac*PAz *in vivo* would be relatively small, unless the turnover of *Ac*NosX re-reduction (perhaps by NosR) would be fast.

Identification of Inhibitory Factor
for the N_2OR Catalytic Cycle

Chloride in Buffer P was identified as an inhibitory factor of the N_2OR catalytic cycle using BV and *Ac*PAz as electron donors (Figure 4.10, 4.11, 4.13). Although N_2OR

was incubated in buffer with or without chloride for 5 min prior to N_2O injection, the initial N_2O reduction rates, which corresponded to the N_2OR activities, were almost comparable (147.4 ± 8.70 U/mg without chloride and 134.9 ± 6.68 U/mg with chloride, Figure 4.13). If the inhibitory reaction between chloride and the enzyme occurred in the absence of N_2O, a significant decrease of the initial N_2O reduction rate should be observed in the buffer with chloride. Therefore, the results indicated that the inhibition of the N_2OR catalytic cycle by chloride occurred in the presence of N_2O. The mechanism of the chloride inhibition effect is still unclear. Two straightforward possibilities are that the electron transfer reactions from electron source (BV or *Ac*PAz) to the active site (Cu_Z) through the Cu_A site are impacted, or that the catalytic reaction of N_2O at the Cu_Z site was inhibited by chloride (see below for more detail).

The electron transfer process from *Ac*PAz to the Cu_Z site, which chloride ions possibly inhibit, can be categorized in two steps, (1) inter-molecular electron transfer step, involving interaction (binding and releasing) between *Ac*PAz and *Ac*N_2OR, and (2) intra-molecular electron transfer step (perturbations of the Cu_A/Cu_Z site and/or electron transfer from the Cu_A to the Cu_Z site).

The inter-molecular electron transfer step might be inhibited by chloride ions. Chloride ions could interrupt the protein-protein interaction between *Ac*PAz and *Ac*N_2OR by blocking release of oxidized *Ac*PAz from *Ac*N_2OR. For rapid catalytic turnover, reduced *Ac*PAz needs to bind to *Ac*N_2OR, donate one electron to the Cu_A site, and then rapidly dissociate for the next *Ac*PAz-*Ac*N_2OR interaction. If chloride ions inhibit the release of oxidized *Ac*PAz from *Ac*N_2OR, the PAz binding site would be blocked and the

catalytic cycle would be blocked by a lack of electrons. However, this is unlikely. In the last step of *Ac*N_2OR purification, a cytochrome *c* agarose affinity column was used (see method section). Since it was reported that both PAz and cytochrome *c* donated electrons to N_2OR through similar docking sites (92; 150; 91; 87), it was expected that the complex of *Ac*N_2OR and cytochrome *c* on the resin was essentially the same as the complex between *Ac*N_2OR and *Ac*PAz in solution. In the purification protocol, bound *Ac*N_2OR on the column was eluted by buffer including NaCl. This fact indicated that chloride ions interrupted the formation of the N_2OR-cytochrome *c* complex. Thus, it was unlikely that chloride ion inhibited release of *Ac*PAz from *Ac*N_2OR. Another possibility of the inhibition effect was that chloride ions occlude the binding sites of *Ac*PAz and/or *Ac*N_2OR, which inhibits proper protein-protein interaction between *Ac*PAz and *Ac*N_2OR. It has been reported that the electron transfer from cytochrome *c* to N_2OR from *Paracoccus pantotrophus* was perturbed with NaCl (over 50 mM) (75). The authors concluded that high ionic strength perturbed the protein-protein interaction between cytochrome *c* and N_2OR (75). Since the interaction of positively and negatively charged amino acids in *Ac*PAz and *Ac*N_2OR was important to form a transient electron transfer complex (92; 91; 87), the perturbation of the electron transfer under high ionic strength could be a consequence of perturbing the interaction between the two proteins by charged species in the buffer. However, this possibility is doubtful in our case because electron transfer only requires a “light touch” between donor and acceptor, and even if binding sites of *Ac*PAz and *Ac*N_2OR were buried in chloride ions, there still would be many chances for a productive transient complex to form. In this case, chloride might decrease

the reaction rate, but it would seem unlikely that it would completely block the reaction as observed. According to the control experiments (Figure 4.12), the electron transfer from *Ac*PAz to *Ac*N_2OR was slightly perturbed under higher ionic strength, but it was not totally inhibited as observed in the presence of chloride, indicating that the inhibition effect was not mainly due to ionic strength. Further, the inhibition was also observed when the small molecule (BV) reductant was used as the electron source (Figure 4.13), suggesting that the inhibition occurred within the N_2OR molecule rather than the electron transfer step between BV and N_2OR (see below). It is less likely that high ionic strength perturbed the interaction between the small molecule (BV) and the protein (N_2OR).

Another possible inhibition mechanism by chloride ions is expected to occur within the N_2OR molecule. Previously, it was reported with UV/Vis spectroscopy that chloride interacted with the Cu_A site in *Ac*N_2OR (80). The binding of chloride ion on the Cu_Z site was also observed and it was hypothesized that the chloride ion influenced the redox potential of the Cu_Z site (Figure 4.15) (74). The chloride on the Cu_Z site was observed in all structure determined N_2ORs (61; 59; 63; 62). It is possible that the chloride on the Cu_Z site inhibited the catalytic reaction by changing the redox potential or by interfering with a step or steps in the reduction mechanism. It is also possible that the redox potential of the Cu_A site would be disturbed with bound chloride. Although no chloride ion was observed around the Cu_A site in the crystal structures of *Ac*N_2OR, three chloride ions were identified around the cupredoxin motif in the C-terminal domain of *Ac*N_2OR, which holds the Cu_A site (Figure 4.15) (59). The Cu_A does not serve as a binding site for chloride, but the remote (20.0 ~ 23.4 Å) chloride binding sites and the

amino acids for coordination of the Cu_A site were located on the same β-sheets. Thus, it might be possible that the binding of the chloride ions affect either the redox potential of the Cu_A site, the electron transfer from *Ac*PAz/BV to the Cu_A, and/or the electron transfer from Cu_A to the Cu_Z by changing the coordination of amino acids around the Cu_A site.

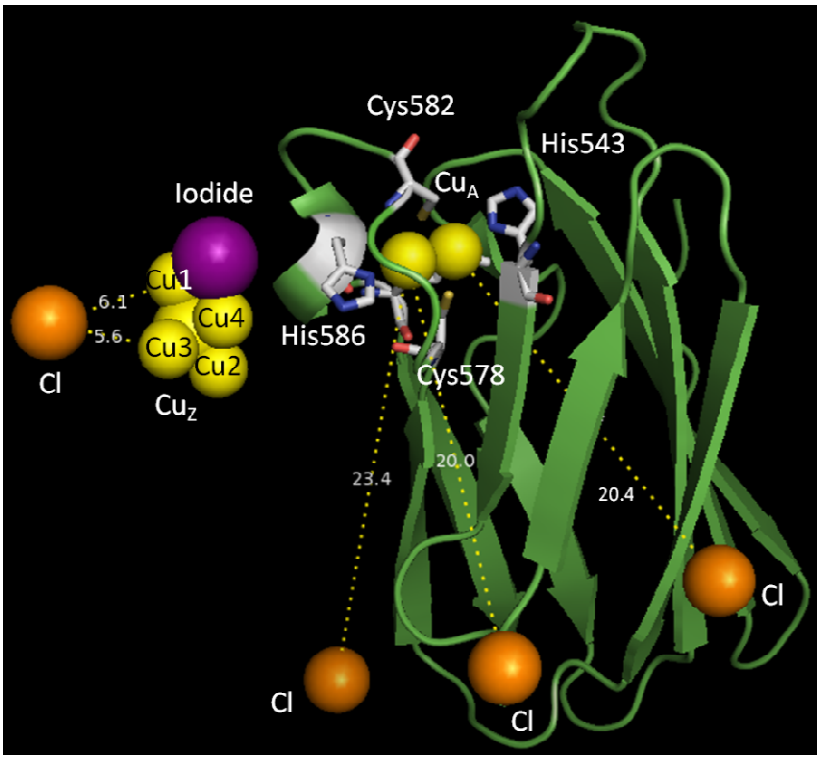


Figure 4.15. The Cu_A, Cu_Z, and chloride binding sites in the C-terminal domain of *Ac*N_2OR (iodide bound form)

It should be noted that the chloride ions around the Cu_A site were only observed in the iodide bound *Ac*N_2OR (PDB: 2IWK) but not the other structure determined N_2ORs (61; 59; 63; 62). It might be interesting to investigate if the chloride inhibition on the electron transfer from physiological electron donor to N_2OR is only observed in *Ac*N_2OR or not. If the other three N_2OR do not show the inhibition effect, these chlorides observed in

AcN_2OR will be suggested to be involved in the inhibition mechanism. As mentioned earlier, it was shown that the electron transfer reaction from cytochrome *c* to N_2OR in *Paracoccus pantotrophus* was perturbed by NaCl (75). Further investigation on the chloride inhibition is required on this N_2OR as well. Also, even though no bound chloride was observed on the Cu_A site in the crystal structure, it did not mean that there was no chloride on the Cu_A site. It is possible that loosely bound chloride, for which occupancy was low and undetectable by X-ray crystallography, might be on the Cu_A site.

Function of *Ac*NosX in the N_2OR Catalytic Cycle

The oxidation of *Ac*NosX during the N_2OR catalytic reaction was not observed (Figure 4.8). If *Ac*NosX could sustain the catalytic reaction, the time course of the absorption at 460 nm should look like the blue spectrum in Figure 4.11. However, such behavior was not observed. The result indicated that *Ac*NosX could not sustain the catalytic reaction. However, as described above, chloride ions in Buffer P inhibited the N_2OR catalytic cycle with *Ac*PAz (Figure 4.10, 4.11). This result brought up a possibility that *Ac*NosX was potentially able to sustain the N_2OR catalytic cycle but the chloride ions from the buffer interfered with the reaction. *Ac*NosX did donate electrons to *Ac*N_2OR when both proteins were mixed in a 1:1 ratio and in the presence of 150 mM NaCl (Figure 4.2). In addition, as described below, free reduced FAD could sustain the N_2OR catalytic cycle at least for a while (Figure 4.9). Therefore, it was likely that *Ac*NosX could sustain the catalytic reaction in the absence of chloride ions. However, even if *Ac*NosX would be able to sustain the catalytic reaction, it was hard to believe that this reaction was physiologically significant. Since the abundance of *Ac*NosX in the cell

was much smaller than *Ac*PAz and *Ac*N_2OR as previously described (91), the contribution of *Ac*NosX on the catalytic reaction as a direct electron donor is expected to be very small.

Free reduced FAD could support the N_2OR catalytic cycle for some period of time (Figure 4.9). However, the oxidation of FAD was stopped after 30 min. The reaction started again by addition of extra *Ac*N_2OR to the cuvette, but not by addition of extra substrate. When the sample was exposed to the air, FAD was further oxidized. These observations indicated that the termination of the catalytic reaction was to due to inhibition of the N_2OR activity, but not due to the lack of substrate (N_2O) or electron source (reduced FAD). Since such behavior was not observed when reduced BV was used as an electron source, free FAD was expected to cause the inhibition. The inhibition mechanism of the N_2OR activity by free FAD was still unknown. Since no chloride was added to the sample, this phenomenon was independent from the inhibition effects by chloride (Figure 4.11).

Stability of *Ac*NosX *in Vitro*

*Ac*NosX required both 150 mM NaCl in buffer and low temperature to be stable *in vitro* (Chapter 3). However, chloride ions were found to inhibit the N_2OR catalytic cycle with *Ac*PAz as an electron donor. This result indicates that chloride would also interrupt the N_2OR catalytic cycle with *Ac*NosX. Thus, it was required to remove chloride ions from the *Ac*NosX sample to measure the N_2OR catalytic cycle with *Ac*NosX. Further, as mentioned in chapter 2, high salt concentration also interrupted *Ac*NosX purification using an ion exchange column. To overcome these obstacles,

screenings for *Ac*NosX stabilization without chloride were carried out using a host of different reagents. Although spermine showed a stabilization effect on *Ac*NosX, it was revealed that FAD was ejected from *Ac*NosX when spermine was added to the sample (Figure 4.14). The pKa of spermine are 11.50, 10.95, 9.79 and 8.90. Thus, spermine is positively charged under the experimental conditions (pH 7.0). It was also indicated that the FAD binding pocket of *Ac*NosX was negatively charged (Figure 3.5). Therefore, it was possible that spermine tended to get into the FAD binding pocket and FAD was replaced with a spermine molecule. Suitable reagent for *Ac*NosX stabilization *in vitro* was not found.

Although *A. cycloclastes* grew at 30 °C, *Ac*NosX immediately precipitated at this temperature *in vitro*. This fact indicates that there should be certain protein(s) and/or small molecule(s) that stabilize *Ac*NosX *in vivo*. *Ac*NosX was shown to be a relatively hydrophobic protein (Figure 3.6). The existence of the large hydrophobic patch might be one of the reasons that *Ac*NosX was easily precipitated *in vitro* (Figure 3.6). In addition, NosR has been implied to be the redox partner of NosX (52; 83). Since NosR is a membrane bound protein, this hydrophobic patch on *Ac*NosX might be important for stabilizing the protein-protein interaction with NosR because NosX needs to get close to the hydrophobic membrane surface to interact with NosR. In other words, NosR would be a strong candidate to stabilize NosX *in vivo*.

Substrate Bound N_2OR Structure from *Pseudomonas stutzeri*

New Hypothesis on the Electron Transfer from Cu_A to Cu_Z.

As described in chapter 1, the structure of N_2OR from *Pseudomonas stutzeri* was recently determined (63). The electron transfer from Cu_A (250 mV) to Cu_Z (60 mV) in N_2OR is thermo-dynamically unfavorable and the mechanism that permits the electron transfer *in vivo* has been unknown (83). The substrate bound structure of N_2OR from *Pseudomonas stutzeri* implied that the substrate received electron(s) directly from the Cu_A site, instead of receiving two electrons from the Cu_Z site as it has been expected and described in Figure 1.9 (71; 7). This hypothesis can explain our observation that *Ac*PAz was able to sustain the N_2OR catalytic cycle (91) even though *Ac*PAz could not donate electrons to the Cu_Z site *in vitro* (Figure 4.3). If the substrate on the Cu_Z site can receive electrons directly from the Cu_A site, *Ac*PAz might be able to sustain the catalytic cycle by donating electrons via the Cu_A site. However, it was also observed that the N_2OR activity was directly correlated with the degree of reduction on the Cu_Z site (70). Also, the Cu_Z site was obviously oxidized when the fully reduced N_2OR was reacted with the substrate (77). These data indicated that reduction of the Cu_Z site was still important for the catalytic reaction and the Cu_Z site was oxidized during the catalytic reaction.

Another possibility of the mechanism that enables the electron transfer from the Cu_A to the Cu_Z site is that the substrate binding to the Cu_Z site alters the redox potential of the site. Our observation that *Ac*PAz could sustain the N_2OR catalytic cycle can be interpreted as *Ac*PAz could donate electrons to the Cu_Z site only in the presence of N_2O.

This hypothesis is supported by the fact that the redox potential of the active center in CuNiR from *Pseudomonas chlororaphis* was tuned with the substrate (NO_2^-) binding to receive electrons (29).

New Definition of the Cu_Z* State. The structure of N_2OR from *Pseudomonas stutzeri* showed an unprecedented Cu_Z structure that included two sulfide ions (Figure 1.10). Based on the structure, it was hypothesized that the [4Cu:2S] form was the Cu_Z state and the [4Cu:1S] form was the Cu_Z* state (63). In *Ac*N_2OR, however, no correlation between the N_2OR activity and the sulfide content of the sample was observed, although a positive correlation between the N_2OR activity and the Cu content was clearly observed (Appendix D; Figure S4.3). The observation indicated that the 2nd sulfide was not involved in the catalytic reaction using reduced BV as an electron source, or *Ac*N_2OR intrinsically does not have the 2nd sulfide in the Cu_Z site. In addition, the Cu_Z* state of N_2OR from *M. hydrocarbonoclasticus* can be fully restored to the active Cu_Z state by incubation with reduced MV (84), which is unlikely to related with a reaction from [4Cu:1S] (Cu_Z*) to [4Cu:2S] (Cu_Z). Further, this N_2OR is relatively active even under O_2, which conflicts with the fact the 2nd sulfur is extremely oxygen sensitive (84; 63). Therefore, to date, the relationship among [4Cu:2S] form, the Cu_Z/Cu_Z* states, and the N_2OR activity are still controversial. Further studies to investigate the presence of the 2nd sulfide in N_2OR from the other species and N_2O reduction mechanism by DFT calculation on the structure will be required.

Conclusions

The function of *Ac*NosX on *Ac*N_2OR was investigated *in vitro*. It was observed that *Ac*NosX could reduce both the Cu_A and Cu_Z sites of *Ac*N_2OR whereas *Ac*PAz reduced only the Cu_A site. This observation was consistent with the relative redox potentials of *Ac*NosX (-230 mV), *Ac*PAz (260 mV), and *Ac*N_2OR (250 mV for the Cu_A and 60 mV for the Cu_Z). *Ac*NosX was expected to facilitate the electron transfer from Cu_A to Cu_Z, which was thermodynamically unfavorable. *Ac*NosX was also shown to donate electrons to *Ac*PAz. It is still unclear whether this electron transfer pathway is physiologically significant. Further, the question of whether *Ac*NosX is able to sustain the N_2OR catalytic cycle was investigated. However, it was found that chloride ion that was essential to stabilize *Ac*NosX *in vitro* inhibited the N_2OR catalytic cycle in the presence of N_2O. Satisfactory replacements for NaCl in *Ac*NosX stabilization could not be identified. Thus, the N_2OR catalytic cycle with *Ac*NosX could not be monitored. However, *Ac*NosX was expected to sustain the N_2OR catalytic cycle because free FAD could do so. Free FAD also showed an inhibition effect on the catalytic reaction. It was possible that *Ac*NosX structure was important scaffold to avoid this inhibition during electron transfer from FAD in *Ac*NosX to *Ac*N_2OR. The regeneration of the Cu_Z* state in *Ac*N_2OR with *Ac*NosX *in vitro* failed. If the new definition of the Cu_Z* state ([4Cu:1S] form) which was proposed recently by Pomowski *et al*. could be applied to *Ac*N_2OR, it implies that the regeneration of the Cu_Z* state with *Ac*NosX by itself was improbable because NosX was not involved in the construction of the Cu_Z site and unlikely to

reconstitute the Cu_Z site. In addition, even if it would be possible, *Ac*NosX would require a sulfide source to re-construct the [4Cu:2S] form.

In conclusion, these investigations support in part the hypothesis that *Ac*NosX donates electrons to *Ac*N_2OR to activate the catalytic center (Cu_Z site). Another hypothesis that *Ac*NosX donates electrons to *Ac*N_2OR to regenerate the inactive Cu_Z* state to the catalytically active Cu_Z state requires further investigation.

CHAPTER 5

CO-CRYSTALLIZATION OF N_2OR AND PSEUDOAZURIN FROM *ACHROMOBACTER CYCLOCLASTES*

Introduction

Pseudoazurin (PAz) works as an electron shuttle among several different proteins in the denitrification system (87). PAz has been observed to donate electrons to several reductases such as cd_1NiR in *Paracoccus pantotrophus* (158), CuNiR in *A. cycloclastes* (159) (Figure 1.3), NOR in *Paracoccus denitrificans* (89), and N_2OR in *Paracoccus pantotrophus* (90). We also showed that PAz from *A. cycloclastes* (*Ac*PAz) could donate electrons to N_2OR from *A. cycloclastes* (*Ac*N_2OR) (Figure 4.2) (91). Although these reductases are structurally different from one another, PAz can donate electrons to the reductases through a pseudo-specific interaction (87). The pseudo-specific interaction between redox proteins was mainly characterized by promiscuous docking motifs based on a hydrophobic patch and surrounding positive/negative amino acids (87). Since hydrophobic interaction is less specific and less directional than the interactions with hydrogen bonds, several proteins that have the docking motifs can interact by the pseudo-specific interaction without any particular structure (87).

Co-crystallization of several proteins is a good way to investigate a binding mode of the proteins in a complex (160). Recently, CuNiR and cytochrome c_{551} from *Achromobacter xylosoxidans* were co-crystallized and a docking structure of the two proteins was solved (161). The structure showed the electron transfer pathway from

cytochrome c_{551} to CuNiR. Although there is no report on the co-crystal of N_2OR and its electron donors (PAz and cytochrome *c*), docking structures of N_2OR and the electron donors have been studied by calculations *in silico* using structures of N_2OR and PAz/cytochrome *c* (92; 150; 93). Possible docking structures of *Ac*N_2OR and *Ac*PAz for electron transfer and several possible electron transfer pathways from the Cu center of *Ac*PAz to the Cu_A site of *Ac*N_2OR were also calculated in our lab (Figure 1.13) (91). However, as of today, there has been no experimental data that confirms the calculated docking structures of N_2OR and the electron donors. It is essential to reveal how *Ac*N_2OR and *Ac*PAz form the transient complex for electron transfer to fully understand the N_2OR catalytic mechanism.

Crosslink of proteins in a crystal helps to solve its structure with X-ray analysis, especially when the proteins in the crystal tended to be out of alignment (162; 163; 164). The interactions between electron donor and acceptor proteins are usually very weak (87). Additionally, DFT calculations indicated that there were several possible binding geometries between electron donor and acceptor (92). These reports suggested that electron transfer proteins in a co-crystal might be disordered. Indeed, X-ray measurements of co-crystals for cytochrome *c* peroxidase and cytochrome *c* could not show the electron density of cytochrome *c* since the cytochrome *c* molecules were disordered in the co-crystals (165). In such a case, the crosslink technique might fix the alignment of the cytochrome *c* molecules in the co-crystals. This can happen to the co-crystal of *Ac*N_2OR and *Ac*PAz as well, and the cross-link technique might stabilize crystals to be prepared.

In this chapter, co-crystallization trials for *Ac*N_2OR and *Ac*PAz are described. Specifically, the co-crystallization of *Ac*N_2OR and *Ac*PAz was attempted to determine the docking structure that suggests the electron transfer pathway from *Ac*PAz to *Ac*N_2OR. Also, the crosslink conditions for *Ac*N_2OR and *Ac*PAz were investigated.

Materials and Methods

Screening of Crystallization Conditions

Protein solutions were prepared as 10 mg/mL (*Ac*N_2OR = 8.35 mg (128.5 µM), *Ac*PAz = 1.67 mg (128.5 µM)) in 10 mM Tris (pH 8.0). The protein solution was prepared in the largest amount possible at one time, and was aliquoted to 55 µL per tube and frozen at -80 °C for further use. High throughput screening for *Ac*N_2OR-*Ac*PAz co-crystallization was carried out with an automated screening robot Honeybee961 (Digilab) using 960 screening reagents (96 reagents × 10 plates, Hampton Research and Emerald BioSystems, Inc.). 0.4 µL of protein solution was mixed with the same amount of each crystallization solution per spot. The screening plates were prepared with the sitting drop method and kept at 22 °C. The conditions of the spots that showed crystals were selected for further optimizations.

Optimization of Crystallization Conditions

The conditions were optimized to obtain bigger crystals by changing buffer pH, incubation temperature, and concentrations of buffer, salt, and precipitant, respectively. 2 µL of protein stock was mixed with the same amount of crystallization solution and the hanging drop method was used. The amount of reservoir was 1 mL (24 holes in a plate).

For optimization of condition #1 (Table 5.1, 100 mM Tris (pH 8.5), 200 mM lithium sulfate, and 30 % PEG 4000), PEG concentration was changed between 20.5 and 35.0 % in increments of 0.5 %, lithium sulfate concentration was changed between 50 and 350 mM in increments of 50 mM, protein amount was changed between 10 and 4 mg/mL in increments of 1 mg/mL, and at the last step of optimization, additive screening reagents (48 conditions, Hampton Research) were added to the modified condition above. In each spot, 2 µL of protein solution, 1.6 µL of crystallization solution, and 0.4 µL of additive screen reagent were mixed on a coverslip. The plates were incubated at 22 °C and checked with a microscope once a week. For optimization of condition #3 (Table 5.1, 50 mM Bis-Tris propane (pH 5.0), 50 mM citric acid, and 16 % PEG 3350), PEG concentration was changed between 5.0 and 19.0 % in increments of 1.0 %, and pH was changed between 4.5 and 7.0 in increments of 0.5. Optimization of condition #4 (Table 5.1, 100 mM Bis-Tris (pH 6.5), and 20 % PEG monomethylether (mme) 5000) was carried out by changing PEG concentration (10.0 – 35.0 %), pH (5.0 – 8.5), additive screen, temperature (22, 18, or 4 °C), and the micro-seeding method. The crystal for the micro-seeding was obtained from the initial screening plate.

Crystal Check for Protein or Salt

To confirm whether the obtained crystals were made of proteins or salt, the crystals were checked with Izit Crystal Dye (Hampton Research) that specifically dyes protein crystals in blue, and SDS-PAGE. 1 µL of Izit Crystal Dye was added to the crystallization droplet with crystals in condition #4 (Table 5.1). The plate was incubated overnight and color change of the crystals was monitored under a microscope. After the

stained crystals were photographed, the crystals were used for SDS-PAGE samples. The stained crystals were scooped with a cryo-loop from the crystallization droplet under the microscope. The crystals were rinsed with freshly prepared crystallization solution (condition #4) several times and solved in 10 µL of water for SDS-PAGE. As a control, the crystallization droplet was scooped with the cryo-loop and the solution within the loop was diluted with the same manner that the crystals were rinsed. The solution was also diluted with 10 µL of water for SDS-PAGE. The crystals from condition #1 (Table 5.1) were also checked with SDS-PAGE after washing the crystals with the crystallization solution (condition #1).

X-ray Measurements of the Co-crystals

The obtained crystals were screened and measured at MSU and Stanford Synchrotron Radiation Lightsource (SSRL). A needle-like crystal (30 × 30 × 500 µm) that was obtained from modified condition #1 (100 mM Tris, 200 mM Lithium sulfate, 24.0 % PEG4000, pH 8.5) was measured with the home source X-ray beam at MSU to see if the crystal showed diffraction patterns. The crystal was scooped with a cryo-loop and frozen with liquid nitrogen immediately. Since condition #1 solution worked as a cryo-protectant, no glycerol was added to the solution prior to crystal freezing. The crystal was measured at 0 ° and 90 ° for 20 min each and 8 hours each at -196 °C.

Several crystals obtained from condition #3 (PEG concentration was modified to 12.0 %, rod shaped crystals, 30 × 30 × 100 µm) and #4 (hexagonal column shaped crystals, 50 × 50 × 50 µm, obtained from the initial screening plate) were incubated in cryo-protectant solutions (crystallization solution with 10 % glycerol) for 0.5 ~ 1 min to

introduce glycerol into the crystals. The crystals were frozen with liquid nitrogen immediately and screened at SSRL (Beam Line 11-1) at 0 °, -45 °, and 90 ° for 10 sec each to see if the crystals showed diffraction patterns.

Crystals from optimized condition #4 (20.0 ~ 21.0 % PEG mme 5000 with micro-seeding) were frozen in the presence of 10 % glycerol. The crystal size was about 100 × 100 × 100 µm, and the crystal shape was a hexagonal column. The crystals were screened as described above at SSRL, and the crystal that showed the highest resolution was selected for data collection for structural analysis. Diffraction patterns from the crystal were obtained from 270 ° to 370 ° in increments of 0.5 °. The data set was analyzed with HKL2000 (HKL Research).

Crystals that were obtained from the optimized condition #4 with micro-seeding were frozen in the presence of either 15 or 20 % MPD (2-methyl 2,4-penatnediol), 15 or 20 % PEG400, and 15 or 20 % glycerol to find optimal cryo-protectant and concentration for the crystal freezing process. The frozen crystals were screened at SSRL and the data set from the crystal that showed the best data quality was obtained from 0 ° to 360 ° in increments of 0.25 ° with 15 sec exposure per flame. The data set was analyzed with HKL2000.

Crystals from the optimized condition #4 with micro-seeding were incubated in the cryo-protectant solution (crystallization solution with 20.0 % glycerol) for overnight before freezing them to improve the mosaicity. The crystallization drops on coverslips were moved from reservoirs with the original crystallization condition (20.0 % PEG mme 5000) to one with 30.0 % PEG mme 5000, and further moved to one with 30.0 % PEG

mme 5000 + 20 % glycerol in a stepwise manner. At each step, the crystals on the plate were incubated for 24 hours to equilibrate the crystallization drops to the condition in the reservoir. This process was called dehydration and it was expected to improve the crystal diffraction as well (162). After the crystallization solutions were equilibrated to the condition that corresponded to 30.0 % PEG mme 5000 + 20 % glycerol, the crystals in the droplets were moved to freshly prepared cryo-protectant solution (100 mM Bis-Tris, 30.0 % PEG mme 5000, 20.0 % glycerol, pH 6.5) and incubated overnight. When the crystals were frozen with liquid nitrogen, an evaporated nitrogen gas layer upon the liquid nitrogen surface was removed by blowing N_2 gas from 30 cm above. This process was reported to alleviate crystal degradation when it was frozen (166). For comparison, several other crystals from the optimized condition #4 with micro-seeding were incubated in the cryoprotectant solution for a few minutes and were also frozen with the same procedure. The crystals were screened at SSRL as described above.

Crosslink of *Ac*N_2OR and *Ac*PAz

EDC (1-Ethyl-3-[3-dimethylaminopropyl] carbodiimide hydrochloride, Thermo) reacts with carboxyl group (Glu or Asp) of protein #1 and forms an amine-reactive *O*-acylisourea intermediate (167). NHS (N-hydroxysuccinimide, Thermo) stabilizes the activated intermediate in solution until it reacts with amine group (most often Lys) of protein #2 (167). The crosslink reaction occurs when the Glu/Asp of protein #1 and Lys of protein #2 interact with each other.

To obtain higher quality of co-crystals, a crosslink between *Ac*N_2OR and *Ac*PAz was attempted with EDC and NHS. The crosslink reaction was carried out under

anaerobic conditions in the glove box using Ar bubbled buffers. First, as a positive control experiment, both *Ac*N_2OR and *Ac*PAz were activated with EDC/NHS and crosslinked at the same time to confirm whether the crosslink reaction occurred. Also, the optimal ratio between [total protein] and [EDC] was examined. 32 µM *Ac*N_2OR and 162.4 µM *Ac*PAz ([*Ac*N_2OR]:[*Ac*PAz] = 1:5) in coupling buffer (10 mM Na_2HPO_4, 1.76 mM KH_2PO_4, 137 mM NaCl (pH 7.4)) was aliquoted in 7 tubes. Each sample was activated and crosslinked with different concentrations of EDC and NHS (the ratio between EDC and NHS was always 1:2.5) for 1 hour at room temperature. The concentration of EDC was changed as 0 mM (control), 0.2 mM (×1 of total protein concentration), 1 mM (×5), 2 mM (×10), 10 mM (×50), 20 mM (×100), and 100 mM (×500). The total volume of each sample was adjusted to 50 µL. The crosslinked protein was monitored with SDS-PAGE. The amounts of crosslinked protein in each condition were calculated with band intensities on the SDS-PAGE gel using Image J (168).

Second, *Ac*N_2OR or *Ac*PAz in activation buffer (100 mM MES, 500 mM NaCl (pH 6.0)) was individually activated in the presence of EDC/NHS ([total protein]:[EDC]:[NHS] = 1:10:25). After 1 hour, the activation reaction was stopped with an Amicon using YM-50 membrane (for *Ac*N_2OR) and a gel filtration column (for *Ac*PAz, since it was much faster than using the Amicon with YM-3 membrane) by removing the reagents. The sample buffer was exchanged to the coupling buffer at the same time. Then, the other protein (*Ac*PAz for activated *Ac*N_2OR, or *Ac*N_2OR for activated *Ac*PAz) was added for the crosslink reaction and the samples were incubated for 4 hours. The amounts

of crosslinked protein at 1, 2, 3, and 4 hours were estimated with SDS-PAGE and Image J as described above.

Third, the effect of NaCl on the crosslink reaction was elucidated by comparing efficiency of the crosslink reaction using the coupling buffer with or without NaCl. *Ac*N_2OR was activated in the activation buffer with EDC/NHS for 1 hour ([*Ac*N_2OR] = 5 nmol, [EDC] = 50 nmol, [NHS] = 125 nmol). After the reagents were removed with the Amicon, the buffer was exchanged with the coupling buffer with or without NaCl. 5-fold amount of *Ac*PAz (~ 25 nmol) was added to the activated *Ac*N_2OR and incubated it for 4 hours. The samples at 2, 3, and 4 hours were checked with SDS-PAGE. The crosslink efficiency was calculated with the band intensity of crosslinked *Ac*N_2OR-*Ac*PAz on the SDS-PAGE gel over the sum of band intensities of the proteins between 66.5 and 170 kDa.

Results

Screening and Optimizations of Crystallization Conditions

The conditions that showed crystals in the initial screening plates were selected and optimized with 24-hole plates. The selected conditions from the initial screenings were listed in Table 5.1.

#	Buffer (pH)		Salt		Precipitant	
1	100 mM	Tris (pH 8.5)	200 mM	Lithium Sulfate	30%	PEG 4000
2	100 mM	Sodium phosphate (pH 6.2)	200 mM	NaCl	35%	2-ethoxyethanol
3	50 mM	Bis-Tris propane (pH 5.0)	50 mM	Citric acid	16%	PEG 3350
4	100 mM	Bis-Tris (pH 6.5)	-	-	20%	PEG mme* 5000

* mme = monomethyl ether

Table 5.1. The initial crystallization conditions for *Ac*N_2OR-*Ac*PAz co-crystal

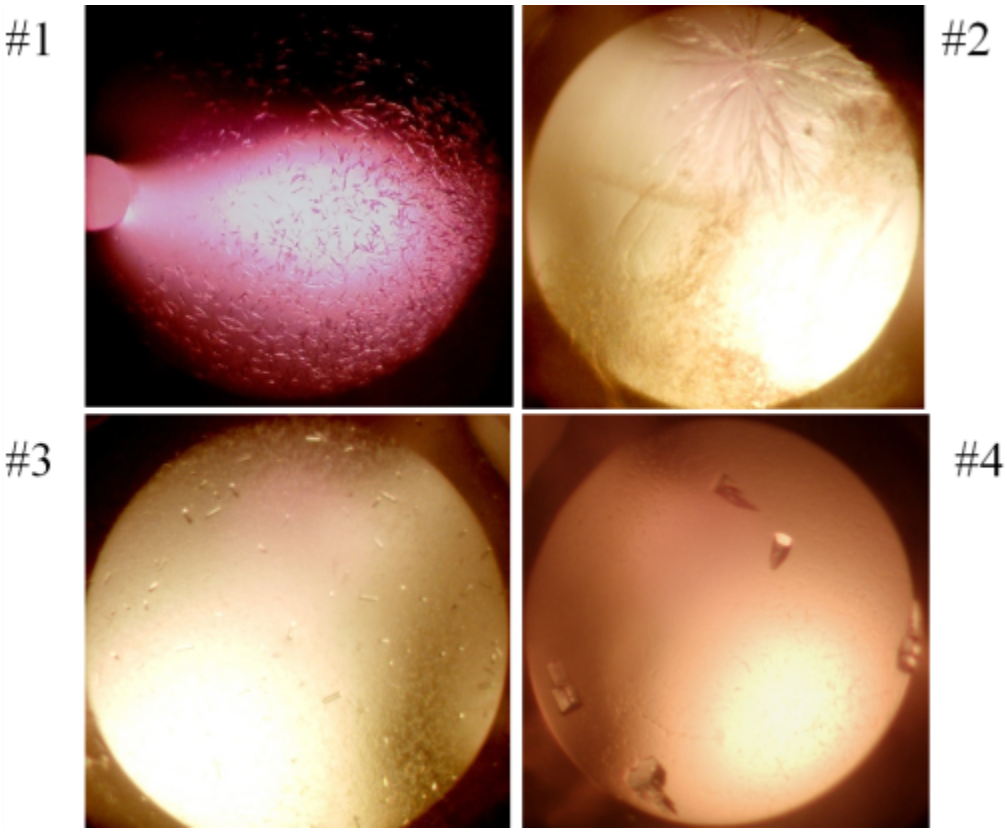


Figure 5.1. Crystals obtained from conditions #1 ~ 4

The initial conditions produced crystals that were shaped like needles (condition #1), branched needles (#2), rods (#3), and hexagonal columns (#4) (Figure 5.1). These crystals were observed at day 7 (#1), day 1 (#2), day 4 (#3), and day 68 (#4) in the initial screening plates. Conditions #1, 3, and 4 were further modified to obtain bigger and higher quality crystals for X-ray measurements. During optimization of condition #1, it was found that both PEG and lithium sulfate concentrations affected the crystal amount and shape. Protein amount affected the crystal growth speed. Additive screens did not show any apparent effect. Crystals were observed between 24.0 and 31.0 % PEG, and between 100 and 250 mM lithium sulfate. In lower concentrations of lithium sulfate (150

mM, 27.0 % PEG), the crystal shapes were feather-like structures (Figure 5.2, left), whereas the crystals became needle like structures in higher concentration of lithium sulfate (250 mM, 27.0 % PEG) (Figure 5.2, right).

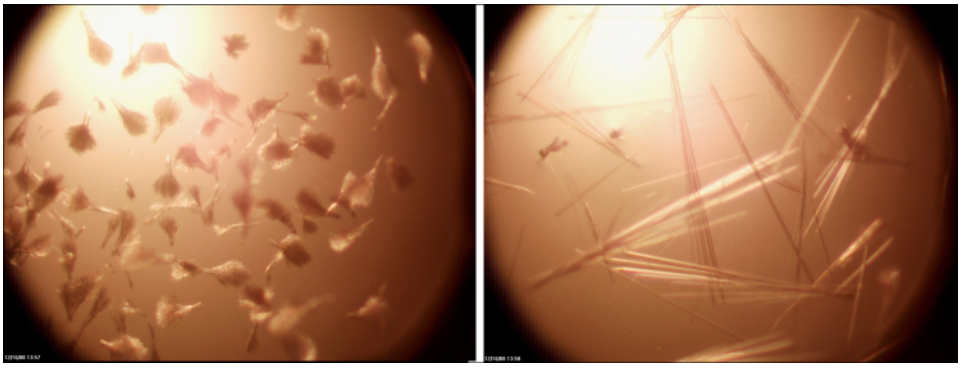


Figure 5.2. Crystal shape transition with 150 and 250 mM lithium sulfate (condition #1)

In optimization of condition #3, crystals were observed between 11 – 15 % PEG. Crystals at higher percentage of PEG (13 – 15 %) were dissolved over time. Changing pH conditions between 4.5 and 7.0 did not show any positive effect on crystal formation. The best condition to date was 50 mM Bis-Tris propane, 50 mM citric acid, 12.0 % PEG3350, pH 5.0 (Figure 5.3). The crystal size was 100 × 30 × 30 µm.

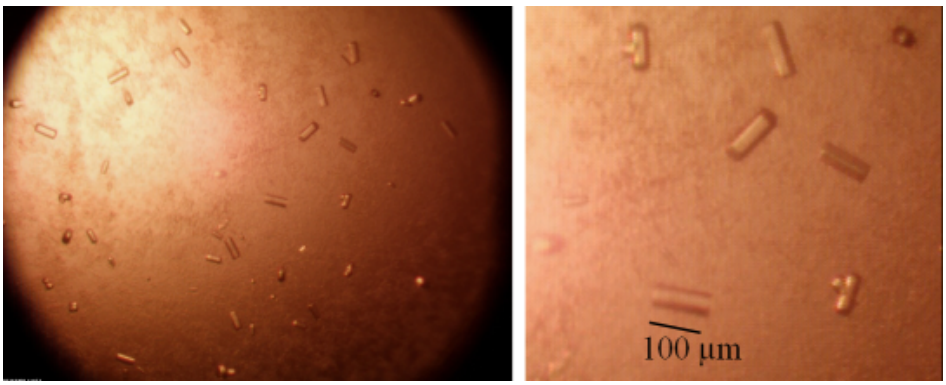


Figure 5.3. Crystals obtained from modified condition #3

In condition #4, the micro-seeding method significantly improved crystal formation. It was revealed that temperature (22 °C) was a critical factor for the crystal growth because the crystals were not observed at 18 and 4 °C. The biggest crystal (100 × 100 × 200 µm) was obtained from 100 mM Bis-Tris, 20.0 % PEG, pH 6.5, 22 °C with the micro-seeding method (Figure 5.4). Several crystals grew as polycrystals (Figure 5.4, left), which were also observed in the initial screening plates (Figure 5.1).

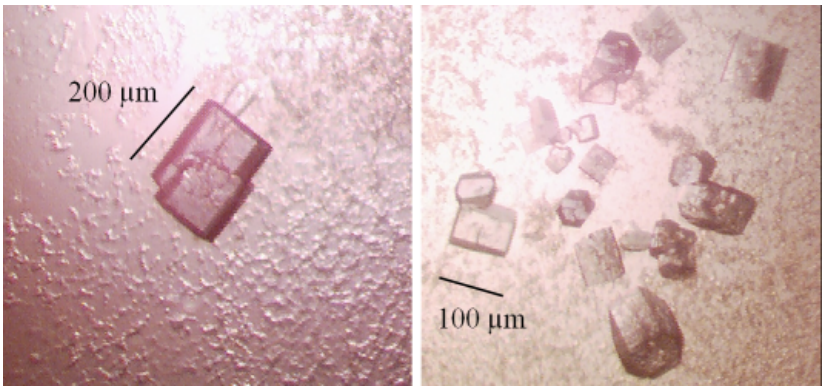


Figure 5.4. Crystals obtained from modified condition #4

Crystal Check for Protein

Salt in crystallization solutions sometimes aggregates as crystals. The crystals obtained from condition #4 were checked with Izit dye to confirm whether they were made of protein or salt. The Izit crystal dye turned the crystals blue, suggesting that the crystals were made of protein (Figure 5.1, and 5.5, left). The crystals from conditions #1 and 4 were also checked with SDS-PAGE to confirm they included both *Ac*N_2OR (66.5 kDa) and *Ac*PAz (13.0 kDa) (Figure 5.5, middle and right). “M” in Figure 5.5 indicates marker, “#1” and “#4” are the crystals from the condition # 1 and #4, “Pos” is a positive control (×20 diluted protein stock for crystallization), and “Neg” is a negative control that

shows the proteins around the crystals (#1 and #4) were completely rinsed out. The results confirmed that the crystals from conditions #1 and #4 were made of protein and included both *Ac*N_2OR and *Ac*PAz.

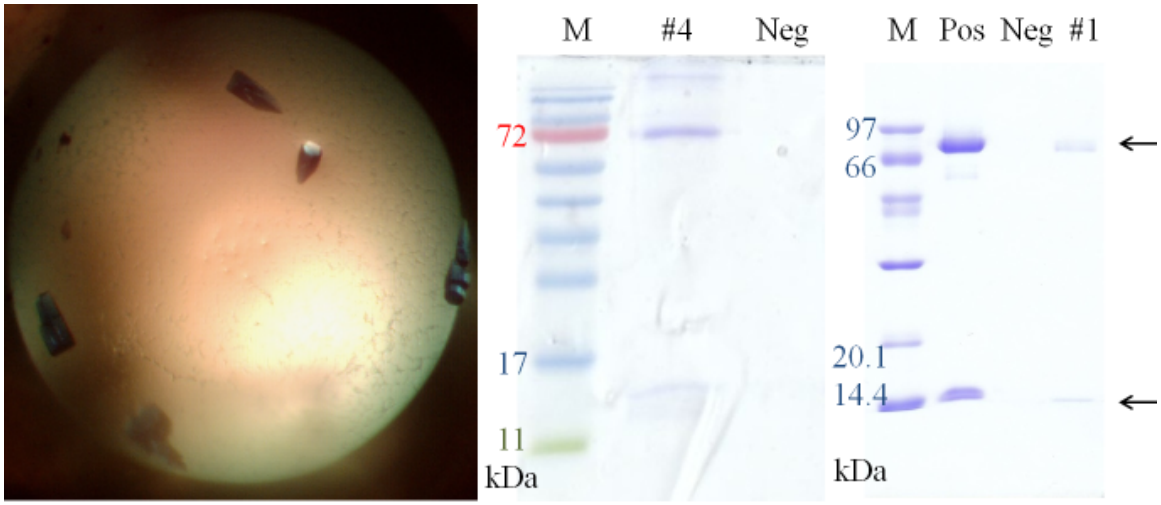


Figure 5.5. Crystal checks with the Izit dye and SDS-PAGE for condition #1 and #4

X-ray Measurements of the Co-crystals

A needle-like crystal (30 × 30 × 500 µm) from modified condition #1 did not show any diffraction pattern with a home source X-ray apparatus. Several crystals from condition #3 (rod shaped) and #4 (hexagonal column shaped) were screened at SSRL and showed some diffractions. A crystal from condition #3 showed some diffraction spots around ~ 18 Å, whereas several crystals from condition #4 showed ~ 4 Å resolution data. Preliminary analysis with the screening data from crystals in condition #4 showed the cell parameters as follows; a = 70.16 Å, b = 70.16 Å, c = 552.10 Å, α = 90.00 °, β = 90.00 °, γ = 120.00 °, mosaicity = 1.322 °. Structural analysis from the crystals could not be carried out because the resolution was too low and the mosaicity was too high, but the data

indicated that crystals from condition #4 were highly promising. Therefore, condition #4 was further optimized for the following measurements.

Crystals obtained from the optimized condition #4 were screened and measured at SSRL. The crystal that showed the best resolution (3.5 Å) in the screening was used for the following measurements and the data set obtained was analyzed with HKL2000. The cell parameters were almost the same as the previous preliminary measurement; a = 69.93 Å, b = 69.93 Å, c = 552.35 Å, α = 90.00 °, β = 90.00 °, γ = 120.00 °, mosaicity = 1.160 °. However, data index failed because of two reasons; (1) the crystal was a polycrystal and two different lattices were overlapped, which precluded further analyses of the data set, (2) the c axis of the cell unit was large (552.35 Å) and diffraction spots from c axis tended to overlap each other, which also hindered further analyses. It was required to obtain single crystals and to reduce mosaicity for further analysis.

To lower the mosaicity, several cryo-protectants (MPD, PEG400, and Glycerol) were applied to the crystal freezing process. Screening and data set collection were carried out at SSRL. The crystal that was incubated with glycerol showed the best mosaicity (0.6 °). The resolution of the data was 3.6 Å. Although the mosaicity had been improved, the data quality was not good enough for analysis and index failed.

Mosaicity usually increases when crystals are freezing. In the previous experiments, the crystals were incubated in the cryo-protectant solutions for 30 seconds to a few minutes prior to freezing. Prolonged cryo-protectant introduction to the crystals might lower the mosaicity. The crystals that were incubated in the cryoprotectant solution for a few minutes or overnight were screened at SSRL to investigate the effect of

incubation time with the cryoprotectant (Figure 5.6). The result showed that the overnight incubation made the diffraction spot shapes crooked (Figure 5.6, right), and the spot size became bigger (= mosaicity became bigger) than the diffraction from the crystals that were incubated for a few minutes (Figure 5.6, left). The analysis (index) of the data failed.

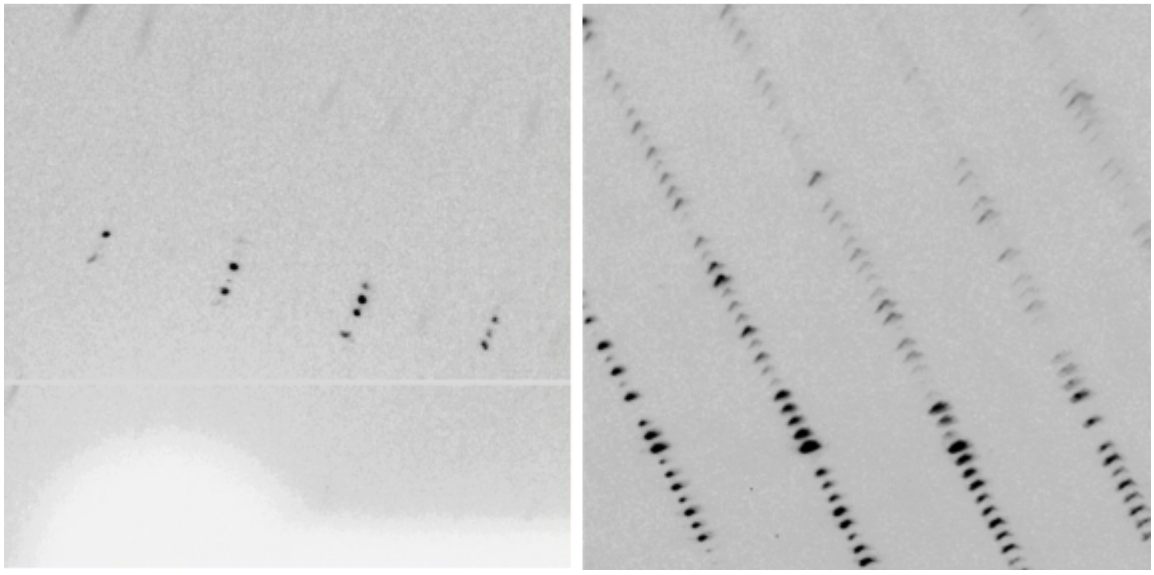


Figure 5.6. Diffractions from the crystals with flash (left) and overnight (right) introduction of cryoprotectant

For the structural analysis of the crystals from condition #4, the mosaicity needed to be less than 0.30 ° to obtain the structural information from the data set (Prof. C. Martin Lawrence, pers. commun.) since the crystals from condition #4 had a large cell unit (c = ~ 550 Å). To date, 0.60 ° was observed as the lowest mosaicity. The freezing condition needs to be further optimized to reduce the mosaicity. Alternatively, optimizations of the other conditions (#1, 2, and 3) might produce appropriate crystals for the structural analyses.

Crosslink of *Ac*N_2OR and *Ac*PAz

Crosslink between *Ac*N_2OR and *Ac*PAz with EDC/NHS was attempted to improve crystal quality. Since Asp and Glu on *Ac*N_2OR were expected to interact with Lys on *Ac*PAz during electron transfer (92; 87), this method was thought to be suitable for crosslink between *Ac*N_2OR and *Ac*PAz as an electron transfer complex. In a preliminary experiment, both *Ac*N_2OR and *Ac*PAz were activated and crosslinked at the same time in the presence of different concentrations of EDC and NHS (Figure 5.7). The crosslinked protein was observed on the SDS-PAGE gel as a 79.5 kDa band (*Ac*N_2OR 66.5 kDa + *Ac*PAz 13.0 kDa) and the band intensity did not increase after the ratio between [total protein] and [EDC] was 1 to 50, which indicated that 50-fold amount of EDC was sufficient to maximize the crosslink reaction.

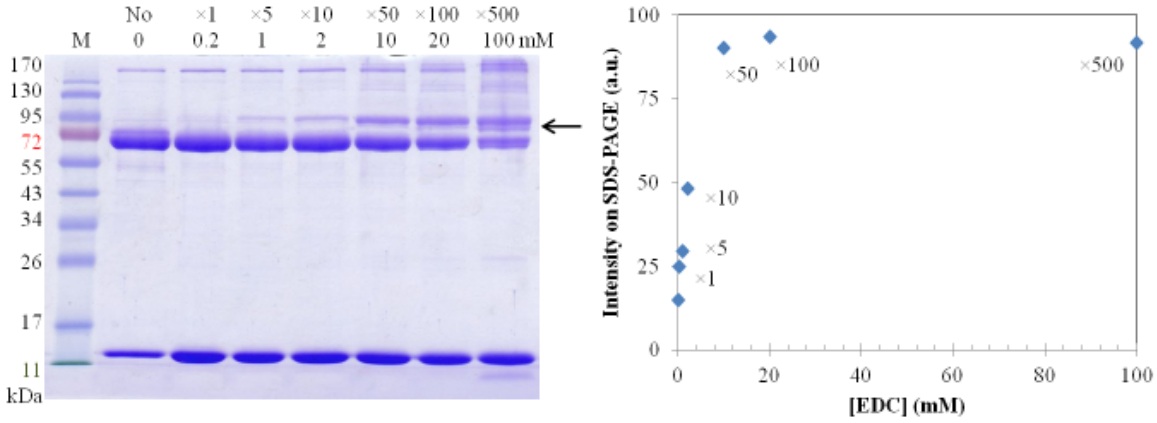


Figure 5.7. SDS-PAGE and band quantification for *Ac*N_2OR-*Ac*PAz crosslink

Either *Ac*N_2OR or *Ac*PAz was activated separately and crosslinked with the other protein (Figure 5.8). “Neg” in Figure 5.8 indicates non-crosslinked sample as a negative control, and “Pos” indicates the crosslinked sample from Figure 5.7 as a positive control.

The SDS-PAGE showed that the crosslink reaction between *Ac*N_2OR and *Ac*PAz occurred only when *Ac*N_2OR was activated. The incubation time (1 ~ 4 hours) did not affect the crosslinked protein yield since the band intensities among the samples did not show any difference (Figure 5.8, right, arrow). It suggested that the crosslink reaction finished within an hour.

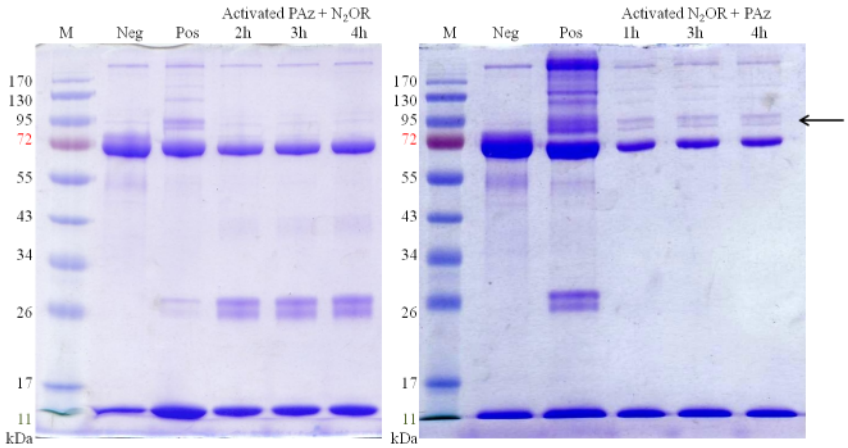


Figure 5.8. *Ac*N_2OR-*Ac*PAz crosslink with activated *Ac*PAz (left) or *Ac*N_2OR (right)

The crosslink efficiency was compared in the presence and absence of NaCl in the coupling buffer, and in terms of incubation times (2, 3, and 4 hours) (Figure 5.9). The crosslink efficiency was calculated with the band intensity of crosslinked protein at 79.5 kDa ("Crosslinked (C)" in Table 5.2) over the band intensities of the other *Ac*N_2OR related bands ("Total N_2OR (T)" in Table 5.2) including *Ac*N_2OR monomer (66.5 kDa), *Ac*N_2OR+*Ac*PAz (79.5 kDa), *Ac*N_2OR dimer (133 kDa), and the other unassigned bands between 66.5 and 170 kDa (Figure 5.9). The crosslink efficiencies of both conditions were calculated as ~ 33 % (Table 5.2). The result showed that NaCl (137 mM) in the coupling buffer had no affect on the crosslink reaction between *Ac*N_2OR and *Ac*PAz.

Also, elongated incubation time did not improve the efficiency as observed in the previous experiments.

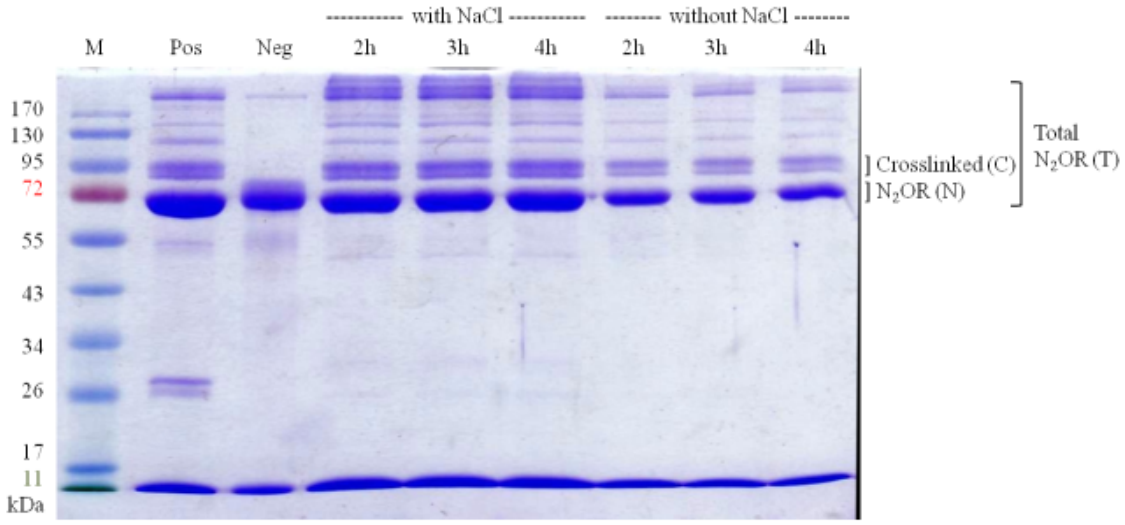


Figure 5.9. *Ac*N_2OR-*Ac*PAz crosslink in the coupling buffer with or without NaCl

		Band intensities on the SDS-PAGE gel (a.u.)			Crosslink Efficiency
NaCl	Lane	Crosslinked (C)	N_2OR (N)	Total N_2OR (T)	C/T
+	2h	100	162	306	33%
	3h	104	160	328	32%
	4h	107	164	333	32%
-	2h	60	100	175	34%
	3h	58	97	169	34%
	4h	54	80	162	33%

Table 5.2. Band intensities on the SDS-PAGE gel in Figure 5.9

Discussion

There is a lot of progress in co-crystallization of *Ac*N_2OR and *Ac*PAz although further optimizations will be required to obtain crystals suitable for structural

determination. To date, the best crystals were obtained from condition #4 (100 mM Bis-Tris (pH 6.5), and 20 % PEG monomethylether 5000). The first crystals in condition #4 appeared after more than 50 days following the initial screening plate preparation. Also, the micro-seeding method significantly improved the crystal formation. These results indicate that nucleation is the rate-limiting step for the crystallization (169).

The crosslink between *Ac*N_2OR and *Ac*PAz was observed only when *Ac*N_2OR was activated (Figure 5.8). The result indicated that Glu and/or Asp on *Ac*N_2OR were crosslinked to Lys on *Ac*PAz. These amino acids were expected to be involved in the formation of *Ac*N_2OR-*Ac*PAz complex for electron transfer (92; 87). Possible interaction sites of *Ac*N_2OR and *Ac*PAz for the electron transfer complex were shown in Figure 5.10 (91). *Ac*N_2OR has a hydrophobic patch close to the Cu_A site, which is surrounded with negatively charged amino acids (Asp and Glu), whereas *Ac*PAz has a hydrophobic patch around the Cu center and positively charged amino acids (Lys) are located around the patch (Figure 5.10). The colors on the *Ac*PAz and *Ac*N_2OR structures in Figure 5.10 indicate the Cu centers (in purple), the hydrophobic amino acids (in blue), the lysines on *Ac*PAz (in red), and the aspartic acids and glutamic acids on *Ac*N_2OR (in red). These hydrophobic patches (shown with orange circles in Figure 5.10) and the charged amino acids (red) were well conserved among species, suggesting that these sites were involved in the electron transfer complex formation (93). Since these Glu and/or Asp on *Ac*N_2OR (Glu331, 333, 588, Asp356, 384, 416 and 536) and Lys on *Ac*PAz (Lys38, 46, 57, 77 and 109) were expected to interact with one another in solution, one or several of these amino acids are candidates for crosslinking.

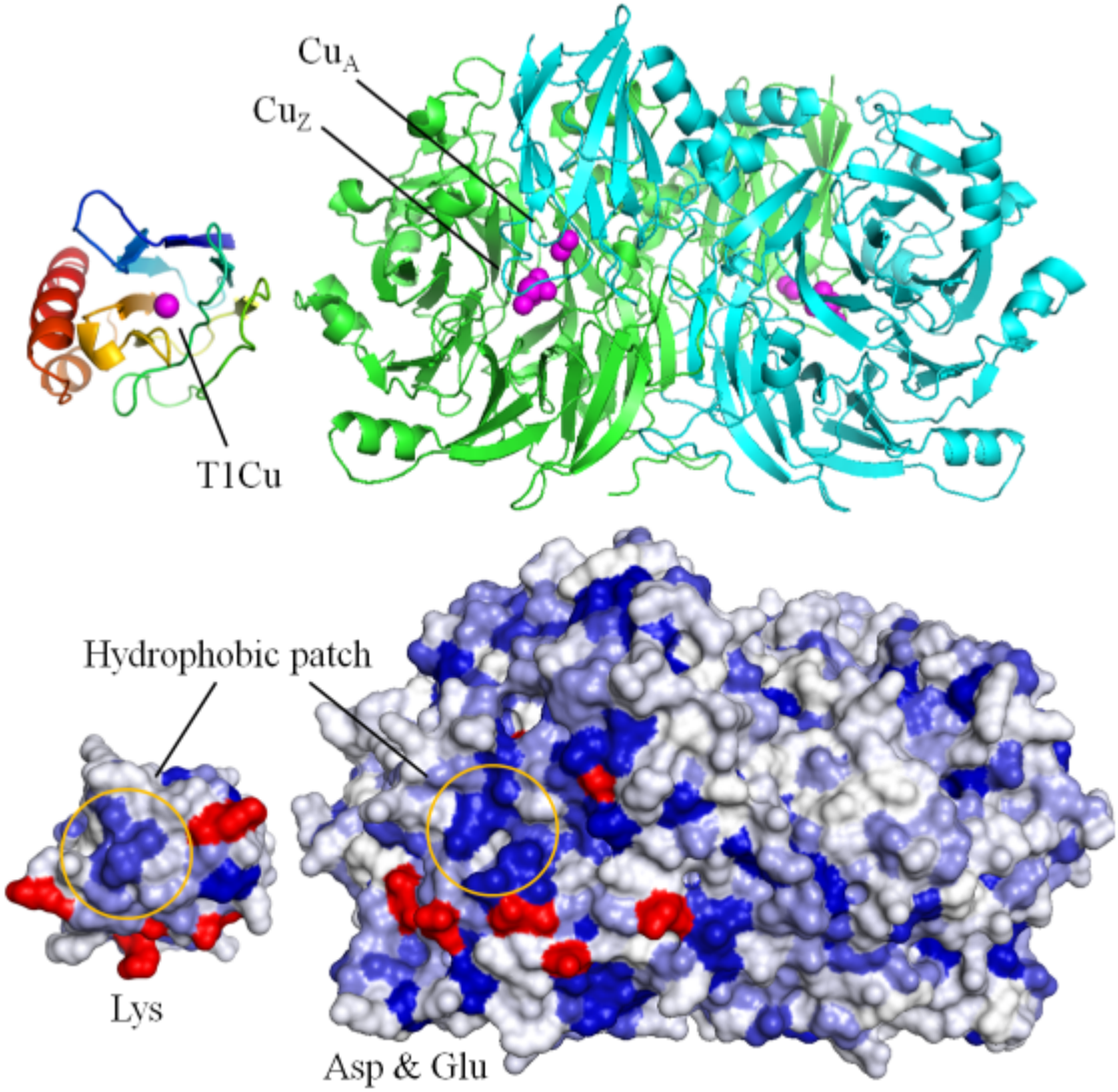


Figure 5.10. Expected crosslink sites of *Ac*PAz (left) and *Ac*N_2OR (right)

NaCl did not affect the crosslink reaction between *Ac*N_2OR and *Ac*PAz (Figure 5.9, Table 5.2). Since chloride ion was found to inhibit the N_2O reduction by *Ac*N_2OR using reduced *Ac*PAz as the electron source (Chapter 4), it was possible that NaCl interrupted formation of the *Ac*N_2OR-*Ac*PAz complex for electron transfer. If so, there would be a difference on the crosslink efficiency with or without NaCl. However, no

such difference was observed regardless of NaCl (Figure 5.9). The result suggested that the interaction between *Ac*N_2OR and *Ac*PAz in solution was not significantly perturbed by NaCl.

Conclusions

The objective of the studies on this chapter was to elucidate the docking structure of *Ac*N_2OR and *Ac*PAz. The *Ac*N_2OR-*Ac*PAz complex structure was investigated with co-crystallization and crosslink of two proteins. The conditions that grew co-crystals including *Ac*N_2OR and *Ac*PAz were successfully identified, although further optimizations for the crystal growth conditions and the freezing process were necessary for the structural analysis. The crosslink experiments suggested that Glu and/or Asp on *Ac*N_2OR interacted with Lys on *Ac*PAz in solution since the crosslink reaction was observed only when *Ac*N_2OR was activated. This observation was consistent with the results from the DFT calculation by Mattila e*t al* (92).

CHAPTER 6

CONCLUDING REMARKS AND FUTURE DIRECTIONS

The main objective of this project was to investigate the structure and function of *Ac*NosX. The results from this project form the basis for the study on NosX and the other Nos proteins, and provided some insights into the mechanism of the N_2OR activation. This research contributes to a field of the electron transfer reactions within the denitrification system.

Prior to the investigations, it was essential to increase the NosX yield since the expression level of NosX was very low and the following experiments required a substantial amount of *Ac*NosX protein. In chapter 2, the optimization of the culture conditions resulted in a great improvement in the NosX yield. It was found that the LB media that was purchased from Fisher brand significantly increased the NosX yield when pMLClustXst plasmid was used. The new expression systems did not show such effects with the LB media. The factor(s) in the LB media and the mechanism of the NosX yield enhancement need to be identified. Also, it would be interesting to monitor if the expression level of the other Nos proteins (NosR, NosD, NosF, NosY, and NosL) are enhanced by the LB media or not. These studies will reveal the regulation system for the *nos* gene expression. Another intriguing result in chapter 2 was that the NosX yield was constant under both aerobic and micro-aerobic conditions. The precise level of oxygen in the media during cultures and the effect of oxygen to the NosX expression should be further investigated.

It is still unclear why the new expression system did not enhance the NosX yield. Northern blot analyses for *nosX* transcripts in *Ac* (wild type), *Ac*/p5-(Np/Pp)-*nosX* and *Ac*/pMLClustXst will be required. Also, it would be a good idea to make a p5-Pp-*paz* plasmid to check if *Ac*PAz was overexpressed in *Ac*/p5-Pp-*paz* as a positive control.

The structure of *Ac*NosX was investigated in chapter 3. The calculated *Ac*NosX model showed several insights for the *Ac*NosX structure. Tyr46 was expected to be important for the FAD binding. This hypothesis needs to be investigated by a site directed mutagenesis. Also, a potential binding site with *Ac*N_2OR for electron transfer was suggested. To confirm if this site interacts with *Ac*N_2OR, a precise structure of *Ac*NosX with X-ray crystallography is required to calculate docking structures with *Ac*N_2OR. With respect to the crystallization trials for *Ac*NosX, further optimization of the conditions is required. Removing the strep-tag of *Ac*NosX with Factor Xa protease might facilitate the crystal growth of *Ac*NosX.

The interaction between *Ac*NosX and *Ac*N_2OR was investigated in chapter 4. The results indicated that *Ac*NosX activated *Ac*N_2OR by donating electrons, which supports the hypothesis by Wunsch *et al* (83). The next question is the function of NosX on the Cu_Z* state. Most importantly, it is essential to define the character and structure of the Cu_Z* state. As recently reported (63), it is required to prove whether the [4Cu:1S] state corresponds to the Cu_Z* state. It was reported that deletion of *nosX* gene resulted in increase of the population of the Cu_Z* state (83). Currently, there are two hypotheses on the function of NosX to explain this observation. First, NosX may be involved in the

regeneration of the Cu_Z* state. If this is the case, the conditions that NosX requires for the regeneration reaction should be identified. In our experiment *in vitro*, it failed (chapter 4). Second, NosX may prevent generation of the Cu_Z* state. In this case, it will be required to identify the process of generation of the Cu_Z* state. If we could monitor the generation process of the Cu_Z* state with or without reduced *Ac*NosX, it would show the effect of *Ac*NosX on the Cu_Z* state generation.

Stabilization of *Ac*NosX *in vitro* is another matter of concern. We could not find any reagent that substituted chloride to stabilize *Ac*NosX in solution. Since chloride inhibited the N_2OR catalytic reaction with *Ac*PAz, the catalytic reaction with *Ac*NosX also could not be measured. It is essential to find how to stabilize *Ac*NosX in solution without using chloride ion for further investigations on the electron transfer from *Ac*NosX to *Ac*N_2OR during the catalytic cycle.

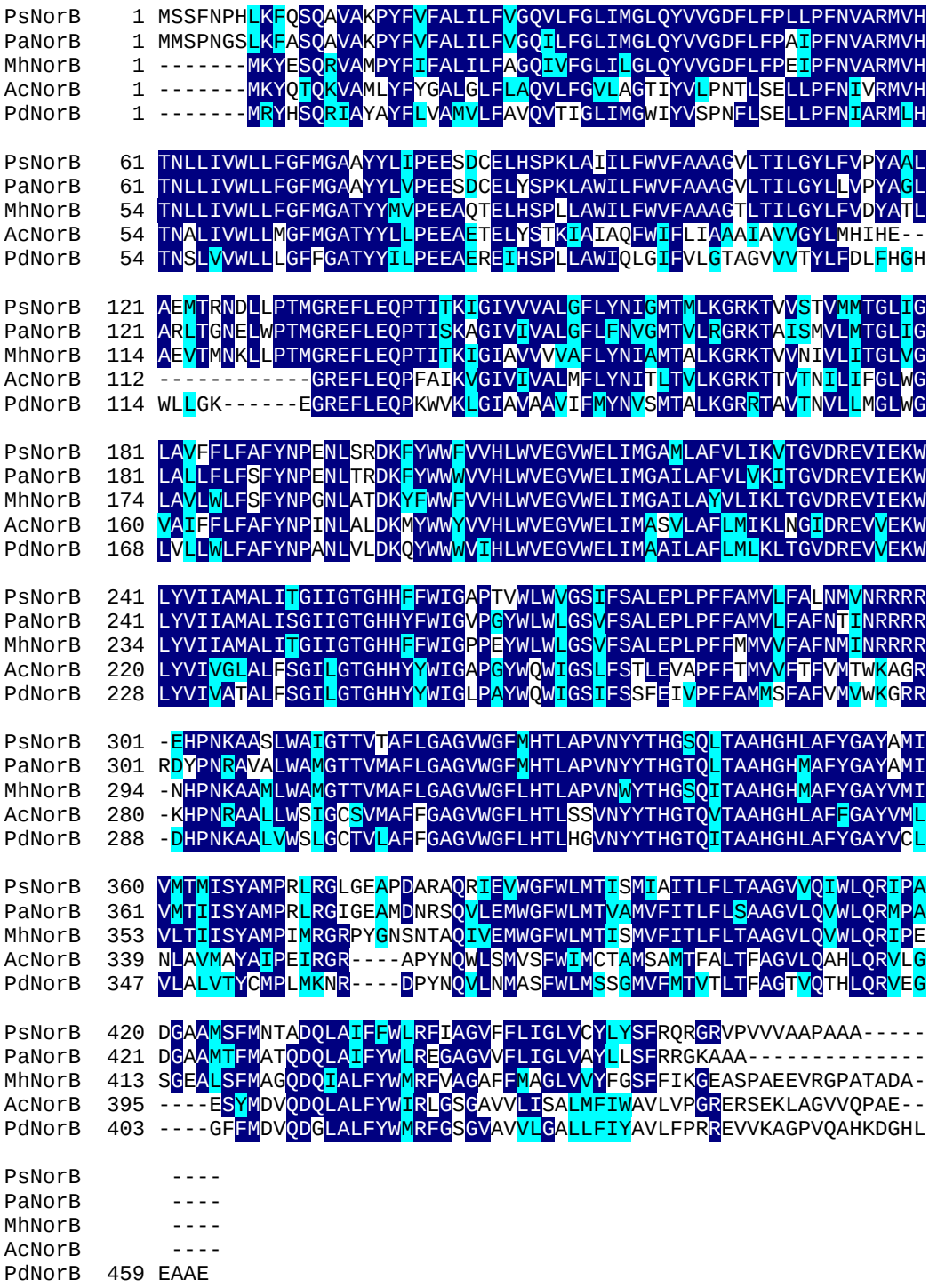
Co-crystallization of *Ac*N_2OR and *Ac*PAz was attempted in chapter 5. To solve the structure, the freezing condition of the crystals from condition #4 needs to be optimized to lower the mosaicity. Another option is the crystals from conditions #2 and 3. Since the optimization has been focused on the crystals from condition #4, there is room for improvement on the crystals from conditions #2 and 3 to solve the structure. Also, the crosslinked *Ac*N_2OR-*Ac*PAz complex needs to be crystallized under these conditions to see if the crosslink technique has some effects on the crystal quality. Alternatively, the crosslink reagents can be added to the crystals to crosslink the proteins in the crystals.

APPENDICES

APPENDIX A

SUPPORTING INFORMATION FOR CHAPTER 1

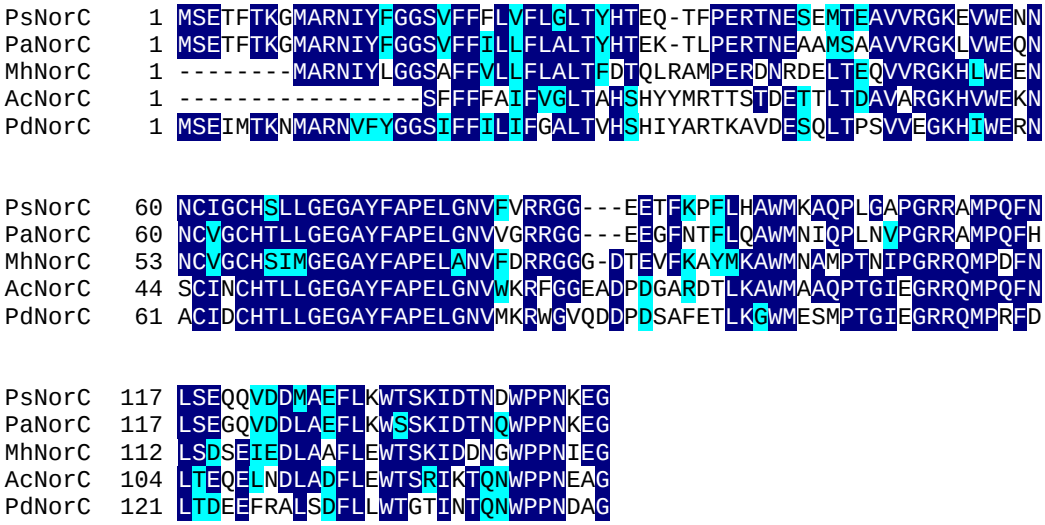
Figure S1.1. Multiple sequence alignment for NorB with CLUSTAL W 2.1 and BoxShade 3.21



Ps, *Pseudomonas stutzeri* (GenBank: CAA82229.1); Pa, *Pseudomonas aeruginosa* (GenBank: BAA07330.1); Mh, *Marinobacter hydrocarbonoclasticus* (GenBank:

CCG96517.1); Ac, *Achromobacter cycloclastes* (GenBank: CAC27381.1); Pd, *Paracoccus denitrificans* (GenBank: BAA32546.1)

Figure S1.2. Multiple sequence alignment for NorC with CLUSTAL W 2.11 and BoxShade 3.21



APPENDIX B

SUPPORTING INFORMATION FOR CHAPTER 2

Table S2.1. List of *Ac*NosX culture (*Ac*/pMLClustXst) and yield

Culture #	Date	Cell (g)	NosX (mg)	mg/10g	LB	Speed (rpm)	24 or 48 h	A_{600}	Riboflavin
1	5-14-08	30.6	0.46	0.15	RPI	120	24	N/A	-
2	5-16-08	29.1	0.37	0.13	RPI	120	24	N/A	-
3	5-19-08	37.2	0.18	0.05	RPI	120	24	N/A	-
4	5-30-08	26.7	0.12	0.04	RPI	120	24	N/A	-
5	6-02-09	25.8	0.13	0.05	RPI	120	24	N/A	-
6	6-09-08	27.4	0.12	0.04	RPI	100	24	N/A	-
7	6-12-08	22.4	-***	-	RPI	100	24	N/A	-
8	6-16-08	27.8	0.12	0.04	RPI	125	24	N/A	-
9	7-07-08	17.5	0.13	0.07	RPI	N/A	24	N/A	-
10	7-09-08	32.2	0.99	0.31	RPI	N/A	24	N/A	-
11	7-11-08	27.4	0.77	0.28	RPI	N/A	24	N/A	-
12	7-14-08	24.9	0.33	0.13	RPI	N/A	24	N/A	-
13	8-11-08	9.3	-***	-	RPI	110	24	N/A	-
14	8-14-08	24	0.37	0.15	RPI	110	24	N/A	-
15	10-20-08	22.1	0.09	0.04	RPI	50	24	2.2	-
16	10-30-08	15.7	0.00	0.00	RPI	50	24	0.3	-
17	7-6-09	22.1	0.07	0.06	RPI	N/A	24	N/A	-
18	7-10-09	25	0.04	0.02	RPI	120	24	N/A	-
19	8-17-09	23.2	0.17	0.07	RPI	N/A	24	1.0	-
20*	8-24-09	36.8	0.37	0.10	RPI	125	24	N/A	-
21**	8-31-09	31.0	0.40	0.13	RPI	125	24	N/A	-
22	9-7-09	25.6	2.79	1.09	Fisher	225	24	N/A	-
23	9-14-09	23.6	1.64	0.69	Fisher	125	24	N/A	75
24	9-22-09	26.8	1.62	0.60	Fisher	N/A	24	N/A	-
25	9-28-09	16.0	1.04	0.65	Fisher	125	24	N/A	-
26	10-5-09	24.2	1.02	0.42	Fisher	N/A	24	N/A	-
27	10-12-09	36.8	0.63	0.17	Fisher	100	24	N/A	-
28**	10-19-09	21.0	0.34	0.16	Fisher	N/A	24	N/A	-
29*	10-26-09	26.3	0.43	0.16	Fisher	125	24	N/A	-
30	11-02-09	16.0	0.73	0.46	Fisher	125	24	N/A	-
31	11-09-09	19.9	1.69	0.85	Fisher	125	24	N/A	-
32	11-16-09	18.9	1.02	0.54	Fisher	125	24	N/A	-
33	11-24-09	28.1	0.34	0.12	Fisher	125	24	N/A	-
34	11-30-09	16.9	0.64	0.38	Fisher	125	24	N/A	50
35	12-07-09	42.5	0.80	0.19	Fisher	125	24	N/A	40
36	12-14-09	43.8	0.92	0.21	Fisher	125	24	1.4	-
37	12-21-09	26.8	0.77	0.29	Fisher	100	24	1.4	-
38	12-28-09	25.4	0.61	0.24	Fisher	100	24	1.1	-
39	1-11-10	19.7	0.36	0.18	Fisher	100	24	1.2	-
40	1-18-10	32.0	0.79	0.25	Fisher	100	24	1.6	-
Culture #	Date	Cell (g)	NosX (mg)	mg/10g	LB	Speed (rpm)	24 or 48 h	A_{600}	Riboflavin

Ac*/p5-Np-nosX ***Ac*/p5-Pp-nosX * cell was used for N_2OR prep

Culture #	Date	Cell (g)	NosX (mg)	mg/10g	LB	Speed (rpm)	24 or 48 h	A_{600}	Riboflavin
41	1-26-10	43.4	0.86	0.20	Fisher	100	24	1.4	-
42	2-1-10	46.0	0.94	0.20	Fisher	100	24	N/A	-
43	2-8-10	40.0	0.81	0.20	Fisher	100	24	1.5	-
44	2-15-10	34.0	0.94	0.28	Fisher	100	24	1.5	50
45	2-22-10	26.8	0.5	0.19	Fisher	100	24	1.5	50
46	3-2-10	42.8	0.35	0.08	Fisher	100	24	1.5	-
47	3-8-10	36.0	1.14	0.32	Fisher	100	24	1.5	70
48	3-15-10	27.6	0.10	0.04	Fisher	0	24	1.5	100
49	3-22-10	25.9	0.17	0.07	Fisher	100	24	1.3	100
50	3-29-10	18.8	0.16	0.09	Fisher	N/A	24	1.1	50
51	4-5-10	21.9	0.22	0.10	Fisher	100	24	1.2	50
52	4-12-10	22.4	0.24	0.11	Fisher	100	24	1.4	50
53	4-19-10	24.3	0.13	0.05	Fisher	N/A	24	1.4	-
54	4-26-10	62.8	3.09	0.49	Fisher	250	24	1.8	-
55	4-30-10	73.6	1.77	0.24	Fisher	250	24	1.9	-
56	5-3-10	82.4	0.45	0.11	Fisher	250	24	1.3	-
57	5-17-10	83.5	0.83	0.10	Fisher	250	24	1.7	-
58	5-24-10	80.7	0.81	0.10	Fisher	250	24	0.9	-
59	6-7-10	65.4	0.25	0.04	Fisher	250	24	0.1	-
60	6-21-10	23.2	-***	-	Fisher	250	24	1.9	-
61	7-6-10	84.5	1.2	0.14	Fisher	250	24	N/A	-
62	7-19-10	73.2	1.34	0.18	Fisher	250	24	1.1	-
63	8-10-10	101.7	5.30	0.52	Fisher	250	48	1.3	-
64	8-17-10	107.2	3.64	0.34	Fisher	250	48	0.8	-
65	9-17-10	105.7	4.37	0.46	Fisher	250	48	1.8	-
66	9-27-10	106.8	2.54	0.24	Fisher	250	48	3.8	-
67	10-18-10	98.0	3.03	0.31	Fisher	250	48	3.0	-
68	12-13-10	94.1	2.10	0.22	Fisher	250	48	N/A	-
69	12-20-10	103.2	1.63	0.16	Fisher	250	48	N/A	-
70	3-1-11	94.8	0.60	0.06	Fisher	250	48	1.2	-
71	3-15-11	85.3	0.85	0.10	Fisher	250	48	2.6	-
72	4-4-11	80.9	2.14	0.26	Fisher	250	48	2.7	-
73	4-11-11	87.7	2.57	0.29	Fisher	250	48	1.1	-
74	4-18-11	80.3	1.6	0.50	Fisher	250	48	1.2	-
75	7-25-11	119.1	2.01	0.17	Fisher	250	48	1.4	-
76	8-1-11	83.6	2.42	0.29	Fisher	250	48	0.8	-
77	8-9-11	88.3	1.61	0.18	Fisher	250	48	0.8	-
78	8-16-11	77.1	3.21	0.42	Fisher	250	48	1.0	-
79	8-23-11	82.7	5.98	0.72	Fisher	250	48	1.0	-
80	9-6-11	80.1	4.78	0.60	Fisher	250	48	1.5	-
81	11-7-11	78.6	0.48	0.22	Fisher	250	48	N/A	-
82	12-16-11	84.9	1.39	0.16	Fisher	250	48	1.3	-
83	12-23-11	68.8	2.51	0.36	Fisher	250	48	0.9	-
84	1-9-12	67.6	4.89	0.72	Fisher	250	48	1.2	-
85	2-13-12				Fisher	250	48	0.9	-
Culture #	Date	Cell (g)	NosX (mg)	mg/10g	LB	Speed (rpm)	24 or 48 h	A_{600}	Riboflavin

APPENDIX C

SUPPORTING INFORMATION FOR CHAPTER 3

Figure S3.1. Surface electrostatic potential of ApbE protein from *Salmonella enterica*.

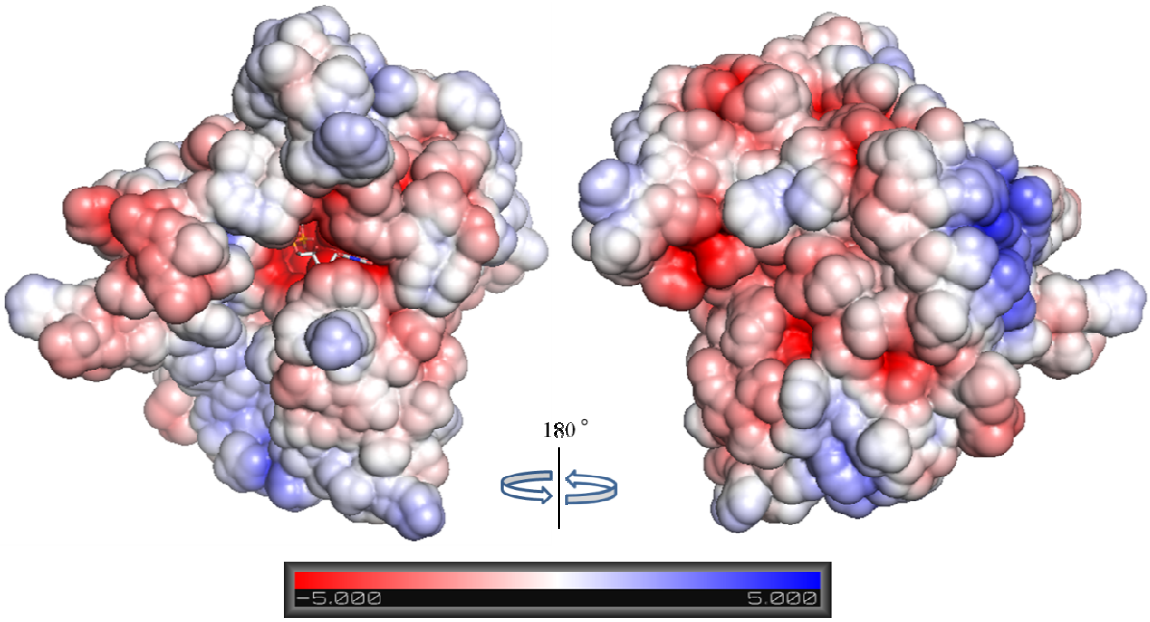
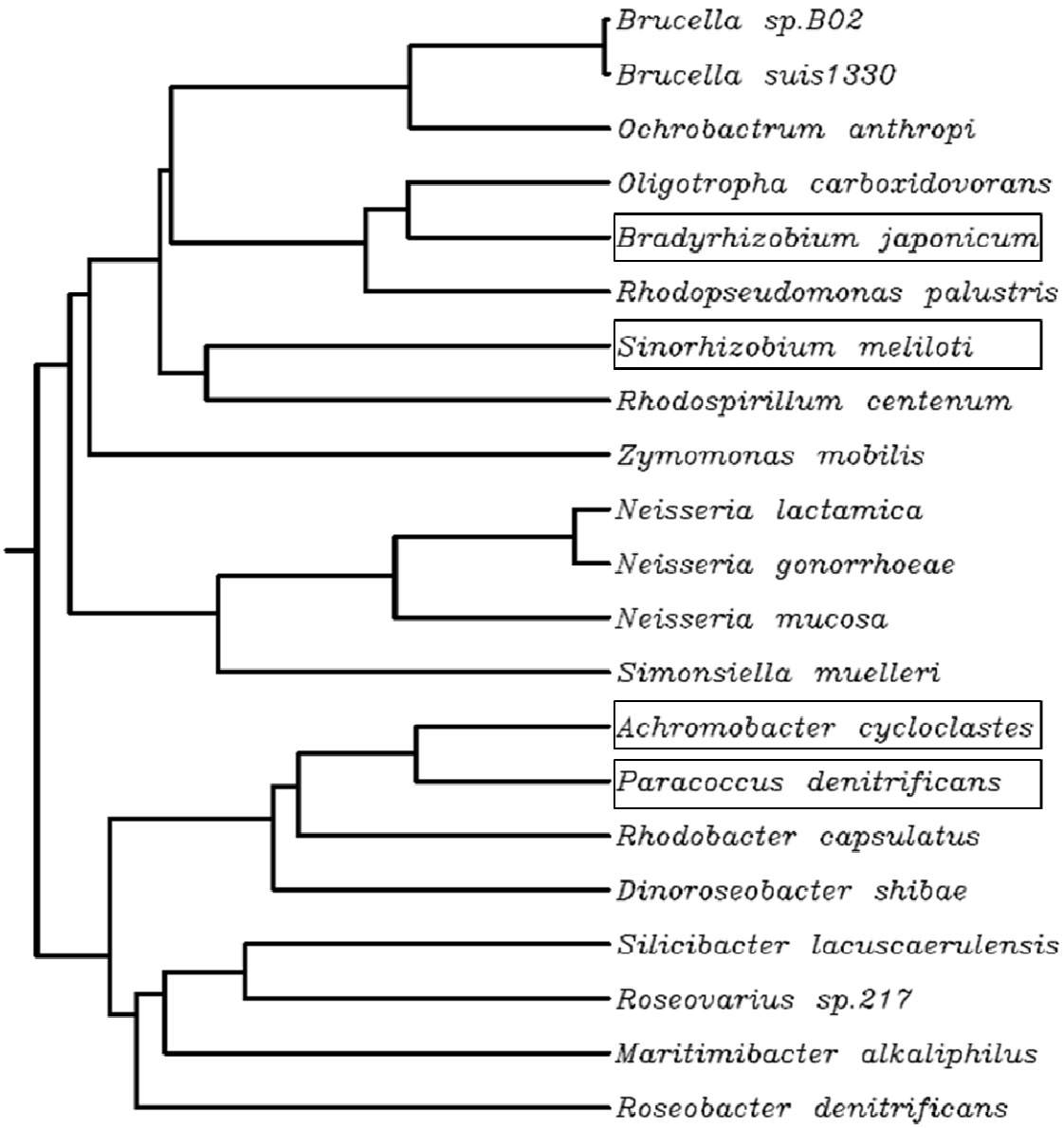


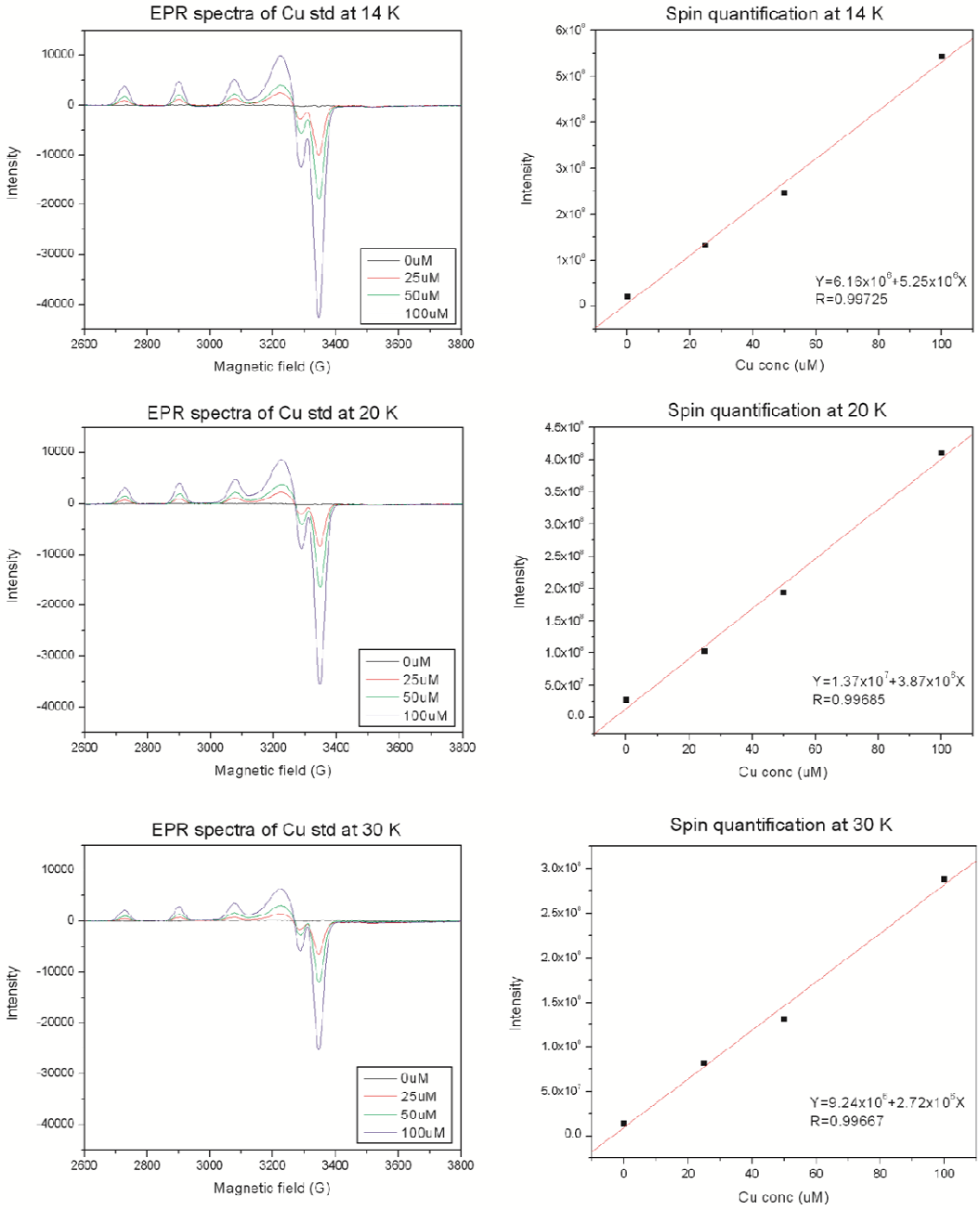
Figure S3.2. Phylogenetic tree based on NosX amino acid sequences.



APPENDIX D

SUPPORTING INFORMATION FOR CHAPTER 4

Figure S4.1. Cu standard curves for spin quantification at 14, 20, and 30 K.



N_2OR Oxidation with Ferricyanide and Cu Content Check with AA.

N_2OR oxidations with ferricyanide and buffer exchange were carried out in a glove box (O_2 < 5 ppm). The "As purified" form of N_2OR (300 µL) was aliquoted into two tubes (150 µL each). To oxidize N_2OR, 10, 45, or 100-fold excess amount of ferricyanide powder (ferri) was added to one sample (labeled as "oxidized (OX)"). The other sample was labeled as "as purified (AP)". 1 mL of 20mM Tris (pH8.0, bubbled with Ar for 1 hour) was added to both tubes. Both samples were centrifuged for 5 – 10 min at 4500 rpm with Amicon centrifuge tubes (YM-50 membrane). 1 mL of buffer was added and again centrifuged. This process was repeated for seven times. Cu amounts of concentrated N_2OR samples (AP and OX) and its corresponding flow-through (FT) were measured with AA and compared in terms of the ratio between [ferricyanide] and [N_2OR].

Analysis of Removed Cu amount from N_2OR.

The measured values of Cu concentrations are listed in Table S4.1. The removed Cu from N_2OR was calculated with a following equation;

$$\text{Removed Cu (\%)} = [\text{Cu}] \text{ in FT}/([\text{Cu}] \text{ in } N_2\text{OR} + [\text{Cu}] \text{ in FT})$$

A positive correlation was observed between the removed Cu from N_2OR and the ferricyanide amount (Figure S4.2). No Cu was detected in the ferricyanide solution (Table S4.1, Exp #4), indicating that the detected Cu in FT was derived from N_2OR.

Table S4.1. Cu concentrations in N_2OR (AP and OX) and flow-through

Exp #		[N_2OR]	[Ferricyanide]	Ratio [Ferri]/[N_2OR]	Cu in N_2OR	Cu in FT	Removed Cu (%)
1	AP	155	-	-	528.0	3.9	0.7%
	OX	155	1500	9.7	532.0	17.1	3.1%
2	AP	20.4	-	-	-	0.0	-
	OX	20.4	911	44.7	55.1	6.5	10.5%
3	AP	43.8	-	-	145.6	12.6	8.0%
	OX	43.8	4378	100	100.1	42.0	29.6%
4	-	-	2126	-	-	0	-

(nmol)

Figure S4.2. Correlation between removed [Cu] from N_2OR and [ferricyanide].

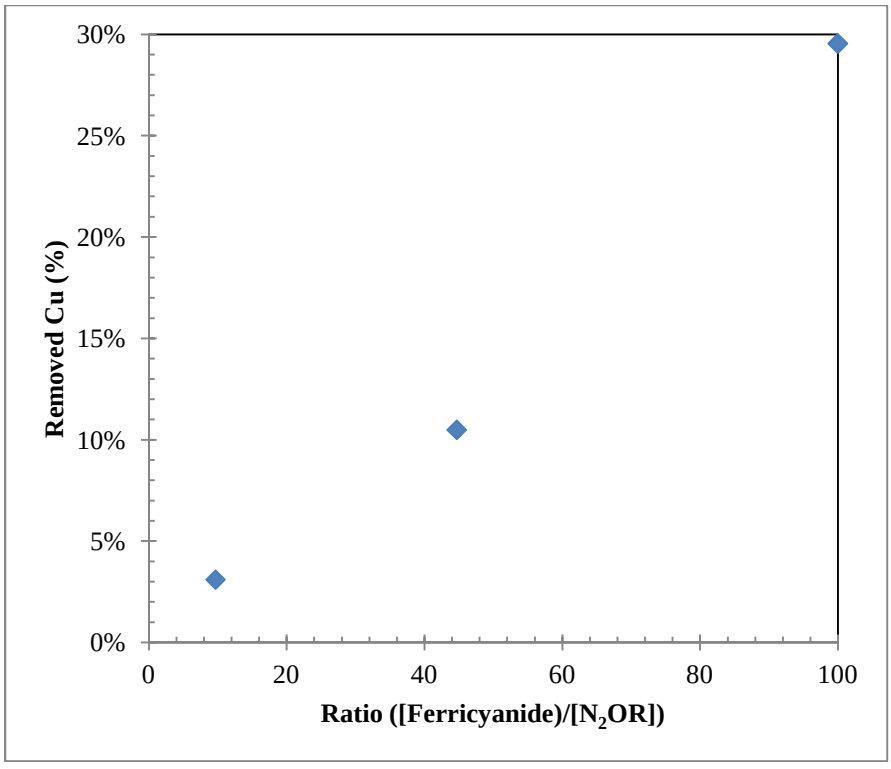


Figure S4.3. UV/Vis spectra of *Ac*N_2OR in Buffer PE

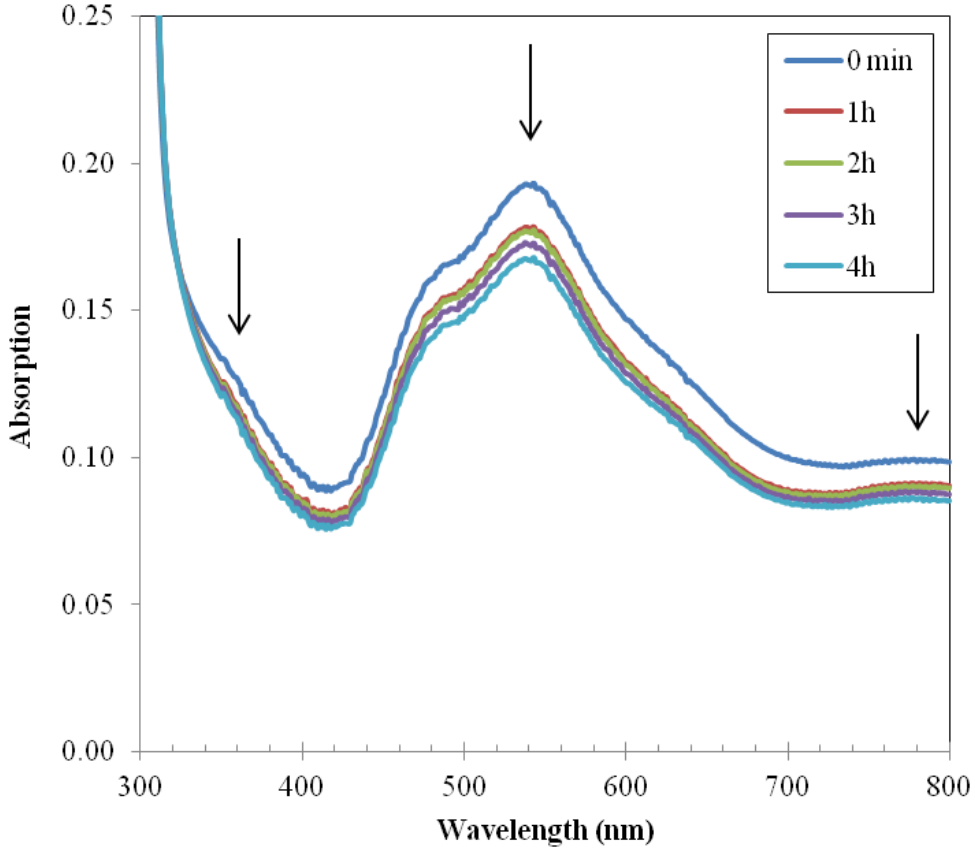
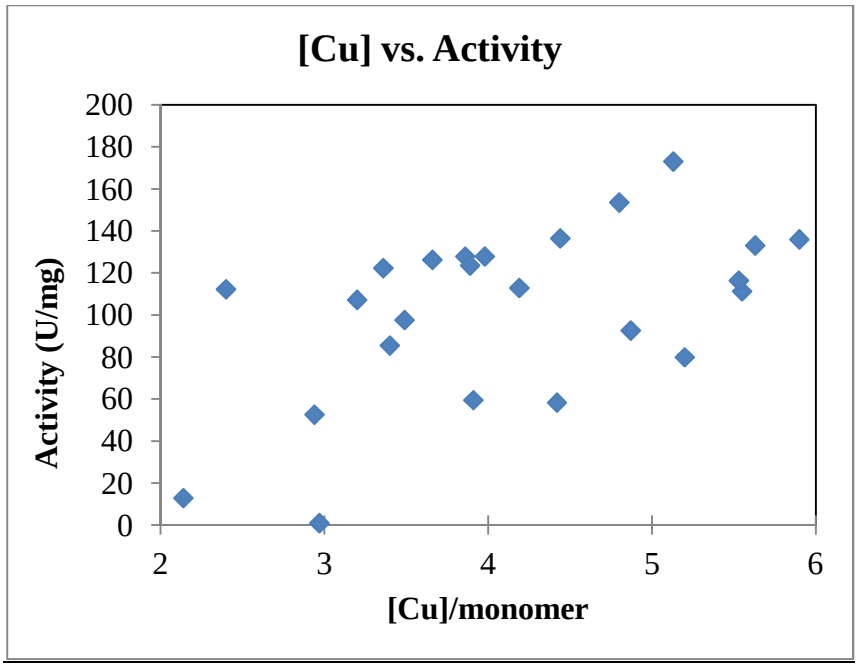


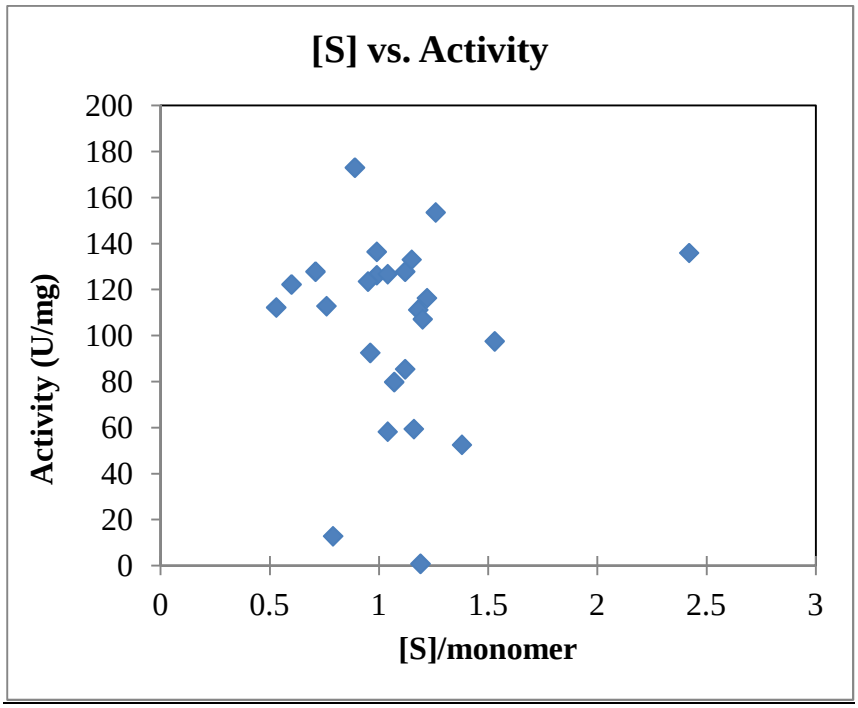
Table S4.2. Concentrations of Cu, sulfide, and activity of N_2OR from different purification batches

Prep #	[Cu]/monomer	[S]/monomer	N_2OR Activity
4	5.55	1.18	111.3
5	3.91	1.16	59.5
6	2.94	1.38	52.6
7	4.42	1.04	58.3
8	3.40	1.12	85.5
9	3.20	1.20	107.2
11	2.97	1.19	0.9
12	3.49	1.53	97.6
13	2.14	0.79	12.9
14	5.20	1.07	79.9
15	4.87	0.96	92.6
18	3.98	1.12	127.9
19	4.44	0.99	136.5
22	2.40	0.53	112.3
23	3.36	0.60	122.3
24	3.66	0.99	126.3
26	3.86	0.71	127.9
27	6.23	1.04	126.8
28	5.90	2.42	136.0
29	3.89	0.95	123.6
30	5.63	1.15	133.1
31	5.13	0.89	173.1
32	4.80	1.26	153.6
33	4.19	0.76	112.9
34	5.53	1.22	116.4
Ave.	4.20	1.09	103.5

(Data set from *Ac*N_2OR prep by Dr. Koyu Fujita)

Figure S4.3. Correlations between Cu or sulfide contents and activity of *Ac*N_2OR (data points are from Table S4.1).





REFERENCES CITED

1. Payne, WJ. Denitrification. 1981.

2. Zehr JP, Kudela RM. Nitrogen cycle of the open ocean: from genes to ecosystems. 2011, *Ann Rev Mar Sci.*, Vol. 3, pp. 197-225.

3. van Spanning RJM, Richardson DJ, Ferguson SJ. Introduction to the Biochemistry and Molecular Biology of Denitrification. Biology of the Nitrogen Cycle. s.l. : Elsevier, 2007, 1, pp. 3-20.

4. Zumft WG, Korner H. Nitrous Oxide Reductases. Biology of the Nitrogen Cycle. s.l. : Elsevier, 2007, 5, pp. 67-81.

5. Berks BC, Ferguson SJ, Moir JW, Richardson DJ. Enzymes and associated electron transport systems that catalyse the respiratory reduction of nitrogen oxides and oxyanions. 3, 1995, *Biochimica et Biophysica Acta*, Vol. 1232, pp. 97-173.

6. Munch JC, Velthof GL. Denitrification anf Agriculture. Biology of the Nitrogen Cycle. s.l. : Elesevier, 2007, 21, pp. 331-341.

7. Tavares P, Pereira AS, Moura JJG, Moura I. Metalloenzymes of the denitrification pathway. 2006, *J Inorg Biochem.*, Vol. 100, pp. 2087-100.

8. Hino T, Nagano S, Sugimoto H, Tosha T, Shiro Y. Molecular structure and function of bacterial nitric oxide reductase. 7, 2012, *Biochim Biophys Acta.*, Vol. 1817, pp. 680-7.

9. Wan S, Mottiar Y, Johnson AM, Goto K, Altosaar I. Expression of the nos operon proteins from *Pseudomonas stutzeri* in transgenic plants to assemble nitrous oxide reductase. 3, 2012, *Transgenic Res.*, Vol. 21, pp. 593-603.

10. Ravishankara AR, Daniel JS, Portmann RW. Nitrous Oxide (N_2O): The Dominant Ozone-Depleting Substance Emitted in the 21st Century. 5949, 2009, *Science*, Vol. 326, pp. 123-125.

11. Fujita K, Chan JM, Bollinger JA, Alvarez ML, Dooley DM. Anaerobic purification, characterization and preliminary mechanistic study of recombinant nitrous oxide reductase from *Achromobacter cycloclastes*.11-12, 2007, *J Inorg Biochem.*, Vol. 101, pp. 1836-44.

12. Zumft, WG. Cell biology and molecular basis of denitrification.4, 1997, *Microbiol Mol Biol Rev.*, Vol. 61, pp. 533-616.

13. Kuňák M, Kučera I, van Spanning RJM. Nitric oxide oscillations in Paracoccus denitrificans: the effects of environmental factors and of segregating nitrite reductase

and nitric oxide reductase into separate cells. 2, 2004, *Arch Biochem Biophys.*, Vol. 429, pp. 237-43.

14. Bakken L, Dorsch P. Nitrous Oxide Emission and Global Changes: Modeling Approaches. Biology of the Nitrogen Cycle. 2007, 25, pp. 381-95.

15. Chèneby D, Perrez S, Devroe C, Hallet C, Couton Y, Bizouard F, Iuretig G, Germon JC, Philippot L. Denitrifying bacteria in bulk and maize-rhizospheric soil: diversity and N_2O-reducing abilities. 7, 2004, *Can J Microbiol.*, Vol. 50, pp. 469-74.

16. Holtan-Hartwig L, Dorsch P, Bakken LR. Comparison of denitrifying communities in organic soils: kinetics of NO-3 and N_2O reduction. 6, 2000, *Soil. Biol. Biochem.*, Vol. 32, pp. 833-43.

17. Stolz JF, Basu P. Evolution of Nitrate Reductase: Molecular and Structural Variations on a Common Function. 2002, *ChemBioChem*, Vol. 3, pp. 198-206.

18. Moura JJG, Brondino CD, Trincao J, Romao MJ. Mo and W bis-MGD enzymes: nitrate reductases and formate dehydrogenases. 2004, *J Biol Inorg Chem*, Vol. 9, pp. 791–799.

19. Bertero MG, Rothery RA, Palak M, Hou C, Lim D, Blasco F, Weiner JH, Strynadka NCJ. Insights into the respiratory electron transfer pathway from the structure of nitrate reductase A. 2003, *Nat Struct Biol.*, Vol. 10, pp. 681-7.

20. Li HT, Chang T, Chang WC, Chen CJ, Liu MY, Gui LL, Zhang JP, An XM, Chang WR. Crystal structure of C-terminal desundecapeptide nitrite reductase from *Achromobacter cycloclastes*. 4, 2005, *Biochem Biophys Res Commun.*, Vol. 338, pp. 1935-42.

21. Sjogren T, Hajdu J. The Structure of an Alternative Form of *Paracoccus pantotrophus* Cytochrome *cd*1 Nitrite Reductase. 31, 2001, *J Biol Chem.*, Vol. 276, pp. 29450-5.

22. Holm RH, Kennepohl P, Solomon EI. Structural and Functional Aspects of Metal Sites in Biology. 1996, *Chem. Rev.*, Vol. 96, pp. 2239-2314.

23. Sakurai T, Kataoka K. Structure and function of type I copper in multicopper oxidases. 19-20, 2007, *Cell Mol Life Sci.*, Vol. 64, pp. 2642-56.

24. Kukimoto M, Nishiyama M, Tanokura M, Adman ET, Horinouchi S. Studies on Protein-Protein Interaction between Copper-containing Nitrite Reductase and Pseudoazurin from *Alcaligenes faecalis* S-6. 23, 1996, *J Biol Chem.*, Vol. 271, pp. 13680-3.

25. Solomon EI, and Bell CB III. Physical Inorganic Chemistry: Principles, Methods, and Reactions. 2010. pp. 1-37.

26. Huang H, Zoppellaro G, Sakurai T. Spectroscopic and Kinetic Studies on the Oxygen-centered Radical Formed during the Four-electron Reduction Process of Dioxygen by Rhus vernicifera Laccase. 46, 1999, *J Biol Chem.*, Vol. 274, pp. 32718-24.

27. Howes BD, Abraham ZHL, Lowe DJ, Bruser T, Eady RR, Smith BE. EPR and electron nuclear double resonance (ENDOR) studies show nitrite binding to the type 2 copper centers of the dissimilatory nitrite reductase of *Alcaligenes xylosoxidans* (NCIMB 11015). 11, 1994, *Biochemistry*., Vol. 33, pp. 3171-7.

28. Antonyuk SV, Strange RW, Sawers G, Eady RR, Hasnain SS. Atomic resolution structures of resting-state, substrate- and product-complexed Cu-nitrite reductase provide insight into catalytic mechanism. 34, 2005, *Proc Natl Acad Sci.*, Vol. 102, pp. 12041-46.

29. Pinho D, Besson S, Brondino CD, de Castro B, Moura I. Copper-containing nitrite reductase from *Pseudomonas chlororaphis* DSM 50135. 12, 2004, *Eur J Biochem*., Vol. 271, pp. 2361-69.

30. Hough MA, Ellis MJ, Antonyuk S, Strange RW, Sawers G, Eady RR, Hasnain SS. High Resolution Structural Studies of Mutants Provide Insights into Catalysis and Electron Transfer Processes in Copper Nitrite Reductase. 2, 2006, *J Mol Biol.*, Vol. 350, pp. 300-309.

31. de Vriesm S, Schroder I. Comparison between the nitric oxide reductase family and its aerobic relatives, the cytochrome oxidases. 4, 2002, *Biochem Soc Trans*., Vol. 30, pp. 662-7.

32. Hino T, Matsumoto Y, Nagano S, Sugimoto H, Fukumori Y, Murata T, Iwata S, Shiro Y. Structural Basis of Biological N_2O Generation by Bacterial Nitric Oxide Reductase. 2010, *Science*, Vol. 330, pp. 1666-70.

33. Kastrau DHW, Heiss B, Kroneck PMH, Zumft WG. Nitric oxide reductase from *Pseudomonas stutzeri*, a novel cytochrome bc complex. 1994, *Eur. J. Biochem.*, Vol. 222, pp. 293-303.

34. Carr GJ, Ferguson SJ. The nitric oxide reductase of *Paracoccus denitrificans*. 2, 1990, *Biochem J*., Vol. 269, pp. 423-429.

35. Kumita H, Matsuura K, Hino T, Takahashi S, Hori H, Fukumori Y, Morishima I, Shiro Y. NO reduction by nitric-oxide reductase from denitrifying bacterium *Pseudomonas aeruginosa*: characterization of reaction intermediates that appear in the single turnover cycle. 53, 2004, *J Biol Chem.*, Vol. 279, pp. 55247-54.

36. Hendriks J, Oubrie A, Castresana J, Urbani A,Gemeinhardt S, Saraste M. Nitric oxide reductases in bacteria. 2-3, 2000, *Biochim Biophys Acta.*, Vol. 1459, pp. 266-73.

37. Householder TC, Fozo EM, Cardinale JA, Clark VL. Gonococcal Nitric Oxide Reductase Is Encoded by a Single Gene, *norB*, Which Is Required for Anaerobic Growth and Is Induced by Nitric Oxide. 9, 2000, *Infect Immun.*, Vol. 68, pp. 5241-6.

38. Huang M, Mei X, Zhang S. Mechanism of nitric oxide production in macrophages treated with medicinal mushroom extracts. 1, 2011, *Int J Med Mushrooms.*, Vol. 13, pp. 1-6.

39. Philippot, L. Denitrification in pathogenic bacteria: for better or worst? 5, 2005, *Trends Microbiol.* Vol. 13, pp. 191-2.

40. Cramm R, Pohlmann A, Friedrich B. Purification and characterization of the single-component nitric oxide reductase from *Ralstonia eutropha* H16. 1, 1999, *FEBS Lett.*, Vol. 460, pp. 6-10.

41. Suharti, Strampraad MJ, Schröder I, de Vries S. A Novel Copper A Containing Menaquinol NO Reductase from *Bacillus azotoformans*. 8, 2001, *Biochemistry.*, Vol. 40, pp. 2632-9.

42. Pichinoty F, de Barjac H, Mandel M, Asselineau J. Description of *Bacillus azotoformans* sp. nov. 3, 1983, *Int J Syst Bacteriol.*, Vol. 33, pp. 660-2.

43. Suharti, Heering HA, de Vries S. NO Reductase from *Bacillus azotoformans* Is a Bifunctional Enzyme Accepting Electrons from Menaquinol and a Specific Endogenous Membrane-Bound Cytochrome c_{551}. 42, 2004, *Biochemistry.*, Vol. 43, pp. 13487-95.

44. Moenne-Loccoz P, de Vries S. Structural Characterization of the Catalytic High-Spin Heme b of Nitric Oxide Reductase: A Resonance Raman Study. 1998, *J. Am. Chem. Soc.*, Vol. 120, pp. 5147-52.

45. Butler CS, Seward HE, Greenwood C, Thomson AJ. Fast cytochrome bo from *Escherichia coli* binds two molecules of nitric oxide at Cu_B. 51, 1997, *Biochemistry*, Vol. 36, pp. 16259-66.

46. Okereke, GU. Growth yield of denitrifiers using nitrous oxide as a terminal electron acceptor. 1993, *World J Microbiol Biotechnol.*, Vol. 9, pp. 59-62.

47. Zheng H, Liu Y, Sun G, Gao X, Zhang Q, Liu Z. Denitrification characteristics of a marine origin psychrophilic aerobic denitrifying bacterium. 11, 2011, *J Environ Sci.*, Vol. 23, pp. 1888-93.

48. Feng L, Wang W, Cheng J, Ren Y, Zhao G, Gao C, Tang Y, Liu X, Han W, Peng X, Liu R, Wang L. Genome and proteome of long-chain alkane degrading *Geobacillus thermodenitrificans* NG80-2 isolated from a deep-subsurface oil reservoir. 13, 2007, *Proc Natl Acad Sci U S A.*, Vol. 104, pp. 5602-7.

49. Mancinelli, RL. The nature of nitrogen: an overview. 1-2, 1996, *Life Support Biosph Sci.*, Vol. 3, pp. 17-24.

50. Honisch U, Zumft WG. Operon Structure and Regulation of the *nos* Gene Region of *Pseudomonas stutzeri*, Encoding an ABC-Type ATPase for Maturation of Nitrous Oxide Reductase. 6, 2003, *J Bacteriol.*, Vol. 185, pp. 1895-1902.

51. Simon J, Einsle O, Kroneck PMH, Zumft WG. The unprecedented *nos* gene cluster of *Wolinella succinogenes* encodes a novel respiratory electron transfer pathway to cytochrome *c* nitrous oxide reductase. 1-3, 2004, *FEBS Lett.*, Vol. 569, pp. 7-12.

52. Chan YK, McCormick WA, Watson RJ. A new *nos* gene downstream from *nosDFY* is essential for dissimilatory reduction of nitrous oxide by *Rhizobium* (*Sinorhizobium*) *meliloti*. 1997, *Microbiology*, Vol. 143, pp. 2817-24.

53. McGuirl MA, Nelson LK, Bollinger JA, Chan YK, Dooley DM. The *nos* (nitrous oxide reductase) gene cluster from the soil bacterium *Achromobacter cycloclastes*: Cloning, sequence analysis, and expression. 3-4, 1998, *Journal of Inorganic Biochemistry*, Vol. 70, pp. 155-169.

54. Zumft WG, Kroneck PMH. Respiratory Transformation of Nitrous Oxide (N_2O) to Dinitrogen by Bacteria and Archaea. 2007, *Advances in Microbial Physiology*, Vol. 52, pp. 109-227.

55. Zumft, WG. Biogenesis of the bacterial respiratory Cu_A, Cu-S enzyme nitrous oxide reductase. 2005, *J Mol Microbiol Biotechnol.*, Vol. 10, pp. 154-66.

56. Dreusch A, Bürgisser DM, Heizmann CW, Zumft WG. Lack of copper insertion into unprocessed cytoplasmic nitrous oxide reductase generated by an R20D substitution in the arginine consensus motif of the signal peptide. 2-3, 1997, *Biochim Biophys Acta.*, Vol. 1319, pp. 311-8.

57. Jones AM, Hollocher TC, Knowles R. Nitrous oxide reductase of Flexibacter canadensis: a unique membrane-bound enzyme. 2, 1992, *FEMS Microbiology Letters*, Vol. 92, pp. 205-209.

58. Hole UH, Vollack KU, Zumft WG, Eisenmann E, Siddiqui RA, Friedrich B, Kroneck PMH. Characterization of the membranous denitrification enzymes nitrite reductase (cytochrome *cd*1) and copper-containing nitrous oxide reductase from *Thiobacillus denitrificans*. 1996, *Arch Microbiol*, Vol. 165, pp. 55-61.

59. Paraskevopoulos K, Antonyuk SV, Sawers RG, Eady RR, Hasnain SS. Insight into catalysis of nitrous oxide reductase from high-resolution structures of resting and inhibitor-bound enzyme from *Achromobacter cycloclastes*. 2006, *J Mol Biol*., Vol. 362, pp. 55-65.

60. Richardson D, Felgate H, Watmough N, Thomson A, Baggs E. Mitigating release of the potent greenhouse gas N_2O from the nitrogen cycle – could enzymic regulation hold the key? 7, 2009, *Trends Biotechnol*., Vol. 27, pp. 388-97.

61. Brown K, Tegoni M, Prudêncio M, Pereira AS, Besson S, Moura JJ, Moura I, Cambillau C. A novel type of catalytic copper cluster in nitrous oxide reductase. 3, 2000, *Nat Struct Biol*., Vol. 7, pp. 191-195.

62. Brown K, Djinovic-Carugo K, Haltia T, Cabrito I, Saraste M, Moura JJG, Moura I, Tegoni M, Cambillau C. Revisiting the catalytic Cu_Z cluster of nitrous oxide (N_2O) reductase. Evidence of a bridging inorganic sulfur. 52, 2000, *J Biol Chem*., Vol. 275, pp. 41133-41136.

63. Pomowski A, Zumft WG, Kroneck PMH, Einsle O. N_2O binding at a [4Cu:2S] copper–sulphur cluster in nitrous oxide reductase. 2011, *Nature*, Vol. 477, pp. 234-237.

64. Savelieff MG, Wilson TD, Elias Y, Nilges MJ, Garner DK, Lu Y. Experimental evidence for a link among cupredoxins: Red, blue, and purple copper transformations in nitrous oxide reductase. 23, 2008, *Proc Natl Acad Sci U S A*., Vol. 105, pp. 7919-24.

65. Holm L, Saraste M, Wikström M. Structural models of the redox centres in cytochrome oxidase. 9, 1987, *EMBO J*., Vol. 6, pp. 2819-2823.

66. Charnock JM, Dreusch A, Korner H, Neese F, Nelson J, Kannt A, Michel H, Garner CD, Kroneck PMH, Zumft WG. Structural investigations of the Cu_A centre of nitrous oxide reductase from *Pseudomonas stutzeri* by site-directed mutagenesis and X-ray absorption spectroscopy. 2000, *Eur. J. Biochem*., Vol. 267, pp. 1368-81.

67. Gamelin DR, Randall DW, Hay MT, Houser RP, Mulder TC, Canters GW, de Vries S, Tolman WB, Lu Y, Solomon EI. Spectroscopy of Mixed-Valence Cu_A-Type Centers: Ligand-Field Control of Ground-State Properties Related to Electron Transfer. 21, 1998, *J. Am. Chem. Soc*., Vol. 120, pp. 5246-5263.

68. Rasmussen T, Berks BC, Butt JN, Thomson AJ. Multiple forms of the catalytic centre, Cu_Z, in the enzyme nitrous oxide reductase from *Paracoccus pantotrophus*. 2002, *Biochem J*., Vol. 364, pp. 807-815.

69. Dell'Acqua S, Pauleta SR, Moura I, Moura JJG. The tetranuclear copper active site of nitrous oxide reductase: the Cu_Z center. 2011, *J Biol Inorg Chem*, Vol. 16, pp. 183–194.

70. Ghosh S, Gorelsky SI, Chen P, Cabrito I, Moura JJ, Moura I, Solomon EI. Activation of N_2O Reduction by the Fully Reduced μ4-Sulfide Bridged Tetranuclear Cu_Z Cluster in Nitrous Oxide Reductase. 51, 2003, *J Am Chem Soc*., Vol. 125, pp. 15708-9.

71. Gorelsky SI, Ghosh S, Solomon EI. Mechanism of N_2O Reduction by the μ4-S Tetranuclear Cu_Z Cluster of Nitrous Oxide Reductase. 2006, *J Am Chem Soc*., Vol. 128, pp. 278-90.

72. Rasmussen T, Berks BC, Sanders-Loehr J, Dooley DM, Zumft WG, Thomson AJ. The Catalytic Center in Nitrous Oxide Reductase, Cu_Z, Is a Copper-Sulfide Cluster. 2000, *Biochemistry*, Vol. 39, pp. 12753-56.

73. Alvarez ML, Ai J, Zumft WG, Sanders-Loehr J, Dooley DM. Characterization of the Copper-Sulfur Chromophores in Nitrous Oxide Reductase by Resonance Raman Spectroscopy: Evidence for Sulfur Coordination in the Catalytic Cluster. 2001, *J. Am. Chem. Soc*., Vol. 123, pp. 576-87.

74. Haltia T, Brown K, Tegoni M, Cambillau C, Saraste M, Mattila K, Djinovic-Carugo K. Crystal structure of nitrous oxide reductase from *Paracoccus denitrificans* at 1.6 A resolution. 2003, *Biochem. J*., Vol. 369, pp. 77-88.

75. Rasmussen T, Brittain T, Berks BC, Watmough NJ, Thomson AJ. Formation of a cytochrome *c*–nitrous oxide reductase complex is obligatory for N_2O reduction by *Paracoccus pantotrophus*. 2005, *Dalton Trans*., Vols. 3501-3505.

76. Page CC, Moser CC, Chen X, Dutton PL. Natural engineering principles of electron tunnelling in biological oxidation-reduction. 6757, 1999, *Nature*, Vol. 402, pp. 47-52.

77. Chan JM, Bollinger JA, Grewell CL, Dooley DM. Reductively activated nitrous oxide reductase reacts directly with substrate. 10, 2004, *J Am Chem Soc*., Vol. 126, pp. 3030-3031.

78. Coyle CL, Zumft WG, Kroneck PMH, Korner H, Jakob W. Nitrous oxide reductase from denitrifying *Pseudomonas perfectomarina*. Purification and properties of a novel multicopper enzyme. 3, 1985, *Eur J Biochem.*, Vol. 153, pp. 159-67.

79. Chen P, Cabrito I, Moura JJG, Moura I, Solomon EI. Spectroscopic and Electronic Structure Studies of the μ4-Sulfide Bridged Tetranuclear Cu_Z Cluster in N_2O Reductase: Molecular Insight into the Catalytic Mechanism. 35, 2002, *J Am Chem Soc.*, Vol. 124, pp. 10497-507.

80. Dooley DM, Alvarez ML, Rosenzweig AC, Hollis RS, Zumft WG. Exogenous ligand binding to *Pseudomonas stutzeri* nitrous oxide reductase. 1996, *Inorganica Chimica Acta.*, Vol. 242, pp. 239-44.

81. Ghosh S, Gorelsky SI, George SD, Chan JM, Cabrito I, Dooley DM, Moura JJG, Moura I, Solomon EI. Spectroscopic, computational, and kinetic studies of the μ4-sulfide-bridged tetranuclear Cu_Z cluster in N_2O reductase: pH effect on the edge ligand and its contribution to reactivity. 13, 2007, *J Am Chem Soc.*, Vol. 129, pp. 3955-65.

82. Wunsch P, Zumft WG. Functional domains of NosR, a novel transmembrane iron-sulfur flavoprotein necessary for nitrous oxide respiration. 6, 2005, *J Bacteriol.*, Vol. 187, pp. 1992-2001.

83. Wunsch P, Körner H, Neese F, van Spanning RJM, Kroneck PMH, Zumft WG. NosX function connects to nitrous oxide (N_2O) reduction by affecting the Cu_Z center of NosZ and its activity *in vivo*. 21, 2005, *FEBS Letters*, Vol. 579, pp. 4605-4609.

84. Dell'Acqua S, Pauleta SR, Moura JJG, Moura I. Biochemical characterization of the purple form of *Marinobacter hydrocarbonoclasticus* nitrous oxide reductase. 1593, 2012, *Philos Trans R Soc Lond B Biol Sci.*, Vol. 367, pp. 1204-12.

85. Hira D, Nojiri M, Suzuki S. Atomic resolution structure of pseudoazurin from the methylotrophic denitrifying bacterium *Hyphomicrobium denitrificans*: structural insights into its spectroscopic properties. 2009, *Acta Crystallogr D Biol Crystallogr.*, Vol. 65, pp. 85-92.

86. Kukimoto M, Nishiyama M, Ohnuki T, Turley S, Adman ET, Horinouchi S, Beppu T. Identification of interaction site of pseudoazurin with its redox partner, copper-containing nitrite reductase from *Alcaligenes faecalis* S-6. 2, 1995, *Protein Engineering*, Vol. 8, pp. 153-158.

87. Williams PA, Fülöp V, Leung YC, Chan C, Moir JWB, Howlett G, Ferguson SJ, Radford SE, Hajdu J. Pseudospecific docking surfaces on electron transfer proteins as

illustrated by pseudoazurin, cytochrome c_{550} and cytochrome *cd*1 nitrite reductase. 1995, *Nature Structural Biology*, Vol. 2, pp. 975-982.

88. Pearson IV, Page MD, van Spanning RJM, Ferguson SJ. A Mutant of *Paracoccus denitrificans* with Disrupted Genes Coding for Cytochrome c_{550} and Pseudoazurin Establishes These Two Proteins as the *In Vivo* Electron Donors to Cytochrome *cd*1 Nitrite Reductase. 21, 2003, *JOURNAL OF BACTERIOLOGY*, Vol. 185, pp. 6308–6315.

89. Moir JWB, Ferguson SJ. Properties of a *Paracoccus denitrificans* mutant deleted in cytochrome c_{550} indicate that a copper protein can substitute for this cytochrome in electron transport to nitrite, nitric oxide and nitrous oxide. 2, 1994, *Microbiology*, Vol. 140, pp. 389-97.

90. Berks BC, Baratta D, Richardson DJ, Ferguson SJ. Purification and characterization of a nitrous oxide reductase from *Thiosphaera pantotropha*. 2, 1993, *Eur J Biochem.*, Vol. 212, pp. 467-76.

91. Fujita K, Hirasawa-Fujita M, Brown DE, Obara Y, Ijima F, Kohzuma T, Dooley DM. Direct electron transfer from pseudoazurin to nitrous oxide reductase in catalytic N_2O reduction. 2012, *J Inorg Biochem.*, Vol. 115, pp. 163-73.

92. Mattila K, Haltia T. How does nitrous oxide reductase interact with its electron donors? - A docking study. 2005, *Proteins*, Vol. 59, pp. 708-722.

93. Dell'Acqua S, Moura I, Moura JJG, Pauleta SR. The electron transfer complex between nitrous oxide reductase and its electron donors. 8, 2011, *J Biol Inorg Chem.*, Vol. 16, pp. 1241-54.

94. Sam KA, Fairhurst SA, Thorneley RN, Allen JW, Ferguson SJ. Pseudoazurin dramatically enhances the reaction profile of nitrite reduction by *Paracoccus pantotrophus* cytochrome *cd*1 and facilitates release of product nitric oxide. 18, 2008, *J Biol Chem.*, Vol. 283, pp. 12555-12563.

95. Zumft WG, Viebrock-Sambale A, Braun C. Nitrous oxide reductase from denitrifying *Pseudomonas stutzeri*: Genes for copper-processing and properties of the deduced products, including a new member of the family of ATP/GTP-binding proteins. 1990, *Eur. J. Biochcm.*, Vol. 192, pp. 591-599.

96. Hoeren FU, Berks BC, Ferguson SJ, McCarthy JEG. Sequence and expression of the gene encoding the respiratory nitrous-oxide reductase from *Paracoccus denitrificans* New and conserved structural and regulatory motifs. 1993, *Eur. J. Biochem.*, Vol. 218, pp. 49-57.

97. Holloway P, McCormick W, Watson RJ, Chan Y. Identification and Analysis of the Dissimilatory Nitrous Oxide Reduction Genes, *nosRZDFY*, of *Rhizobium meliloti*. 6, 1996, *J Bacteriol*., Vol. 178, pp. 1505-14.

98. Arai H, Mizutani M, Igarashi Y. Transcriptional regulation of the *nos* genes for nitrous oxide reductase in *Pseudomonas aeruginosa*. 2003, *Microbiology*, Vol. 149, pp. 29-36.

99. Velasco L, Mesa S, Xu C, Delgado MJ, Bedmar EJ. Molecular characterization of *nosRZDFYLX* genes coding for denitrifying nitrous oxide reductase of *Bradyrhizobium japonicum*. 2004, *Antonie Van Leeuwenhoek.*, Vol. 85, pp. 229-35.

100. Wunsch P, Herb M, Wieland H, Schiek UM, Zumft WG. Requirements for Cu(A) and Cu-S center assembly of nitrous oxide reductase deduced from complete periplasmic enzyme maturation in the nondenitrifier *Pseudomonas putida*. 3, 2003, *J Bacteriol*., Vol. 185, pp. 887-96.

101. Bergaust L, van Spanning RJM, Frostegård Å, Bakken LR. Expression of nitrous oxide reductase in *Paracoccus denitrificans* is regulated by oxygen and nitric oxide through FnrP and NNR. Pt 3, 2012, *Microbiology*., Vol. 158, pp. 826-34.

102. Arai H, Kodama T, Igarashi Y. Cascade regulation of the two CRP/FNR-related transcriptional regulators (ANR and DNR) and the denitrification enzymes in *Pseudomonas aeruginosa*. 6, 1997, *Mol Microbiol*., Vol. 25, pp. 1141-8.

103. Vollack KU, Zumft WG. Nitric oxide signaling and transcriptional control of denitrification genes in *Pseudomonas stutzeri*. 8, 2001, *J Bacteriol*., Vol. 183, pp. 2516-26.

104. Torres MJ, Rubia MI, Bedmar EJ, Delgado MJ. Denitrification in *Sinorhizobium meliloti*. 6, 2011, *Biochem Soc Trans*., Vol. 39, pp. 1886-9.

105. Körner H, Zumft WG. Expression of denitrification enzymes in response to the dissolved oxygen level and respiratory substrate in continuous culture of *Pseudomonas stutzeri*. 7, 1989, *Appl Environ Microbiol*., Vol. 55, pp. 1670-6.

106. Cuypers H, Viebrock-Sambale A, Zumft WG. NosR, a membrane-bound regulatory component necessary for expression of nitrous oxide reductase in denitrifying *Pseudomonas stutzeri*. 16, 1992, *J Bacteriol*., Vol. 174, pp. 5332-5339.

107. Dooley DM, McGuirl MA, Rosenzweig AC, Landin JA, Scott RA, Zumft WG, Devlin F, Stephens PJ. Spectroscopic studies of the copper sites in wild-type *Pseudomonas stutzeri* N_2O reductase and in an inactive protein isolated from a mutant deficient in copper-site biosynthesis. 1991, *Inorg. Chem*., Vol. 30, pp. 3006-11.

108. McGuirl MA, Bollinger JA, Cosper N, Scott RA, Dooley DM. Expression, purification, and characterization of NosL, a novel Cu(I) protein of the nitrous oxide reductase (*nos*) gene cluster. 2001, *J Biol Inorg Chem*, Vol. 6, pp. 189-95.

109. Fath MJ, Kolter R. ABC Transporters: Bacterial Exporters. 4, 1993, *Microbiol Rev.*, Vol. 57, pp. 995-1017.

110. Zumft WG, Kroneck PMH, Hausinger RP, Eichorn GL, Marzilli LG. Mechanisms of Metallocenter Assembly. New York : VCH Publishers, 1996. p. 193.

111. Ciccarelli FD, Copley RR, Doerks T, Russell RB, Bork P. CASH- a b-helix domain widespread among carbohydrate-binding proteins. 2002, *Trends Biochem Sci.*, Vol. 27, pp. 59-62.

112. Taubner LM, McGuirl MA, Dooley DM, Copié V. Structural Studies of Apo NosL, an Accessory Protein of the Nitrous Oxide Reductase System: Insights from Structural Homology with MerB, a Mercury Resistance Protein. 40, 2006, *Biochemistry*, Vol. 45, pp. 12240-52.

113. Dreusch A, Riester J, Kroneck PMH, ZUMFT WG. Mutation of the conserved Cys165 outside of the Cu_A domain destabilizes nitrous oxide reductase but maintains its catalytic activity. Evidence for disulfide bridges and a putative protein disulfide isomerase gene. 1996, *Eur. J. Biochem.*, Vol. 237, pp. 447-53.

114. Saunders NF, Hornberg JJ, Reijnders WN, Westerhoff HV, de Vries S, van Spanning RJ. The NosX and NirX proteins of *Paracoccus denitrificans* are functional homologues: their role in maturation of nitrous oxide reductase. 18, 2000, *J Bacteriol.*, Vol. 182, pp. 5211-5217.

115. Philippot, L. Denitrifying genes in bacterial and Archaeal genomes. 3, 2002, *Biochim Biophys Acta.*, Vol. 1577, pp. 355-76.

116. Vollack K, Xie J, Hartig E, Romling U, Zumft WG. Localization of denitrification genes on the chromosomal map of *Pseudomonas aeruginosa*. 2, 1998, *Microbiology.*, Vol. 144, pp. 441-8.

117. Philippot L, Mirleau P, Mazurier S, Siblot S, Hartmann A, Lemanceau P, Germon JC. Characterization and transcriptional analysis of *Pseudomonas fluorescens* denitrifying clusters containing the *nar*, *nir*, *nor* and *nos* genes. 3, 2001, *Biochim Biophys Acta.*, Vol. 1517, pp. 436-40.

118. Viebrock A, Zumft WG. Molecular Cloning, Heterologous Expression, and Primary Structure of the Structural Gene for the Copper Enzyme Nitrous Oxide Reductase

from Denitrifying *Pseudomonas stutzeri*. 10, 1988, *J Bacteriol*., Vol. 170, pp. 4658-68.

119. Beck BJ, Downs DM. A periplasmic location is essential for the role of the ApbE lipoprotein in thiamine synthesis in *Salmonella typhimurium*. 23, 1999, *J Bacteriol*., Vol. 181, pp. 7285-7290.

120. Skovran E, Downs DM. Lack of the ApbC or ApbE protein results in a defect in Fe-S cluster metabolism in *Salmonella enterica serovar Typhimurium*. 2003, *J Bacteriol*., Vol. 185, pp. 98-106.

121. Boyd JM, Endrizzi JA, Hamilton TL, Christopherson MR, Mulder DW, Downs DM, Peters JW. FAD binding by ApbE protein from *Salmonella enterica*: a new class of FAD-binding proteins. 4, 2011, *J Bacteriol*., Vol. 193, pp. 887-95.

122. Volkl P, Huber R, Drobner E, Rachel R, Burggraf S, Trincone A, Stetter KO. *Pyrobaculum aerophilum sp. nov*., a novel nitrate-reducing hyperthermophilic archaeum. 9, 1993, *Appl Environ Microbiol*., Vol. 59, pp. 2918-26.

123. Davidson EA, Bustamante MM, de Siqueira Pinto A. Emissions of nitrous oxide and nitric oxide from soils of native and exotic ecosystems of the Amazon and Cerrado regions of Brazil. 2, 2001, *ScientificWorldJournal*., Vol. 1, pp. 312-319.

124. Labes M, Pühler A, Simon R. A new family of RSF1010-derived expression and lac-fusion broad-host-range vectors for gram-negative bacteria. 1, 1990, *Gene*, Vol. 89, pp. 37-46.

125. Henery, SM. PhD thesis: Purification and characterization of gene products of the nitrous oxide reductase gene cluster. 2001.

126. McGuirl, MA. PhD thesis: Characterization of NosL, a Novel Cu(I) Protein of the Nitrous Oxide Reductase Gene Cluster. 1999.

127. Rodionov DA, Dubchak IL, Arkin AP, Alm EJ, Gelfand MS. Dissimilatory metabolism of nitrogen oxides in bacteria: comparative reconstruction of transcriptional networks. 5, 2005, *PLoS Comput Biol*., Vol. 1, pp. 415-31.

128. Vollack KU, Härtig E, Körner H, Zumft WG. Multiple transcription factors of the FNR family in denitrifying *Pseudomonas stutzeri*: characterization of four *fnr*-like genes, regulatory responses and cognate metabolic processes. 6, 1999, *Mol Microbiol.*, Vol. 31, pp. 1681-94.

129. Lloyd, D. Aerobic denitrification in soils and sediments: From fallacies to facts. 10, 1993, *Trends Ecol Evol*., Vol. 8, pp. 352-6.

130. Thomsen JK, Geest T, Cox RP. Mass Spectrometric Studies of the Effect of pH on the Accumulation of Intermediates in Denitrification by *Paracoccus denitrificans*. 2, 1994, *Appl Environ Microbiol*., Vol. 60, pp. 536-41.

131. Strep-tag Purification Protocol. s.l. : IBA, 2007.

132. Saunders NF, Houben EN, Koefoed S, de Weert S, Reijnders WN, Westerhoff HV, De Boer AP, Van Spanning RJ. Transcription regulation of the *nir* gene cluster encoding nitrite reductase of *Paracoccus denitrificans* involves NNR and NirI, a novel type of membrane protein. 1, 1999, *Mol Microbiol*., Vol. 34, pp. 24-36.

133. Aliverti A, Curti B, Vanoni MA. Identifying and quantifying FAD and FMN in simple and in iron-sulfur-containing flavoproteins. Methods in Molecular Biology:Flavoprotein Protocols. s.l. : Humana Press, 1999, Vol. 131, pp. 1-9.

134. Ijima F, Brown DE, Fujita K, Henery SM, Okonski KM, Bollinger JA, Dooley DM. Electron Transfer to Nitrous Oxide Reductase by the Flavoprotein NosX from *Achromobacter cycloclastes*. (paper in preparation).

135. Massey, V. A simple method for the determination of redox potentials. 1990. *Proceedings of the Tenth International Symposium*. pp. 59-66.

136. Lei B, Wang H, Yu Y, Tu SC. Redox Potential and Equilibria in the Reductive Half-Reaction of Vibrio harveyi NADPH−FMN Oxidoreductase. 2005, *Biochemistry*, Vol. 44, pp. 261-7.

137. Meiler J, Baker D. Coupled prediction of protein secondary and tertiary structure. 21, 2003, *Proc Natl Acad Sci U S A.*, Vol. 100, pp. 12105-10.

138. Jones, DT. GenTHREADER: an efficient and reliable protein fold recognition method for genomic sequences. 4, 1999, *J Mol Biol*., Vol. 287, pp. 797-815.

139. Akiyama Y, Onizuka K, Noguchi T, Ando M. Parallel Protein Information Analysis (PAPIA) system running on a 64-node PC Cluster. 1998, *Genome Inform Ser Workshop Genome Inform*., Vol. 9, pp. 131-40.

140. Notredame C, Higgins D, Heringa J. T-Coffee: A novel method for multiple sequence alignments. 2000, Journal of Molecular Biology, Vol. 302, pp. 205-17.

141. Arnold K, Bordoli L, Kopp J, Schwede T. The SWISS-MODEL Workspace: A web-based environment for protein structure homology modelling. 2006, *Bioinformatics*, Vol. 22, pp. 195-201.

142. Baker NA, Sept D, Joseph S, Holst MJ, McCammon JA. Electrostatics of nanosystems: application to microtubules and the ribosome. 2001, *Proc. Natl. Acad. Sci. USA*, Vol. 98, pp. 10037-41.

143. Rother, K. rTools 0.7.2. [Online] http://www.rubor.de/pymol_extensions_en.html.

144. Larkin MA, Blackshields G, Brown NP, Chenna R, McGettigan PA, McWilliam H, Valentin F, Wallace IM, Wilm A, Lopez R, Thompson JD, Gibson TJ, Higgins DG. ClustalW and ClustalX version 2. s.l. : 23, 2007, *Bioinformatics* , Vol. 21, pp. 2947-48.

145. [Online] http://www.ch.embnet.org/software/BOX_form.html.

146. Minnaert, K. Measurement of the equilibrium constant of the reaction between cytochrome *c* and cytochrome *a*. 1965, *Biochim. Biophys. Acta*, Vol. 110, pp. 42-56.

147. Kohzuma T, Dennison C, McFarlane W, Nakashima S, Kitagawa T, Inoue T, Kai Y, Nishio N, Shidara S, Suzuki S, Sykes AG. Spectroscopic and electrochemical studies on active-site transitions of the type 1 copper protein pseudoazurin from *Achromobacter cycloclastes*. 43, 1995, *J Biol Chem.*, Vol. 270, pp. 25733-8.

148. Dym O, and Eisenberg D. Sequence-structure analysis of FAD-containing proteins. 9, 2001, *Protein Sci.*, Vol. 10, pp. 1712-28.

149. Chapman SK, Reid GA. Flavoprotein Protocols. 1999. Vol. 131.

150. Dell'acqua S, Pauleta SR, Monzani E, Pereira AS, Casella L, Moura JJG, Moura I. Electron transfer complex between nitrous oxide reductase and cytochrome c_{552} from *Pseudomonas nautica*: kinetic, nuclear magnetic resonance, and docking studies. 41, 2008, *Biochemistry.*, Vol. 47, pp. 10852-62.

151. Abdelhamid RF, Obara Y, Uchida Y, Kohzuma T, Dooley DM, Brown DE, Hori H. Pi–pi interaction between aromatic ring and copper-coordinated His81 imidazole regulates the blue copper active-site structure. 2, 2007, *J Biol Inorg Chem.*, Vol. 12, pp. 165-73.

152. Rajan RS, Tsumoto K, Tokunaga M, Tokunaga H, Kita Y, Arakawa T. Chemical and pharmacological chaperones: application for recombinant protein production and protein folding diseases. 1, 2011, *Curr Med Chem.*, Vol. 18, pp. 1-15.

153. Andi B, West AH, Cook PF. Stabilization and characterization of histidine-tagged homocitrate synthase from *Saccharomyces cerevisiae*. 2, 2004, *Arch Biochem Biophys.*, Vol. 421, pp. 243-54.

154. Bachrach, U. Naturally Occurring Polyamines: Interaction with Macromolecules. 6, 2005, *Curr Protein Pept Sci.*, Vol. 6, pp. 559-66.

155. Miller AW, Robyt JF. Stabilization of dextransucrase from *Leuconostoc mesenteroides NRRL B-512F* by nonionic detergents, poly(ethylene glycol) and high-molecular-weight dextran. 3, 1984, *Biochim Biophys Acta*., Vol. 785, pp. 89-96.

156. Chen P, DeBeer George S, Cabrito I, Antholine WE, Moura JJ, Moura I, Hedman B, Hodgson KO, Solomon EI. Electronic Structure Description of the μ4-Sulfide Bridged Tetranuclear Cu_Z. 2002, *J. Am. Chem. Soc*., Vol. 124, pp. 744-5.

157. Lappalainen P, Aasa R, Malmström BG, Saraste M. Soluble Cu_A-binding domain from the *Paracoccus* cytochrome *c* oxidase. 35, 1993, *J Biol Chem*., Vol. 268, pp. 26416-21.

158. Moir JWB, Baratta D, Richardson DJ, Ferguson SJ. The purification of a *cd*1-type nitrite reductase from, and the absence of a copper-type nitrite reductase from, the aerobic denitrifier *Thiosphaera pantotropha*; the role of pseudoazurin as an electron donor. 2, 1993, *Eur J Biochem*., Vol. 212, pp. 377-85.

159. Kataoka K, Kondo A, Yamaguchi K, Suzuki S. Spectroscopic and electrochemical properties of the Met86Gln mutant of *Achromobacter cycloclastes* pseudoazurin. 1-4, 2000, *J Inorg Biochem*., Vol. 82, pp. 79-84.

160. Zhao K, Marmorstein R. Protein Co-crystallization for X-ray Structure Determination. 2005. pp. 301-15.

161. Nojiri M, Koteishi H, Nakagami T, Kobayashi K, Inoue T, Yamaguchi K, Suzuki S. Structural basis of inter-protein electron transfer for nitrite reduction in denitrification. 7269, 2009, *Nature*, Vol. 462, pp. 117-20.

162. Newman, J. A review of techniques for maximizing diffraction from a protein crystal in stilla. 1, 2006, *Acta Crystallogr D Biol Crystallogr*., Vol. 62, pp. 27-31.

163. Lusty, CJ. A gentle vapor-diffusion technique for cross-linking of protein crystals for cryocrystallography. 1999, *J Appl Crystallogr*., Vol. 32, pp. 106-12.

164. Churbanova IY, Poulos TL, Sevrioukova IF. Production and characterization of a functional putidaredoxin reductase-putidaredoxin covalent complex. 1, 2010, *Biochemistry*, Vol. 49, pp. 58-67.

165. Poulos TL, Sheriff S, Howard AJ. Cocrystals of yeast cytochrome *c* peroxidase and horse heart cytochrome *c*. 29, 1987, *J Biol Chem*., Vol. 262, pp. 13881-4.

166. Warkentin M, Berejnov V, Husseini NS, Thorne RE. Hyperquenching for protein cryocrystallography. 6, 2010, *J Appl Crystallogr*., Vol. 39, pp. 805-11.

167. Grabarek Z, Gergely J. Zero-length crosslinking procedure with the use of active esters. 1, 1990, *Anal Biochem*., Vol. 185, pp. 131-5.

168. Abramoff MD, Magalhaes PJ, Ram SJ. Image Processing with ImageJ. 7, 2004, *Biophotonics International*, Vol. 11, pp. 36-42.

169. Bergfors, T. Seeds to crystals. 2003, *J Struct Biol*., Vol. 142, pp. 66-76.